Ultrafast Acoustic Strain Generation and Effects in Semiconductor Nanostructures

ERIC SZE KIT YOUNG, MSci(Hons) AMInstP

Thesis Submitted to the University of Nottingham
for the Degree of Doctor of Philosophy
December 2014

Abstract

The nature of ultrafast acoustic strain generation and effects in III-V semiconductor-based nanostructures is explored in this thesis via experimental observations that are supported by theoretical analysis.

Specifically, coherent phonon generation processes in bulk gallium arsenide (GaAs) are investigated through remote hypersonic detection using a double quantum well-embedded *p-i-n* diode, after which strain-induced effects in a double barrier quantum well resonant tunnelling diode are examined. Finally, preliminary studies on acoustic modulation of a double barrier quantum dot resonant tunnelling diode are also considered, with recommendations for future experimentation.

It was experimentally observed that the transduction of strain in bulk GaAs produces an initial acoustic wavepacket that is strongly asymmetric with a heavily damped leading edge. This was determined to be due to photogeneration of a supersonically expanding electron-hole plasma near the irradiated GaAs surface. Coupled with its propagation from the free surface, the plasma generates stress and therefore strain in the system that is caused by a combination of the deformation potential and thermoelasticity; the former and latter are shown to be dominant for low and high optical excitation densities, respectively. These acoustic waves cannot escape the plasma until it has decelerated to subsonic velocities, which is achieved in a finite time, thus resulting in the observed asymmetry and damped leading edge. This finite acoustic escape time was reduced at high optical excitation densities due to plasma expansion limitation by increased non-radiative Auger recombination of electron-hole pairs.

This conclusion is substantiated by analytical expressions derived from the inhomogeneous wave equation, and analysis of the spatially- and temporally-expanding plasma density based on the deformation potential mechanism only. Numerical simulations based on these expressions are fitted to the experimental data, and the thermoelasticity contribution at high excita-

tion densities is deduced from a non-linear deviation of the electron-hole recombination rate and a change in the duration of the leading edge. This contribution expressed a square-law behaviour in the former parameter, which is attributed to non-radiative Auger processes.

Strain-induced effects on a double barrier quantum well resonant tunnelling diode resulted in the detection of current modulation on a picosecond timescale only when the device was biased within its resonance region, with the largest modulations at the resonance threshold and peak biases. Through analysis of the device structure and stationary current-voltage characteristics, it is demonstrated that the observed current changes are due to variations of the resonant tunnelling rate caused by acoustic modulation of the confined ground state energies in the diode itself.

Numerical analysis of the tunnelling rates provided excellent agreement with the experimental data, particularly when comparing charge transfer rates, where the limited temporal response of the experimental device could be ignored. Furthermore, the charge transferred at the resonance threshold and peak has a set polarity regardless of optical excitation density, and therefore the device possesses "rectifying" behaviour. As such, it has been demonstrated that, by exploiting this *acoustoelectronic pumping effect*, control of picosecond charge transfer in a resonant tunnelling diode or its application as a hypersonic detector are possible.

In closing, the mechanisms for strain generation in bulk GaAs and the utilisation of the *acoustoelectronic pumping effect* in a double barrier quantum well resonant tunnelling diode are both exhibited in this work, and provide promising evidence and novel hypersonic detection methods for future research into ultrafast acoustic effects in semiconductor nanostructures.

Publications and Conferences

The following four papers were published during the course of this degree, and the second and third papers are directly related to the work presented in Chapters 5 and 4 of this thesis, respectively,

A. V. Akimov, E. S. K. Young, J. S. Sharp, V. Gusev, and A. J. Kent. Coherent hypersonic closed-pipe organ like modes in supported polymer films. *Applied Physics Letters*, 99(2):021912, July 2011. doi: 10.1063/1.3605567. URL http://scitation.aip.org/content/aip/journal/apl/99/2/10.1063/1.3605567.

E. S. K. Young, A. V. Akimov, M. Henini, L. Eaves, and A. J. Kent. Subterahertz Acoustical Pumping of Electronic Charge in a Resonant Tunneling Device. *Physical Review Letters*, 108:226601, May 2012. doi: 10.1103/PhysRevLett.108.226601. URL http://link.aps.org/doi/10.1103/PhysRevLett.108.226601.

E. S. K. Young, A. V. Akimov, R. P. Campion, A. J. Kent, and V. Gusev. Picosecond strain pulses generated by a supersonically expanding electron-hole plasma in GaAs. *Physical Review B*, 86:155207, October 2012. doi: 10.1103/PhysRevB.86.155207. URL http://link.aps.org/doi/10.1103/PhysRevB.86.155207.

E. S. K. Young, A. D. Bouravleuv, G. E. Cirlin, V. Dhaka, H. Lipsanen, M. Tchernycheva, A. V. Scherbakov, A. V. Platonov, A. V. Akimov, and A. J. Kent. Electrical detection of picosecond acoustic pulses in vertical transport devices with nanowires. *Applied Physics Letters*, 104(6):062102, February 2014. doi: 10.1063/1.4864637. URL http://scitation.aip.org/content/aip/journal/apl/104/6/10.1063/1.4864637.

The experiments conducted in Chapter 5 were also selected for a contributed oral presentation at

XIV International Conference on Phonon Scattering in Condensed Matter *Phonons 2012*, 8–12 July 2012, University of Michigan, Ann Arbor, Michigan, USA,

with funding gratefully received from the University of Nottingham School of Physics & Astronomy, the University of Nottingham Kilby Scholarship, and the Institute of Physics C. R. Barber Trust Fund.

Acknowledgements

First and foremost, I would like to thank both my doctoral supervisors, Professor Anthony Kent and Professor Andrey Akimov, whose insight, understanding, and steadfast support have been invaluable to the success of my work.

Special thanks must also be given to Professor Mohamed Henini and Dr Richard Campion for their epitaxial growth of some exceptional samples, as well as Professor Vitalyi Gusev for his experience in the theoretical basis of my work, and Professor Laurence Eaves for enlightened discussions regarding resonant tunnelling diodes. I am also indebted to Dr Oleg Makarovsky for locating single quantum dot samples when I could not, and to the Engineering and Physical Sciences Research Council (EPSRC) for funding my research.

I would also like to extend my gratitude to Dr Dan Moss for providing a springboard for my research, Dr Ryan Beardsley and Dr Maryam Kamil for their indispensable support and assistance throughout my doctoral studies, especially in its formative years, and Sarah Heywood and Caroline Poyser for enduring my writing woes towards the end.

In addition, I am grateful to all the staff at the University of Nottingham School of Physics & Astronomy, particularly Jas Chauhan, Dave Holt, Chris Pallender, Mike Parker, Andy Stuart, Dave Taylor, and Ian Taylor, whose technical assistance and knowledge have been indispensable for my research. Also thank you to Paul Munday, the second year undergraduate students that I have taught, and my fellow demonstrators for a thoroughly enjoyable teaching experience, and a great diversion from my studies.

To my fellow postgraduate students and postdoctoral researchers that I have met, past and present, thank you for keeping me entertained in and out of the School. Special mention to Lucy Goff who has been through almost eight years at Nottingham with me, Jenn Gaskell for keeping me fit and far away from my desk, Dr Toni Mey for the port and cheese, Dr Joe Shearring for teaching me to climb (and to Bex Chapman for helping as well), and also

for providing me with essential thesis guidance alongside Dr Elisa Antolín. And thanks to those who have shared in the great times in the tea room and beyond, particularly Suzie Abbs, Richard Cousins, Dr Sam Fahy, Duncan Parkes, Vicky Hills, Dr Mark Patton, and Dr Pete Wadley.

Thank you also to Dr Rajeev Kini and his students at the Indian Institute of Science Education and Research, Thiruvananthapuram for the warm welcome and friendship I received on my visit, and to all those who befriended and looked after me stateside during and after the Phonons 2012 conference.

My gratitude to all my friends and those that I have met along the way, especially to a certain few who have kept me grounded throughout; Tom Beaney for guiding me through the both degrees and inspiring future generations to do the same, Jennie Bennett for getting me out and about in Nottingham, Sabina Brimson for the travelling and random conversations from all over the world, Lauren Guyett for the comedy and stories of adventure, Sue Kempson and Marie Paxton for all the laughter, advice, and extended (and very necessary) breaks, Nathan Stowe for hitting the slopes with me on the powder days and braving the icy ones too, and Anett Varga for the music supply and the (excessive) food in London.

To some of the most important people in my life, thank you Claire, Annabel, Simon, Alex, and Cheryl for the advice, encouragement, friendship, and unwavering support you have given me for nearly a decade, and Jordana for seeing me through right to the very end; without you all, none of this would have been possible.

Finally, I would not be here if it were not for the constant love and support from my family, especially from my mother, father, and brother Lorenzo who have been there for me from the beginning, and for that I will be eternally grateful.

For my family, CASA, and my friends

Contents

Abstract **ii**

Publications and Conferences **iv**

Acknowledgements **vi**

Contents **ix**

List of Figures **xii**

List of Tables **xvii**

Supplementary Copyright Notice **xviii**

1 Introduction **1**

1.1 Ultrafast Acoustics in Nanostructures 1
1.2 Properties of Gallium Arsenide (GaAs) 2
1.3 Properties of Acoustic Pulses 4
1.4 Strain-Induced Transport Detection 5
1.4.1 *p*-*n* Junction and *p*-*i*-*n* Photodetector Diode 6
1.4.2 Quantum Well-Embedded *p*-*i*-*n* Diode Detector . . . 10
1.5 Motivation for the Work and Thesis Outline 15

2 Theoretical Description of Strain Pulse Generation, Propagation, and Detection **17**

2.1 Strain Pulse Generation 17
2.2 Coherent Phonon Propagation 21
2.2.1 Phonon Attenuation 22
2.2.2 Dispersion of Strain Pulses 22
2.2.3 Acoustic Soliton Formation 25
2.3 Optical Strain Detection 28

2.4 Electron-Phonon Coupling Mechanisms 28
2.4.1 Deformation Potential 29
2.4.2 Piezoelectric Coupling 30
2.4.3 Pekar Mechanism 30
2.4.4 Ripple Effect 31

3 Microfabrication Processes, and Experimental Methodology 32
3.1 Microfabrication Processes 32
3.1.1 Wafer Polishing 33
3.1.2 Wafer Scribing 35
3.1.3 Surface Cleaning 35
3.1.4 Optical Photolithography 35
3.1.5 Chemical Wet Etching 38
3.1.6 Thermal Evaporation 39
3.1.7 Rapid Thermal Annealing 40
3.1.8 Sample Packaging 40
3.2 Experimental Methodology 41
3.2.1 Transport Measurements 41
3.2.2 Photocurrent Pump-Probe Measurements 43
3.2.3 Fast Electrical Measurements 45

4 Coherent Phonon Generation in a Bulk GaAs Substrate 47
4.1 Wafer Profile and Processing 48
4.2 Transport Measurements 50
4.3 Photocurrent Pump-Probe Experiments using a Bulk GaAs Transducer 53
4.3.1 Comparison of Coherent Phonon Generation in Bulk GaAs and Metal Film Transducers 55
4.4 Modelling Strain Pulse Generation in a Supersonically Expanding Electron-Hole (e-h) Plasma 60
4.4.1 Thermoelastic Contribution to the Initial Strain . . . 62
4.4.2 Calculation of the Electron-Hole (e-h) Plasma Density 63
4.4.3 Deformation Potential Contribution to the Initial Strain 64
4.4.4 Interpretation of the Theoretical Model 66
4.5 Comparison of the Theoretical Model to Experimental Data 67
4.5.1 Examination of Decay Rate Dependence on Fluence . 71

4.6 Conclusions 74

5 Double Barrier Quantum Well Resonant Tunnelling Diode 76
5.1 Stationary RTD Operation 77
5.1.1 Zero Applied Bias 77
5.1.2 Resonance Threshold and Resonance Peak 78
5.1.3 Off Resonance 80
5.2 Resonance Tunnelling Mechanism 81
5.2.1 Coherent Tunnelling 82
5.2.2 Sequential Tunnelling 83
5.2.3 Tunnelling from a Quasi-Two-Dimensional Electron Gas Emitter 84
5.2.4 Space-Charge Buildup and Bistability Effects 85
5.3 Acoustic Modulation 87
5.4 Wafer Profile and Processing 90
5.5 Transport Measurements 92
5.5.1 Calculation of Stationary Device Parameters 94
5.6 Fast Electrical Measurements 99
5.6.1 Strain-Induced Effects in a Resonant Tunnelling Diode 101
5.6.2 Calculation of the Quantum Well Fermi Energy Level 103
5.6.3 Acoustic Modulation of Current 105
5.6.4 Picosecond Charge Transfer and the Acoustoelectronic Pumping Effect 110
5.7 Conclusions 112

6 Conclusions and Potential Future Research 113
6.1 Potential Future Research 116
6.1.1 Asymmetric Strain Pulse Effects on a Resonant Tunnelling Diode 117
6.1.2 Acoustoelectronic Pumping in Other Resonant Tunnelling Structures 118
6.1.3 Quantum Dot Resonant Tunnelling Diode 119

A Useful Formulae, and Derivations 126

B Material, and Figure Calculation Parameters 129

Bibliography 134

List of Figures

1.1 Sketch of the conventional unit cell of gallium arsenide (GaAs) depicting its zinc-blende structure. 3

1.2 Typical current-voltage bias (I-V) characteristic of a p-n junction diode. 6

1.3 (top) Circuit diagram and (bottom) energy band diagram of a typical p-n junction diode for various device voltages V. . 7

1.4 Energy band structure of GaAs (left) in the absence of strain, and (right) under compressive uniaxial [111] strain. 9

1.5 Energy band diagram of a stationary quantum well (QW)-embedded p-i-n diode in its (a) relaxed state, and (b) after photoexcitation. 12

1.6 Energy band diagram of an idealised semiconductor quantum well (QW) depicting the piezospectroscopic effect. 14

2.1 Incident strain profile after injection into a GaAs substrate from a 100 nm Al transducer film. 20

2.2 A typical low power bipolar strain pulse (initial amplitude $\eta_0 = 10^{-6}$) after propagation through a 375 µm thick GaAs substrate showing strain amplitude against co-moving time $t - t_0$, where t_0 is the arrival time of the low frequency components of the strain pulse. 21

2.3 GaAs dispersion curve of phonon frequency ν_k against reduced (dimensionless) wavevector q at room temperature showing both optical (O) and acoustic (A) branches; longitudinal (L) and transverse (T) branches are marked with crosses and circles, respectively, and a linear fit of the LA branch is indicated with a dashed, red line. 23

2.4 Propagation of a high power bipolar strain pulse (initial amplitude $\eta_0 = 10^{-3}$) through a 375 µm thick substrate with (top) approximately zero nonlinearity and dispersion ($C_3 \approx 0$, $\chi \approx 0$, respectively), (middle) only nonlinearity ($C_3 < 0$, $\chi \approx 0$), and (bottom) both nonlinearity and dispersion ($C_3 < 0$, $\chi > 0$). 27

3.1 Effect of, and required apparatus for the mechanical and mechanochemical polishing of indium contaminated samples. 34
3.2 Example soda lime glass photomasks for device microfabrication with chrome-patterned contact design. 37
3.3 Chemical wet etching of a representative sample showing greater undercutting of the top surface over time. 39
3.4 Electrical circuit diagrams used for conducting stationary current-voltage (I_0-V) measurements on resonant tunnelling diodes (RTDs) and double quantum well (QW)-embedded *p*-*i*-*n* devices. 42
3.5 Experimental setup for photocurrent pump-probe measurements conducted on MN653 samples processed with double quantum well (QW)-embedded *p*-*i*-*n* devices on the photoexcited side. 44
3.6 Experimental setup for fast electrical measurements conducted on NU165 samples using optical pump pulses to excite strain pulses in a 100 nm Al film deposited on the rear surface of the sample. 46

4.1 Typical sample holder used to perform transport and photocurrent pump-probe measurements on samples fabricated from MN653. 49
4.2 Stationary current-voltage (I_0-V) characteristics for a typical double quantum well (QW)-embedded *p*-*i*-*n* hypersonic detector in dark (solid, blue line) and light (dashed, red line) conditions. 51
4.3 Stationary current-voltage (I_0-V) characteristics for a double quantum well (QW)-embedded *p*-*i*-*n* hypersonic detector under both pulsed (solid, blue line) and CW illumination (dashed, red line) from a Ti:Sapphire oscillator at 10.8 K. . . 52

4.4 Photocurrent pump-probe measurements from a double quantum well (QW)-embedded *p-i-n* hypersonic detector of strain generated in bulk GaAs substrate for a range of pump beam fluences W. 54
4.5 Photocurrent pump-probe experimental comparison of phonon generation from (top) bulk GaAs and (bottom) 30 nm Al film transducers in the *linear* regime. 56
4.6 Representative sketch of strain transduction in bulk GaAs in the (a) *static* and (b) *supersonic* regimes. 59
4.7 Fitting of experimental data to the theoretical model for (a) bulk GaAs and (b) 30 nm Al film transducers, with (inserts) the deduced initial strain profiles for each material. 68
4.8 Fitting of simulated propagated strain pulses (dashed, red lines) to experimental data (solid, blue lines) in the *non-linear* regime for varying pump beam fluences W. 70
4.9 Fitted values and simulated curves of the dependence of inverse compressive strain duration ω_{+}, and recombination rate ω_{R} against pump beam fluence W. 73

5.1 Typical conduction band (CB) diagram of a resonant tunnelling diode (RTD) in the absence of a strain pulse (stationary operation), comprising two barriers surrounding a quantum well (QW). 78
5.2 Conduction band (CB) diagram of a resonant tunnelling diode (RTD) biased at the (a) resonance threshold and (b) resonance peak. 79
5.3 Conduction band diagram of a resonant tunnelling diode (RTD) biased off resonance. 80
5.4 Representative sketch of the electrostatic feedback mechanism in resonant tunnelling diodes (RTDs) that gives rise to bistability. 86
5.5 Acoustic modulation of energy levels by an incoming hypersonic wavepacket $\eta\,(t)$ in the conduction band (CB) of a resonant tunnelling diode (RTD) biased at the resonance threshold. 89

5.6 (a) Typical sample holder and (b) circuit diagram used for stationary current-voltage (I_0-V) and fast electrical measurements of NU165 samples. 92
5.7 Stationary current-voltage (I_0-V) characteristics of a resonant tunnelling diode (RTD) processed from NU165 in both increasing (solid, blue line) and decreasing (dashed, red line) applied voltage, with the direction shown using arrows in their corresponding colours and stroke styles. 93
5.8 Calculation of stationary resonant tunnelling diode (RTD) characteristics by examining charge densities at the resonance threshold and peak. 95
5.9 Fast electrical measurements conducted on a NU165 100 µm diameter resonant tunnelling diode (RTD) for various applied biases, recorded with 4 ps resolution and 500 averages at a pump beam fluence $W = 12.7\,\mathrm{mJ\,cm^{-2}}$. 100
5.10 Strain-induced shift of energy levels within the emitter and quantum well (QW) regions of a resonant tunnelling diode (RTD). 103
5.11 (a) Experimental and (b) simulated results for current change due to acoustic modulation in a resonant tunnelling diode (RTD) $\Delta I\,(t)$ against time at the resonance threshold, mid-resonance, and resonance peak. 106
5.12 (a) Current change $\Delta I\,(t)$ against time t in a 10 ns window after the arrival time of the strain pulse and (b) the AC equivalent circuit of the resonant tunnelling diode (RTD). . . 109
5.13 (a) Experimental and (b) simulated charge transfer across a resonant tunnelling diode (RTD) due to strain-induced effects. 111

6.1 Strain-induced shift ($\Delta\,(t) - \Delta_0$) modelling of a highly asymmetric strain pulse transduced from bulk GaAs ($M_0^{\mathrm{GaAs}} = 6.3$) in a resonant tunnelling diode (RTD). 118
6.2 (a) Top-down photograph and (b) side-on sketch (not to scale) of samples processed from wafer NU2217. 121
6.3 (a) Sample holder and (b) circuitry used to conduct transport and preliminary electrical-optical measurements on a sample processed from wafer NU2217. 122

6.4 Stationary current-voltage bias (I_0-V_b) characteristics taken using an Agilent 34401A Digital Multimeter over a resistor $R = 100\,\mathrm{k\Omega}$, with voltage bias applied from Keithley 230 Programmable Voltage Source. 123
6.5 Preliminary electrical-optical measurements of current change ΔI against voltage bias V_b taken from a sample processed from wafer NU2217. 124

List of Tables

4.1 MN653 wafer profile used for the fabrication of double quantum well (QW)-embedded *p*-*i*-*n* hypersonic detectors. 48

5.1 Wafer profile for NU165 comprising two $Al_{0.4}Ga_{0.6}As$ barriers encompassing a layer of GaAs, with various regions labelled in bold. 91

6.1 Wafer profile for NU2217 double barrier quantum dot (QD) resonant tunnelling diode (RTD) samples. 119

B.1 Referenced and calculated material parameters for aluminium (Al). 129

B.2 Referenced and calculated material parameters for gallium arsenide (GaAs). 130

B.3 Simulation parameters for figures in Chapter 2. 130

B.4 Simulation parameters for figures in Chapter 4. 131

B.5 Simulation parameters for figures in Chapter 5. 132

B.6 Simulation parameters for figures in Chapter 6. 133

Supplementary Copyright Notice

For Figures 1.4 and 2.3, the following supplementary copyright notice also applies:

Readers may view, browse, and/or download material for temporary copying purposes only, provided these uses are for non-commercial personal purposes. Except as provided by law, this material may not be further reproduced, distributed, transmitted, modified, adapted, performed, displayed, published, or sold in whole or part, without prior written permission from the American Physical Society.

Chapter 1

Introduction

The work presented in this thesis explores the effects that ultrafast acoustic pulses have on semiconductor nanostructures, and their potential applications.

This introductory chapter provides a general description of acoustic pulses, and outlines previous contributions to the field. An overview of ultrafast acoustics in nanostructures is given, after which properties of gallium arsenide are outlined, with regards to its suitability for the formation of these nanostructures. Next, general properties of acoustic pulses are discussed, and a summary of strain-induced transport detection methods already known in the field is subsequently presented. The final section of this chapter explains the motivation behind the present research, and briefly outlines the structure of the thesis.

1.1 Ultrafast Acoustics in Nanostructures

The field of ultrafast acoustics has been evolving since the late twentieth century as a method of determining the structural, mechanical, and electrical properties of materials. This is achieved by generating and detecting short strain pulses, comprised of coherent longitudinal acoustic (LA) phonons, through the use of picosecond or sub-picosecond optical pulses [1].

Initially, picosecond ultrasonics was mainly focussed on non-destructive testing of thin films, calculation of acoustic velocities in materials, and the determination of various phenomena, such as electron-phonon scattering rates. These experiments involved pumping a thin opaque film with ultrafast optical pulses, and probing the changes in optical reflectivity due to phononic

effects at the same surface [1–5].

Subsequent experiments determined properties of transparent materials by applying an opaque, thin film transducer to these materials, as well as the properties of multilayered structures [6–8]. These results allowed for the characterisation of strain pulses and analysis of their formation, thus opening potential avenues for future research. Later research looked at alternatives to thin films for the generation and detection of acoustic pulses, for example using superlattices (SLs) [9–11], and examined other acoustic phenomena such as phonon dispersion [12], carrier diffusion [13], and solitons [14, 15].

Concurrently, research into the use of phonons to modulate electronic properties in known devices was conducted; Kent et al. [16] explored heat pulse-induced conductivity measurements in silicon (Si) metal-oxide semiconductor field-effect transistors (MOSFETs), and the work by Ouali et al. [17] showed experimentally that thermally generated, non-equilibrium acoustic phonon-assisted tunnelling within double barrier structures was also possible. Later research conducted by Fowler et al. [18] revealed the ability to control charge transport through devices using optically transduced coherent phonons; the experimental setup differed from others, as the system was optically pumped but electrically probed.

Later, Moss et al. [19] demonstrated the ultrafast gating of photocurrent in a quantum well (QW)-embedded *p*-*i*-*n* diode using coherent acoustic wavepackets, and the possibility of using such a *p*-*i*-*n* diode as a hypersonic detector [20]. The work was extended to Schottky diodes, where strain pulses could also be used for ultrafast control of the device's electrical properties [21]. The indications of these general applications of strain pulses in semiconductor nanostructures have led onto the current research.

1.2 Properties of Gallium Arsenide (GaAs)

The work presented in this thesis primarily concerns nanostructures grown from and on gallium arsenide (GaAs). This section briefly covers some important properties of GaAs, discusses its suitability for the formation of heterostructures, and its advantages over the more commonly used Si. Specific acoustic properties are discussed elsewhere in this thesis, and a list of useful GaAs properties can be found in Table B.2; more detailed analyses of the structure and properties of GaAs can be found in many other references [22–26].

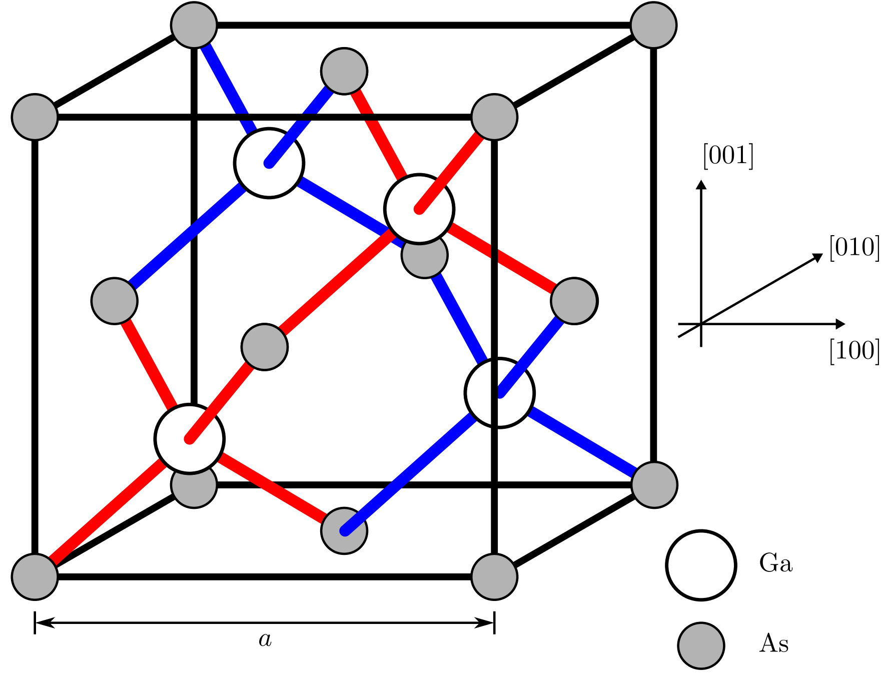

Figure 1.1: Sketch of the conventional unit cell of gallium arsenide (GaAs) depicting its zinc-blende structure. Labelled in the figure is the lattice constant of GaAs $a = 5.65\,\text{Å}$ [29], elemental components, and the crystal orientation. Note that the bonds between the gallium and arsenic atoms are shaded differently for clarity only, and comprise approximately 31 % ionic and 69 % covalent bonds [22].

GaAs is a III-V semiconductor formed from a compound of gallium and arsenic that is primarily covalently bonded, but consists of approximately 31 % ionic bonds [22]. It is arranged in a zinc-blende structure in its conventional unit cell, as sketched in Figure 1.1, which can be interpreted as two interpenetrating face centred cubic lattices [27]. The crystal structure of GaAs gives rise to a lattice constant $a = 5.65\,\text{Å}$, density $\rho = 5317\,\text{kg}\,\text{m}^{-3}$, and Γ-valley conduction band effective mass $m^* = 0.063m_0$ [28, 29]. Furthermore, it is a direct-gap semiconductor with a band gap energy $E_g = 1.42\,\text{eV}$ at room temperature, and consequently is transparent to optical excitation in most of, and beyond the near-infrared part of the spectrum ($\gtrsim 875\,\text{nm}$). The temperature dependence of E_g in eV is given by [29]

$$E_g = 1.519 - 5.405 \times 10^{-4} \frac{T^2}{T + 204}, \tag{1.1}$$

which results in $E_g = 1.52\,\text{eV}$ at $T = 4\,\text{K}$, and transparency at optical excitations in excess of $\sim 818\,\text{nm}$ wavelength.

GaAs-based heterostructures are normally created with AlAs and intermediary Al alloys of $Al_xGa_{1\text{-}x}As$ due to excellent lattice matching between the materials; although AlAs has a relatively much larger band gap of $E_g^{\mathrm{AlAs}} = 2.16\,\mathrm{eV}$ than GaAs at room temperature, their lattice constants differ by only 8×10^{-3} Å [26]. This allows for the formation of excellent material interfaces that reduce both discontinuities and defects within the overall crystal, and is exploited herein to form the various nanostructures that are modulated by incoming strain pulses; further details regarding growth of these nanostructures, and their wafer profiles can be found in Chapters 3–6.

Although Si is more widely used for commercial purposes, GaAs possess several noteworthy advantages as a basis for electronic devices [30]. Specifically, GaAs has a much higher electron mobility than Si[1], which allows GaAs transistors to switch much faster than their Si counterparts. Additionally, GaAs is more efficient at emitting and absorbing photons than Si, as the latter is an indirect band gap semiconductor and so requires phononic interaction to conserve both momentum and energy in any optical transition. Undoped GaAs also has a high resistivity in comparison to Si, and so is considered to be semi-insulating; this is advantageous in certain device designs as additional resistive layers are not required to insulate the GaAs-based device, unlike semi-conducting Si-based device designs [30].

1.3 Properties of Acoustic Pulses

A typical strain pulse is conventionally depicted as the derivative of the displacement, and comprises coherent phonons with multiple frequencies generated within a sub-nanosecond timescale. The strain pulses in this work are normally of about 15 ps duration with phonon frequencies in the sub-THz and THz regimes. The pulse is bipolar in form at generation in a thin film transducer, although its shape changes with propagation.

Various methods of generating and detecting ultrafast strain pulses have been devised over the past three decades, with the most common technique being the pump-probe experiment. A thin film transducer on a sample is optically pumped using ultrafast laser pulses that penetrate through to sub-surface levels and a coherent phonon wavepacket is generated due

[1]See, for example, Figure D4.2 in Ng [26].

to thermoelastic effects. The acoustic wavepacket propagates through the sample, and may interact with sample interfaces and/or reflect off the sample surfaces.

The resultant strain pulse is detected by optically probing the sample at an angle either on the same or opposing surface of the pump excitation. This optical probe comprises laser pulses identical to the pump but of a much lower power, and probing is achieved due to a change of optical reflectivity on the sample surface caused by acoustic effects from the strain pulse. The reflected optical probe pulse is directed towards a photodiode where these changes in optical reflectivity, and therefore a measure of the strain pulse, can be detected. Further detail regarding acoustic pulse generation, propagation, detection, and their effects on transport properties are provided in Chapter 2.

1.4 Strain-Induced Transport Detection

An alternative to the optical detection methods is to examine strain-induced transport effects. This method exploits devices whose carrier transport characteristics can be modulated by an incoming wavepacket due to electron-phonon interactions. These interactions are considered later in Section 2.4, and lead to specific effects in these devices, such as the piezojunction effect and piezospectroscopic effect; one such device that will be discussed here is the QW-embedded *p*-*i*-*n* diode [19, 20].

As is appropriate, a brief description of a *p*-*n* junction and *p*-*i*-*n* photodetector diode will be provided first in Section 1.4.1, after which an overview of the piezojunction effect will be given. The operation of a QW-embedded *p*-*i*-*n* diode, as well as the employment of the piezospectroscopic effect for strain-induced transport detection, will subsequently be presented in Section 1.4.2.

A modified version of the QW-embedded *p*-*i*-*n* device is utilised in this work to measure phonon generation in bulk GaAs, as outlined in Chapter 4. Strain-induced transport effects on an additional device, the double barrier resonant tunnelling diode (RTD), were also explored in this work; an appropriate discussion of the device, its operation, and determined effects can be found in Chapter 5.

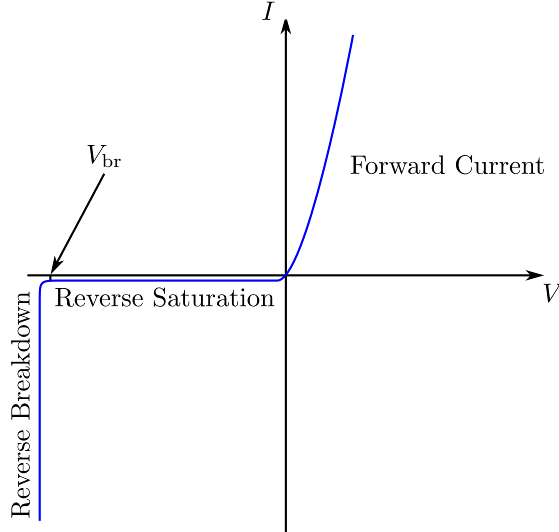

Figure 1.2: Typical current-voltage bias (I-V) characteristic of a p-n junction diode. Labelled are the breakdown voltage V_{br}, forward current, reverse saturation, and reverse breakdown regions. For $V = 0$, the system is in equilibrium, thus no current is generated. However, for $V > 0$, diffusion processes dominate generating a positive, forward current. Conversely, for $V_{\mathrm{br}} < V < 0$, there is negligible diffusion, and drift processes dominate to give a small negative, reverse saturation current. For $V \leq V_{\mathrm{br}}$, a larger negative current is generated as the system enters the reverse breakdown regime due to the Zener effect and avalanche breakdown.

1.4.1 *p*-*n* Junction and *p*-*i*-*n* Photodetector Diode

Current-voltage (I-V) characteristics of a p-n junction are shown in Figure 1.2, with its circuitry and energy band diagram in equilibrium and various applied device voltages V in Figure 1.3.

In equilibrium ($V = 0$), as shown in Figure 1.3(a), majority carrier diffusion over the potential barrier ($V_0 - V$) equals minority carrier drift along the electric field, thus resulting in zero net current. An applied forward voltage ($V > 0$; Figure 1.3(b)) causes a reduction in the barrier, therefore increasing majority carrier diffusion, and so generates a positive net current (forward current); note that this does not occur at $V = 0$, as the built-in potential must first be overcome before forward current is generated. The opposite occurs for an applied reverse voltage ($V < 0$; Figure 1.3(c)), whereby the barrier height increases with a corresponding reduction in carrier diffusion. Consequently, a small negative net current (reverse saturation current) is generated due to minority carrier drift, which is not sensitive to the barrier [31]. Increased reverse bias will eventually result in a significant increase of the negative net current at the breakdown voltage V_{br} due to the Zener effect and/or avalanche breakdown; these I-V characteristics are labelled in Figure 1.2.

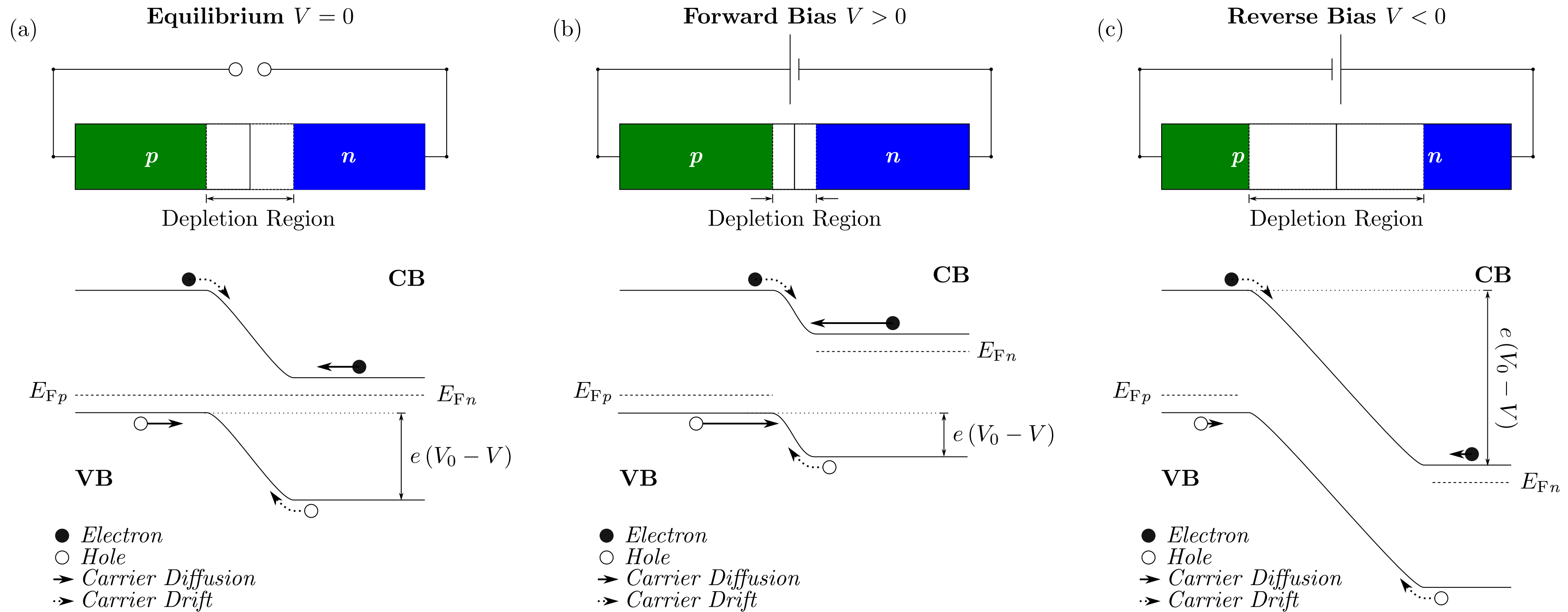

Figure 1.3: (top) Circuit diagram and (bottom) energy band diagram of a typical p-n junction diode for various device voltages V. (a) In the absence of an applied voltage ($V = 0$), a depletion region is formed around the interface of the p- and n-doped regions, where carriers diffuse across the interface and recombine to leave charged acceptors and donors. This gives the above energy band diagrams, where the Fermi energies levels of the p- and n-doped regions ($E_{\mathrm{F}p}$ and $E_{\mathrm{F}n}$, respectively) are equal, and CB and VB denote the conduction and valence bands, respectively. In this equilibrium state, the rate of majority carrier diffusion (solid arrows) to minority carrier drift (dotted arrows) is also equal, resulting in a zero net current across the junction. The separation between the doped regions is given by $e\,(V_0 - V)$. (b) By applying a positive (forward) voltage ($V > 0$), the depletion region reduces in size due to increased carriers in each doped region. This reduces the energy separation and the electrostatic potential barrier at the junction, resulting in an increase of majority carrier diffusion and net current. (c) For a reverse voltage ($V < 0$), the depletion region, potential barrier, and band separation are all increased. This inhibits carrier diffusion, and so minority carrier drift dominates thus generating a small negative net current.

p-i-n Photodetector Diode

A variant of the *p-n* junction diode is the *p-i-n* photodetector diode. Here, the depletion region is expanded upon by growing an intrinsic region in between the *p*- and *n*-doped regions.

When the diode is reversed biased, the majority of incident photons on the diode would be absorbed in this intrinsic region. This leads to the photogeneration of electron-hole (*e-h*) pairs, which will then drift as minority carriers towards their respective opposing regions. In combination with carriers that are thermally excited in the doped regions and within diffusion length of the intrinsic region [27], this results in an increase of the magnitude of the drift current.

As the drift process is relatively fast in comparison to the diffusion process [31], this structure allows for the fast detection of incoming photons, hence the requirement that most *e-h* pairs are generated within the intrinsic, and not the doped regions. A modified version of this photodetector is utilised in this work for strain-induced transport detection, and this QW-embedded *p-i-n* hypersonic detector is discussed in more depth in Section 1.4.2.

Piezojunction Effect

The piezojunction effect is caused by both the deformation potential and the piezoelectric effect, and is attributed to a change in the relative positions of the conduction band (CB) and valence band (VB) in a junction. This disturbs the symmetry of the crystal, thus modifying its electronic structure, such as the band gap, and therefore its conductivity [32].

As a result, the modulation of the band gap in a *p-n* junction due to incident strain can present interesting phenomena. Initial studies concentrated on Ge *p-n* junctions [33] revealed that increased pressure (i.e. strain η) on a junction device would result in changes in its resistivity in both forward and reverse bias, as initially theorised by Shockley [34]. Additional studies were conducted on GaAs *p-n* junctions [35], and the conclusions from these works found that the resistance changes here were primarily due to band-gap widening, as well as defects in the diode itself. To fully understand these conclusions, it is useful to first examine electron-phonon coupling effects in stressed bulk GaAs substrates.

Studies of stressed bulk GaAs [36–38] indicated that there would be a splitting of the degenerate GaAs VB in the presence of uniaxial compressive

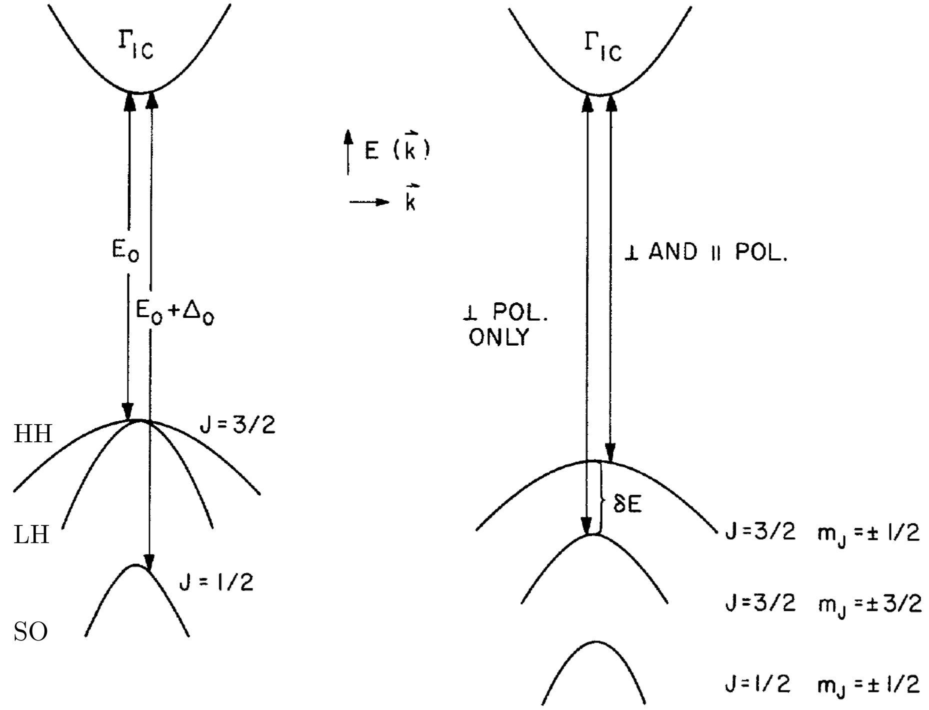

Figure 1.4: Energy band structure of GaAs (left) in the absence of strain, and (right) under compressive uniaxial [111] strain. Figure 1.4 is taken from Pollak et al. [36], with the conduction band (CB) and valence band (VB) depicted at the top and bottom of the figure, respectively. (left) In unstrained GaAs, the two degenerate light- (LH) and heavy-hole (HH) VBs (J = 3/2) are separated from CB by the band gap energy E_0, whilst the split-off (SO) band (J = 1/2, $m_J = \pm 1/2$) transition to CB is separated by an energy $E_0 + \Delta_0$. (right) Applied uniaxial compressive strain causes a splitting of the degenerate HH and LH bands ($m_J = \pm 1/2$ and $m_J = \pm 3/2$, respectively), whilst the hydrostatic component increases VB-CB transition energies. Note that similar observations were made for stress along both [100] and [110] directions, and that the polarisations refer to incident light used in piezoelectroreflectance measurements. Reprinted with permission from F. H. Pollak, M. Cardona, and K. L. Shaklee, *Physical Review Letters*, 16:942–944, May 1966. Copyright 2014 by the American Physical Society.

strain, hence causing an energy separation between the light- (LH) and heavy-hole (HH) VBs. In addition, the hydrostatic component of this strain would result in both a further separation between the CB and VB (i.e. a larger band gap), and a reduction in the energy separation between the split-off (SO) band and HH band, as shown in Figure 1.4 for [111] strain. These effects are caused primarily by the deformation potential, as will be discussed in Section 2.4.1, and both the LH-HH splitting and increased band gap energy are directly proportional to hydrostatic and shear deformation potentials [24, 36].

In relation to GaAs *p*-*n* junctions, this stress-induced band gap widening caused an approximately 30 % change in the measured current in both forward and reverse biases, and V_{br} was also found to have decreased. As

the band gap widens, the minority carrier density decreases since it is mainly dependent on the thermal generation of *e*-*h* pairs in the absence of photoexcitation [31]. As a result, fewer electrons have the energy to traverse the band gap, and so the magnitude of the drift current decreases. The shift of V_{br} to larger negative values can also be explained by band gap widening, as both the Zener effect and avalanche breakdown are reliant on it; for the former, a wider band gap reduces the probability of tunnelling across the junction, whilst the latter is dependent on carrier drift, which is reduced as previously mentioned.

The experiments discussed above all concentrated on slowly varying stress on a *p*-*n* junction, however the strain pulses generated in this work were modulated on a much faster timescale. Moss et al. [39] examined such a case using femtosecond optical pulses to generate acoustic wavepackets. Their results showed that coherent phonons modified the electronic structure of the junction via the deformation potential. This caused a change in the measured current due to the sudden change in electrostatic potential by the strain pulse.

1.4.2 Quantum Well-Embedded *p*-*i*-*n* Diode Detector

The previous subsection has given a general description of the operation of a *p*-*n* junction, as well as the various strain-induced effects it exhibits. As mentioned, a *p*-*i*-*n* photodiode detector can be fabricated by growing an intrinsic region between the *p*- and *n*-doped regions. This has the advantage of providing fast detection of incoming photons due to the dominant minority carrier drift current.

The *p*-*i*-*n* diode is also susceptible to the ultrafast piezojunction effect, although to a lesser extent than in a *p*-*n* junction as the potential is more widespread due to the intrinsic region, and not as abrupt [39]. However, the signal due to this ultrafast piezojunction effect contains other undesirable characteristics, such as a charge storage recovery component.

As an alternative detector, Moss et al. [19] fabricated a *p*-*i*-*n* tunnelling diode incorporating a QW embedded within its intrinsic region. By selecting suitable growth parameters for the diode and wavelength of incoming photons, it was possible for photoexcitation to occur only within the QW. An incident strain pulse would subsequently modulate the confined QW carrier states due to the piezospectroscopic effect. As this device is used to obtain the

results presented in Chapter 4, the remainder of this section will disclose a detailed description of its stationary operation, and the exploitation of the piezospectroscopic effect for strain detection.

Stationary Operation

Figure 1.5 depicts the energy band diagram of a QW-embedded *p*-*i*-*n* hypersonic detector (hereafter *p*-*i*-*n* detector) utilised in experiments by Moss et al. [19] and Moss et al. [20]. The hypersonic detector is reverse biased, such that an energy drop between the *p*- and *n*-doped regions of eV is established. The QW ground state energy levels in the conduction ($E_{1\text{C}}$) and valence ($E_{1\text{V}}$) bands are marked with blue dotted and green dashed lines, respectively.

As shown in Figure 1.5(a), an electron is confined at $E_{1\text{V}}$ when the device is illuminated on the *p*-doped side by a photon of energy $\hbar\omega$. Provided that $\hbar\omega$ is greater than or equal to the energy separation between the QW ground states, i.e. $\hbar\omega \geq (E_{1\text{C}} - E_{1\text{V}}) = E_{11}$, the absorption of this photon will result in photoexcitation of the electron from the QW VB to the QW CB, leaving a positive vacancy (hole) behind; this process is labelled (1) in Figure 1.5(b). Due to the electrostatic potential gradient in the device, and thus the presence of an electric field, these photoexcited minority carriers will tunnel through the QW barriers, and drift into their respective doped regions. This process is labelled (2) in the same figure, and results in the generation of a measurable photocurrent.

If the device is illuminated with a photon of energy of at least E_{11} but less than the material band gap, it is possible to restrict photogeneration of *e*-*h* pairs in the junction to the intrinsic QW alone. In addition, the value of E_{11} decreases with increasing reverse bias due to the quantum-confined Stark effect [40], thus it is possible to tune the device to the incoming photon energy by changing the applied bias according to a linear relationship [20]. Full technical details regarding the microfabrication of a *p*-*i*-*n* detector, and its material composition are given in Chapters 3–4.

Piezospectroscopic Effect

The piezospectroscopic effect exploits the deformation potential coupling mechanism to shift energy levels within a crystal. Kaplyanskii and Przhevuskii [41] reported this effect in ruby crystals, whereby uniaxial compression

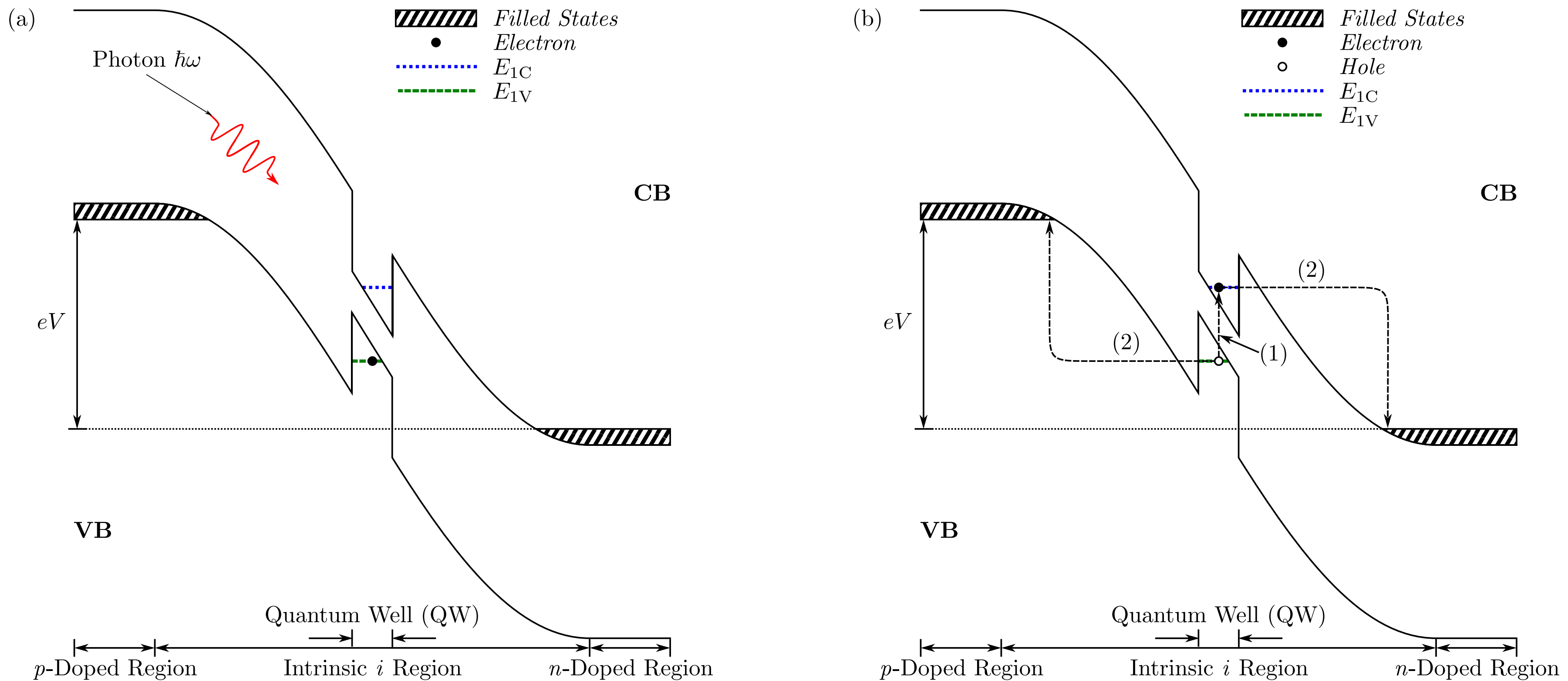

Figure 1.5: Energy band diagram of a stationary quantum well (QW)-embedded p-i-n diode in its (a) relaxed state, and (b) after photoexcitation. (a) The device comprises a p- and n-doped region encompassing an intrinsic i region with a QW at its centre. A reverse voltage across the device V results in an energy shift of eV, and the device is illuminated by a photon of energy $\hbar\omega$ on the p-doped side. Due to quantum confinement, an electron is trapped in the QW valence band (VB) ground state energy $E_{1\mathrm{V}}$. (b) If $\hbar\omega$ is greater than the QW ground state energy separation, (1) the electron can be photoexcited to at least the QW conduction band (CB) ground state energy $E_{1\mathrm{C}}$, and this photoexcitation leaves behind a positively charged vacancy (hole). (2) Due to the electric field within the junction, the minority carriers drift against the diffusion gradient to the doped regions via tunnelling mechanisms, thus providing a measurable change in current.

of samples resulted in displacement of the observed spectra lines.

Detailed analysis of its effect on nanostructures, specifically in a GaAs *p-i-n* detector [19, 20], showed the piezospectroscopic effect causes a significant modulation of confined QW energy levels. In corroboration with previous studies [41–43], it was observed that compressive strain ($\eta < 0$) would raise (lower) energy levels confined within the QW CB (VB) relative to its stationary state ($\eta = 0$), with the opposite observation under tensile strain ($\eta > 0$), as shown in Figure 1.6. This strain-induced shift would result in a change of the absorption and emission spectra of a given nanostructure due to the band gap modulation.

Particularly, it was found that the stationary detuning parameter Δ_0, which is the energy difference between E_{11} and $\hbar\omega$, would be modulated by an incoming strain pulse due to the piezospectroscopic effect and the deformation potential constant Ξ, such that [20]

$$\Delta(t) = \Xi\eta_{\mathrm{W}}(t) + \Delta_0, \tag{1.2}$$

where $\Delta(t)$ is the time-varying detuning parameter, and $\eta_{\mathrm{W}}(t)$ is the strain pulse in the QW. Provided that $\Delta(t) < E_{11}$, the change in measured photocurrent ΔI is such that

$$\Delta I \propto \Xi\eta_{\mathrm{W}}(t). \tag{1.3}$$

As a result, photoexcitation of the *p-i-n* detector with a spectrum of photon energies centred just below E_{11} would generate a maximum current under tension, and a minimum current under compression relative to the stationary current I_0.

Moss et al. [19] and Moss et al. [20] utilised the *p-i-n* detector to obtain picosecond resolution detection of a hypersonic wavepacket. This wavepacket was generated thermoelastically in a 100 nm Al film, and propagated through 375 µm thick GaAs substrate before interacting with the detector. Photoexcited carriers were generated in the detector using a laser pulse centred at 1.55 eV with a width of 60 meV.

Their work showed that it was possible to gate photocurrent generation in the *p-i-n* detector on a picosecond timescale using the above discussed effects. By examining the dependence of electric field on applied bias, it was also determined that the majority of photoexcited carriers contributed to

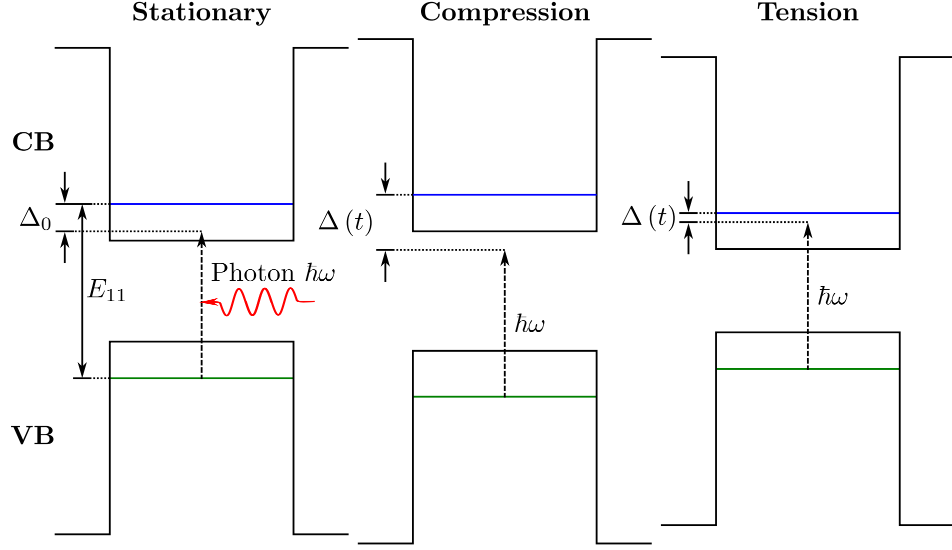

Figure 1.6: Energy band diagram of an idealised semiconductor quantum well (QW) depicting the piezospectroscopic effect. The QW conduction band (CB) and valence band (VB) ground states are shown with blue and green solid lines, respectively, with the energy separation between these two levels labelled E_{11}, and the stationary detuning parameter labelled Δ_0. The electron VB to CB transition due to absorption of an incoming photon of energy $\hbar\omega$ is shown by a dashed arrow. (left) The first panel shows the stationary case, where there is an absence of strain (i.e. $\eta = 0$). (centre) The QW first encounters the compressive component of an incoming strain pulse ($\eta < 0$). This results in further separation of the energy band structure, and so modulates the now time-dependent detuning parameter $\Delta(t)$ ($\Delta(t) - \Delta_0 > 0$) as given by Equation 1.2, before (right) the tensile component ($\eta > 0$) shifts the band structure closer ($\Delta(t) - \Delta_0 < 0$). Note that this diagram assumes a bipolar strain pulse where the maximum strain amplitudes for the compressive and tensile parts are identical, and that the CB and VB deformation potentials are identical, thus producing the same shift. This strain-induced shift is exploited as a detection method in this work.

the photocurrent, given that the carrier QW tunnelling time was estimated to be at least one order of magnitude faster than the carrier recombination time. In addition, it was observed that the remainder of the device was not affected by the strain pulse on this timescale, and thus the effect was strictly limited to the QW.

These properties of the p-i-n detector present it as an ideal candidate for strain pulse detection, and a similar device has been employed in the detection of strain pulses generated from bulk GaAs, as reported in Chapter 4.

1.5 Motivation for the Work and Thesis Outline

The motivation for this work is to build upon the studies conducted by Moss [44] through the use of the *p*-*i*-*n* detector described therein, and to examine strain generation in various media with a high (picosecond) resolution, and a high signal-to-noise ratio. Furthermore, strain-induced effects in known transport devices will be explained, so as to provide novel hypersonic detectors through existing, known microfabrication techniques and recipes, whilst concurrently investigating future avenues for further research.

This thesis comprises an additional five chapters that disclose relevant theory, microfabrication and experimental techniques, and results obtained during the research period. Appendices A and B include useful formulae, derivations, material parameters, and calculation values used to generate certain figures within this work.

The following chapter, Chapter 2, provides a theoretical description of strain pulse generation, propagation, and detection. The theory of strain generation in thin metal films will be presented, alongside mathematical models used to simulate strain profiles. Afterwards, attenuation, dispersion, and soliton formation will be discussed, before a brief consideration of optical strain detection methods is given. Although a concise overview of strain-induced transport detection methods has been explored in Section 1.4, further details regarding electron-phonon coupling mechanisms are studied in this chapter as well, such as the deformation potential, piezoelectric coupling, the Pekar mechanism, and the ripple effect.

Chapter 3 relates to experimental methodology, and is separated into two main sections. The first section is dedicated to microfabrication techniques, with specific emphasis on all aspects required to produce viable samples for testing. The second section generally outlines the experimental apparatus and setups used to determine sample characteristics, and to obtain the subsequent results. For the latter case, two main optical configurations are employed; the photocurrent pump-probe, and fast electrical measurement techniques.

The next two chapters discuss results acquired from two separate experiments. Chapter 4 examines coherent phonon generation in bulk GaAs

transducers using a slightly modified version of the QW-embedded p-i-n hypersonic detector described in Section 1.4.2. Specific details regarding the sample structure, and the transport characteristics of the device are also given in this chapter. Results taken from photocurrent pump-probe measurements are presented afterwards, alongside theoretical simulations. Analyses of these results are conducted initially with a comparison to the known case of generation in Al films researched by Moss et al. [19], before an examination of coherent phonon generation mechanisms is made. Finally, the implications of strain pulse generation in bulk GaAs are considered.

Chapter 5 looks at the possibility of utilising other known nanostructures for acoustic control of charge transfer. Particularly, the use of a double barrier QW RTD for charge transfer control will be explored. This chapter will provide a general discussion of the operation of a RTD in the absence of strain, before giving specifics about the sample and its transport characteristics. Fast electrical measurement results will be presented alongside simulations and theoretical analysis of the results that show the RTD charge control attribute termed the *acoustoelectronic pumping effect*.

The final chapter, Chapter 6, states an overall conclusion to the work presented in this thesis, as well as potential future avenues of research. Preliminary findings aimed at advancing the work discussed in Chapter 5 by exploiting strain-induced effects in a double barrier quantum dot (QD) RTD will be given, alongside recommendations for the successful completion of said work.

Chapter 2

Theoretical Description of Strain Pulse Generation, Propagation, and Detection

The following chapter provides an overview of the theory behind strain pulse generation, propagation, and detection. Specifically, thermoelastic generation of strain in thin metal films will be considered, alongside mathematical models used to simulate initial strain profiles. The effects of attenuation and dispersion on coherent phonon propagation will also be examined, before focussing on the formation of solitons due to the balancing of dispersive effects and crystal nonlinearity.

A brief summary of optical strain detection methods will be subsequently presented, before a detailed description of electron-phonon coupling mechanisms used in the strain-induced transport detection method discussed in Section 1.4 are given. These mechanisms include the deformation potential, piezoelectric coupling, the Pekar mechanism, and the ripple effect; as is later discussed, the deformation potential is considered to be the dominant mechanism responsible for strain-induced transport detection.

2.1 Strain Pulse Generation

As briefly discussed in Section 1.3, strain pulses may be optically excited in materials by surface and sub-surface heating; there are alternative generation methods, such as electrical excitation using the Wannier-Stark ladder effect [45], but these are not considered here as optical excitation was the sole

method of phonon generation in this work. In this section, the basic theory regarding strain generation in thin metal films will be provided, alongside a description of historical attempts to theoretically model the strain profile and the assumptions therein; Chapter 4 examines generation in thin metal films, and bulk GaAs in more detail and departs from some of these assumptions.

For optical excitation, an ultrafast laser pulse is directed at an opaque film of thickness d_{F} with full width at half maximum (FWHM) duration of less than 1 ps. It illuminates an area of the transducer film with fluence W, and transfers energy to the surface and sub-surface layers in the direction of illumination z. In doing so, there is a temperature change in the film [2]

$$\Delta T\left(z\right)=\left(1-R_{\mathrm{F}}\right)\frac{W}{c_{\mathrm{F}}\rho_{\mathrm{F}}\zeta_{\mathrm{F}}}\exp\left(-\frac{z}{\zeta_{\mathrm{F}}}\right), \tag{2.1}$$

where R_{F} is the reflectivity coefficient, c_{F} is the specific heat capacity, ρ_{F} is the density, and ζ_{F} is the absorption length of the film. The absorption length of the transducer is determined by

$$\zeta_{\mathrm{F}}=\alpha_{\mathrm{F}}^{-1}=\left(\frac{4\pi\kappa_{\mathrm{F}}\left(\lambda\right)}{\lambda}\right)^{-1}, \tag{2.2}$$

where α_{F} is the absorption coefficient, $\kappa_{\mathrm{F}}\left(\lambda\right)$ is the imaginary part of the complex refractive index of the film for the laser wavelength λ, and $\zeta_{\mathrm{F}} \ll d_{\mathrm{F}}$.

The energy transferred to the film transduces an isotropic stress

$$\delta\sigma_{\mathrm{F}}=-3B_{\mathrm{F}}\beta_{\mathrm{F}}\Delta T\left(z\right), \tag{2.3}$$

where B_{F} and β_{F} are the film bulk modulus and linear expansion coefficient, respectively. This is due to the long expansion time of the transducer to relieve stress compared to the relatively fast relaxation of excited electrons and holes [1].

As the diameter of the illuminated beam spot is large relative to ζ_{F}, it can be assumed that the transducer is uniformly heated at and near the surface; although the beam spot is Gaussian, this assumption is valid due to its large size. Assuming that the film is elastically isotropic, and that the beam is parallel to the z-direction, the uniform heating of the transducer also only occurs along this axis. Consequently, the particle displacement in the x- and y-coordinates is constant; given that strain is the derivative of displacement, there is no strain component along these axes, and thus only

coherent longitudinal phonons are generated [1, 46]. As such, the following equations of elasticity are established [2]

$$\sigma_{\mathrm{F}} = \rho_{\mathrm{F}} v_{\mathrm{F}}^2 \eta - 3B_{\mathrm{F}}\beta_{\mathrm{F}}\Delta T\left(z\right), \tag{2.4}$$

$$\rho_{\mathrm{F}} \frac{\partial^2 u}{\partial t^2} = \frac{\partial \sigma_{\mathrm{F}}}{\partial z}, \tag{2.5}$$

$$\eta = \frac{\partial u}{\partial z}, \tag{2.6}$$

where σ_{F} is the stress, v_{F} is the film longitudinal acoustic (LA) velocity, η and u are the strain and displacement in the z-direction, respectively, and the initial boundary conditions are $\eta = 0$, and $\sigma_{\mathrm{F}} = 0$ at $z = 0$.

When including heat diffusion, imperfections in the film, reflections at the film/substrate interface, and smearing of sharp features in experimental conditions, the solution to Equations 2.4–2.6 can be approximated by [47]

$$\eta\left(t\right) = \frac{2A_{\mathrm{F}}\zeta_{\mathrm{F}}}{v_{\mathrm{F}}\tau^2}\left(1 - R_{\mathrm{I}}\right)\sum_{j=0}^{\infty} R_{\mathrm{I}}^j \left(t - \frac{\left(2j+1\right)d_{\mathrm{F}}}{v_{\mathrm{F}}}\right) \times \exp\left[-\frac{1}{\tau^2}\left(t - \frac{\left(2j+1\right)d_{\mathrm{F}}}{v_{\mathrm{F}}}\right)^2\right], \tag{2.7}$$

where R_{I} is the reflectivity at the film/substrate interface, τ is a parameter defined by electron diffusion [4, 48] and imperfections in the film [47], and

$$A_{\mathrm{F}} = 3\left(1 - R_{\mathrm{F}}\right)\frac{W B_{\mathrm{F}}\beta_{\mathrm{F}}}{2c_{\mathrm{F}}\zeta_{\mathrm{F}}\rho_{\mathrm{F}}^2 v_{\mathrm{F}}^2}. \tag{2.8}$$

Equation 2.7 models the initial profile immediately after injection of the strain pulse into the substrate from the transducer film, and was originally derived for the specific experimental setup in Akimov et al. [47]. The summation term therein defines the strain pulse profile after j reflections at the film/substrate interface and, in the limit where only the incident strain pulse is examined (i.e. $j = 0$), Equation 2.7 becomes

$$\eta\left(t\right) = \frac{2A_{\mathrm{F}}\zeta_{\mathrm{F}}}{v_{\mathrm{F}}\tau^2}\left(1 - R_{\mathrm{I}}\right)\left(t - t_{\mathrm{F}}\right)\exp\left[-\frac{\left(t - t_{\mathrm{F}}\right)^2}{\tau^2}\right], \tag{2.9}$$

where $t_{\mathrm{F}} = d_{\mathrm{F}}/v_{\mathrm{F}}$ is the propagation time through the metallic film. The penultimate and final terms in Equation 2.9 define the strain pulse profile, whilst all the terms define its initial amplitude η_0. This equation is modelled

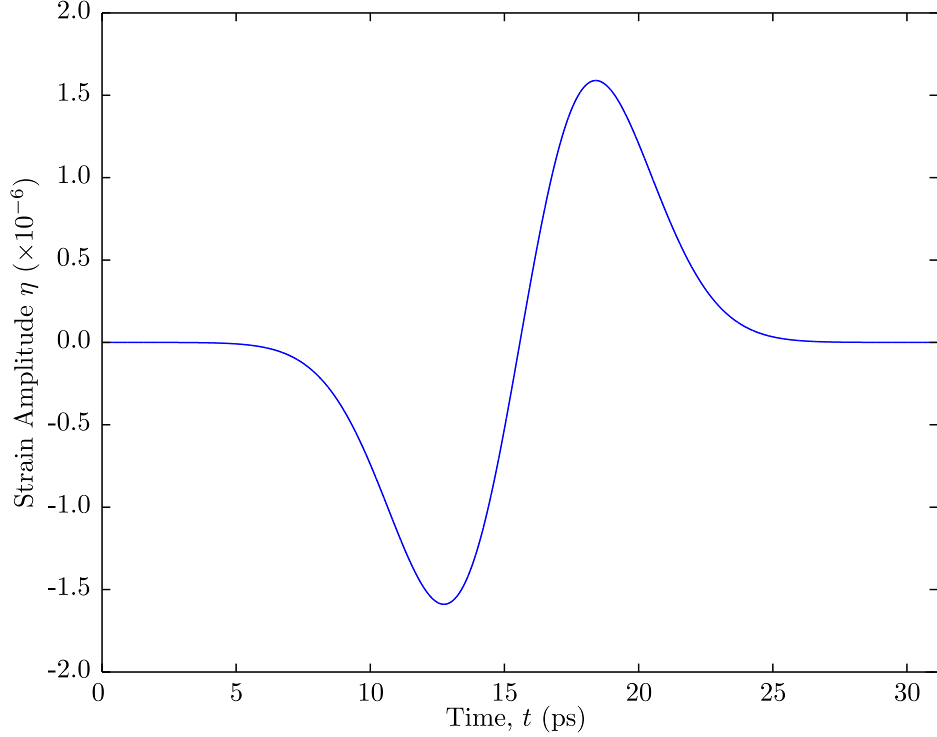

Figure 2.1: Incident strain profile after injection into a GaAs substrate from a 100 nm Al transducer film. This was calculated using Equation 2.9, and the pulse is bipolar and near-Gaussian in shape in each of its compressive ($\eta < 0$) and tensile ($\eta > 0$) components. The sharp rise in the central region is formed of oscillations in the sub-THz and THz regimes. Parameters used for generation of this figure can be found in Appendix B.

in Figure 2.1 for injection from a 100 nm thick Al film into a GaAs substrate, where $v_{\mathrm{F}} = 6.42 \times 10^3\,\mathrm{m\,s^{-1}}$, $R_{\mathrm{I}} = 0.19$, and $\tau = 5\,\mathrm{ps}$.

As shown in Figure 2.1, the strain profile is bipolar in shape, near-Gaussian for each of its compressive ($\eta < 0$) and tensile ($\eta > 0$) components, and has a relatively sharp central region; this central region consists of frequency components in the sub-THz and THz regimes. The bipolar nature of the pulse originates from the propagation of the strain pulse in both directions along the z-axis. Initially, both these components are negative as the radiating strain pulse causes compression of the lattice. This is due to optical absorption, which causes expansion of the lattice, and thus reduces the distance between displaced and stationary atoms in the crystal resulting in an initial compression in both directions. As the rearward-propagating component (i.e. travelling in the negative z-direction) interacts with the vacuum/Al interface, it is reflected and inverted back into the film due to a π-phase change at $z = 0$, and this component subsequently forms the tensile part of the wavepacket.

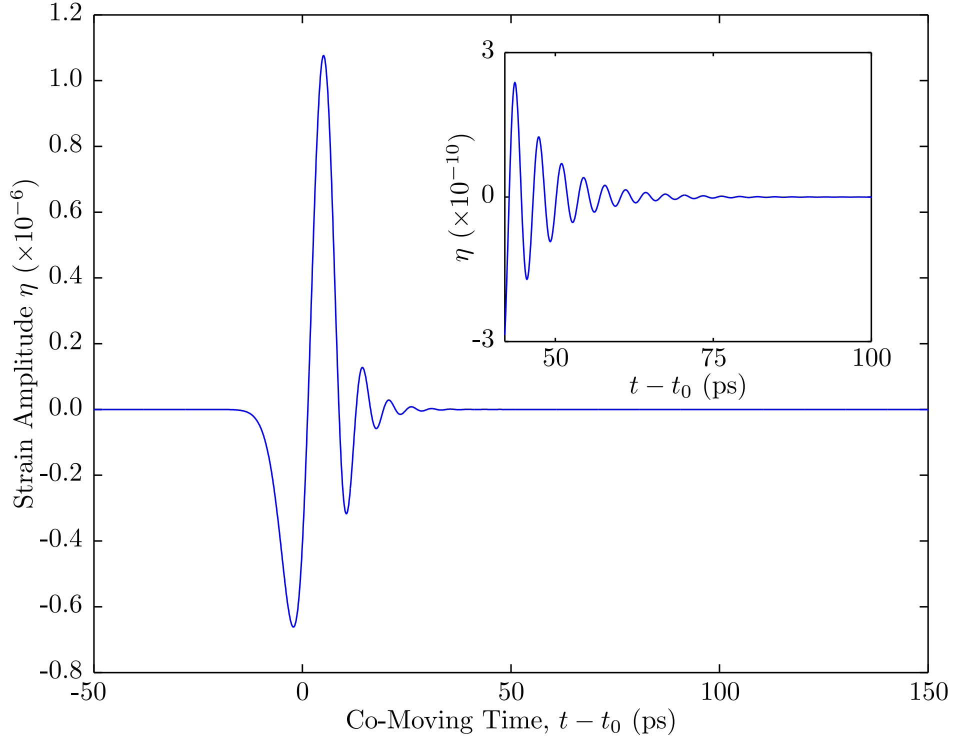

Figure 2.2: A typical low power bipolar strain pulse (initial amplitude $\eta_0 = 10^{-6}$) after propagation through a 375 µm thick GaAs substrate showing strain amplitude against co-moving time $t - t_0$, where t_0 is the arrival time of the low frequency components of the strain pulse. Note how higher frequencies have a much reduced amplitude due to dispersion and attenuation, respectively, and arrive later ($t - t_0 > 0$; see also, insert); this characteristic shape is known as the dispersive tail, and the causes are discussed in Sections 2.2.1–2.2.2. The initial strain pulse was modelled without any reflected film components for simplicity, and full calculation parameters for this figure can be found in Appendix B.

2.2 Coherent Phonon Propagation

Coherent phonons propagate through the sample perturbing the lattice structure of the sample as they progress. During this propagation, the shape of the strain pulses themselves are modified due to several phenomena that are discussed in the following subsections; a sketch of a low power strain pulse after propagation through a typical 375 µm thick GaAs substrate is shown in Figure 2.2.

In this figure, the amplitude of higher frequency oscillations is relatively smaller, and these oscillations arrive much later in comparison to lower frequencies; this is due to attenuation and dispersion, respectively, and results in this characteristic dispersive tail. These effects, alongside the formation of solitons for high power strain pulses, are considered in depth in Sections 2.2.1–2.2.3.

2.2.1 Phonon Attenuation

During propagation through the substrate, the strain pulse is attenuated as it disturbs the substrate from equilibrium. Two approaches have been established to determine the root cause of phonon attenuation [49], one from a microscopic approach, i.e. based on individual phonons, and the other from a macroscopic view of the entire strain pulse.

The latter theory states that thermal phonons are coupled to strain, and thus the propagating pulse frequency-shifts thermal phonons from equilibrium. Attenuation therefore is due to their anharmonic relaxation back to equilibrium through collisions between thermal phonons [12, 49, 50]. The temperature dependence of attenuation of 56 GHz longitudinal phonons in GaAs has been examined in depth by Chen et al. [50]; here, it was noted that attenuation is particularly problematic at room temperature, where an attenuation length of approximately 26 µm was recorded.

Other processes aside from phonon relaxation were considered in their analysis, such as the Herring process. This involves the collision of a longitudinal and a transverse phonon, resulting in a production of another transverse phonon with a different frequency and wavevector. However, these mode conversion processes were not thought to be the main contribution to phonon attenuation, since the Herring contribution was calculated to be two orders of magnitude below the measured value. Nonetheless, it is thought that Herring interactions would have a greater effect for phonons with frequency in excess of 500 GHz [50].

As a result, picosecond ultrasonic experiments are generally conducted below 70 K to minimise these attenuation effects [12]; this is especially important where a strain pulse must propagate through a long distance relative to the attenuation length, and/or where acoustic echoes are examined.

2.2.2 Dispersion of Strain Pulses

In addition to attenuation, a strain pulse containing high frequency components is also subject to dispersion. These dispersive effects are caused by the propagation of frequencies through a medium at different group velocities, and become significant for certain frequencies if the propagation distance is sufficiently long. The frequency condition is easily satisfied by the strain pulse depicted in Figure 2.1, as the comparatively sharp change between its compressive and tensile components will provide the necessary

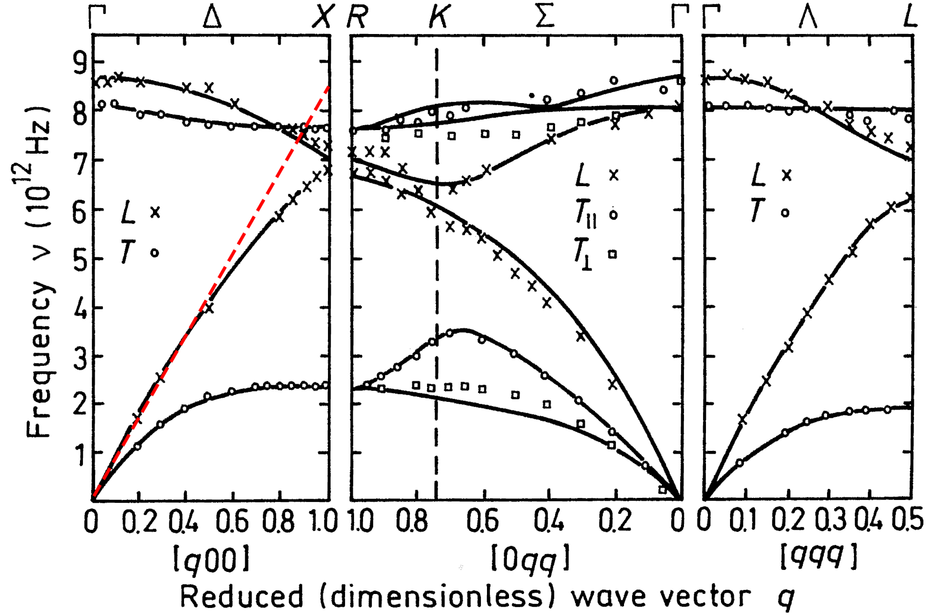

Figure 2.3: GaAs dispersion curve of phonon frequency ν_k against reduced (dimensionless) wavevector q at room temperature showing both optical (O) and acoustic (A) branches; longitudinal (L) and transverse (T) branches are marked with crosses and circles, respectively, and a linear fit of the LA branch is indicated with a dashed, red line. As phonon propagation is solely along the <100> direction, only the dispersion curve shown on the left panel is considered in this thesis; here, the O and A branches are above and below 7 THz, respectively, with the most relevant being the LA branch. The figure is from Levinshtein and Rumyantsev [29], and the solid, black lines are calculated according to the dipole approximation force constant model by Waugh and Dolling [51]. The linear fit was made according to $\nu = v_{\mathrm{LA}} q/a$, where v_{LA} is the LA velocity of GaAs, $|q| = ka/(2\pi)$ is reduced (dimensionless) wavevector, k is the wavevector, and a is the GaAs lattice constant; see also Figure 7 in Blakemore [22]. Reprinted with permission from J. L. T. Waugh and G. Dolling, *Physical Review*, 132:2410–2412, December 1963. Copyright 2014 by the American Physical Society.

high frequencies, and the propagation distance equal to the typical substrate thickness is sufficient for dispersive effects to become apparent.

In the [100]-orientated GaAs substrates used throughout this work, higher frequencies travel slower than lower frequencies, which result in a dispersive tail comprising of oscillations of increasing frequency. This is evident when examining the dispersion relations of phonon frequency against the reduced dimensionless wavevector q, where $|q| = ka/(2\pi)$, as shown in Figure 2.3.

In this figure from Levinshtein and Rumyantsev [29], the GaAs dispersion curves for three different crystal orientations were measured experimentally, and modelled according to the dipole approximation force constant by Waugh and Dolling [51]; the experimental results are shown with black cross and circles to denote the longitudinal (L) and transverse (T) branches, respectively, and the fitted model is drawn with solid, black lines. As

the strain pulse is solely propagated along the <100> direction, only the dispersion curve shown in the left panel is considered in this thesis; here, the optical (O) and acoustic (A) branches are shown above and below 7 THz, respectively, with the most relevant being the LA branch.

Dispersed Frequencies

At the long wavelength limit, the dispersion relation is approximately linear, i.e. $\omega_k = v_{\mathrm{LA}} k$, where ω_k is the phonon angular frequency, and v_{LA} is the substrate LA velocity. As such, the phonons with these frequencies will not disperse as they have identical group velocity $v_{\mathrm{g}k} = \partial\omega_k/\partial k$ and thus propagate at the same speed. However, as k increases, the dispersion relationship becomes increasingly sublinear; this can be seen in Figure 2.3 for the linear fit[1] (dashed, red line) applied to the LA branch for $v_{\mathrm{LA}} = 4730\,\mathrm{m\,s^{-1}}$ [29]. It is these phonon frequencies that result in dispersion, as larger frequencies have a smaller $v_{\mathrm{g}k}$ comparatively. Consequently, high ω_k LA phonons propagate slower through the GaAs substrate, and hence arrive later than lower ω_k LA phonons.

For small k, the dispersion relation can be defined as [12, 52]

$$\omega_k = v_{\mathrm{LA}} k - \chi k^3 + \dots, \tag{2.10}$$

where the dispersion parameter $\chi = 7.40 \times 10^{-18}\,\mathrm{m^3\,s^{-1}}$ for [100]-orientated GaAs [12]. It can be shown (see Appendix A) that the angular dispersive frequencies $\omega_{k,\mathrm{disp}}$ are

$$\omega_{k,\mathrm{disp}} = v_{\mathrm{LA}}^2 \sqrt{\frac{\tau_0}{3\chi z_0}}, \tag{2.11}$$

where $\tau_0 = t - t_0$, t_0 is the arrival time of the low frequency components of the strain pulse, and z_0 is the propagation distance. Equation 2.11 is only valid when examining oscillations in the dispersive tail that arrive later relative to the low frequency components, and where the relative arrival time difference τ_0 is much greater than the period of the oscillations, i.e. $t_0 \gg \tau_0 \gg \omega_{k,\mathrm{disp}}^{-1}$ [12].

[1] See also Figure 7 in Blakemore [22].

Minimum Propagation Distance for Significant Dispersion

As aforementioned, significant dispersive effects can only be seen experimentally provided that the strain pulse propagates over a minimum distance; this distance is dependent on both the pulse width $\Delta z_0 = k_{\max}^{-1}$, where $k_{\max}$ is the maximum wavenumber, and χ.

Hao and Maris [12] determined that the pulse broadens after a distance z_0 by $z_0 \chi k_{\max}/v_{\mathrm{LA}}$, with the high frequency components arriving later than the lower frequency ones. As a result, the minimum propagation distance $z_{0\min}$ for dispersive effects to separate frequencies of a certain pulse width Δz is

$$z_{0\min} = \frac{v_{\mathrm{LA}} \left(\Delta z\right)^3}{\chi}. \tag{2.12}$$

From Equation 2.12, it can be shown that for a standard $z_{0\min} = 375\,\mu\mathrm{m}$ [100]-orientated GaAs substrate, frequencies greater than approximately 90 GHz should be discernible experimentally.

2.2.3 Acoustic Soliton Formation

For low strain amplitudes, the mechanisms for phonon propagation described in the previous subsections dominate since the system is in its linear regime. However, as the strain amplitude is increased, the nonlinear properties of the lattice come into effect and produce interesting phenomena such as the formation of solitary waves.

These solitons are formed due to a balancing of dispersion effects and the anharmonicity of interatomic crystals in the lattice [14]. They exist only in the compressive component of the strain pulse, and exhibit properties such as a constant amplitude that increases linearly with increasing distance from the trailing edge of the pulse for each individual soliton. In addition, each soliton moves at a velocity linearly proportional to its amplitude, so the first travels faster relative to the last one in the leading edge, causing a separation between each given soliton. Furthermore, solitons that interact with one another reappear almost unchanged by the interaction [53].

Their properties are mathematically described by the Korteweg-de Vries-Burgers (KdV-Burgers) equation [15, 54], which includes non-linearity, dis-

persion, and viscosity (or acoustic attenuation) ϵ terms in the form

$$\frac{\partial \eta}{\partial t} = \frac{\epsilon}{2\rho}\frac{\partial^2 \eta}{\partial z^2} - \chi \frac{\partial^3 \eta}{\partial z^3} - \frac{C_3}{2 v_{\mathrm{LA}} \rho} \eta \frac{\partial \eta}{\partial z}, \tag{2.13}$$

where $C_3 = C_{111} + 3C_{11}$, C_{11} and C_{111} are the second- and third-order elastic constants respectively [14], and ρ is the substrate density. Equation 2.13 can be solved numerically using a composite Runge-Kutta (CRK43) method developed by Driscoll [55]. A MATLAB® script employing this method to model the KdV-Burgers equation was written and kindly supplied by Emmanuel Péronne [15], and was used extensively to fit the experimental results given in Chapter 4.

As simulated in Figure 2.4, in the absence of both nonlinearity and dispersion ($C_3 \approx 0$, $\chi \approx 0$, respectively), the bipolar strain pulse propagates without any change in its profile; note that these parameters are approximately zero in the figure due to software limitations. However, if only nonlinearity of the lattice is taken into account ($C_3 < 0$, $\chi \approx 0$), an N-wave is formed as the peak of the compressive part moves faster due to its amplitude than the rest of the leading edge, and the opposite occurs for the tensile component with respect to the trailing edge. This self-steepening is due to the pressure dependence of the velocity caused by non-linearity in the lattice, resulting in propagation at velocities above and below the material LA velocity, and shock wave formation. By introducing dispersion into the system ($C_3 < 0$, $\chi > 0$), the dispersive and nonlinear effects can be balanced to generate solitons in the leading edge [56].

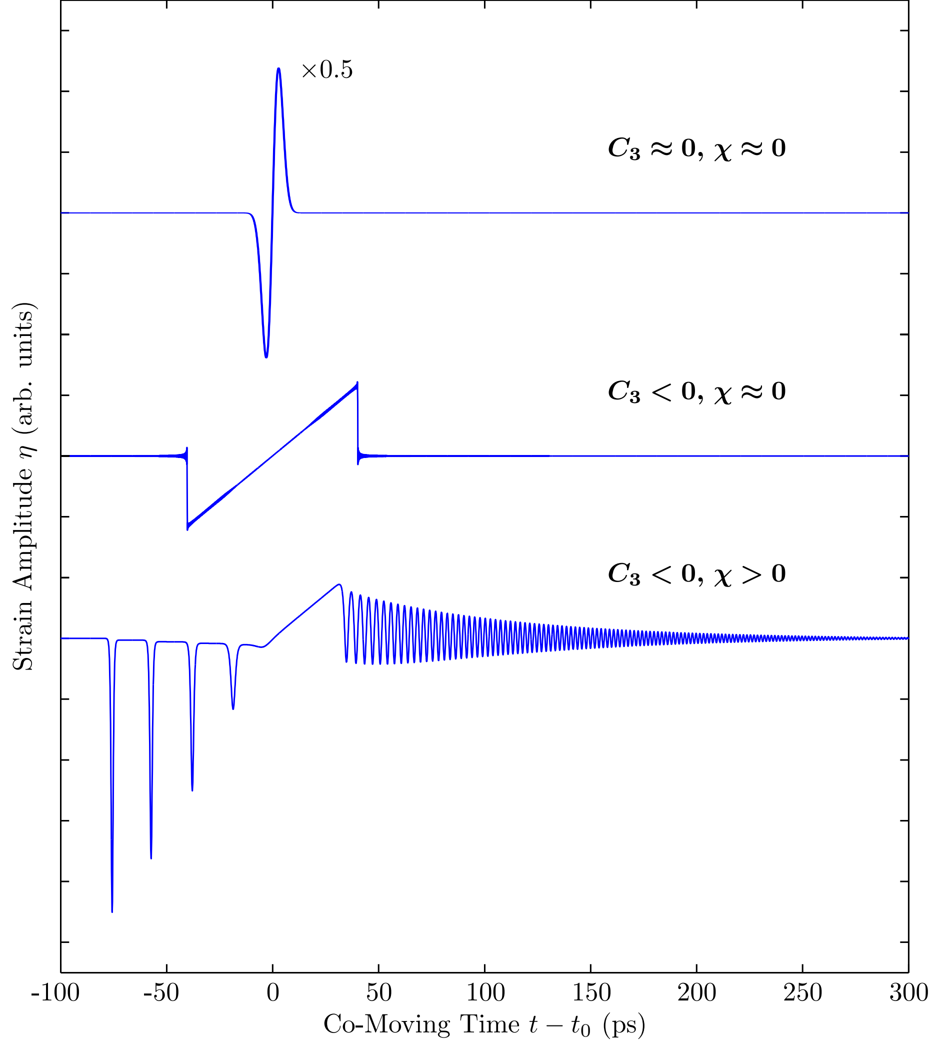

Figure 2.4: Propagation of a high power bipolar strain pulse (initial amplitude $\eta_0 = 10^{-3}$) through a 375 µm thick substrate with (top) approximately zero nonlinearity and dispersion ($C_3 \approx 0$, $\chi \approx 0$, respectively), (middle) only nonlinearity ($C_3 < 0$, $\chi \approx 0$), and (bottom) both nonlinearity and dispersion ($C_3 < 0$, $\chi > 0$). The figures were generated on the same scale, although the amplitude of the top figure ($C_3 \approx 0$, $\chi \approx 0$) has been halved for display purposes. (top) As shown, without nonlinearity and dispersion, the strain pulse propagates unchanged through the substrate. (middle) However, when nonlinearity is taken in account, an N-wave is established as the compressive peak moves faster relative to the leading edge, whilst the opposite occurs for the tensile peak relative to the trailing edge. (bottom) Where both nonlinearity and dispersive effects are present, balancing in the compressive part of these effects results in the formation of solitons with increasing amplitude further from the trailing edge. These figures were generated using MATLAB® code supplied by Emmanuel Péronne [15]. The initial bipolar strain pulse does not contain any reflected film components for simplicity, and approximately zero values are used for C_3 and χ due to software limitations, hence the minor oscillations present at the edges of the N-wave. The parameters are taken for a GaAs substrate with full calculation values noted in Appendix B.

2.3 Optical Strain Detection

Conventionally, strain pulses are detected some time after generation through optical methods. These range from piezoreflectance measurements, i.e. observing the change in reflectivity at the probed surface [2, 4, 12, 14, 47], to interferometric measurements conducted at or some distance beneath the surface [7, 15, 54, 57].

In essence, the optical probe pulse is identical to the pump beam except that it is of lower power, and travels on a delayed optical path so that the full scope of the strain pulse can be observed. This delayed optical path can be quite long depending on the propagation distance; for a typical 375 µm thick GaAs substrate, detection of a single pass through the substrate would require a temporal delay of approximately 79 ns, which is equivalent to an optical path distance of about 24 m. As it is usually infeasible to establish such a long delay, subsequent yet identical laser pulses are used as the probe beam to reduce the delay path length [12].

In the various optical detection methods discussed in the above references, the probe beam is reflected off a surface or sub-surface region and directed towards a photodiode, where reflectivity changes can be measured. These changes occur due the modification of the real and complex refractive indices of the material by strain interaction [2].

However, signals recorded using these measurement techniques generally required further data manipulation to distinctly see various features in the signal, and the amplitudes of the signals themselves can be comparable to background noise (see figures in the above references). These limitations are not present in the strain-induced transport detection methods, where background noise is negligible in comparison to the raw data.

2.4 Electron-Phonon Coupling Mechanisms

The following section discloses the various electron-phonon coupling mechanisms that are exploited by an alternative detection method to those discussed in Section 2.3. This detection method relies on strain-induced transport measurements, and is used extensively in this thesis.

A general overview of the detection method was given in Section 1.4, but it is necessary to examine coupling mechanisms such as the deformation potential, piezoelectric coupling, the Pekar mechanism, and the ripple effect

to fully appreciate how strain can be used to modulate transport mechanisms in nanostructures. As will be seen in the following subsections, it is considered that the deformation potential is the dominant mechanism for strain-induced transport in the devices presented in this work.

2.4.1 Deformation Potential

The deformation potential was defined by Bardeen and Shockley [58] as the motion of energy band boundaries, i.e. the conduction band (CB) and valence band (VB), under acoustic waves of high frequency. In essence, uniaxial strain propagating through a lattice modulates the interatomic spacing, and thus changes the energy separation (band gap) between the CB and VB of the bulk material. The energy shift δE_0 caused by the deformation potential is given by

$$\delta E_0 = \Xi\eta, \tag{2.14}$$

where Ξ is the deformation potential constant. In a single crystal, electrostatic potentials may also be established, as relaxed and stressed regions of the crystal adjust their Fermi levels to establish an equilibrium.

At the Γ-point of GaAs, there are four deformation potentials; three potentials for holes in the VB, and one for electrons in the CB [59, 60]. One deformation potential from each of the CB and VB is a result of hydrostatic strain, which shifts all bands by a set amount, whilst the remaining two VB potentials are dependent on uniaxial (shear) strain along both the [100] and [111] orientations.

There are various methods for determining deformation potentials, such as via analyses of carrier transport, free-carrier absorption, and deep level transient spectroscopy (DLTS), but the obtained values vary greatly. These variations occur for a number of reasons, such as fitting parameters and assumptions, although generally for the conduction band deformation potential $\Xi \geq -10\,\text{eV}$ [60–63]. As such, it can be shown that, using Equation 2.14, $\delta E_0 \geq -10\,\text{meV}$ for $\Xi = -10\,\text{eV}$ and $\eta = 10^{-3}$. Although the strain-induced effects apply to both CB and VB in this thesis, only effects in the CB will be examined outside of this chapter for simplicity.

2.4.2 Piezoelectric Coupling

Piezoelectric coupling arises due to the fact that GaAs, as a zinc blende crystal, has no centre of inversion symmetry [64]. Consequently, under an applied strain in a given direction, a piezoelectric field is established because of the formation of electric dipoles due to unit cell asymmetry.

For GaAs, piezoelectric coupling is strongest along the <111> direction, and therefore a component will exist along the <100> direction as well. However, shear stresses are required to cause a piezoelectric effect in GaAs [23, 65], and so the effect is not considered any further in this work given that only longitudinal, not transverse (shear), acoustic phonons are examined here. These transverse phonons also propagate at slower speeds (transverse acoustic velocity $v_{\mathrm{TA}} = 3350\,\mathrm{m\,s^{-1}}$ [29]), and so do not detract from the main results.

2.4.3 Pekar Mechanism

A third electron-phonon coupling mechanism that must be accounted for is the Pekar effect. This effect arises from the dependence of the relative permittivity of a crystal to strain in a static electric field [66], and is related to electrostriction [67]. From these analyses, it was determined that the Pekar mechanism would only be dominant in a bulk crystal with a very large relative permittivity, and for high frequency phonons.

Glavin et al. [68] observed that, as the dimensions of the sample are reduced to the scale of typical nanostructures, the confined electric fields generated in these nanostructures can result in the Pekar mechanism being the dominant electron-phonon interaction. It was also noted that the mechanism in these nanostructures could be controlled by an external electric field, is more important for non-piezoelectric materials, and is not reliant on crystal symmetry/asymmetry, unlike the piezoelectric coupling mechanism discussed in Section 2.4.2.

However, given the size and composition of the nanostructures examined in this thesis, there was a negligible Pekar contribution to strain-induced transport compared to deformation potential coupling, as calculated kindly by Boris Glavin for similar structures [44].

2.4.4 Ripple Effect

The ripple effect occurs at interfaces of the nanostructures, where the incoming strain pulse modulates the width of the nanostructure in its entirety. For example, in quantum wells (QWs), this would result in either an expansion or a contraction of the well width, thus resulting in a modulation of the confined QW energy levels. Knipp and Reinecke [69] observed that the ripple effect dominated over the deformation potential for $In_xGa_{1-x}As$ quantum dot (QD) sizes less that 50 nm.

This ripple effect for the QW ground state can be calculated (see Appendix A), and, for a typical GaAs well width of 5 nm, it induces a shift equivalent to $\Xi_r = -0.48$ meV for a strain amplitude $\eta = 10^{-3}$, which is significantly less than Ξ.

Chapter 3

Microfabrication Processes, and Experimental Methodology

The following chapter outlines microfabrication processes and experimental methodologies employed in this work. For the former, a general overview is provided of all processes used to fabricate the devices used; specific growth and consumable parameters for the double quantum well (QW)-embedded *p*-*i*-*n* devices and resonant tunnelling diodes (RTDs) can be found in Chapters 4 and 5, respectively.

The latter part of this chapter provides a general summary of various experimental setups used to obtain device transport characteristics, photocurrent pump-probe, and fast electrical measurements. The first technique is used regardless of the device to determine fabrication quality and device suitability, whilst the second and third arrangements are used to electrically record strain-induced effects in *p*-*i*-*n* and RTD devices, respectively.

3.1 Microfabrication Processes

This section describes the microfabrication processes used to create the semiconductor devices in this thesis. The samples were grown on 375 µm thick, 2 inch diameter [100]-orientated GaAs substrate wafers at the University of Nottingham by molecular beam epitaxy (MBE). These substrates were either semi-insulating or *n*-doped, and MBE growth was performed by Mohamed Henini or Richard Campion, with wafer names prefixed by ‘NU’ and ‘MN’,

respectively.

Extrinsic p- and n-type regions were formed by introducing dopants during epitaxial growth; silicon was the latter dopant for all samples, whilst beryllium and carbon were the p-type dopants for NU and MN wafers, respectively. The specific growth profiles for each device type can be found in the relevant device chapters.

Where possible, the samples were cleaned by solvent treatment prior to each microfabrication stage to remove surface containments and other residues that may remain from previous processes, as discussed in Section 3.1.3. Stages involving scribing, solvents, photoresists and developers, etchants, and other chemicals were performed on flow- and exhausted-ventilated wet decks to prevent inhalation of toxic fumes and/or particles.

3.1.1 Wafer Polishing

NU substrates were indium mounted in the MBE machine, and thus residual contaminants were deposited on its In mounted face surface and sub-surface layers. The resultant surface roughness rendered the face unsuitable for optical strain generation without further processing, as shown in Figure 3.1(a). This unsuitability arises from the scattering of optical pump pulses and acoustic phonons due to the surface and subsurface containments, respectively.

Indium containments were removed via mechanical and mechanochemical polishing on a lapping machine. Initially, a diamond lapping paste was applied, and this acted as an abrasive to physically remove contaminated layers of the substrate. Subsequently, a GaAs polishing agent was applied that etched the substrate material to provide an optically flat finish, as shown in Figure 3.1(b). Due to the presence of toxic materials in the sample, suitable measures were taken regarding clothing, such as the use of gloves and eye protection, and the disposal of consumable materials.

The two polishing processes were performed on a Metals Research Ltd. Multipol lapping machine. A wafer piece was mounted device-side down onto a disc mount using wax, and attached to a polishing jig. To ensure even polishing, the wafer piece was aligned perpendicular to the jig axis using its provided alignment controls and a basic optical alignment system; images of the lapping machine and polishing jig, as well as a diagram of the optical alignment system, can be seen in Figures 3.1(c)–(e).

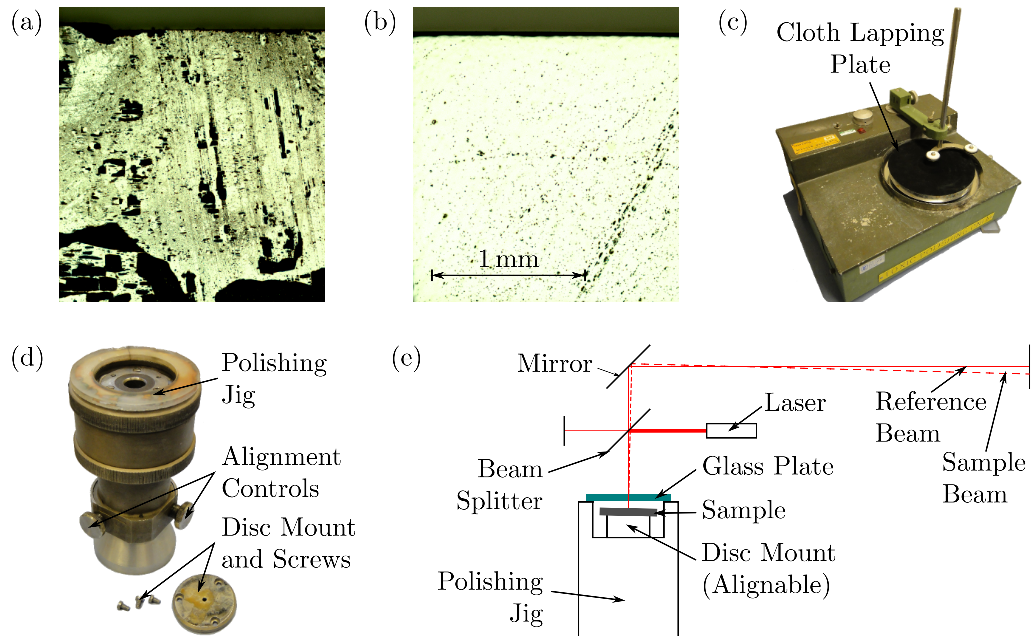

Figure 3.1: Effect of, and required apparatus for the mechanical and mechanochemical polishing of indium contaminated samples. (a) Image captured with an optical microscope showing surface and sub-surface damage (shown in black) of an unpolished sample due to the use of In mounting during MBE growth. (b) Removal of In containments via mechanical and mechanochemical polished resulted in an optically flat sample surface compared with an unpolished sample, as shown in (a). The scale shown in (b) also applies for (a); only one was drawn for clarity purposes. (c) Metals Research Ltd. Multipol lapping machine with cloth lapping plate attached for the mechanochemical polishing stage, and (d) upturned polishing jig with labelled alignment controls, and disc mount with screws. (e) Basic optical alignment system designed to ensure even polishing of the surface by aligning the sample beam (dotted) to the reference beam (dashed), which are caused by reflections from the sample surface and glass plate, respectively.

Once aligned, Kemet Type KD Diamond Compound (14-KD-C1) lapping paste [70, 71] was applied to the area around the wafer piece, and a solder lapping plate was attached to the machine. Gentle rotation of the lapping plate, combined with frequent lubrication and examination of the wafer surface, resulted in a uniform surface.

For the mechanochemical stage, a cloth lapping plate was coated with a polishing agent comprising 1.15 g of INSEC FP Compound Semiconductor Polish powder by Fujimi Incorporated, Japan mixed with 25 ml of distilled water [72], and the wafer piece was polished with this solution until an optically flat mirror finish was attained. As the acoustic phonon propagation time was required for both determining the temporal origin of the strain-induced effects, and establishing a suitable optical delay path for the experiments, thickness measurements were performed using a micrometer once the wafer piece had been dismounted and washed in acetone.

3.1.2 Wafer Scribing

As only small wafer pieces are required for experimentation, the wafer was scribed into a sample between 5×5 mm and 10×10 mm in size with a diamond-tipped scribing pen; normally a few samples were processed simultaneously in case of accidental damage, or unforeseeable processing contamination. A respirator was worn at all times due to the release of toxic GaAs dust during this process, and appropriate measures were taken for the disposal of consumables.

3.1.3 Surface Cleaning

Samples were solvent cleaned to remove surface organic impurities where possible with ethyl lactate, acetone, methanol, and isopropyl alcohol (IPA), stated here in order of increasing purity.

Typically the sample was immersed in each organic solvent of increasing purity at room temperature for a minimum of ten minutes in an ultrasonic bath. However, when dealing with delicate samples, a stirring plate or manual gentle agitation was used instead. Afterwards, the sample was removed, gently sprayed with the solvent to remove any immersion residues, and dried with pressurised nitrogen gas. As acetone leaves striations on the surface due to its high evaporation rate, the N_2 drying stage was replaced by a methanol spray when cleaning with acetone.

3.1.4 Optical Photolithography

Optical photolithography is the process by which a required pattern can be applied to a given surface; this pattern is used for further processes to obtain the desired device, such as by wet etching or evaporation. It is achieved by applying chemical photoresist to the sample surface in an even layer, hardening it, and exposing the relevant areas to ultraviolet radiation.

Depending on whether a positive or negative photoresist is used, the UV radiation photochemically destabilises or stabilises the exposed areas, respectively. The less stable regions are therefore more soluble when immersed in photoresist developing solution, and are thus removed to leave the required pattern. Waycoat BPRS 150 positive photoresist supplied by Olin Hunt Speciality Products, Inc. USA, and AZ 400 K Developer from AZ Electronic Materials GmbH, Germany were used for photolithography for all samples.

Sample Preparation

The sample was solvent-cleaned, as detailed in Section 3.1.3, to ensure successful photoresist adhesion and patterning on the surface; this is a necessary stage, since the sample cannot be cleaned in subsequent processes due to the susceptibility of BRPS 150 photoresist to organic solvents. These solvents were removed from the sample surface by dehydration in an oven set at 130 °C for ten minutes, and the sample was allowed to thermally re-stabilise to room temperature to prevent thermal shock, which could lead to crack propagation and therefore sample damage.

The substrate-exposed (rear) surface of the sample was mounted onto a small glass slide using a thin layer of BPRS 150, which was subsequently soft baked on a hot plate at 90 °C for two minutes. Once dried, the edges of this photoresist mounting were checked to ensure an adequate seal between the sample and glass slide. This process protected the rear surface from exposure to etchants and other chemicals that could otherwise reduce the sample thickness and/or damage the surface uniformity; both of these parameters are essential for ultrafast acoustic experiments, as the former would reduce the propagation distance for dispersion, and potentially increase the difficulty of handling the sample, whereas the latter would result in scattering of optical pulses thus reducing the efficiency of opto-acoustic conversion processes.

Spin Coating

To form an even photoresist layer, the sample was vacuum mounted onto a Solitec Spin Coater. A thin layer of BPRS 150 was applied to the surface using a micro pipette syringe, and the sample was rotated at 4000 RPM for 30 s to spread the fluid evenly across the surface. This resulted in a 1.5 µm thick layer on the sample surface except at the edges, where there was edge beading formation. This beading was carefully removed so that adequate contact between the uniform photoresist layer and the photomask could be achieved during future UV exposure. The sample was soft-baked in an oven at 110 °C for thirty minutes to harden the photoresist, and allowed to cool to room temperature.

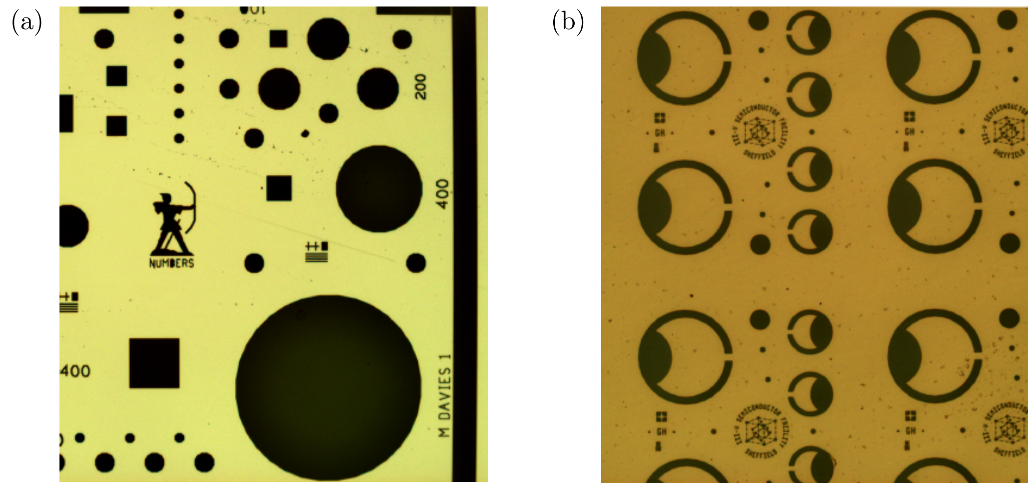

Figure 3.2: Example soda lime glass photomasks for device microfabrication with chrome-patterned contact design. (a) The Robin Hood photomask set fabricates electrical mesas (no optical access) from 30 µm to 800 µm in diameter with identical top and bottom contact material; this set comprises an etch mask, and a contact mask, and was used to fabricate the resonant tunnelling diodes (RTDs) discussed in Chapter 5. (b) The Sheffield photomask set produces mesas from 200 µm to 400 µm with a distinct horseshoe shape to allow both optical access, and the prevention of an unwanted inductance current in the top contact if the device is placed in a magnetic field. This set allows for different top and bottom contact materials, and consists of etch, top contact, and bottom contact masks. The Sheffield mask set was used to process the double quantum well (QW)-embedded *p-i-n* hypersonic detectors considered in Chapter 4.

Ultraviolet Exposure, Pattern Developing, and Photoresist Removal

UV exposure was performed using a Karl Suss MJB3 Mask Aligner and a suitable soda lime glass, chrome-patterned photomask. Two different photomask sets were used for device fabrication, and an image of each set can be seen in Figure 3.2. Each set comprised at least two patterns for etching and contact material evaporation, and all photomasks were solvent cleaned prior to use, as described in Section 3.1.3. The photoresist-hardened sample was UV exposed for 6 s with a mercury lamp power of 11 mW; the exposure time was increased accordingly for lower lamp powers.

The Robin Hood mask, imaged in Figure 3.2(a), formed cylindrical, electrical mesas projecting from the substrate. These mesas had no optical access, and were used to fabricate the RTDs discussed in Chapter 5. The Sheffield mask set shown in Figure 3.2(b) formed cylindrical mesas projecting from the substrate with optical access on the top surface, due to the distinct horseshoe shape of the contact mask. This was used to process the double QW-embedded *p-i-n* hypersonic detectors, detailed in Chapter 4.

The post-exposure sample was immersed with gentle agitation in a 1:8 developing solution of AZ 400 K and deionised (DI) water, washed in DI water, and dried with N_2 gas. The development progress was checked regularly with an optical microscope to prevent overdeveloping of the photoresist, with the sample not normally immersed for more than 30 s in total.

When the photoresist pattern was no longer needed, it was removed in a covered bath of acetone heated to 52 °C for ten minutes; this lift-off process also removed the protective glass slide, and the solvent bath was allowed to cool prior to sample removal due to the release of vapours when heated.

3.1.5 Chemical Wet Etching

To access specific sample layers and produce mesas of the required dimensions, etchant chemicals were used to remove material from areas exposed by optical photolithography (see Section 3.1.4). As the chemicals react with the sample, soluble material is formed, and the sample is etched into the required pattern. For the devices discussed in this work, wet etching was performed to access the bottom contact layer of each sample so that voltage could be applied across the active region of the device, and electrical measurements could be taken.

Although there are many chemicals that produce a fast etchant rate, a 1:1:100 solution of ammonia, hydrogen peroxide, and deionised (DI) water was used to produce the devices disclosed in this work; this etchant solution has a typical etch rate of $0.35\,\mu m\,min^{-1}$, and allowed for precise control of the process. Due to etch rate dependency on crystal face, the NH_4OH:H_2O_2:H_2O etchant formed vertically cylindrical mesas with 45°-sloped sidewalls [73–75]. Undercutting occurred beneath the photoresist pattern, thus reducing the diameter of the top surface of the resultant mesa, as shown in Figure 3.3. The etchant solution was neutralised by washing the sample in DI water, and dried with N_2 gas. The etch rate was also monitored regularly using either a DekTak 3 Surface Profilometer, or a KLA-Tencor AlphaStep D-120 Stylus Profiler.

The samples generally had a minimum etch depth of 1 μm thus, for accuracy, the above process was performed three times; the first process was conducted for 60 s to establish the actual etch rate of the solution, and the second was timed so that it would etch through the active region of the device to the bottom contact layer. A final process was required to etch into

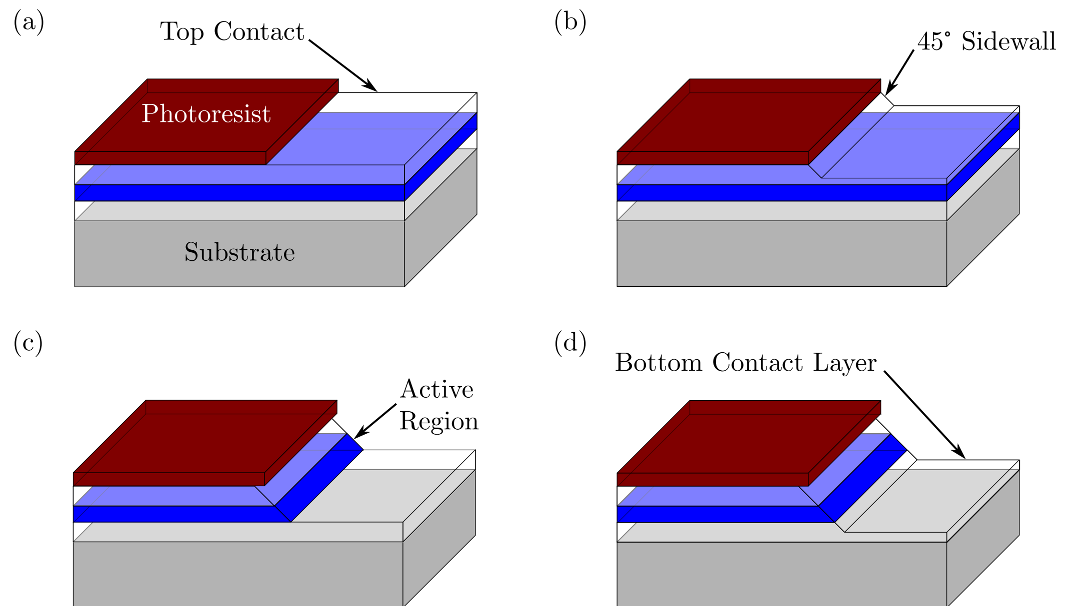

Figure 3.3: Chemical wet etching of a representative sample showing greater undercutting of the top surface over time. (a) The sample is shown here with its layers grown by MBE on to a substrate, with the required photoresist (red) pattern applied by optical photolithography on top of these layers (see Section 3.1.4). (b) It is first immersed in etchant for 60 s to determine the etch rate, with minor undercutting occurring and the creation of 45° sidewalls, as material is removed from the top contact layer. (c) The determined etch rate is used to calculate the immersion time for the second etching process so that material is removed from the active region of the device on approach to the bottom contact layer. (d) The final etch process removes approximately half of the bottom contact layer to ensure successful ohmic contacting of the device in later stages; note the more pronounced undercutting of the photoresist layer due to prolonged immersion in the etchant solution.

the central region of the bottom contact layer for optimal contact formation; the timing of this stage was based on a revised etch rate from the second process, as the quality of the etchant solution, and therefore the etch rate, would decay rapidly once mixed.

3.1.6 Thermal Evaporation

Thin films were deposited on the samples by thermal evaporation under high vacuum, where their thickness could be controlled to sub-nanometre accuracy. The desired material was evaporated by a heated filament and expanded into the chamber, before condensing onto the sample surface. The amount of deposited material was controlled by a film thickness monitor, which consisted of a piezoelectric crystal that was gradually strained with increased deposition, thus allowing for thickness measurements with suitable calibration.

Thermal evaporation was necessary to metallise the sample for contact formation, and thus surface oxides were removed from the samples with a 1:1 solution of hydrochloric acid and DI water for 60 s for optimal adhesion of the evaporated material; if possible, the desired material was solvent cleaned prior to mounting on the evaporator filament. In addition, evaporations were conducted in a vacuum of at least 10^{-6} mbar to minimise contaminants and damage to the sample or filament. n-type metallisations were conducted in an Edwards E306A Coating System, whilst p-type metallisations were performed in an Edwards Auto 305 Turbo evaporator.

Contact metallisation required a separate evaporation to deposit each material during the same process, as an adhesion layer must first be deposited on the sample surface for successful Au capping. For n- and p-type metallisations, 40 nm InGe (1:1 by mass) with a 100 nm Au cap, and 20 nm Mg with a 200 nm Au cap were deposited onto the sample, respectively.

3.1.7 Rapid Thermal Annealing

Ohmic contacts were formed by rapid thermal annealing (RTA) the metallised film deposited by thermal evaporation (see Section 3.1.6). This caused diffusion of materials across the metal-semiconductor interface in both directions, which reduced the interface barrier height. Coupled with high doping of the semiconductor layer, the diffusion across the interface resulted in ohmic contact formation [73, 76, 77].

RTA was performed using an AnnealSys AS-One Rapid Thermal Processing Furnace with H_2/Ar processing gas and a graphite susceptor, where Mg-Au p- and InGe-Au n-type contacts were annealed at 420 °C and 380 °C for dwell times of 25 s and 15 s, respectively. The selection of these materials results in a shallow diffusion of around 20 nm [78], thus reducing the possibility of accidental diffusion of contact material into the active region of the device.

3.1.8 Sample Packaging

Samples were mounted onto a sample holder using a small amount of GE/IMI 7031 Varnish supplied by Cambridge Magnetic Refrigeration, UK, and left to dry at RTP for 10 minutes [79]. The sample holder consisted of a printed circuit board with copper plating for electrical connection through a 50 Ω $0 \rightarrow 18$ GHz SMA end launch connector. For the RTD devices, an additional

$50\,\Omega$ resistor and a 10 nF capacitor were soldered in series with the device; detailed circuit diagrams can be found in the relevant device chapters.

Each device was connected to the copper plating of the sample holder with 25 µm diameter Al wires by a Kulicke and Soffa Industries Model 4123 Wedge Bonder. Multiple bottom contact wires were bonded to increase thermal conduction to the device, which was especially important due to the use of a continuous-flow cryostat in the experimental setups detailed in Section 3.2.

3.2 Experimental Methodology

In this section the main experimental techniques applied in this thesis will be discussed. Initially, an overview of transport measurements to record stationary current-voltage (I_0-V) characteristics of both RTDs and *p*-*i*-*n* devices will be provided. Afterwards, the two principal optical setups utilised in Chapters 4 and 5 will be examined. For all the discussed setups in this section, the samples were mounted within an Oxford Instruments Optistat CF-V Liquid Helium (LHe) Continuous Flow Optical Cryostat.

Both of these optical setups were performed using an amplified titanium-sapphire laser system comprising four main components manufactured by Spectra-Physics. The system consisted of a Millennia Pro solid state continuous-wave (CW) green laser pumping a Tsunami ultrafast Ti:Sapphire oscillator to produce optical pulses. These pulses were directed into a Spitfire Pro amplifier pumped by an Empower diode-pumped pulsed green laser. The amplifier outputted 0.5 mJ optical pulses of 800 nm wavelength, 60 fs duration, and 5 kHz repetition rate.

3.2.1 Transport Measurements

Transport measurements were conducted to determine I_0-V characteristics of the nanofabricated devices. These measurements were used to check successful processing, and verify that the device displayed ideal properties. I_0-V measurements were made both at room temperature and at approximately 4.7 K. Figure 3.4 depicts two separate circuit diagrams used to obtain these measurements for both RTDs and QW-embedded *p*-*i*-*n* devices.

The circuit shown in Figure 3.4(a) was used to obtain I_0-V characteristics where additional components were mounted onto the holder aside from the

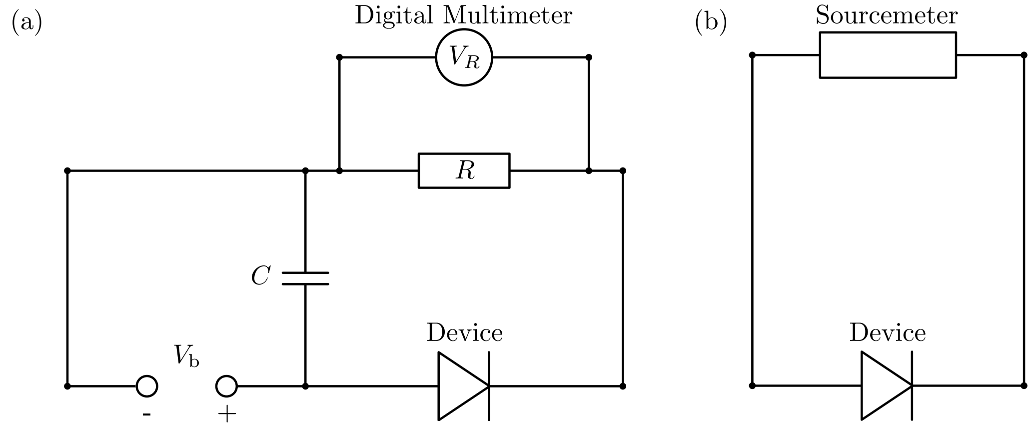

Figure 3.4: Electrical circuit diagrams used for conducting stationary current-voltage (I_0-V) measurements on resonant tunnelling diodes (RTDs) and double quantum well (QW)-embedded *p*-*i*-*n* devices. (a) RTD I_0-V characteristics where measured using this setup, as the sample holder comprised both a $R = 50\,\Omega$ resistor and a $C = 10\,\text{nF}$ capacitor in addition to the sample. The voltage drop across the resistor V_R was measured using a Agilent 34401A Digital Multimeter, and a voltage bias V_b was applied externally using a Keithley 230 Programmable Voltage Source; the resultant I_0-V characteristics could be calculated using Equations 3.1-3.2. Note that this setup could be used on *p*-*i*-*n* devices, although the capacitor branch would be absent and a $R = 22\,\text{k}\Omega$ resistor would have to be connected externally, as only the *p*-*i*-*n* sample was present on the holder. (b) I_0-V measurements on both the RTD and *p*-*i*-*n* devices were conducted using this setup, where V and I_0 were both applied and measured, respectively, by a Keithley 2400 Sourcemeter.

sample itself; for the RTDs, these additional components were a $R = 50\,\Omega$ resistor and a $C = 10\,\text{nF}$ capacitor. The voltage drop across the resistor V_R was measured externally using an Agilent 34401A Digital Multimeter with an external voltage bias V_b applied from a Keithley 230 Programmable Voltage Source. The I_0-V characteristics were subsequently determined using the following equations

$$V = V_b - V_R - \frac{V_R R_{SP}}{R}, \tag{3.1}$$

$$I_0 = \frac{V_R}{R}, \tag{3.2}$$

where V is the voltage across the device, I_0 is the stationary current flowing through the device, and R_{SP} is the spreading resistance of the device, if applicable; this is the resistance in the bottom contact layer from the base of the mesa to where the actual wire bond to the bottom contact is made. Measurements of the *p*-*i*-*n* devices could also be taken with the setup in Figure 3.4(a), although the capacitor branch would not exist and a $R = 22\,\text{k}\Omega$ resistor would have to be connected externally, given that there are no additional components on the *p*-*i*-*n* sample holder; further details

can be found in the relevant device results chapters.

The alternative setup shown in Figure 3.4(b) could also be used to obtain I_0-V characteristics from both the RTD and *p*-*i*-*n* devices. Here, a Keithley 2400 Sourcemeter was operated externally to both apply the voltage across the device V, and measure I_0.

3.2.2 Photocurrent Pump-Probe Measurements

Photocurrent pump-probe measurements were conducted on samples from MN653 maintained at 4.7 K with liquid helium. These samples comprised a semi-insulating (SI) bulk GaAs substrate as an acoustic transducer on one face, and a processed double QW-embedded *p*-*i*-*n* hypersonic detector on the other face; the comparison Al transducer sample was measured using a different setup that is briefly discussed in Section 4.5.

The optical setup is depicted in Figure 3.5, where pulses from the Spitfire Pro were split into pump and photoexcitation beams (both labelled in bold). The sample was orientated so that the former and latter beams were incident on the transducer and *p*-*i*-*n* detector, respectively. The pump beam was frequency doubled so that 400 nm wavelength pulses were focussed onto a beam spot of diameter 200 µm with a maximum fluence of 3.0 mJ cm^{-2}. The 800 nm wavelength photoexcitation beam was reflected off various mirrors to introduce an optical path delay, and was focussed onto the *p*-*i*-*n* detector with a spot diameter of 50 µm and maximum fluence of 10 µJ cm^{-2}. Both beams were aligned so that the pump beam excited an area on the transducer directly opposite the *p*-*i*-*n* detector.

The photoexcitation beam was delayed so that it would excite carriers in one of the QWs at approximately the same time as the arrival of the strain pulse, thus resulting in measurable strain-induced effects. This delay was dependent on the propagation of the strain pulse through the sample, and was calculated to be 80.73 ns for a GaAs thickness of 387.5 µm. This is equivalent to an optical delay path of 24.22 m, and was achieved through multiple reflections of the photoexcitation beam between two parallel bar mirrors, labelled M_{P1} and M_{P2}, and the static retroreflector shown in the Figure 3.5.

As previously discussed in Section 2.2, the temporal duration of the strain pulse increases with propagation due to dispersion. Consequently, the optical delay between both optical beams must be changed slightly to observe the

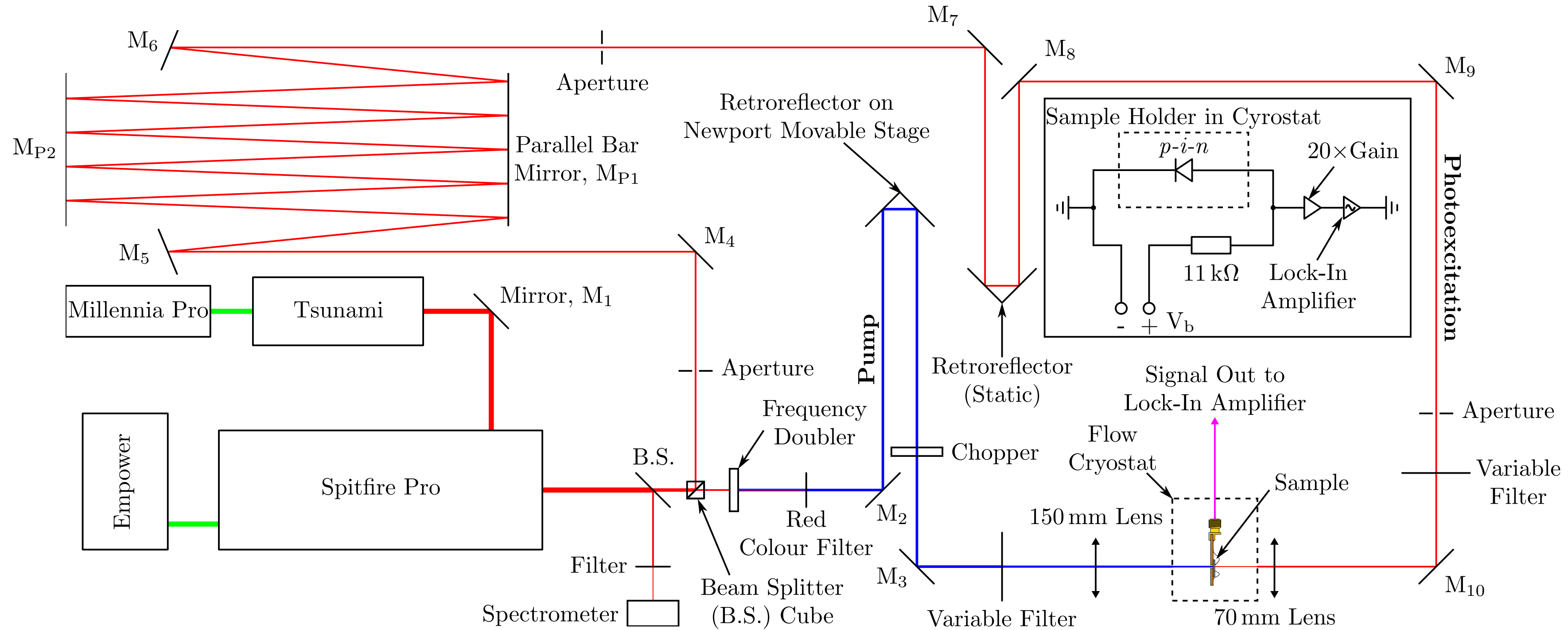

Figure 3.5: Experimental setup for photocurrent pump-probe measurements conducted on MN653 samples processed with double quantum well (QW)-embedded *p-i-n* devices on the photoexcited side. Optical pulses were generated from an amplified titanium-sapphire laser system created by Spectra-Physics. This comprised a Millennia Pro continuous-wave (CW) green laser pumping a Tsunami ultrafast laser, whose output was fed into a Spitfire Pro ultrafast amplified pumped by an Empower pulsed green laser. The outputted pulses were of 800 nm wavelength, 60 fs duration, 5 kHz repetition rate, and were split into pump and photoexcitation beams (labelled in bold); the former was frequency doubled so that 400 nm wavelength pulses were focussed onto the rear of the sample with a diameter of 200 µm to transduce coherent phonons. Excited carriers in the QW were generated by the photoexcitation beam, which was delayed so that the strain pulse and photoexcitation pulse would coincide at the QW. Analysis of the propagating strain pulse was obtained through controlled movement of the pump beam retroreflector, and the sample was maintained at 4.7 K within an Oxford Instruments Optistat CF-V Liquid Helium (LHe) Continuous Flow Optical Cryostat. (insert) The device was biased and electrically probed using the given circuit, and the change in photocurrent was measured through a Stanford Research Systems SR830 DSP Lock-In Amplifier referenced to the chopper.

full strain pulse profile. This was achieved through the use of a retroreflector mounted on a movable Newport M-IMS600PP High Performance Linear Stage with ±1.25 µm accuracy, which was swept through the duration of the propagated strain pulse to obtain its full profile.

The *p*-*i*-*n* detector was electrically probed using the circuit shown in the insert of Figure 3.5, in which the signal was fed through a 20× gain high impedance amplifier with > 20 MHz bandwidth. This signal included a photocurrent component I_{P} in the QW due to the photoexcitation beam and, to observe changes in the photocurrent δI_{P} over the stationary current I_0, the amplified signal was sent to a Stanford Research Systems SR830 DSP Lock-In Amplifier, which was referenced to the chopper set at 2.5 kHz in Figure 3.5. Data was recorded over a 200 ps time window with 500 fs resolution, and the time constant of the lock-in amplifier was set at 0.1 s.

3.2.3 Fast Electrical Measurements

Fast electrical measurements were conducted on RTDs fabricated from NU165 using the setup drawn in Figure 3.6, and maintained at 4.7 K with liquid helium. Amplified pulses from the Spitfire Pro were directed through various optical components so that 400 nm wavelength pulses were focussed to a beam spot diameter of 200 µm. The spot was aimed onto an Al film evaporated on the rear surface of the sample directly behind the connected RTD.

A voltage bias was applied externally using a Keithley 230 Programmable Voltage Source, and the electrical signal from the device was passed through two 10 dB amplifiers before being recorded on a 12.5 GHz analogue bandwidth Textronix DPO71254 Digital Phosphor Oscilloscope, which allowed for real-time observation of strain-induced effects in RTDs; a circuit diagram of this setup is shown in the insert for Figure 3.6. A maximum fluence of 17.8 mJ cm^{-2} was incident on the Al film thus generating a bipolar strain pulse via thermoelastic effects, as considered in Section 2.1. The oscilloscope was triggered by the triggering photodiode shown in Figure 3.6, and data was recorded with a 4 ps resolution and 500 averages.

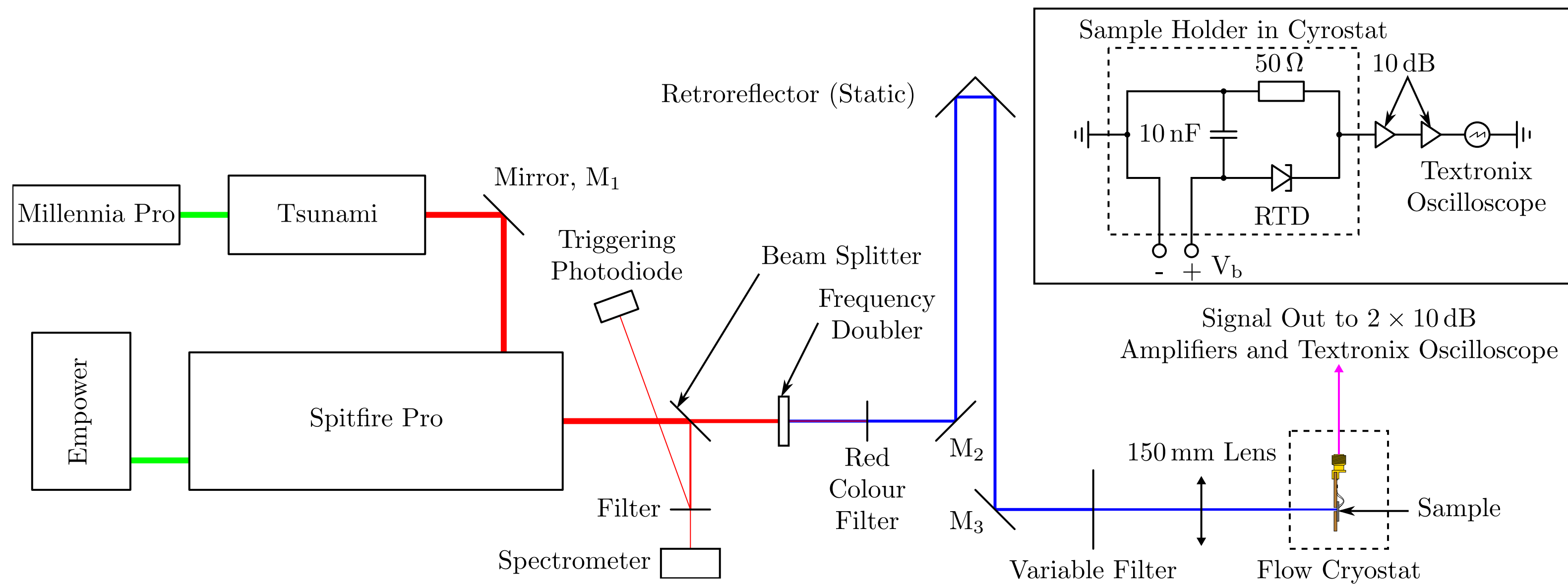

Figure 3.6: Experimental setup for fast electrical measurements conducted on NU165 samples using optical pump pulses to excite strain pulses in a 100 nm Al film deposited on the rear surface of the sample. The optical pump pulses were generated using a titanium-sapphire laser system manufactured by Spectra-Physics, which comprised a Millennia Pro continuous-wave (CW) green laser pumping a Tsunami ultrafast oscillator. This in turn was used to seed a Spitfire Pro ultrafast amplifier pumped using an Empower pulsed green laser. The system outputted optical pulses of 800 nm wavelength, 60 fs duration, and 5 kHz repetition rate that were passed through a frequency doubler to form 400 nm wavelength pulses. The optical pulses were directed through various optical components so that a 200 µm diameter beam spot was focussed onto the Al film directly opposite the device. This optical excitation formed bipolar strain pulses via thermoelastic effects that propagated through the sample and generated a signal. The sample was maintained at 4.7 K within an Oxford Instruments Optistat CF-V Liquid Helium (LHe) Continuous Flow Optical Cryostat. (insert) A voltage bias, V_b was applied across the RTD device externally, and the device signal was amplified externally using two 10 dB amplifiers before being measured on a 12.5 GHz analogue bandwidth Textronix DPO71254 Digital Phosphor Oscilloscope.

Chapter 4

Coherent Phonon Generation in a Bulk GaAs Substrate

This chapter examines coherent phonon generation in a bulk GaAs substrate, and considers the various mechanisms behind it. These mechanisms were determined remotely by electrically probing the propagated strain pulse using a double quantum well (QW)-embedded *p*-*i*-*n* hypersonic detector, hereafter *p*-*i*-*n* detector, which is a modified version of that utilised by Moss et al. [19] and Moss et al. [20].

The wafer profile used to fabricate the *p*-*i*-*n* detector is first given in this chapter, alongside sample-specific processing considerations, before transport measurements are presented. These stationary current-voltage (I_0-V) measurements were conducted under both dark and light (laser illumination) conditions, and provided evidence of successful processing and desired device functionality. Specifically, it will be demonstrated that photoexcitation of carriers under laser illumination is possible in the hypersonic detector, and that this can be tuned to a specific QW within the device itself by selecting either an appropriate laser wavelength, and/or applied bias.

Photocurrent pump-probe measurements conducted using a bulk GaAs substrate transducer will next be discussed, in conjunction with theoretical descriptions of acoustic wavepacket transduction. These descriptions are based on theoretically modelling initial strain profiles, simulating their propagation using the Korteweg-de Vries-Burgers (KdV-Burgers) equation, and comparing the propagated result to the measured, propagated strain. The experimental results are also compared with strain generated from an Al film transducer to establish differences between the strain generation

	MN653 Wafer Profile		
	Material	**Thickness (nm)**	**Doping (cm^{-3})**
TC	p-$Al_{0.33}Ga_{0.67}As$	200	2×10^{18}
B	$Al_{0.33}Ga_{0.67}As$	100	–
WW	GaAs	10	–
B	$Al_{0.33}Ga_{0.67}As$	3.4	–
NW	GaAs	5	–
B	$Al_{0.33}Ga_{0.67}As$	100	–
BC	n-$Al_{0.33}Ga_{0.67}As$	200	1.3×10^{18}
	375 µm Semi-Insulating (SI) GaAs Substrate		

Table 4.1: MN653 wafer profile used for the fabrication of double quantum well (QW)-embedded *p-i-n* hypersonic detectors. This wafer comprised of a bottom contact layer (**BC**) grown on top of a 375 µm semi-insulating (SI) GaAs substrate, which consisted of n-type $Al_{0.33}Ga_{0.67}As$, Si-doped to a concentration of 1.3×10^{18} cm^{-3}, followed by the intrinsic region layers, and the top contact layer (**TC**) of p-type $Al_{0.33}Ga_{0.67}As$, C-doped to 2×10^{18} cm^{-3}. The intrinsic region comprised of three undoped $Al_{0.33}Ga_{0.67}As$ barriers (**B**) encompassing two undoped GaAs QWs. The barriers were of thicknesses 100 nm, 3.4 nm, and 100 nm, and encompassed a narrow QW (**NW**) and a wide QW (**WW**) of thickness 5 nm and 10 nm, respectively.

methods, and to confirm the validity of the theoretical propagation model used. Physical bases for the initial strain profiles are also given in the relevant sections, after which an overall conclusion of phonon generation in bulk GaAs is presented.

4.1 Wafer Profile and Processing

The *p-i-n* detector was fabricated from wafer MN653 grown via molecular beam epitaxy (MBE) by Richard Campion, and its profile is given in Table 4.1. This wafer comprised of a 200 nm thick n-type $Al_{0.33}Ga_{0.67}As$ bottom contact layer (**BC**) grown on top of a commercially available 375 µm thick semi-insulating (SI) GaAs substrate. This bottom contact layer was doped with Si to a concentration of 1.3×10^{18} cm^{-3}.

The intrinsic region of the device comprised of a barrier (**B**) of 100 nm undoped $Al_{0.33}Ga_{0.67}As$ on one side of the first, narrow QW (**NW**) of 5 nm undoped GaAs, with a second 3.4 nm $Al_{0.33}Ga_{0.67}As$ barrier (**B**) forming the central barrier between the two QWs. The second, wide QW (**WW**) consisted of undoped GaAs grown to a thickness of 10 nm, and a final 100 nm thick barrier of $Al_{0.33}Ga_{0.67}As$ (**B**) completed the intrinsic region. A top contact layer (**TC**) was deposited above the intrinsic region, and

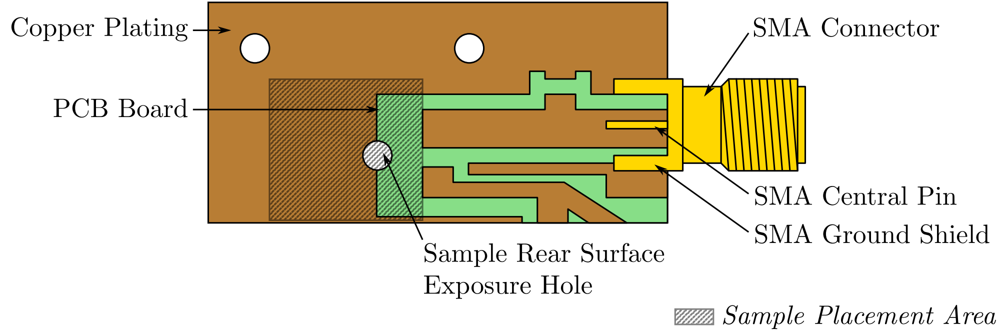

Figure 4.1: Typical sample holder used to perform transport and photocurrent pump-probe measurements on samples fabricated from MN653. The holder was designed by Ian Taylor, and consisted of a patterned, copper plated PCB board. A SMA connector was subsequently soldered onto the holder so that measurements from the devices could be made. The sample was adhered within the shaded region so that the rear surface exposure hole was directly opposite the required device. Al wire was wedge bonded from the top p-contact and the bottom n-contact to the copper plating connected to the SMA central pin and ground shield, respectively.

comprised of 200 nm p-type $Al_{0.33}Ga_{0.67}As$, C-doped to a concentration of $2 \times 10^{18}\,cm^{-3}$.

All samples from MN653 were processed using the methods discussed in Section 3.1 with the Sheffield mask set, and were mounted onto the sample holder in the shaded area of Figure 4.1. In addition, a 30 nm thick Al film was also evaporated onto the rear surface of the reference, metal transducer sample. The top p- and bottom n-contacts were Al wire bonded to the copper plating connected to the central SMA pin and ground shield, respectively, to form the circuit given in the insert of Figure 3.5. Measurements were then performed using this circuitry with the experimental setups described in Sections 3.2 and 4.2.

The wafer was initially grown to determine whether or not resonant tunnelling between coupled QWs could be modulated by an incoming acoustic pulse, hence the presence of a double QW structure in this device. Preliminary measurements conducted for this purpose found no discernible strain-induced effects, possibly due a smaller scattering time over the coupling time of the QWs. This was in spite of the ability to distinguish between photoexcitation of each QW in both transport and pump-probe measurements; further detail of this ability can be found in Sections 4.2–4.3. Accordingly, work progressed onto the determination of phonon generation in a bulk GaAs transducer using only one of the two embedded QWs, the 10 nm wide QW, as a hypersonic detector; this operated in a similar manner to the hypersonic detector discussed in Section 1.4.2.

4.2 Transport Measurements

Transport measurements were conducted on all samples to verify the quality of the processed devices, and their correct operation. A representative I_0-V measurement taken under dark and light conductions for the Al film sample is provided in Figure 4.2. These characteristics were obtained using the circuitry shown in Figure 3.4(a), where $R = 22\,\mathrm{k\Omega}$, when the device was maintained at 10.8 K in an Oxford Instruments Optistat Bath Dynamic Variable Temperature Cryostat. The device was illuminated using a Spectra-Physics Tsunami Ultrafast Ti:Sapphire oscillator pumped by a Spectra-Physics Millennia XS solid state continuous-wave (CW) green laser. This oscillator was set to output 800 nm wavelength pulses with 150 fs duration, and 82 MHz repetition rate. This beam was focussed onto the *p*-*i*-*n* detector with a 50 µm diameter beam spot to give a photoexcitation fluence $W_{\mathrm{PE}} = 0.5\,\mathrm{\mu J\,cm^{-2}}$.

In dark conditions (solid, blue line), the *p*-*i*-*n* detector had a forward turn-on voltage of $V = 0.94\,\mathrm{V}$, a reverse saturation current $I_0 = -25\,\mathrm{pA}$, and a reverse breakdown voltage $V_{\mathrm{br}} = -4.53\,\mathrm{V}$. Note that the forward turn-on voltage is not at 0 V, as the built-in potential of the diode must first be overcome before there is any forward current. When illuminated by the oscillator (dashed, red line), there was a significant change in the I_0-V characteristics due to the inclusion of a photocurrent component. Specifically, the characteristics are near-identical in shape for $V > 0.44\,\mathrm{V}$, except for a larger negative current in the illuminated signal due to photoexcitation of carriers across the entire device. At smaller device voltages, the current rapidly dropped to $I_0 = -5.4\,\mathrm{\mu A}$ at $V_{\mathrm{WW}} = -1.65\,\mathrm{V}$, which corresponded to photoexcitation of the wide QW. The current then steadily increased before falling once more at V_{br}; note that there was a small deviation in the increase of current at approximately $V_{\mathrm{NW}} = -3.97\,\mathrm{V}$, which was due to photoexcitation of the narrow QW.

The main trough and later deviation from the steadily increasing current are both evidence of the additional photocurrent contribution generated by the embedded wide and narrow QWs respectively. In the absence of these QWs, the profile of the I_0-V characteristics under dark and light conditions would be identical, except for a negative offset in the latter due to the device photocurrent contribution[1]. Although it is clear that there is an

[1]See e.g. Figure 55.3, p. 433 in Ng [26]

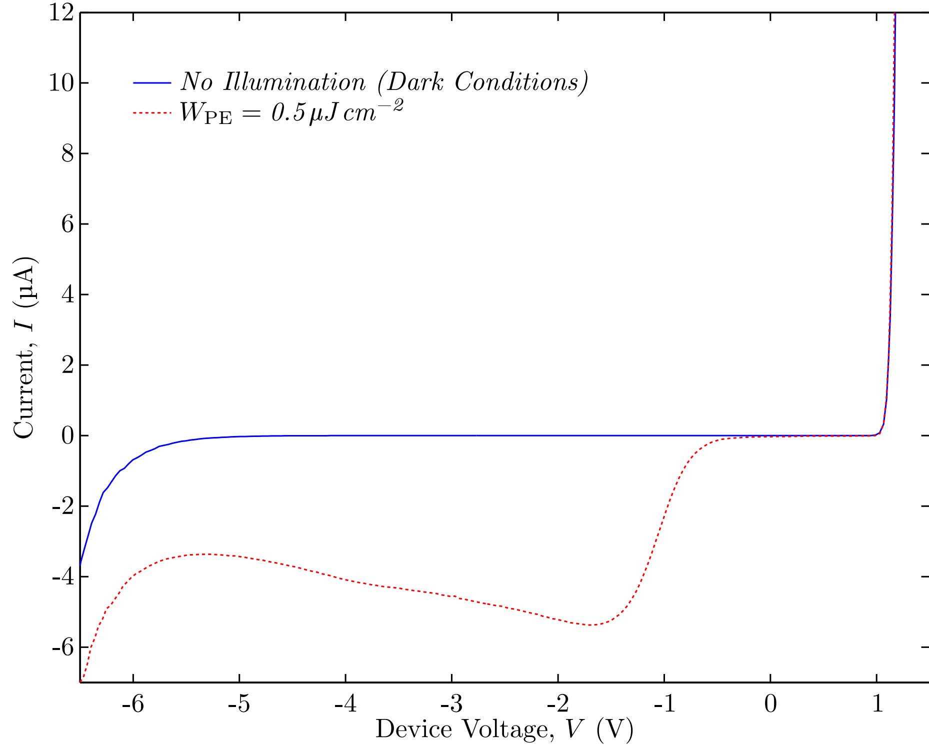

Figure 4.2: Stationary current-voltage (I_0-V) characteristics for a typical double quantum well (QW)-embedded p-i-n hypersonic detector in dark (solid, blue line) and light (dashed, red line) conditions. Under dark conditions, the device has a forward turn-on voltage $V = 0.94\,\mathrm{V}$, reverse saturation current $I_0 = -25\,\mathrm{pA}$, and reverse breakdown voltage $V_{\mathrm{br}} = -4.53\,\mathrm{V}$. When illuminated from a Ti:Sapphire oscillator operating at 800 nm wavelength, 150 fs duration, and 82 MHz repetition rate, the resultant pulses of fluence $W_{\mathrm{PE}} = 0.5\,\mu\mathrm{J\,cm^{-2}}$ significantly changed these I_0-V characteristics due to photoexcitation of carriers across the device and the double QW structure. In the absence of QWs, the illuminated and dark profiles would have been identical except for a negative offset in the former due to the photocurrent contribution [26]. Distinguishing the photocurrent contribution from each QW is difficult in this signal, due to the smearing of finer features by the relatively broad spectral width of the optical pulses from the oscillator.

effect from the QWs in the I_0-V characteristics, the contribution from each single QW is not immediately distinguishable. This was due to smearing of the finer features caused by the broad excitation pulse emitted from the oscillator, which had a spectral width of about 60 meV; this corresponded to a wavelength range of 770 nm to 832 nm when centred at 800 nm.

A narrower bandwidth is achieved under CW operation of the oscillator, and was used to identify the specific QW responsible for each photocurrent contribution; this system was previously used to determine the same contribution in a 7.5 nm thick single QW-embedded p-i-n hypersonic detector used by Moss et al. [19] and Moss et al. [20]. I_0-V measurements performed under these conditions are graphically represented in Figure 4.3 for another

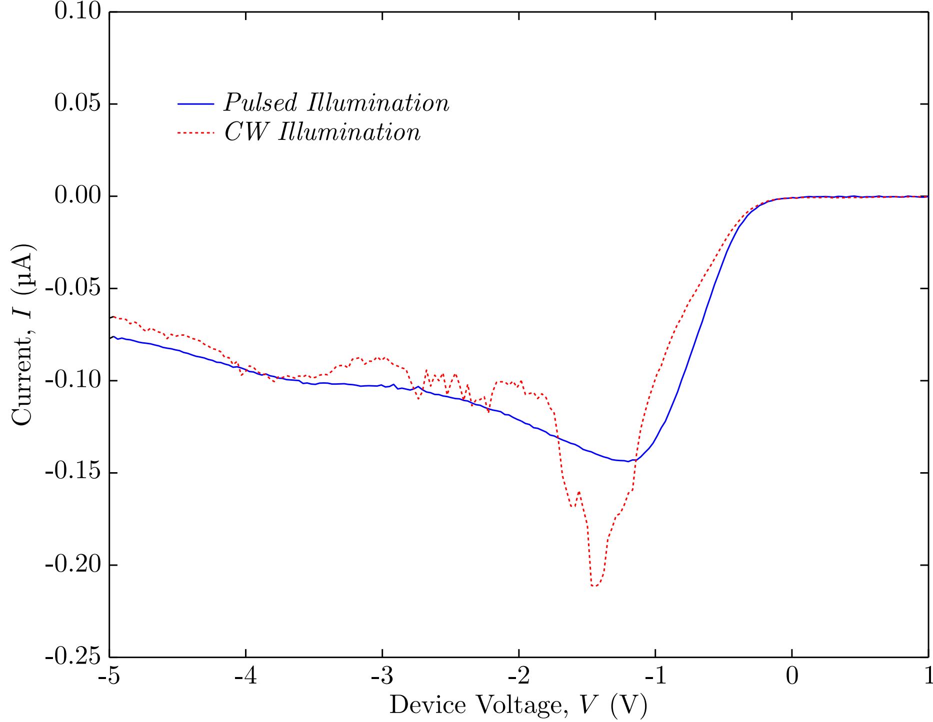

Figure 4.3: Stationary current-voltage (I_0-V) characteristics for a double quantum well (QW)-embedded *p*-*i*-*n* hypersonic detector under both pulsed (solid, blue line) and CW illumination (dashed, red line) from a Ti:Sapphire oscillator at 10.8 K. The oscillator was set to output 800 nm wavelength photons, with a fluence $W_{\mathrm{PE}} = 24.4\,\mathrm{nJ\,cm^{-2}}$. The additional noise shown in the CW data was due to laser instability when operating in this mode. As can be seen in the figure, two troughs in the measured CW signal are evident at $V_{\mathrm{WW}} = -1.40\,\mathrm{V}$ and $V_{\mathrm{NW}} = -3.70\,\mathrm{V}$, which were due to photoexcitation of carriers in the wide and narrow QWs, respectively. However, under identical conditions, the troughs are smeared out in the pulsed signal due to its relatively broad spectral width, and thus it is difficult to determine the individual QW photocurrent contribution under pulsed excitation.

sample, illuminated at $W_{\mathrm{PE}} = 24.4\,\mathrm{nJ\,cm^{-2}}$; the minor differences in device characteristics between these figures were due to slight, inherent discrepancies when processing separate samples, and does not detract from the overall conclusion, or suitability of the devices.

The differences between pulsed (solid, blue line) and CW (dashed, red line) illumination are evident in this figure. There is a distinct contribution to I_0 from the QWs in the pulsed signal but the distinction between them is unclear. However, under CW illumination, the apparent contributions of each QW were distinguishable, and can be seen for the wide and narrow QWs at $V_{\mathrm{WW}} = -1.40\,\mathrm{V}$ and $V_{\mathrm{NW}} = -3.70\,\mathrm{V}$, respectively; the noise evident in this signal was due to laser instability, as the oscillator was not designed to operate in CW mode.

4.3 Photocurrent Pump-Probe Experiments using a Bulk GaAs Transducer

Photocurrent pump-probe measurements were conducted on a *p-i-n* hypersonic detector with an exposed SI bulk GaAs substrate acting as a transducer in accordance with the setup described in Section 3.2.2. The device was biased at $V_\mathrm{b} = -2\,\mathrm{V}$, with a pump beam fluence ranging from $W = 0.1\,\mathrm{mJ\,cm^{-2}}$ to $3.0\,\mathrm{mJ\,cm^{-2}}$ and a constant photoexcitation beam fluence of $W_\mathrm{PE} = 10\,\mathrm{\mu J\,cm^{-2}}$; the results for this pump fluence range are given in Figure 4.4.

Here, the time axis has been zeroed to coincide with the arrival of the incident strain pulse, and the interaction from the returning strain pulse reflected off the free surface occurred approximately 126 ps later with a π-phase change. High frequency oscillations with decreasing amplitude were also detected in the trailing edge (tensile component) of the incident pulse, as expected from attenuation and dispersion effects (see Sections 2.2.1–2.2.2). Furthermore, the separation between the incident and reflected peaks corresponded to the expected transit time of the acoustic wavepacket from the wide QW to the free surface and back, given the dimensions of the device, and would have been approximately 6 ps longer if the narrow QW had been photoexcited. Note the absence of any echo as seen by Moss et al. [20], as strain is directly transduced in the bulk GaAs substrate rather than in an Al film, where these delayed echoes were formed from multiple reflections at the film/substrate interface. These measurements are an appropriate gauge of the strain-induced effects on the *p-i-n* hypersonic detector, as the relationship between induced photocurrent change and strain is such that [20]

$$\Delta I \propto \Xi\eta, \tag{4.1}$$

where ΔI is the change in photocurrent measured by the lock-in amplifier, and $\Xi = -1\,\mathrm{eV}$ for this experiment [80].

For $W < 1.0\,\mathrm{mJ\,cm^{-2}}$, the profile of the propagated strain pulse remained relatively identical with a linear increase of detected amplitude with pump beam fluence; phonon generation can thus be considered to be in the *linear* regime for these fluences. In addition, the temporal separation between the compressive and tensile peaks for these fluences ranges from $\Delta t_\mathrm{ct} =$

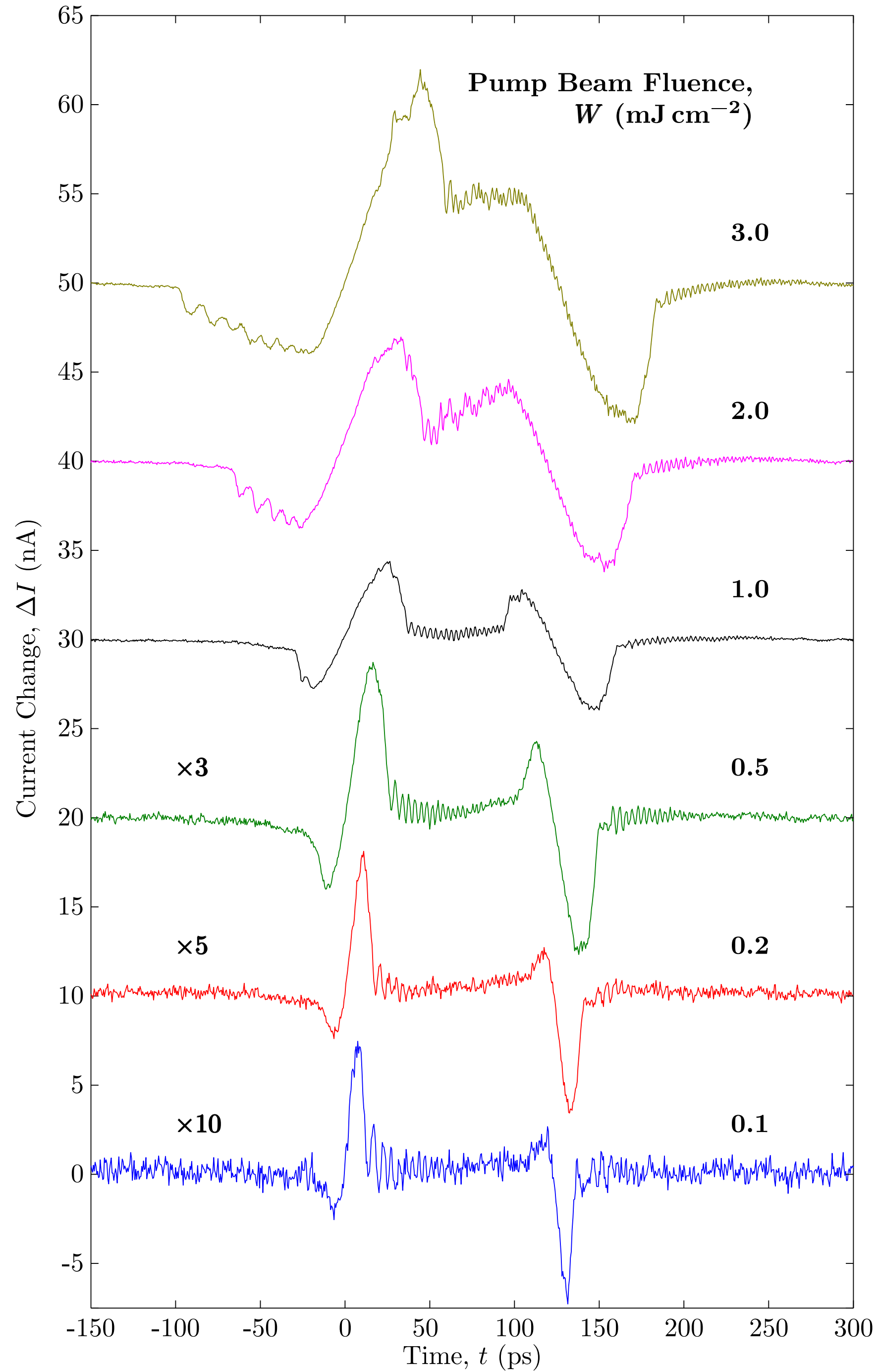

Figure 4.4: Photocurrent pump-probe measurements from a double quantum well (QW)-embedded *p*-*i*-*n* hypersonic detector of strain generated in bulk GaAs substrate for a range of pump beam fluences W. These fluences are labelled on the right, with the three lowest magnified, and all signals are offset for clarity. For $W < 1.0\,\mathrm{mJ\,cm^{-2}}$, the propagated strain pulse exhibits *linear* properties with increasing fluence, whereas for $W \geq 1.0\,\mathrm{mJ\,cm^{-2}}$ *non-linear* effects, including the formation of solitons, are seen.

14 ps to 28 ps, and also increased linearly. Furthermore, the durations of the damped trailing edge in these signals were approximately $\Delta t_{\mathrm{c}}^{\mathrm{GaAs}} = 20\,\mathrm{ps}$, which are around six times larger than expected if strain were generated within the bulk GaAs optical penetration depth.

In contrast, for $W \geq 1.0\,\mathrm{mJ\,cm^{-2}}$, soliton formation becomes apparent in the compressive peak as non-linear processes come into effect (see Section 2.2.3). Specifically, in the incident compressive peak, the number of detected solitons increases from two at $W = 1.0\,\mathrm{mJ\,cm^{-2}}$ to eight at $W = 3.0\,\mathrm{mJ\,cm^{-2}}$. As expected, the compressive peak arrives earlier with larger soliton numbers, and eventually the incident and reflected signals overlap with one another at the highest W; the formation of this N-wave at higher fluences is described by non-linear effects. Additionally, the temporal separation between the compressive and tensile peaks non-linearly increases with fluence in this *non-linear* regime.

4.3.1 Comparison of Coherent Phonon Generation in Bulk GaAs and Metal Film Transducers

The presence of solitons and these other aforementioned properties at higher fluences supports the assumption that the generated strain pulse must be of short duration and high amplitude, as seen in other experiments conducted with metal film transducers [14, 15, 42, 54, 56, 81–84]. However, strain generation in bulk GaAs possesses certain differences over those generated in metal transducers such as Al films, which are most easily differentiated in the linear regime. This is presented in Figure 4.5, where it can be seen that the propagated strain profiles are inherently dissimilar for these two transducer materials.

An oscillator system was used to measure the 30 nm thick Al film sample shown in Figure 4.5, as the sample exhibited non-linear characteristics when pumped with the lowest possible fluence using the amplifier system. This oscillator was identical to that used to illuminate the sample in Section 4.2, with a 800 nm wavelength pump beam fluence $W = 4.3\,\mathrm{\mu J\,cm^{-2}}$, and a 800 nm wavelength photoexcitation beam fluence $W_{\mathrm{PE}} = 0.7\,\mathrm{\mu J\,cm^{-2}}$; the different pump wavelengths used on the Al film and bulk GaAs transducers were due to frequency-dependent absorption parameters of the two materials, and the relatively small maximum fluence of oscillator pulses when frequency doubled. The signal was recorded with 100 fs resolution when the device was

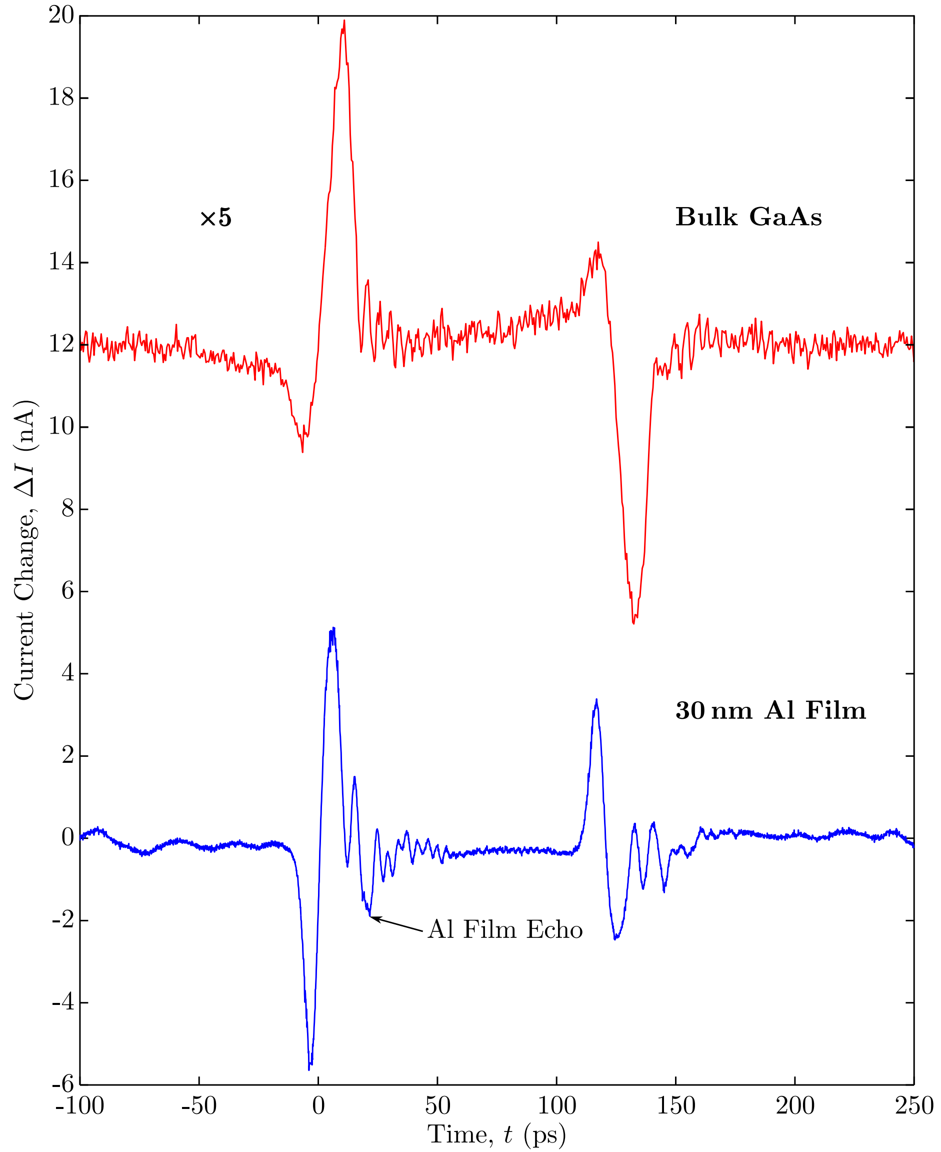

Figure 4.5: Photocurrent pump-probe experimental comparison of phonon generation from (top) bulk GaAs and (bottom) 30 nm Al film transducers in the *linear* regime. The former is magnified by five times and offset from the latter for clarity, and a strongly asymmetric strain pulse is detected here, in comparison to the Al case. The ratio of the initial compressive to tensile peak provides values of $M^{\mathrm{Al}} = 0.96$ and $M^{\mathrm{GaAs}} = 3.1$ for the Al film and bulk GaAs transducers, respectively. The former was attributed to the bipolar nature of *static* strain generation via thermoelastic effects, whilst the latter was due to the deformation potential mechanism acting in a *supersonically* expanding electron-hole (e-h) plasma.

biased at $V_\mathrm{b} = -2\,\mathrm{V}$ via a Stanford Research Systems SR830 DSP Lock-In Amplifier with a time constant of 30 ms, referenced to an acousto-optic modulator (AOM) in the pump beam set at 30.3 kHz.

Although both signals exhibited dispersion and attenuation effects, as well as the presence of incident and reflected components, the ratio of the initial compressive to tensile peak amplitudes was significantly dissimilar. In addition, there was an additional echo in the Al transducer signal due to reflection and subsequent transmission of a component in the strain pulse in the Al film; this effect has been previously considered elsewhere [20, 47], and thus is ignored hereafter.

As evident in the figure, the ratio of compressive peak ($\eta < 0$) to tensile peak ($\eta > 0$) was determined to be $M^{\mathrm{Al}} = 0.96$, and thus is near symmetric. This can be attributed to the bipolar nature of the initial strain pulse in the Al film that is generated by thermoelastic effects; this is known to be the dominant phonon generation mechanism in thin metal films, as optically excited carriers generate coherent phonons via relaxation and non-radiative recombination.

Indeed, it can be considered that the strain generated in thin metal films is transduced by thermoelasticity at a localised point of generation. The phonons propagate away from this point, and generate a bipolar strain pulse from those phonons that propagating away from the free surface of the metal film (compressive component), and those that undergo a π-phase change upon reflection at the free surface (tensile). The latter is delayed relative to the former, and so the symmetric compressive and tensile components can be considered as the leading and trailing edge of the strain pulse, respectively.

However, it is clear from a cursory examination of the bulk GaAs sample that this ratio is asymmetric, and analysis reveals a ratio of $M^{\mathrm{GaAs}} = 3.1$. Assuming that the strain pulse in both the bulk GaAs and Al transducer samples propagated in the GaAs substrate under the same conditions outside of the excitation region, it can be reasoned that strain generation was solely responsible for the different amplitude ratios. Previous theoretical and experimental studies of transduction in bulk semiconductors [13, 84–87] had predicted this asymmetry, but both asymmetry and a damped leading part of a picosecond strain pulse have not been previously observed. Based on these works, it was postulated here that the dominant mechanism for strain generation in bulk GaAs was the deformation potential at lower fluences, with an increased thermoelastic contribution at higher fluences [80].

In contrast to the thermoelastic effect, the deformation potential is a direct mechanism for strain generation whereby optoacoustic conversion of the incoming pump pulse forms the coherent wavepacket. Specifically, the interband absorption of an incoming pulse in the sub-surface layers of the semiconductor photogenerates a plasma of electron-hole (e-h) pairs. The modifications of interatomic interactions due to the formation of this plasma induces stress in the system [13, 88], and its density is defined by both diffusion and recombination of the e-h pairs [86]. A representative sketch of two transduction regimes useful in describing the initial strain profile is given in Figure 4.6.

By neglecting carrier diffusion, i.e. in the *static* regime, it can be considered that the coherent phonons are emitted from a static point of generation. The resultant strain pulse would then be bipolar in shape for similar reasons as in the thermoelastic case given for metal films. The duration of the compressive component may be estimated from examining the optical properties of the bulk GaAs, and would be equivalent to the absorption length of the incident photons in the bulk GaAs, as depicted in Figure 4.6(a).

However, with the inclusion of carrier diffusion, the velocity of the plasma affects the profile of the eventual strain pulse. If this velocity is greater than the longitudinal acoustic (LA) velocity, i.e. $v_{eh} > v_{\mathrm{LA}}$, the acoustic wave comprising the leading edge of the pulse cannot escape the supersonically expanding e-h plasma until $v_{eh} \leq v_{\mathrm{LA}}$. As such, in the *supersonic* regime, the duration of this leading edge is both longer in duration and smaller in amplitude, as the compressive strain component is elongated with respect to time (see Figure 4.6(b)). Furthermore, the trailing edge is affected by the rapid deceleration of the plasma at the free surface, and consequently the strain pulse exhibits a strongly asymmetric shape with a damped leading edge; an overview of the mathematical treatment for a model initial strain pulse is provided in Section 4.4 for the deformation potential mechanism only.

Analogies may be drawn between the supersonically expanding e-h plasma and the supersonic diffusion of non-equilibrium electrons in metal, but it has been shown that these electrons would only diffuse supersonically for $< 1\,\mathrm{ps}$ [4, 5, 89, 90]. Therefore, in metal films, the stress contribution from the deformation potential is insignificant in comparison to the thermoelastic contribution.

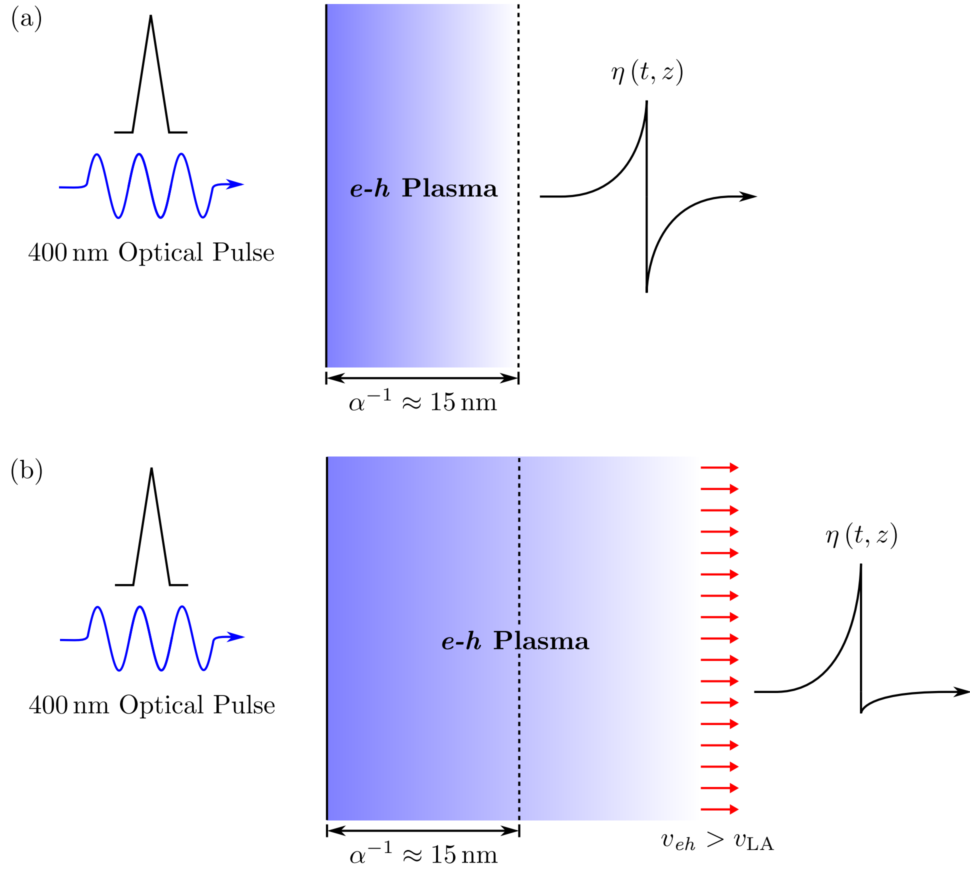

Figure 4.6: Representative sketch of strain transduction in bulk GaAs in the (a) *static* and (b) *supersonic* regimes. (a) In the static regime, i.e. in the absence of plasma diffusion, it can be considered that strain is transduced from a static point, much the same as in the case of metal film transduction. The subsurface depth of this point is equivalent to the absorption length α^{-1} of the photons in the material. From here, an initial bipolar strain pulse $\eta(t, z)$ is generated from coherent phonons induced from the excited electron-hole *e-h* plasma that propagate away from (compressive; leading), and towards (tensile; trailing) the free surface. (b) However, in the supersonic regime, the plasma is initially travelling faster than the longitudinal acoustic (LA) velocity, i.e. $v_{eh} > v_{\text{LA}}$, and so the acoustic waves generated by the *e-h* plasma cannot escape it until it is no longer expanding supersonically. Accordingly, there is strong asymmetry and a damped leading edge to $\eta(t, z)$.

4.4 Modelling Strain Pulse Generation in a Supersonically Expanding Electron-Hole (*e-h*) Plasma

The following section provides an overview of the mathematical model for the initial profile of a strain pulse generated within a supersonically expanding *e-h* plasma in a SI bulk GaAs. This model[2] was theorised by Vitalyi Gusev of Maine University, Le Mans, France, and is derived herein based on Young et al. [80] and Gusev [91].

The inhomogeneous one-dimensional wave equation for the displacement u of a particle is given by [13, 80, 85–87]

$$\rho\left(\frac{\partial^2 u}{\partial t^2} - v_{\mathrm{LA}}^2\frac{\partial^2 u}{\partial z^2}\right) = \Xi\frac{\partial n_{eh}}{\partial z} - B\beta\frac{\partial T}{\partial z}, \tag{4.2}$$

where ρ is the GaAs substrate density, n_{eh} is the *e-h* plasma density B is the GaAs substrate bulk elastic modulus, β is the thermal expansion coefficient of the GaAs substrate, and T is the temperature increase due to laser irradiation. Equation 4.2 assumes that there is no contribution from piezoelectric stress, given the orientation of the GaAs substrate (see Section 2.4.2). The terms contained within the round brackets of Equation 4.2 denote the homogeneous wave equation, whilst the first and second terms on the right hand side of the equation are photoinduced stress derivatives that are caused by the deformation potential and thermoelastic effects, respectively. As there is zero stress at the free surface, Equation 4.2 has the following boundary condition at $z = 0$ [85]

$$\frac{\partial^2 u}{\partial z^2} \underset{z=0}{=} -\frac{1}{\rho v_{\mathrm{LA}}^2}\left(\Xi\frac{\partial n_{eh}}{\partial z} - B\beta\frac{\partial T}{\partial z}\right).$$

The spatial and temporal evolution of the *e-h* plasma can be modelled by examining its initial generation due to a femtosecond laser pulse, its subsequent diffusion, and its reduction over time due to recombination of *e-h* pairs, such that

$$\frac{\partial n_{eh}}{\partial t} = \alpha N\delta(t)\exp(-\alpha z) + D\frac{\partial^2 n_{eh}}{\partial z^2} - \frac{n_{eh}}{\tau_{\mathrm{R}}}, \tag{4.3}$$

[2]See Appendix A in Young et al. [80] for discussions directly relevant to this model, and other references for similar models [13, 85–87].

where α is the absorption coefficient of the GaAs substrate for the given laser excitation wavelength, the Dirac delta function $\delta(t)$ provides the assumption that laser excitation is instantaneous, D is the ambipolar diffusivity parameter, and τ_{R} is the e-h pair recombination time. $N = (1 - R_{\mathrm{S}})\, W/h\nu$ is the sheet density of absorbed photons, and is the proportion of laser fluence W per unit photon energy $h\nu$ absorbed at the GaAs surface with reflectivity coefficient R_{S}. Equation 4.3 is bounded by

$$\frac{\partial n_{eh}}{\partial z} \underset{z=0}{=} 0, \quad n_{eh} \underset{z=\infty}{=} 0,$$

given that there is zero plasma flux at the free surface, and zero plasma infinitely far from the surface.

Similarly, the spatial and temporal evolution of the laser-induced temperature rise can be considered from examining thermal diffusivity, and the proportions of photon energy transferred into heat due to excited carrier relaxation E_T and non-radiative recombination of the e-h pairs E_{NR}, where $h\nu = E_T + E_{\mathrm{NR}} = 3.11\,\mathrm{eV}$ for $400\,\mathrm{nm}$ wavelength optical excitation. In its simplest form, this diffusive heat conductivity can be modelled as

$$\frac{\partial T}{\partial t} = D_T \frac{\partial^2 T}{\partial z^2} + \frac{E_T}{\rho c_{\mathrm{S}}} \alpha N \delta(t) \exp(-\alpha z) + \frac{E_{\mathrm{NR}}}{\rho c_{\mathrm{S}}} \frac{n_{eh}}{\tau_{\mathrm{NR}}}, \tag{4.4}$$

where D_T and c_{S} are the thermal diffusivity, and specific heat capacity, respectively, of GaAs, and τ_{NR} is the non-radiative recombination time of e-h pairs. Equation 4.4 is likewise bounded such that

$$\frac{\partial T}{\partial z} \underset{z=0}{=} 0, \quad T \underset{z=\infty}{=} 0,$$

as the temperature flux at the free surface is zero, as is the temperature infinitely far from the surface.

The solutions to Equations 4.2–4.4 can be found by applying either of the following t-Fourier, or inverse ω-Fourier transforms

$$\tilde{f}(\omega, z) = \mathcal{F}\{f(t, z)\} = \int_{-\infty}^{\infty} f(t, z) \exp(i\omega t)\, \mathrm{d}t, \tag{4.5}$$

$$f(t, z) = \mathcal{F}^{-1}\left\{\tilde{f}(\omega, z)\right\} = \frac{1}{2\pi} \int_{-\infty}^{\infty} \tilde{f}(\omega, z) \exp(-i\omega t)\, \mathrm{d}\omega, \tag{4.6}$$

for a given function $f(t, z)$, where ω is the frequency domain, or either of

the following z-Laplace, or inverse p-Laplace transforms

$$\hat{f}(\omega, p) = \mathcal{L}\left\{\tilde{f}(\omega, z)\right\} = \int_0^\infty \tilde{f}(\omega, z) \exp(-pz)\, \mathrm{d}z, \tag{4.7}$$

$$\tilde{f}(\omega, z) = \mathcal{L}^{-1}\left\{\hat{f}(\omega, p)\right\} = \frac{1}{2\pi i} \int_{K_1 - i\infty}^{K_1 + i\infty} \hat{f}(\omega, p) \exp(pz)\, \mathrm{d}p, \tag{4.8}$$

where p is Laplace domain, and K_1 is a positive, arbitrary constant that defines the interval of integration [92].

The model mathematically described herein assumes that the strain generation is dominated solely by the deformation potential mechanism. As such, only the solutions to a reduced form of Equation 4.2 and Equation 4.3 are given in the following subsections so as to solely model the deformation potential contributions to the initial strain pulse $\eta(\tau)$. Although this will be subsequently shown to be true for the linear regime in Section 4.5, there is a rapidly increasing to dominant contribution from thermoelasticity in the non-linear regime; this is due to greater non-radiative recombination with larger e-h plasma density, which is negligible for low excitation densities. This assumption has been made as the model outcome provides an excellent representation of the experimental data in the linear regime, and deviations from it can be clearly seen and attributed to thermoelasticity in the non-linear regime. Moreover, a detailed mathematical interpretation of the deformation potential and thermoelastic contributions was provided by Gusev [91], and summarised in Young et al. [80]. Accordingly, only a brief overview of the latter contribution is given in Section 4.4.1, before a rigorous analytical derivation and interpretation of the deformation potential model is disclosed in Sections 4.4.2–4.4.4.

4.4.1 Thermoelastic Contribution to the Initial Strain

As aforementioned, only a brief consideration of the thermoelastic contribution will be provided here, as more detailed discussions and estimations can be found elsewhere [80, 91]. In the case of a supersonically expanding e-h plasma, it can be supposed that the thermoelastic mechanism is described by two processes; the first is the near instantaneous relaxation of carriers upon photoexcitation by the laser pulse, and the second is caused by the subsequent non-radiative recombination of the e-h pairs. This is described by Equation 4.4, where the first D_T term can be ignored as it is subsonic,

and the second and third terms describe the above first and second processes, respectively; the thermal diffusivity is subsonic as $M_T^{\mathrm{GaAs}} = \alpha D_T / v_{\mathrm{LA}} < 1$ for $D_T = 0.31\,\mathrm{cm}^2\,\mathrm{s}^{-1}$ [29].

It is estimated from previous works that coherent phonon generation from this first process occurs on a timescale of around 100 fs in bulk GaAs [93], which is shorter than the escape time from the excited region $\omega_\alpha^{-1} \approx 3\,\mathrm{ps}$ for $\alpha = 6.54 \times 10^5\,\mathrm{cm}^{-1}$ at 400 nm optical excitation wavelength. As a result, coherent phonons are generated here with a bipolar shape in a static regime, but are nonetheless subsequently caught in the expanding supersonic *e*-*h* plasma. As such, this term can be considered as having a negligible influence on the resultant strain profile in comparison to the deformation potential mechanism. This can be quantitatively deduced in the linear regime from the long duration of the leading edge in the experimental results, where $\omega_+^{-1} \gg \omega_\alpha^{-1}$. Accordingly, this first process of near instantaneous relaxation of photoexcited carriers can also be ignored from Equation 4.4.

However, the second process, the non-radiative recombination of *e*-*h* pairs, is strongly dependent on the *e*-*h* plasma density. This in turn is dependent on pump beam fluence, and so this process cannot be ignored in certain instances. In brief, non-radiative recombination is negligible in the linear regime, but rapidly increases with larger fluences. Further detail regarding the role of non-radiative processes, and consequently the thermoelastic effect, on strain generation are given later in Section 4.4.4–4.5, where the departure from the deformation potential model is evident after comparison with experimental data.

4.4.2 Calculation of the Electron-Hole (*e*-*h*) Plasma Density

By applying the Fourier transform to Equation 4.3, it can be shown that the frequency spectrum of the *e*-*h* plasma density $\tilde{n}_{eh}(\omega, z)$ is a second-order linear ordinary differential equation (ODE) given by

$$\frac{\partial^2 \tilde{n}_{eh}(\omega, z)}{\partial z^2} - q_n^2 \tilde{n}_{eh}(\omega, z) + \frac{\alpha N}{D} \exp(\alpha z) = 0, \tag{4.9}$$

where $q_n = \sqrt{(-i\omega + \omega_{\mathrm{R}})/D}$ for positive real values of the square root term only, and $\omega_{\mathrm{R}} = \tau_{\mathrm{R}}^{-1}$ is the *e*-*h* pair recombination rate. The solution to

Equation 4.9 with respect to its boundary conditions is denoted by

$$\tilde{n}_{eh}(\omega, z) = \frac{\alpha N}{q_n D\left(\alpha^2 - q_n^2\right)}\left[\alpha \exp\left(-q_n z\right) - q_n \exp\left(-\alpha z\right)\right]. \tag{4.10}$$

At the bulk GaAs surface, the plasma density is at a maximum due to the instantaneous laser irradiation, and therefore $\tilde{n}_{eh}(\omega, z = 0)$ is given by

$$\tilde{n}_{eh}(\omega, z = 0) \approx \frac{N}{q_n D}, \tag{4.11}$$

as $\alpha \gg q_n$ for the experimental parameters subsequently determined. Using the inverse Fourier transform, and substituting for an equation in the form of the inverse Laplace transform, the e-h plasma density at the surface is therefore given by

$$\begin{aligned} n_{eh}(t, z = 0) &= \frac{N}{\sqrt{\pi D t}} \exp\left(-\omega_{\mathrm{R}} t\right), \\ &= \frac{\left(1 - R_{\mathrm{S}}\right) W}{h\nu\sqrt{\pi D t}} \exp\left(-\omega_{\mathrm{R}} t\right). \end{aligned} \tag{4.12}$$

4.4.3 Deformation Potential Contribution to the Initial Strain

The following ODE for the frequency spectrum of u when excited solely by the deformation potential mechanism, i.e. $B\beta T_z = 0$, is obtained by Fourier transforming Equation 4.2 to give

$$\frac{\partial^2 \tilde{u}(\omega, z)}{\partial z^2} = -q_v^2 \tilde{u}(\omega, z) - \frac{\Xi}{\rho v_{\mathrm{LA}}^2} \frac{\partial \tilde{n}_{eh}(\omega, z)}{\partial z}, \tag{4.13}$$

where $q_v = \omega / v_{\mathrm{LA}}$ is the acoustic phonon wavevector. If the boundary condition is satisfied, and as we are only considering radiation propagating in the positive z-direction, i.e. the coefficient of the $\exp\left(-iq_v z\right)$ term is zero, an appropriate solution for $\tilde{u}(\omega, z)$ can be found. As $\eta = u_z$, the frequency spectrum of the strain pulse excited only by the deformation potential mechanism is

$$\begin{aligned} \tilde{\eta}_n(\omega, z) = \frac{\eta_{\mathrm{im}}}{D\left(\alpha^2 - q_n^2\right)} \Bigg[&\left(\frac{1}{\alpha^2 + q_v^2} - \frac{\alpha}{q_n\left(q_n^2 + q_v^2\right)}\right) q_v^2 \exp\left(iq_v z\right) \\ &+ \frac{\alpha^2}{\alpha^2 + q_v^2} \exp\left(-\alpha z\right) - \frac{\alpha q_n}{q_n^2 + q_v^2} \exp\left(-q_n z\right) \Bigg], \end{aligned} \tag{4.14}$$

where $\eta_{\mathrm{im}} = \Xi\alpha N/\rho v_{\mathrm{LA}}^2$ denotes the characteristic strain that would be generated in an immobile plasma. The two final exponential terms in Equation 4.14 are only photoinduced within the excitation region, and are consequently zero outside of it. As such, Equation 4.14 can be reduced outside of the excitation region in a co-moving time frame, i.e. $\tau = t - z/v_{\mathrm{LA}}$, to

$$\tilde{\eta}_n(\omega) = -\frac{i\omega^2\eta_{\mathrm{im}}}{\omega - i\Delta\omega}\left[\frac{1}{(\omega - i\omega_\alpha)(\omega + i\omega_\alpha)} - \frac{\sqrt{\omega_D}}{\sqrt{-i(\omega + i\omega_{\mathrm{R}})}(\omega - i\omega_+)(\omega + i\omega_-)}\right], \tag{4.15}$$

where $\omega_\alpha = \alpha v_{\mathrm{LA}}$ and $\omega_D = \alpha^2 D$ are the inverse time of acoustic propagation and plasma diffusion across the absorption region, respectively, $\Delta\omega = \omega_D - \omega_R$,

$$\omega_\pm = \frac{1}{2}\omega_c\left[\sqrt{1 + 4(\omega_{\mathrm{R}}/\omega_c)} \pm 1\right], \tag{4.16}$$

and $\omega_c = v_{\mathrm{LA}}^2/D$ is the characteristic frequency that defines the inverse time when the acoustic and plasma waves have travelled an identical distance, i.e. the inverse time when the plasma has decelerated to v_{LA}. For $\tau < \omega_c^{-1}$, $v_{eh} > v_{\mathrm{LA}}$ and the acoustic pulse cannot escape the supersonic diffusion of the *e-h* plasma. At longer times, i.e. $\tau \geq \omega_c^{-1}$, $v_{eh} \leq v_{\mathrm{LA}}$ and the coherent wavepacket can escape the subsonic *e-h* plasma, thus forming the asymmetric pulse.

It was shown by Gusev [91][3] that, by approximating the experimental parameters to $\alpha^{-1} \approx 15\,\mathrm{nm}$, $v_{\mathrm{LA}} \approx 4.8 \times 10^3\,\mathrm{m\,s^{-1}}$, and $D \geq 3\,\mathrm{cm^2\,s^{-1}}$, the dominant contributions to the co-moving temporal solution to the inverse Fourier transform of Equation 4.15 are

$$\frac{\eta_n(\tau < 0)}{\eta_{\mathrm{im}}} = \frac{\omega_+^2}{\sqrt{\omega_D}\sqrt{\omega_+ + \omega_{\mathrm{R}}}(\omega_+ + \omega_-)}\exp(\omega_+\tau), \tag{4.17}$$

$$\frac{\eta_n(\tau > 0)}{\eta_{\mathrm{im}}} = -\exp\left[(\omega_D - \omega_{\mathrm{R}})\tau\right]\mathrm{erfc}\left(\sqrt{\omega_D\tau}\right), \tag{4.18}$$

where Equations 4.17 and 4.18 define the leading (compressive) and trailing (tensile) edges, respectively.

[3] See Appendix A1 in Young et al. [80] for general details

4.4.4 Interpretation of the Theoretical Model

At $t = 0$, the *e*-*h* plasma is travelling at a supersonic drift velocity equivalent to $v_{eh} = \alpha D = M_0^{\text{GaAs}} v_{\text{LA}} = 2.61 \times 10^4\,\text{m}\,\text{s}^{-1}$, where $M_0^{\text{GaAs}} = 5.5$ is the initial Mach number for $\alpha = 6.54 \times 10^5\,\text{cm}^{-1}$ and $D = 4\,\text{cm}^2\,\text{s}^{-1}$ [80]. The shock wave increases (decreases) the duration (amplitude) of the leading edge until the decelerating plasma attains a subsonic velocity at $\omega_c^{-1} \geq 17.9\,\text{ps}$ in the deformation potential model, where the characteristic duration of the leading edge is defined by ω_+^{-1} due to the exponential term in Equation 4.17. This is qualitatively demonstrated in the experimental data, where the propagated strain durations in the linear regime are of the order of ω_+^{-1}, and will be further investigated in Section 4.5.1. Given this definition of the duration of the compressive strain, the plasma density $n_{eh}(t, z)$ temporally evolving from the surface, which is given by Equation 4.12, at time ω_+^{-1} is

$$n_{eh}\left(\omega_+^{-1}, 0\right) = \frac{(1 - R_{\text{S}})\,W}{h\nu} \left(\frac{w_c \left[\sqrt{1 + 4\left(\omega_{\text{R}}/\omega_c\right)} + 1\right]}{2\pi D} \right)^{\frac{1}{2}} \times \exp\left(- \frac{2\omega_{\text{R}}}{\omega_c \left[\sqrt{1 + 4\left(\omega_{\text{R}}/\omega_c\right)} + 1\right]} \right). \tag{4.19}$$

It was demonstrated by Gusev [91] that the non-radiative recombination rate $\omega_{\text{NR}} = \tau_{\text{NR}}^{-1} \propto n_{eh}^2$, which in turn is dependent on the fluence due to the form of Equation 4.19. As such, ω_{NR} would be a small component of the mean recombination rate ω_{R} at low excitation densities, and thus the dominant component of the leading edge is denoted purely by the deformation potential mechanism. However, in the non-linear regime, ω_{NR} rapidly increases, and thermoelasticity becomes progressively more important in defining the shape of the leading edge, as it reduces ω_+^{-1} due to the increased non-radiative recombination. It is estimated that for the highest excitation density, the thermoelastic contribution is approximately 71 % of the overall leading edge [80]; a comparison of this simulated square-law behaviour of ω_{NR} with theoretical parameters fitted to experimental data is considered later in Section 4.5. Consequently, it can be concluded that thermoelasticity becomes the dominant mechanism for strain generation in bulk GaAs at high fluences, especially for $W > 1.0\,\text{mJ}\,\text{cm}^{-2}$.

4.5 Comparison of the Theoretical Model to Experimental Data

As previously stated at the end of Section 4.4, thermoelastic effects play a negligible role in the initial strain profile in the linear regime, but have a much larger effect in the non-linear regime. However, as the deformation potential remains the dominant mechanism for $W \leq 1.0\,\mathrm{mJ\,cm^{-2}}$, the measured data was fitted solely to the model governed by Equations 4.17–4.18. The relative effects of thermoelasticity on characteristic inverse leading edge duration ω_+ and recombination rate ω_R, and consequently the deviation from the deformation potential model, will be examined in due course in Section 4.5.1.

Figure 4.7 depicts the same experimental data (bottom) shown in Figure 4.5 for both bulk GaAs and 30 nm thick Al film transducers. Initial, theoretical strain pulses (insert) were propagated numerically using the Korteweg-de Vries-Burgers (KdV-Burgers) equation and a composite Runge-Kutta method, as described in Section 2.2.3, where the parameters for these initial strain pulses were modified until an appropriate fit was obtained. The simulated propagations (top) do not completely reflect the measured data in their trailing edge, and this can be resolved by considering that the model may not sufficiently describe the dispersive and attenuation effects that are found in this region.

The initial strain pulse provided in Figure 4.7(b) is based on the following equation [80]

$$\eta_\mathrm{Al}(\tau) = -\left(\frac{2}{1+\exp\left(\frac{\tau}{T_1}\right)} - 1\right) + \frac{1}{1+\exp\left(\frac{\tau+T_2}{T_1}\right)} - \frac{1}{1+\exp\left(-\frac{\tau+T_2}{T_1}\right)}, \tag{4.20}$$

where $T_1 = 0.3\,\mathrm{ps}$ and $T_2 = 7.0\,\mathrm{ps}$. The initially simulated pulse was bipolar in nature (dashed, red line), but an additional reflected component was included (solid, blue line) to represent echoes in the Al film for a slightly more accurate representation of the associated data. It is noted that only one Al film echo has been included in this initial profile; in reality, there would be multiple, sequential echoes, hence the differences between the simulated and experimental dispersive tails. Nevertheless, this does not detract from the

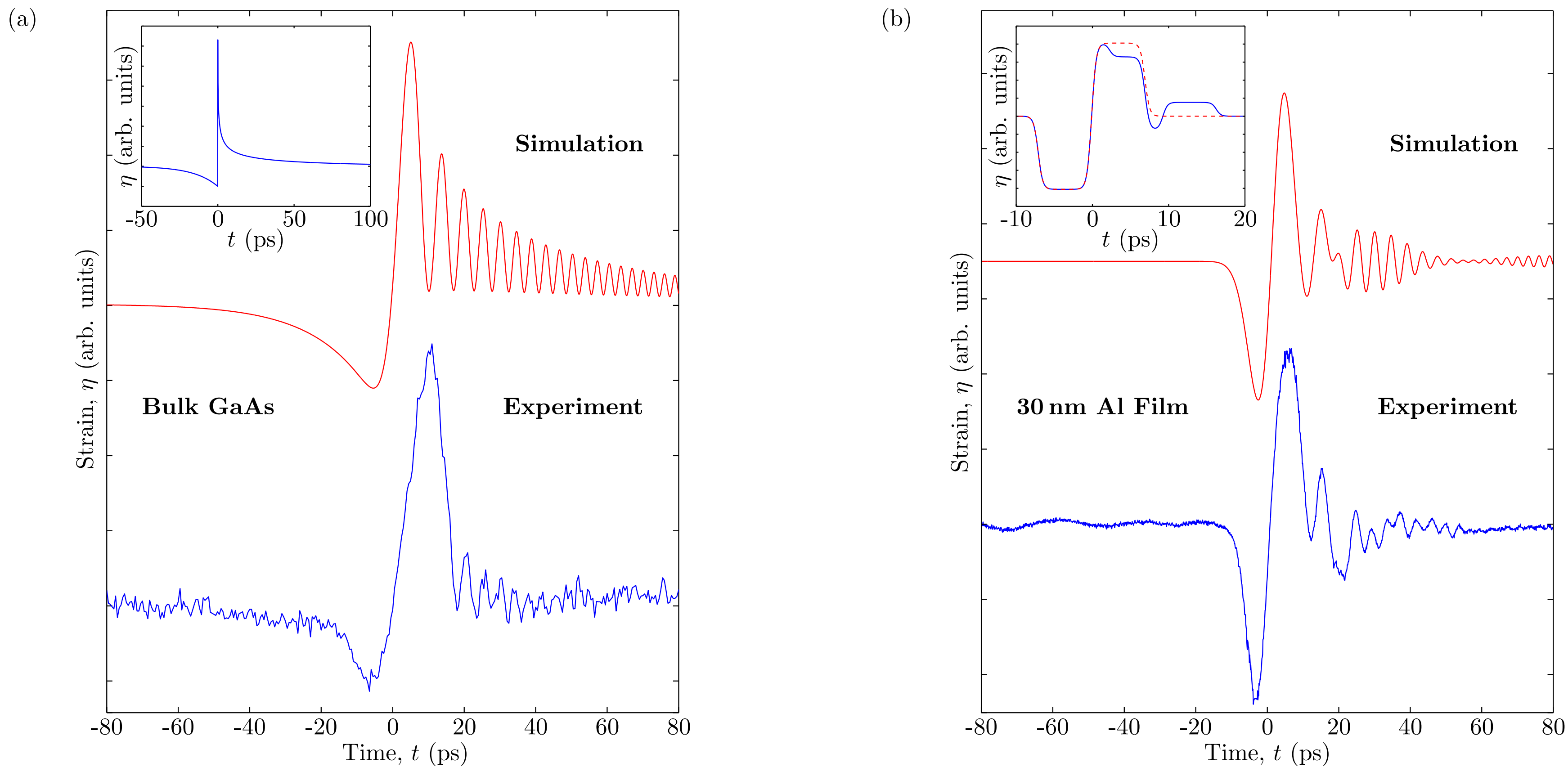

Figure 4.7: Fitting of experimental data to the theoretical model for (a) bulk GaAs and (b) 30 nm Al film transducers, with (inserts) the deduced initial strain profiles for each material. (a) The asymmetric experimental result for $W = 0.2\,\mathrm{mJ\,cm^{-2}}$ (bottom) can only be fitted (top) using an asymmetric initial strain pulse (insert) calculated from Equation 4.17–4.18, with propagation simulated by Equation 2.13. (b) Similarly, the symmetric experimental pulse for the Al transducer (bottom) can only be fitted (top) using an initial bipolar strain pulse (insert) with the reflection within the Al film included (solid, blue line); the initial profile without this echo is shown with a dashed, red line.

overall result that an initially bipolar strain pulse ($M_0^{\mathrm{Al}} = 1.0$) is required to form the subsequently near bipolar propagated strain pulse ($M^{\mathrm{Al}} = 0.96$), and indicates that the propagation model used herein is valid for application to the bulk GaAs transducer data.

Similarly for a bulk GaAs transducer in the linear regime, it can be seen in Figure 4.7(a) that a strongly asymmetric initial pulse is required to provide an adequate theoretical fit to the experimental data. The parameters of the initial strain profile were modified until a sufficient propagated fit of the leading edge was ascertained, i.e. the duration of the compressive component ω_+^{-1}, and amplitude (Mach) ratio matched the experimental data. By applying this fitting criterion, an initial Mach ratio $M_0^{\mathrm{GaAs}} = 6.3$ that reduces to $M_{\mathrm{th}}^{\mathrm{GaAs}} = 3.1$ after propagation through the substrate was numerically determined, with a characteristic compressive strain duration $\omega_+^{-1} = 15.5\,\mathrm{ps}$. This optimum fit was determined for the values of $\omega_{\mathrm{R}}^{-1} \geq 100\,\mathrm{ps}$ and $D = 4\,\mathrm{cm}^2\,\mathrm{s}^{-1}$ for the given initial strain pulse. As the fit is in good agreement with the experimentally measured values, it provides some validation of the above-mentioned qualitative discussion, and mathematical model in Sections 4.3–4.4.

For $W \geq 1.0\,\mathrm{mJ\,cm}^{-2}$, the experimental results begin to exhibit non-linear properties. Accordingly, initially higher amplitude strain pulses must be simulated so that their numerically propagation generates the expected non-linearity, especially with respect to the formation of solitons. Propagation of these non-linear effects, whether as seen experimentally or via numerically solving the KdV-Burgers equation, result in a profile that is significantly different to the initial strain profile. Furthermore, there is an inherently limited temporal response in the experimental setup that leads to a progressively dissimilar compressive profile with respect to the simulated data, as seen in Figure 4.8; this temporal response integrates the sharp features evident in the simulated data, culminating in the different shape displayed in the experiment data.

Since it is no longer only dispersion and attenuation that shape the strain pulse on propagation, but also the non-linearity of the GaAs crystal and the limited temporal response of the setup, the fitting criteria for this non-linear regime cannot be identical to that of the linear regime. Instead, the simulated propagation of the initial strain pulse was fitted so that the temporal separation between the first and second solitons was matched with the experimental data. This was accomplished by modifying both the

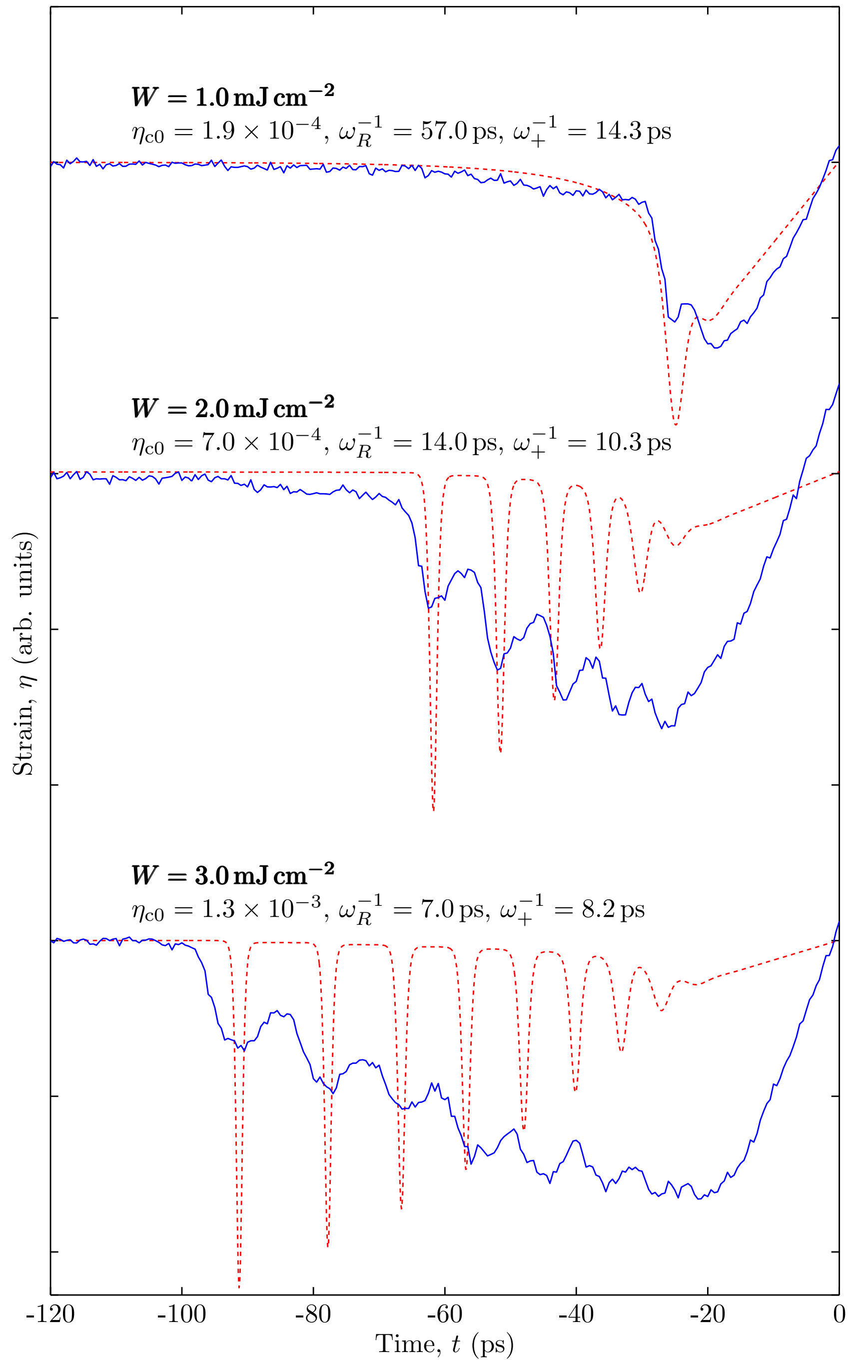

Figure 4.8: Fitting of simulated propagated strain pulses (dashed, red lines) to experimental data (solid, blue lines) in the *non-linear* regime for varying pump beam fluences W. Note the presence of non-linear effects that are not seen in the linear regime, and hence a difference fitting criteria was employed for these experimental results than in Figure 4.7(a). The fitting parameters for the initial compressive strain component η_{c0}, recombination rate ω_{R}, and duration of the compressive strain ω_{+} for each data set are also labelled. Note that the initial strain pulse for each of these simulations is strongly asymmetric, as shown in the insert for Figure 4.7(a), except that the durations of the compressive and tensile components for the above fits are much shorter.

amplitude of the compressive strain component η_{c0}, ω_{R}, and consequently ω_+, whilst keeping $D = 4\,\mathrm{cm}^2\,\mathrm{s}^{-1}$ independent of W; the results of this comparison are shown in Figure 4.8. This fitting criterion was also applied due to the increasing thermoelastic contribution to the resultant strain pulse, as it becomes the dominant mechanism for coherent phonon generation in the bulk GaAs at these fluences.

In this figure, it is clear that the theoretical model still provides good agreement with the experiment results. Nonetheless, with increasing fluence, the duration of the compressive strain component ω_+ decreases by nearly a factor of two between $W = 1.0\,\mathrm{mJ\,cm}^{-2}$ to $3.0\,\mathrm{mJ\,cm}^{-2}$, whilst the recombination rate falls by nearly an order of magnitude. Consequently, $\omega_+ \to \omega_\alpha$ for the highest excitation density, indicating that there is a greater thermoelastic contribution to the initial strain pulse; note that the general shape of this initial strain pulse is still strongly asymmetric, as in the insert of Figure 4.7(a), with $M_0^{\mathrm{GaAs}} = 8.6$.

This deduction could be made as it can be reasoned that an increased thermoelastic contribution concurrently increases ω_{NR} and therefore ω_{R}. At high fluences where ω_{NR} was relatively large, non-radiative recombination became a limiting factor to the progression of the *e*-*h* plasma. Specifically, as *e*-*h* pairs rapidly recombined, the plasma diffusion length was greatly reduced, and allowed the acoustic wavepacket to escape at times less than ω_c. Proof of this deduction can be obtained by examining the dependence of the numerically fitted parameters ω_+ and ω_{R} on W, as considered in Section 4.5.1.

4.5.1 Examination of Decay Rate Dependence on Fluence

The recombination rate ω_{R} can be considered as a combination of radiative and non-radiative components such that

$$\omega_{\mathrm{R}} = \omega_{\mathrm{R0}} + Bn_{eh} + An_{eh}^2, \tag{4.21}$$

where ω_{R0} is the linear recombination rate, B is the bimolecular recombination coefficient, and A is the effective Auger coefficient. For the present experiment, ω_{R0} was determined [80, 91] to be negligibly small in comparison to the other two non-linear recombination rates, and the plasma density was

estimated not to exceed $n_{eh} \sim 2 \times 10^{20}\,\mathrm{cm}^{-3}$.

For bulk GaAs, Strauss et al. [94] determined that these coefficients were $B = 1.7 \times 10^{-10}\,\mathrm{cm}^3\,\mathrm{s}^{-1}$ and $A = 7 \times 10^{-30}\,\mathrm{cm}^6\,\mathrm{s}^{-1}$, and so it can be seen that the Auger component in Equation 4.21 at the maximum fluence of $W = 3.0\,\mathrm{mJ\,cm}^{-2}$ is approximately an order of magnitude faster than that of the bimolecular component. As such, ω_{NR} dominates at high fluences, and so Equations 4.16 and 4.21 can be reduced to

$$\omega_{\mathrm{R}} \approx \omega_{\mathrm{NR}} = A n_{eh}^2, \tag{4.22}$$

$$\omega_{+} \approx \frac{\omega_c}{2}\left[\sqrt{1 + 4\left(\frac{A n_{eh}^2}{\omega_c}\right)} + 1\right]. \tag{4.23}$$

In addition, applying Equation 4.22 to Equation 4.19 provides

$$\begin{aligned} n_{eh} \approx \frac{(1 - R_{\mathrm{S}})\,W}{h\nu} & \left(\frac{\omega_c\left[\sqrt{1 + 4\,(A n_{eh}^2/\omega_c)} + 1\right]}{2\pi D}\right)^{\frac{1}{2}} \\ & \times \exp\left(-\frac{2 A n_{eh}^2}{\omega_c\left[\sqrt{1 + 4\,(A n_{eh}^2/\omega_c)} + 1\right]}\right), \end{aligned} \tag{4.24}$$

which can be solved for the range $n_{eh} \leq 2 \times 10^{20}\,\mathrm{cm}^{-3}$ to give the dependence of n_{eh} on W, and therefore the dependence of ω_{R} and ω_{+} on W; the latter two dependencies are graphically represented in Figure 4.9.

The dependence of ω_{+} on W presents a good agreement between the fitted parameters (symbols) and the simulated curves (lines), whilst this is only true for $W \geq 1.0\,\mathrm{mJ\,cm}^{-2}$ for the dependence of ω_{R} against W. When examining this fluence range, the accord between the fitted parameters and the theoretically generated curves implies that the assumption that ω_{R} is dominated by Auger non-radiative recombination processes is correct in this regime. This assumption does not apply for the linear regime, where ω_{R} is linear with W due to $\omega_{\mathrm{R}} \ll \omega_c$; this condition reduces the dependence of ω_{+} on W to a constant, hence the initially constant value of the simulated ω_{+} curve for $W \lesssim 0.3\,\mathrm{mJ\,cm}^{-2}$, and the near identical experimentally fitted values for $W \leq 0.5\,\mathrm{mJ\,cm}^{-2}$. Thus it can be ascertained from Figure 4.9

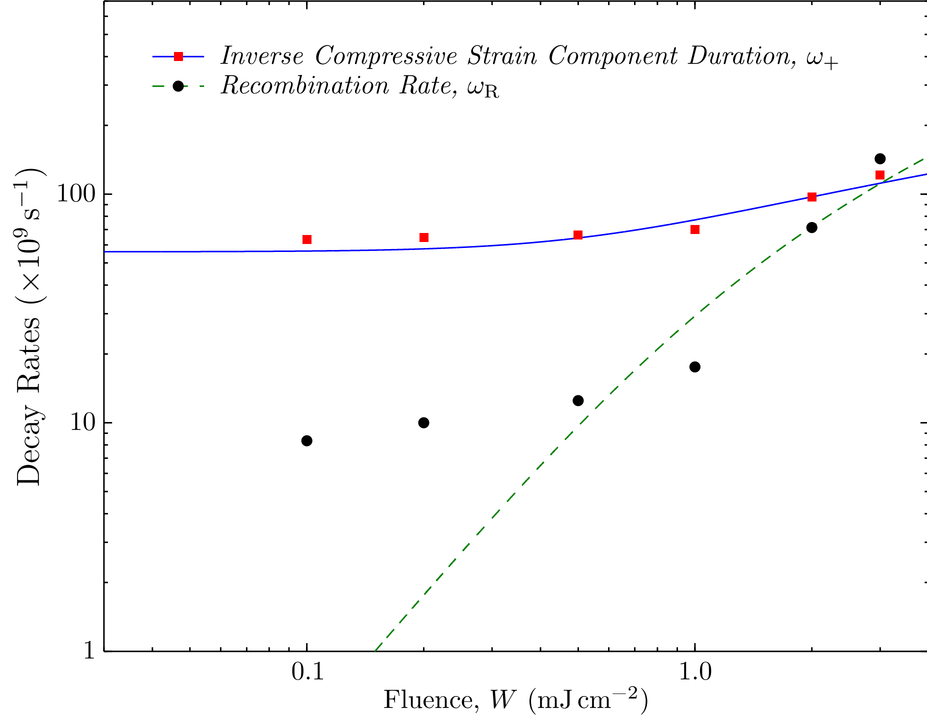

Figure 4.9: Fitted values and simulated curves of the dependence of inverse compressive strain duration ω_+, and recombination rate ω_R against pump beam fluence W. The former is shown with a solid, blue line for the simulated curve, and red squares for the fitted values, whilst the latter is represented by a dashed, green line, and black circles for the simulated curves, and fitted values, respectively. The decay rate curves have been calculated by including only Auger non-radiative recombination, such that $\omega_R = An_{eh}^2$, where $A = 7 \times 10^{-30}\,\mathrm{cm}^6\,\mathrm{s}^{-1}$ is the effective Auger coefficient [94], and n_{eh} is the electron-hole (e-h) plasma density. There is good agreement between fitted and simulated ω_+, but not for the linear regime in ω_R due to the minimal effect of Auger recombination at these fluences.

that

$$\omega_R \propto \begin{cases} W, & \text{in the linear regime,} \\ W^2, & \text{in the non-linear regime.} \end{cases}$$

Given the above analysis, it can be concluded that non-radiative recombination Auger effects do not have a significant effect on the overall profile of the initial strain pulse in the linear regime. In fact, the values of $\omega_+ \approx \omega_c$ implied that the acoustic waves could not escape the supersonically expanding plasma waves until $v_{eh} \leq v_{LA}$, as discussed earlier in Section 4.3.1. Similarly, it can be deduced that the deformation potential mechanism for strain generation is dominant in this regime from the excellent agreement between the deformation potential model derived in Section 4.4 and the experimental data.

However, in the non-linear regime, thermoelasticity becomes rapidly dominant with increasing excitation density, as the non-radiative Auger recombination of *e*-*h* pairs acts as a limiting factor to the supersonic progression of the plasma. As a result, the duration of the compressive region ω_+^{-1}, a measure of the effect of this supersonic progression, decreases as does the *e*-*h* recombination time ω_{R}^{-1}. The relative contributions of these two mechanisms to the initial compressive strain amplitude η_{c0} were determined elsewhere by others in Young et al. [80], and also corroborated the conclusions made herein.

4.6 Conclusions

In this chapter, it has been confirmed that a double QW-embedded *p*-*i*-*n* diode can be successfully used as a high frequency phonon detector. In addition, the initial strain profile of the remotely detected coherent LA phonons can be determined through the application of various fitting criteria, and numerically propagating the result using the KdV-Burgers equation computed by the composite Runge-Kutta method.

As is known from previous works and verified herein, the initial profile for acoustic wavepackets transduced in thin metal films is bipolar in nature, thus resulting in the remote, experimental detection of a nearly bipolar propagated pulse by the hypersonic *p*-*i*-*n* detector. Differences between the simulated, and experimental propagated strain profiles are attributed to both dispersive effects and attenuation.

However, transduction of strain from bulk GaAs causes the formation of a strongly asymmetric pulse with a damped leading edge. Both of these properties are accredited to a supersonically expanding *e*-*h* plasma, which is generated upon ultrafast optical excitation of the bulk semiconductor. Specifically, laser irradiation causes the formation of an *e*-*h* plasma, whose expansion and subsequent relaxation forms the strain pulse. The plasma itself is initially travelling at supersonic speeds, and thus the strain pulse cannot escape the plasma until it has decreased to subsonic levels. Therefore the initial strain pulse is both highly asymmetric with a damped leading edge.

However, the system enters a non-linear regime with increasing fluence, and the density of the plasma increases alongside the *e*-*h* recombination rate, which is dominated by Auger processes. Accordingly, this non-radiative

recombination becomes a limiting factor in the progression of the supersonic plasma, and allows the strain pulse to escape at much shorter times than in the absence of non-radiative recombination, i.e. thermoelastic effects in this case. As such, the duration of the damped leading edge decreases with increasing fluence, although the asymmetric profile remains due to supersonic plasma expansion outside of the optical excitation region.

The above properties for both the linear and non-linear regimes have been verified by the mathematical model given in Section 4.4, through solving the inhomogeneous wave equation for photoinduced stress by the deformation potential. The validity of this model was checked against known behaviour in a 30 nm thick Al film transducer sample, before being applied to the bulk GaAs transducer data. As shown in Section 4.5, it was deduced that the deformation potential was the dominant mechanism for strain generation in the linear regime, but that thermoelasticity had an increasingly larger effect in the non-linear regime. Verification of these assertions was determined by assuming that the recombination rate ω_{R} was dependent on only non-radiative Auger recombination processes, as defined in photoinduced thermoelastic stress. This assumption only matched experimental data in the non-linear regime, thus indicating an increased thermoelastic contribution that eventually dominates over the deformation potential mechanism.

In conclusion, it is evident that the dominant mechanism of strain generation in bulk GaAs can be controlled by the pump beam fluence. At low fluences, the deformation potential is dominant, whereas at high fluences coherent phonon generation is due to thermoelasticity. In addition, it has been shown that a spatially- and temporally-evolving *e*-*h* plasma generated by these mechanisms has a strong effect on the profile of the initial strain that leads to an asymmetric pulse and a damped leading edge, where the temporal duration of the latter property is dependent on the generation mechanism.

Chapter 5

Double Barrier Quantum Well Resonant Tunnelling Diode

The following chapter presents the experimental results obtained from a double barrier quantum well (QW) resonant tunnelling diode (RTD). They show acoustic modulation of charge transfer across such a diode in what has been termed the *acoustoelectronic pumping effect*. This effect has been demonstrated experimentally, and verified both by theory and simulations [95].

A general overview of a typical RTD operating in its stationary state (i.e. in the absence of acoustic modulation) is first given in this chapter to establish basic device principles, alongside a brief examination of the resonant tunnelling mechanism. Acoustic modulation of nanostructures with specific emphasis on its effects in RTDs will subsequently be described qualitatively in the following section.

Next, details regarding the wafer profile used in the experiments and microfabrication conditions will be provided, after which the experimental results will be presented. These results comprise transport measurements, conducted to determine the electronic properties of the RTD in its stationary state, and fast electrical measurements to ascertain the effects caused by coherent phonon wavepackets. Various stationary RTD parameters can be extracted from the former measurements, and are determined here numerically. The latter measurements are verified with numerical simulations based on a theoretical model describing strain-induced modulation of charge transfer, and a full consideration of the *acoustoelectronic pumping effect* is given at the conclusion of this chapter.

5.1 Stationary RTD Operation

The stationary operation of a RTD is well established in the literature, such as in the work by Chang et al. [96] where the first clear evidence of resonant tunnelling through double-barrier structures was observed.

This section qualitatively details the workings of a RTD under various applied biases so that an understanding of the basic principles of its operation can be grasped; a more detailed explanation of the resonant tunnelling mechanism can be found in Section 5.2. Initially, the zero applied bias case will be discussed before the effects of bringing the system into and out of resonance are examined. A purely sequential tunnelling model demonstrates these operational principles here, and validity of this model for the devices discussed in this chapter is presented in Sections 5.2 and 5.5.1.

5.1.1 Zero Applied Bias

The active region of a typical RTD consists of two semiconductor barrier layers encompassing another semiconductor layer of relatively lower band gap to form an effective QW. These layers are surrounded by regions of doped, lower band gap material to form contactable regions, which provide carriers for current flow. Details regarding the wafer growth profile of the actual devices used can be found in Section 5.4.

A diagrammatic representation of a typical RTD conduction band is shown in Figure 5.1. Here, the QW ground state (dashed, black line) and its corresponding wavefunction (solid, blue curve) have been labelled, and the filled states in the doped regions surrounding the barriers are shaded. In this zero applied voltage (equilibrium) case, only a minimal current is measured, as electron ground states of the emitter region and QW are not in alignment thus preventing resonant tunnelling; the minimal current originates from thermionic emission of carriers over the barriers, and non-resonant tunnelling of carriers through the barriers [27, 97, 98]. The energy difference between these two electron ground states is denoted by the stationary detuning parameter Δ_0. This is directly related to the amount of resonant tunnelling occurring in the system, as will be described elsewhere in this chapter; in this equilibrium case, Δ_0 is much greater than Fermi energy of the emitter region E_{FE}.

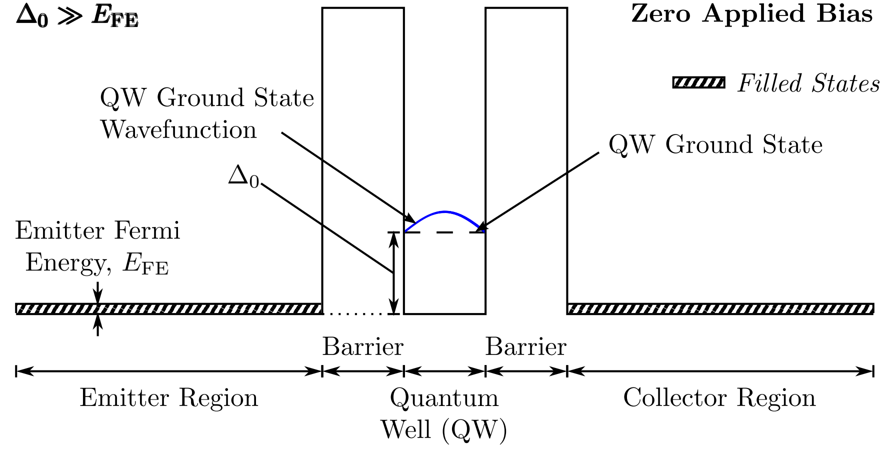

Figure 5.1: Typical conduction band (CB) diagram of a resonant tunnelling diode (RTD) in the absence of a strain pulse (stationary operation), comprising two barriers surrounding a quantum well (QW). Labelled are the Fermi energy of the emitter E_{FE}, QW ground state (dashed, black line), QW ground state wavefunction (solid, blue curve), and the stationary detuning parameter Δ_0. Δ_0 is defined as the energy separation between the electron states in the 2D emitter and QW. Note that no resonant tunnelling occurs in this state, as the ground states of the emitter and QW regions are not aligned, and therefore the QW ground state comprises of unfilled states, and $\Delta_0 \gg E_{FE}$.

5.1.2 Resonance Threshold and Resonance Peak

When a voltage V is applied across the device, the RTD band structure shifts as an energy difference equivalent to eV is formed between the emitter and collector regions. This confines electrons in the emitter, due to the low doping concentration in this region, and forms a quasi-two-dimensional electron gas (quasi-2DEG); further detail regarding how this quasi-confinement affects tunnelling through the emitter barrier is provided in Section 5.2.3. If V is large enough to bring E_{FE} and the QW electron ground state into alignment, i.e. when $\Delta_0 \approx E_{\mathrm{FE}}$, the device is biased at the resonant threshold, as exemplified in Figure 5.2(a).

Here, carriers begin to resonantly tunnel through the emitter barrier into the QW at a given tunnelling rate w_{E} (thin, dashed, green arrow). These carriers occupy unfilled states within the QW, leading to an increase of the QW Fermi energy E_{FW}. They are eventually able to tunnel out of the QW to the collector through the corresponding barrier at a rate w_{C} (thin, dashed, red arrow). This resonant tunnelling contribution increases charge flow, and therefore an increase in current is measured.

The resonant tunnelling contribution continues to increase concurrently with V until the system reaches the resonance peak. In this case, shown in Figure 5.2(b), the ground states of the emitter and QW regions are in align-

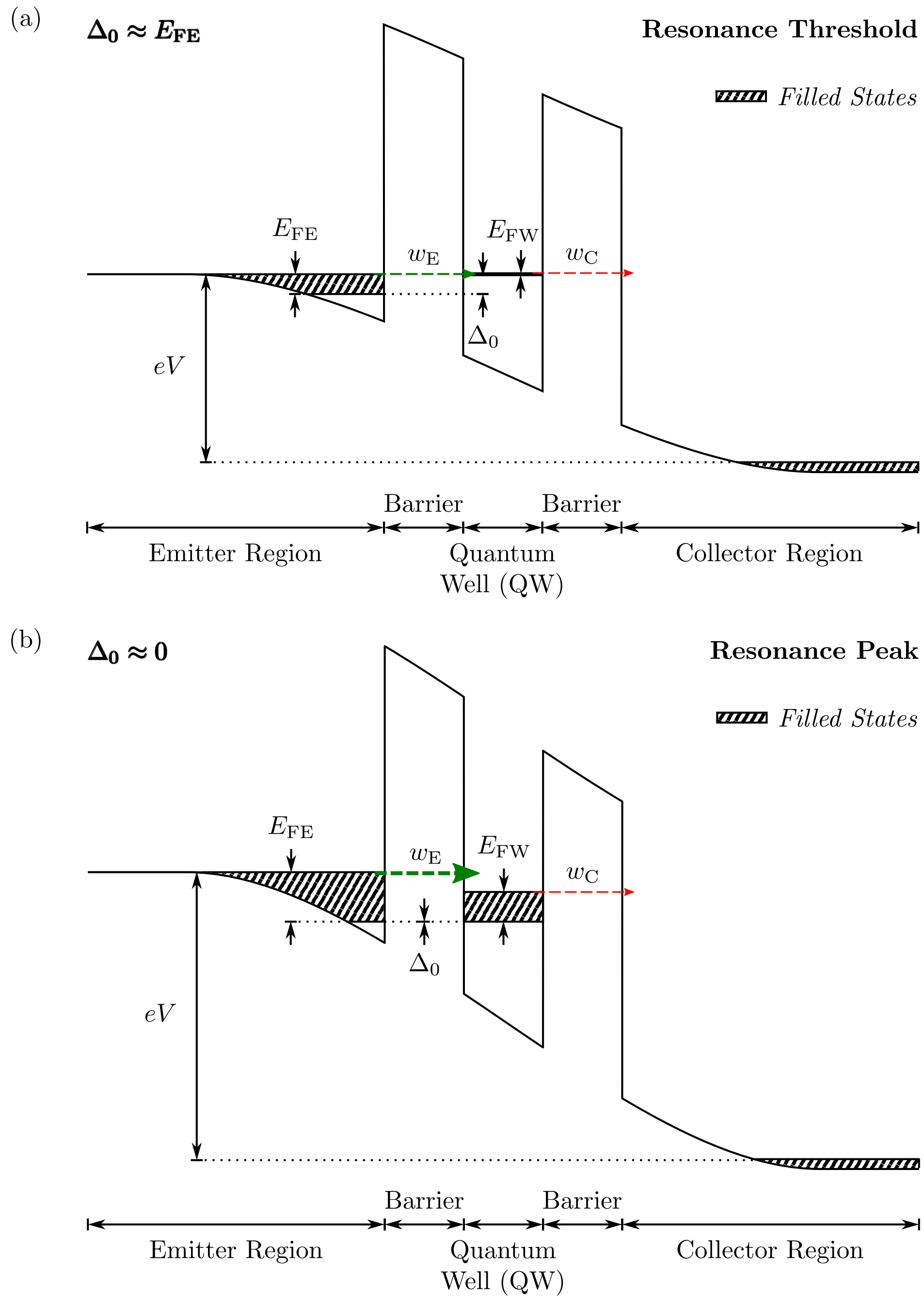

Figure 5.2: Conduction band (CB) diagram of a resonant tunnelling diode (RTD) biased at the (a) resonance threshold and (b) resonance peak. An applied voltage across the device V creates an energy difference between the emitter and collector regions eV. (a) At a given voltage, the QW ground state aligns with the emitter Fermi energy level E_{FE}, thus bringing the system into resonance. At this resonance threshold, the stationary detuning parameter $\Delta_0 \approx E_{\mathrm{FE}}$, and carriers are able to resonantly tunnel into the QW through the emitter barrier at a small rate w_{E} (thin, dashed, green arrow). These carriers increase the QW Fermi energy level E_{FW}, and also the number of available carriers to tunnel out to the collector at a rate of w_{C} (thin, dashed, red arrow), resulting in a larger measured current. (b) Further increases of V provide more available empty QW states, leading to a corresponding increase in charge/current flow. Maximum w_{E} (thick, dashed, green arrow) is achieved when the system is biased at the resonance peak, which occurs when $\Delta_0 \approx 0$.

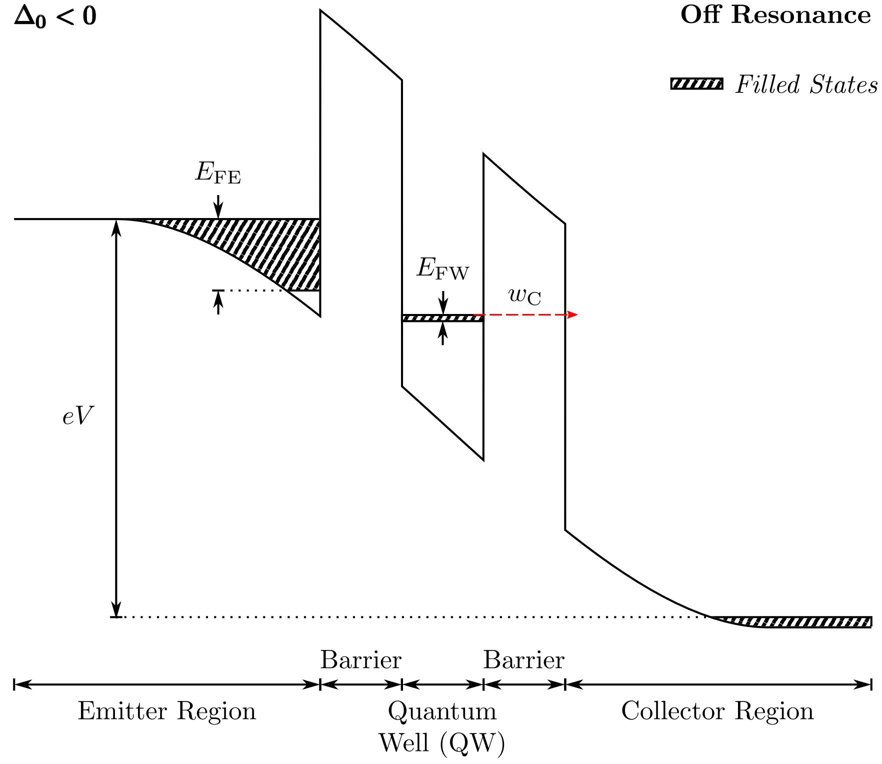

Figure 5.3: Conduction band diagram of a resonant tunnelling diode (RTD) biased off resonance. As the emitter and QW states are no longer aligned, $\Delta_0 < 0$ and there is no resonant tunnelling contribution to the measured current. Carriers within the QW continue to tunnelling through the collector barrier (thin, dashed, red arrow), thus reducing E_{FE} due to the absence of resonance tunnelling, and the measured current.

ment with $\Delta_0 \approx 0$. Consequently, the maximum number of empty QW states are available for tunnelling carriers, and therefore the resonant tunnelling contribution and corresponding current flow are also at a maximum.

5.1.3 Off Resonance

For V beyond the resonance peak, the RTD is shifted off resonance; in this case, $\Delta_0 < 0$, and the electron states in the emitter and QW regions are no longer aligned, as can be seen in Figure 5.3. Consequently, the resonant tunnelling contribution to charge transfer is approximately zero, as the device is in a similar state to that discussed in Section 5.1.1.

Carriers continue to tunnelling into the QW via thermionic emission and non-resonant tunnelling, but E_{FW} decreases due to carriers escaping through the collector barrier at a given rate w_{C}, which is assumed to be independent of the detuning parameter [95]. As a result, there is a drop in the measured current, and the device exhibits negative differential resistance (NDR) in its stationary current-voltage (I_0-V) characteristics in the region immediately

following the resonance peak, since increasing V results in decreasing I_0. This is caused by the buildup of charge in the QW, and its subsequent dissipation when the system is off resonance, as detailed later in Section 5.2.4.

Further increases of applied bias beyond the NDR region generates increased current. Initially, this is due to scattering-assisted transitions, before the system is biased such that either the QW first excited state is in alignment with E_{FE} [99], and/or the emitter ground state level is significantly raised due to the large eV to allow for greater thermionic emission of carriers over the barriers [97].

5.2 Resonance Tunnelling Mechanism

The resonant tunnelling mechanism can be explained by two treatments; the first, coherent tunnelling, was proposed by Tsu and Esaki [100], and utilised by Chang et al. [96]. This method draws similarities with the Fabry-Pérot interferometer, in that the transmission coefficient within the RTD is enhanced for certain wavelengths; a full and rigorous treatment of this method can be found in Ricco and Azbel [101] and Payne [102]. The second method, sequential tunnelling, was put forward by Luryi [103] in response to the work of Sollner et al. [104]. This work by Sollner et al. [104] was based on the coherent tunnelling model, which supposedly lacked both an explanation of the NDR effect, and the inclusion of scattering effects. However, it was subsequently shown by Weil and Vinter [105] that both theoretical descriptions of resonant tunnelling are valid, as they produced identical results, at least in the absence of scattering.

By including scattering, Jonson and Grincwajg [106] proved that resonant tunnelling is comprised of a combination of both treatments, provided that the energy width of QW quasi-bound state is much less than E_{FE} or the separation of the QW states [99, 106, 107]; both these conditions are satisfied in the present work, as confirmed later in Section 5.5.1. As such, a completely sequential tunnelling approach has been adopted in this thesis for ease, although this does not strictly apply for the present device.

As the exact representation of the resonant tunnelling mechanism is unimportant in the scope of this work, only a brief overview of both theories is given here, alongside a concise summary of tunnelling from a quasi-2DEG emitter, and charge-buildup and bistability effects; in fact, it has

been suggested that the true tunnelling mechanism is only important when coherence of the electron wavefunction is necessary [106]. A detailed and complete discussion of these methods and effects can be found in the thesis by Leadbeater [99], and other references [26, 27, 108].

5.2.1 Coherent Tunnelling

In the model of coherent tunnelling, the electron wavefunction must be solved in the entire RTD structure simultaneously [27]. When the system is off resonance, there is a finite probability that electrons in the emitter with energy E will be transmitted or reflected by the barriers; note that $E \neq E_n$, as the system is off resonance, where E_n is the energy of n discrete subbands formed in the QW due to size quantisation, such that [109]

$$E_n = \frac{\pi^2 \hbar^2 n^2}{2m^* w^2}, \quad n = 1, 2, 3, \ldots, \tag{5.1}$$

where m^* is the QW effective mass, w is the QW width, and assuming an infinite barrier.

The transmission coefficient $T\left(E\right)$ in a finite QW case is then approximately equal to the product of the transmissions coefficients of the emitter barrier T_{E} and collector barrier T_{C}, i.e.

$$T\left(E\right) \approx T_{\mathrm{E}} T_{\mathrm{C}}. \tag{5.2}$$

Equation 5.2 thus indicates that the probability of electron transmission through both barriers off resonance would be almost equivalent to transmission through a global barrier of width equal to the sum of the widths of the two barriers [101].

If the system is shifted into resonance, i.e. $E = E_n$, the wavefunction builds up within the QW so that the reflected components are cancelled out, whilst the transmitted components constructively interfere. This results in a higher probability of electron transmission $T_{\mathrm{res}}\left(E = E_n\right)$, such that [101]

$$T_{\mathrm{res}}\left(E = E_n\right) \approx \frac{T_{\mathrm{min}}}{T_{\mathrm{max}}}, \tag{5.3}$$

where T_{min} and T_{max} are the smallest and largest transmission coefficients of the two barriers. Thus unity transmission can theoretically be achieved by symmetric emitter and collector barriers [103, 108, 110], and the electron

should be able to tunnel through the barriers as if they were non-existent, hence why parallels are drawn with the operation of a Fabry-Pérot interferometer.

5.2.2 Sequential Tunnelling

The sequential tunnelling model has been employed throughout this chapter, and was qualitatively described in Sections 5.1.1–5.1.3. In this model, tunnelling through each of the emitter and the collector barriers in the RTD is considered as separate events, with the former tunnelling component being the dominant mechanism for current flow [27]. This is in contrast to coherent tunnelling, which considers the device in totality, and not as individual components.

This incoherent tunnelling model assumes that lateral momentum of an electron $k_\perp = \sqrt{k_x^2 + k_y^2}$ is conserved in the x- and y-directions when tunnelling into a QW along the z-direction, as k_z is quantised in the well [26, 27]. Thus the energy of electrons in the well E_W, and in the emitter E_E are

$$E_\mathrm{W} = E_n + \frac{\hbar^2 k_\perp^2}{2m^*}, \tag{5.4}$$

$$E_\mathrm{E} = E_\mathrm{E0} + \frac{\hbar^2 k_z^2}{2m^*} + \frac{\hbar^2 k_\perp^2}{2m^*}, \tag{5.5}$$

where E_E0 is the ground state energy in the emitter. Both energy and lateral momentum are conserved during the tunnelling process, and so the following condition

$$E_\mathrm{E0} + \frac{\hbar^2 k_z^2}{2m^*} = E_n, \tag{5.6}$$

must also be satisfied. Consequently, tunnelling can only occur when $E_\mathrm{E0} < E_n < E_\mathrm{FE}$, with a maximum number of electrons available for tunnelling from the emitter when $E_\mathrm{E0} = E_n$ of areal density [103]

$$n_\mathrm{E} = \frac{m^* E_\mathrm{FE}}{\pi \hbar^2}. \tag{5.7}$$

Experimental evidence of sequential tunnelling was determined in the work by Leadbeater et al. [111], and Leadbeater and Eaves [112], where a lightly-doped asymmetric RTD was examined. Here, the dwell time in the

QW was calculated to be larger than the relaxation time, indicating that electrons could thermalise to the lattice and form the Fermi level E_{FW}, and thus it was ascertained that the tunnelling mechanism was purely sequential. In addition, Eaves et al. [113] showed that interband scattering in a RTD also constituted at least partial sequential tunnelling.

5.2.3 Tunnelling from a Quasi-Two-Dimensional Electron Gas Emitter

It was noted by Leadbeater [99] that the above two models are ideal for determining the resonant tunnelling mechanism where E_{FE} is for a three-dimensional electron gas. However, as stated therein, where the regions encompassing the barriers are lightly doped ($\lesssim 10^{16}\,\mathrm{cm}^{-3}$) and a voltage bias is applied across the device, the electrons in the emitter are confined as a quasi-2DEG.

As such, there are various limitations that the above models have in simulating experimental data; namely, that the coherent model would neglect the scattering of electrons from the bulk contact into the 2DEG emitter, and that the sequential process would ignore the effect of thin barriers and large electric fields. Specifically, carriers trapped in the emitter 2DEG may either tunnel through the emitter barrier, or may scatter back into the bulk contact region. Consequently, the number of filled states is dependent on both the tunnelling and scatter rates, and thus leads to an energy distribution in the 2DEG emitter that must be accounted for [99].

An approximate approach derived by Lassnig and Boxleitner [114] was to consider electrons in the emitter not as bound states, but as incoming free waves. These free waves are of a given energy, and an approximation of the transmission coefficient is made at said energy. Using this *quasi-free* treatment, and the Fang-Howard wavefunction [115, 116], it was shown that the average distance of electrons in the 2DEG emitter from the emitter barrier is [99]

$$\lambda_{\mathrm{E}} = 2\left(\frac{9\varepsilon_0\varepsilon_{\mathrm{r}}\hbar^2}{11e^2m^*n_{\mathrm{E}}}\right)^{\frac{1}{3}}, \tag{5.8}$$

where $\varepsilon_{\mathrm{r}} = 12.9$ is the relative permittivity of GaAs. This distance is used later to extract carrier density and Fermi energy level information from the RTD I_0-V characteristics, which are given in Section 5.5.

5.2.4 Space-Charge Buildup and Bistability Effects

RTDs exhibit bistability effects in that the I_0-V characteristics differ depending on the direction of applied bias, and these are caused by space-charge buildup in the QW. A qualitative discussion of these effects is provided here, as further detail can be found elsewhere [99, 111, 112, 117–120]. These effects can be described by both coherent and sequential tunnelling models, although only the latter will be used here.

In the sequential model, a RTD can be treated as two capacitors connected in series [120], as shown in Figure 5.4. The first capacitor encompasses the emitter, emitter barrier, and the first half of the QW, whilst the second consists of the remainder of the QW, the collector barrier, and the collector; the common central plate corresponds to the QW. The overall voltage drop across the device is then represented as the summation of the voltage drops across the two capacitors, i.e. $V = V_{\mathrm{E}} + V_{\mathrm{C}}$, where V_{E} and V_{C} are the voltage drops across the first and second capacitors, respectively. Note that this representation of the RTD as a series of capacitors neglects the tunnelling mechanisms involved, and is therefore limited to a static charge representation of the device at a given applied bias.

In Figure 5.4(a), the charge in the emitter and collector regions when there are no electrons in the QW is denoted by q_{E} and q_{C}, respectively. As carriers tunnel into the well, the charge on the QW common plate is increased to $-q$ whilst the charge on the emitter plate is reduced to $q_{\mathrm{E}} - q$; note that the collector plate is unaffected by this change, as represented in Figure 5.4(b). These confined electrons remain in the QW for a finite dwell time τ_{C} before tunnelling out of the collector barrier, hence causing space-charge buildup in the QW. The reduction in emitter charge also reduces V_{E}, thus causing bending of the conduction band, and a reduction in the overall voltage drop across the device so that $E < eV$. As the applied bias must be maintained throughout the RTD, a charge equivalent to $-q/2$ must flow from the collector to the emitter to compensate for the voltage drop (see Figure 5.4(c)). As a result, both the band structure of the system (dashed-dotted, green line), and the position of the QW ground state (dashed, red line) are shifted from their original configuration, with the latter having a higher energy than would be expected in the absence of the electrostatic feedback mechanism.

As the system reaches the resonance peak ($\Delta_0 \approx 0$), both current flow

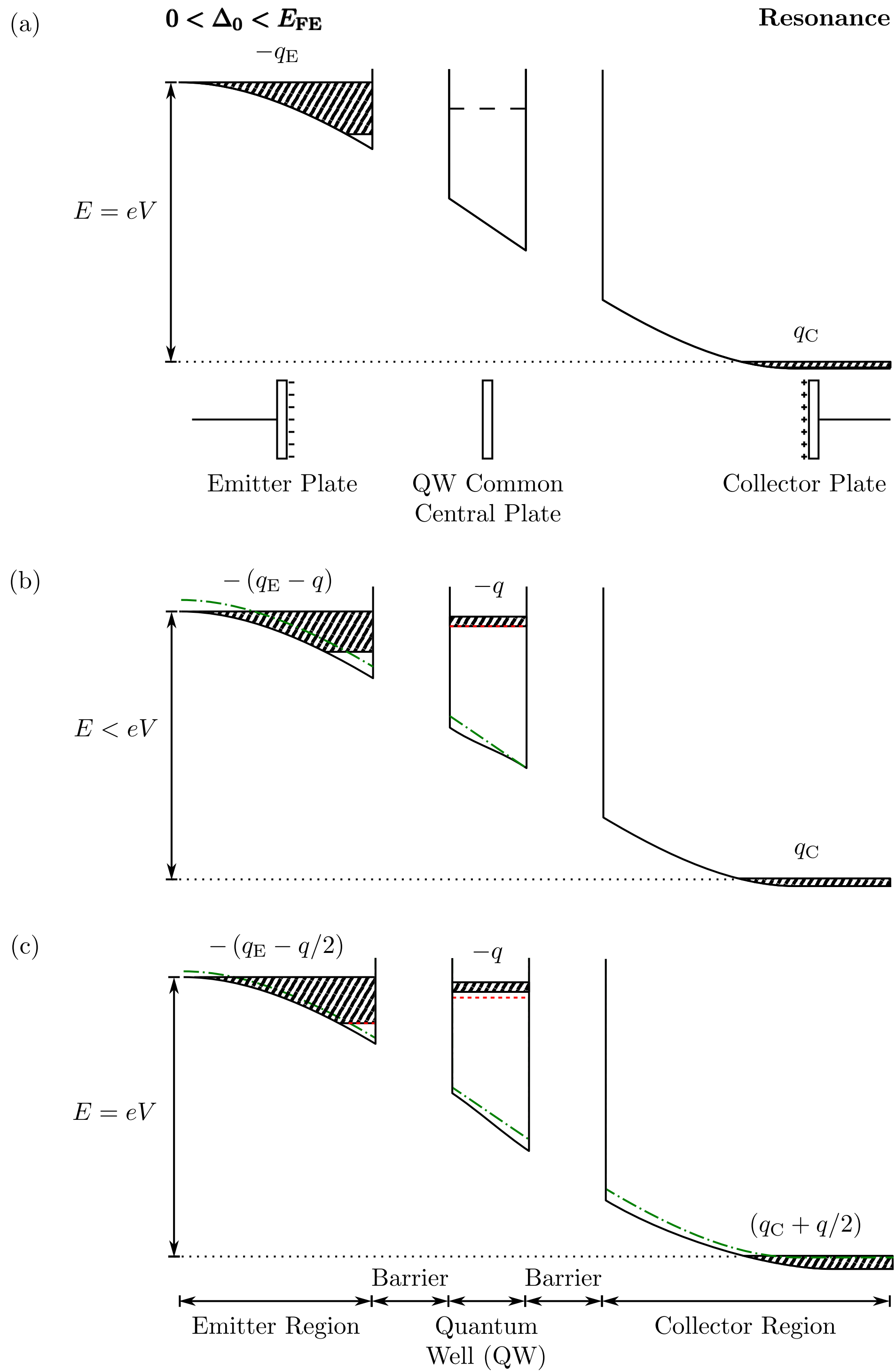

Figure 5.4: Representative sketch of the electrostatic feedback mechanism in resonant tunnelling diodes (RTDs) that gives rise to bistability. (a) Conduction band diagram (top) of a RTD between the resonance threshold and peak at $E = eV$ for device voltage V, with q_E and q_C the charges in the emitter and collector regions, respectively, and (bottom) the corresponding RTD representation as a series of capacitor plates. The conduction band and QW ground state here are represented in the subsequent figures as dashed-dotted, green and dashed, red lines, respectively. (b) Charge on the QW common plate q reduces the emitter charge to $q_E - q$, and consequently $E < eV$. (c) To maintain the energy drop across the RTD, $-q/2$ must feedback from the collector to the emitter so that $E = eV$.

and QW areal electron density n_W are at a maximum, as is the compensatory effect caused by the electrostatic feedback mechanism; here V_E and V_C are reduced and increased, respectively, by $q_{max}/2$, where $q_{max} = A_W n_W e$, where A_W is the area of the QW. This allows resonant tunnelling to occur at much higher V than would be expected if space-charge buildup was ignored.

Beyond this point ($\Delta_0 < 0$), resonant tunnelling no longer occurs and the charge drops as electrons tunnel out of the QW. Consequently, the compensatory effect is reversed to maintain V thus increasing V_E, and E_n is found at a much lower energy than expected in the absence of charge buildup. If the direction of applied bias is reversed, the resonance peak is found at a lower V than in the opposite direction, given the electrostatic feedback mechanism, and hence the presence of bistability in RTDs [99].

5.3 Acoustic Modulation

Previous studies have shown that it is possible to acoustically modulate energy levels within confined nanostructures by exploiting the piezospectroscopic effect [19, 20], as reviewed in Section 1.4.2. A theoretical description of coherent phonon generation and propagation has already been given in Chapter 2, and so only a brief overview relevant to RTD acoustic modulation is provided here; note that, for simplicity, the non-linear propagation of strain pulses have been ignored.

An incoming bipolar hypersonic wavepacket $\eta(t)$ comprises compressive ($\eta(t) < 0$) and tensile ($\eta(t) > 0$) components; the sharp shape change at the interface of these two components is formed from high frequency oscillations, which are in the sub-THz to THz regime [95]. As the wavelengths of these oscillations are comparable to the size of the nanostructures themselves, they significantly affect any confined energy levels in the active region; oscillations outside of this region, for example in the bulk substrate, or those with longer wavelengths will modulate the entire substrate or region, respectively, resulting in zero net effect. These relevant oscillations raise and lower the confined energy levels within the nanostructure according to the piezospectroscopic effect as they propagate through it. It is known that the energy levels in the conduction band (CB) and valence band (VB) in GaAs for $\eta(t) < 0$ are raised and lowered, respectively, relative to their stationary positions. The opposite occurs for $\eta(t) > 0$, where states in the CB (VB) are lowered (raised).

The acoustic modulation of a RTD by $\eta(t)$ is idealised in Figure 5.5 for the CB of a device biased at the resonance threshold only. The stationary state is first shown in Figure 5.5(a), which is a magnified version of Figure 5.2(a); here, only E_{FE}, E_{FW}, and Δ_0 have been labelled for clarity. As stated previously in Section 5.1.2, a minimal net current is generated as electrons resonantly tunnel through the emitter barrier to fill states in the QW ground state at a small rate w_{E}, before tunnelling out through the next barrier into the collector region (not shown).

As $\eta(t)$ enters the active region of the device, $\eta(t) < 0$ arrives first, and raises the emitter ground state from its stationary position, as represented by the thick, green arrow in Figure 5.5(b). This reduces the energy difference between emitter and QW ground states, defined by the now time-dependent detuning parameter $\Delta(t)$, and shifts the system into resonance. Consequently, w_{E} increases, and a greater net current is generated. Further propagation of $\eta(t)$ causes $\eta(t) < 0$ and $\eta(t) > 0$ to enter the QW and emitter regions, respectively, as in Figure 5.5(c). Accordingly, the ground states are correspondingly lowered and raised with respect to their original positions, and the system is shifted off resonance. This is similar to the situation discussed in Section 5.1.3, and a reduction in current is measured since E_{FW} decreases due to carriers tunnelling out through the collector barrier. The final case in Figure 5.5(d) occurs when $\eta(t) > 0$ enters the QW, and there is no strain component in the emitter region. Here, the system is brought back into resonance, resulting in larger current generation as more carriers tunnel into the QW. Once $\eta(t)$ has passed through the active region, the system returns to the stationary state represented in Figure 5.5(a).

If the device is biased at the resonance peak, as discussed in Section 5.1.2, a maximum current is already being generated in its stationary state. Consequently, any modulation of the energy levels ($|\Delta(t) - \Delta_0| < 0$) in the emitter and QW relative to one another will cause a drop in the measured current, as the system will be shifted away from its maximum resonance.

A simple model is used in Section 5.6.1 to simulate acoustic modulation, and it ignores both dispersion and non-linear effects on the propagation of the strain pulse. Accordingly, the model uses a similar profile to that shown in Figure 2.1 to calculate acoustic modulation in the RTD. The spatial width of this profile is in the order of 70 nm, which is wider than the size of the barriers and QW in a typical RTD; for the sample examined in this chapter, the spatial width of the barriers and QW (see Table 5.1 for exact dimensions)

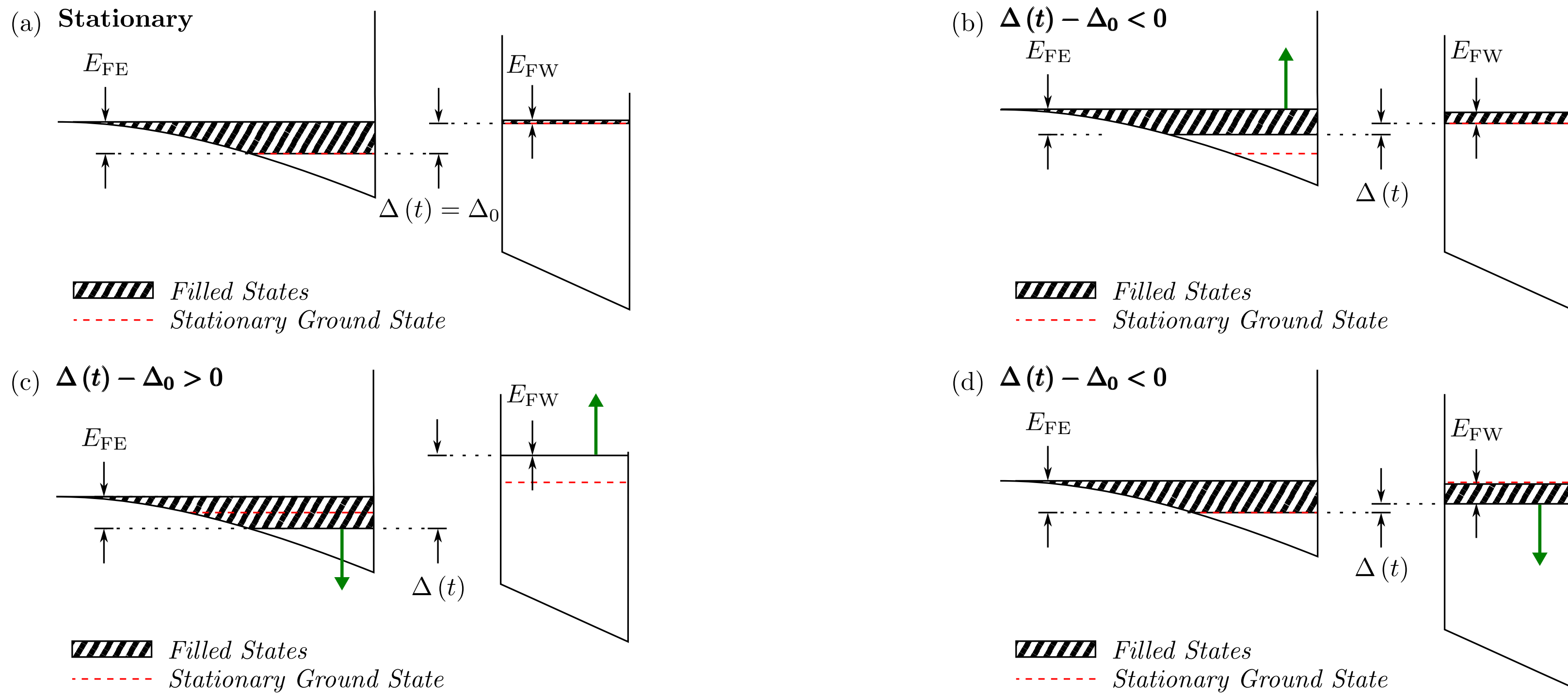

Figure 5.5: Acoustic modulation of energy levels by an incoming hypersonic wavepacket $\eta(t)$ in the conduction band (CB) of a resonant tunnelling diode (RTD) biased at the resonance threshold. (a) The initial stationary state is identical to Figure 5.2(a); the Fermi energy levels in the emitter and quantum well (QW) are labelled E_{FE} and E_{FW}, respectively, as is the stationary detuning parameter Δ_0, which is the energy difference between the emitter and QW ground states (dashed, red lines). (b) The compressive component of $\eta(t)$ arrives first, and raises the emitter ground state relative to its stationary position due to the piezospectroscopic effect (thick, green arrow), as discussed in Section 1.4.2. This decreases the now time-dependent detuning parameter $\Delta(t)$ relative to Δ_0, shifts the system into resonance, and generates a larger net current. (c) As $\eta(t)$ propagates through the device, the compressive and tensile components move into the QW and emitter, respectively. Consequently, $\Delta(t) - \Delta_0 > 0$ and the net current falls to a minimum since the system is moved off resonance. (d) Subsequently, the tensile component enters the QW, bringing the system back into resonance ($\Delta(t) - \Delta_0 < 0$), and increasing the net current. After the strain pulse has passed, the system returns to its stationary state shown in Figure 5.5(a).

is only 16 nm, whilst the entire active region (emitter to collector regions) is 121 nm in width.

Whilst the peaks of both the compressive and tensile components of the strain pulse do not have an effect on the device, as the emitter and QW ground states would both be acoustically shifted by equal amounts, the interaction between the ground states and the strain pulse in its remaining regions would have an effect. This is especially apparent where the differences in strain in the emitter and QW are the greatest, i.e. in the central (high frequency) region of the strain pulse. This spatial width consideration has been taken into account in the simple model, and has been substantiated through comparison with the experimental results, as shown later in Section 5.6.3.

5.4 Wafer Profile and Processing

Experiments were performed on a wafer designated NU165, and its profile is given in Table 5.1. The wafer was grown on a 375 µm thick semi-insulating (SI) GaAs substrate that was In mounted in a MBE machine by Mohamed Henini.

The *n*-*i*-*n* type RTD structure comprises a 3 µm thick bottom contact layer (**BC**) consisting of *n*-type GaAs doped to a concentration of 2×10^{18} cm^{-3}, and a 500 nm thick top contact layer (**TC**) of the same doping type and concentration. The emitter region (**E**) consists of a 50 nm thick *n*-type GaAs layer with linearly decreasing doping concentration (2×10^{16} cm^{-3} to 5×10^{14} cm^{-3}) grown on top of the bottom contact. This is followed by a 2.5 nm thick intrinsic GaAs spacer layer (**S**), which prevents unintentional diffusion of dopants into the barriers [27]. These undoped 5.5 nm $Al_{0.4}Ga_{0.6}As$ barriers (**B**) encompass an effective QW formed from 5 nm of undoped GaAs (**QW**). An additional 2.5 nm thick undoped GaAs spacer layer (**S**) was grown on top of the second barrier, again to prevent accidental dopant diffusion from the collector region into the active region. The structure of the collector region (**C**) is an inversion of the emitter region, and the top contact layer was deposited on above of this collector region.

Devices were fabricated from the grown layers using the Robin Hood mask set in accordance with the processes discussed in Section 3.1 to form cylindrical electrical mesas with InGe-Au metallisation of the top and bottom contact layers. For strain generation purposes, a 100 nm Al film was thermally

	NU165 Wafer Profile		
	Material	**Thickness (nm)**	**Doping (cm^{-3})**
TC	n-GaAs	500	2×10^{18}
C	n-GaAs	50	$2 \times 10^{16} \rightarrow 5 \times 10^{14}$
S	GaAs	2.5	–
B	$Al_{0.4}Ga_{0.6}As$	5.5	–
QW	GaAs	5	–
B	$Al_{0.4}Ga_{0.6}As$	5.5	–
S	GaAs	2.5	–
E	n-GaAs	50	$5 \times 10^{14} \rightarrow 2 \times 10^{16}$
BC	n-GaAs	3000	2×10^{18}
	375 µm Semi-Insulating (SI) GaAs Substrate		

Table 5.1: Wafer profile for NU165 comprising two $Al_{0.4}Ga_{0.6}As$ barriers encompassing a layer of GaAs, with various regions labelled in bold. The wafer was grown on a semi-insulating (SI) GaAs substrate In mounted in a MBE by Mohamed Henini at the University of Nottingham. The bottom contact layer (**BC**) was deposited on top of the substrate, after which the active region was grown. This comprised the emitter region (**E**), an undoped spacer layer (**S**), two $Al_{0.4}Ga_{0.6}As$ barriers (**B**) encompassing an effective GaAs quantum well (**QW**). Next, another spacer region (**S**) and the collector region (**C**) were layered onto the wafer, before the deposition of the top contact layer (**TC**).

evaporated onto the exposed SI substrate surface. Subsequently, each sample was mounted Al film side down onto a holder shown in Figure 5.6(a), with the desired 100 µm diameter device positioned directly over the sample rear surface exposure hole. This mounted device was subsequently wedge bonded with Al wire so that the circuit in Figure 5.6(b) was created for future transport and fast electrical measurements.

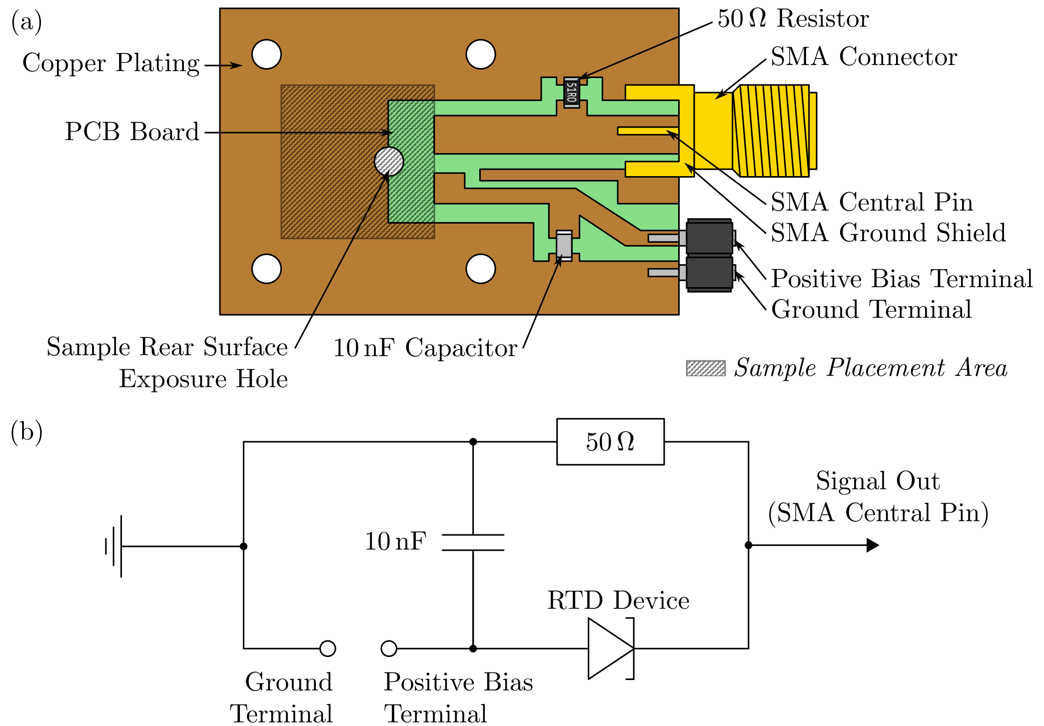

Figure 5.6: (a) Typical sample holder and (b) circuit diagram used for stationary current-voltage (I_0-V) and fast electrical measurements of NU165 samples. (a) The sample holder was designed by Ian Taylor, and comprised of a copper plated PCB board patterned as shown. A SMA connector, 50 Ω resistor, 10 nF capacitor, and pins for voltage bias application were soldered onto the PCB, and the sample was mounted onto the holder in the shaded region using GE varnish, as discussed in Section 3.1.8. It was positioned so that the Al film surface directly opposite the desired 100 µm diameter resonant tunnelling diode (RTD) was over the exposure hole for strain generation purposes. Al wire was wedge bonded from the top contact to the copper plate connected to the SMA central pin, and from the bottom contact to the copper connected to the positive bias terminal to give the circuit diagram in (b).

5.5 Transport Measurements

I_0-V characteristics were measured using the setup depicted in Figure 3.4(b), and were performed on a 100 µm diameter RTD cylindrical mesa fabricated from NU165, maintained at 4.7 K; this device had an estimated spreading resistance $R_{\mathrm{SP}} = 6\,\Omega$. The results of this measurement are given in Figure 5.7 for both increasing and decreasing applied voltage bias; the former is distinguished by a solid, blue line, whilst the latter has been plotted as a dashed, red line; both have corresponding arrows to indicate the direction of applied bias.

The characteristics shown here match the qualitative and theoretical descriptions of stationary RTD operation given in Sections 5.1–5.2. Specifically, there was minimal current between 0 V ($I = 66$ pA) and the resonant thresh-

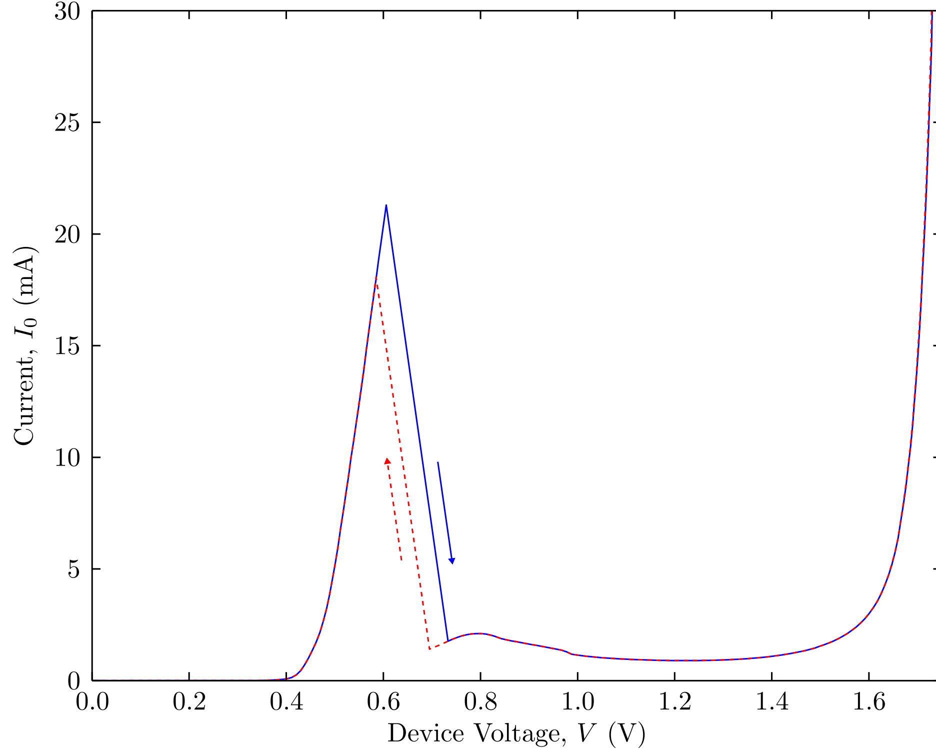

Figure 5.7: Stationary current-voltage (I_0-V) characteristics of a resonant tunnelling diode (RTD) processed from NU165 in both increasing (solid, blue line) and decreasing (dashed, red line) applied voltage, with the direction shown using arrows in their corresponding colours and stroke styles. The characteristics are typical for an RTD, as discussed in Section 5.1. It shows minimal I_0 generation before the resonance threshold at a device voltage $V_{\mathrm{th}} = 0.47\,\mathrm{V}$ for increasing applied voltage. This value was obtained by fitting the linear resonance slope between $V = 0.50\,\mathrm{V}$ to $0.60\,\mathrm{V}$. Subsequently, I_0 increased due to resonant tunnelling, until a maximum I_0 was generated at the resonance peak of $V_{\mathrm{pk}} = 0.61\,\mathrm{V}$. Beyond this point, I_0 dropped as the system entered its negative differential resistance (NDR) region, and was shifted off resonance. Bistability effects were also present in the device, and were dependent on the direction of applied voltage, as differentiated in the figure by the distinct lines and arrows.

old voltage, which was generated via non-resonant tunnelling and thermionic processes; this minimal current increased due to the complementary change in barrier height with applied voltage V.

At the resonance threshold, $\Delta_0 \approx E_{\mathrm{FE}}$ and resonant tunnelling was initiated via the mechanisms considered in Section 5.2. A fit of the linear slope between $V = 0.50\,\mathrm{V}$ to $0.60\,\mathrm{V}$ provided a threshold voltage $V_{\mathrm{th}} = 0.47\,\mathrm{V}$, with a leakage current of $I_{\mathrm{th}} = 2.1\,\mathrm{mA}$. Increasing V led to a corresponding increase in current as the system was brought towards the resonance peak at $V_{\mathrm{pk}} = 0.61\,\mathrm{V}$, where a maximum current flow of $I_{\mathrm{pk}} = 21\,\mathrm{mA}$ was recorded; at this bias, n_{W} and the resonant tunnelling current contribution are both at a maximum. Beyond the resonance peak, the system entered its NDR region given that carriers could no longer resonantly tunnel into the QW from the

emitter. Subsequent increases in current occurred at $V \approx 1.2\,\mathrm{V}$ as the RTD left its NDR due to various processes discussed in Section 5.1.3. In addition, the typical RTD bistability effects due to space-charge buildup are evident in the I_0-V characteristics, as the resonance peak occurs at a lower bias of $V_{\mathrm{pk}} = 0.59\,\mathrm{V}$ for decreasing applied bias; this difference of $\Delta V_{\mathrm{pk}} = 20\,\mathrm{mV}$ was as expected [120].

5.5.1 Calculation of Stationary Device Parameters

Various device parameters can be obtained from the above transport measurements; namely, it is possible to estimate both n_{W}, and E_{FW} at the resonance peak, as well as the tunnelling times through the collector barrier τ_{C}.

To obtain these values, n_{E} must first be found; it is known from Leadbeater et al. [111] that n_{E} remains relative constant between V_{th} and V_{pk} for a 2DEG emitter. Examination of the periodicity of magnetoquantum oscillations conducted on a near-identical device[1] found an emitter electron areal density of approximately $4.79 \times 10^{11}\,\mathrm{cm}^{-2}$. This device from wafer NU104 was grown identically to NU165 except that the doping concentration of the emitter and collector regions was set at $2 \times 10^{16}\,\mathrm{cm}^{-3}$. Thus the emitter electron density in NU104 would be larger than in the present wafer, and so an estimated value of $n_{\mathrm{E}} = 4.0 \times 10^{11}\,\mathrm{cm}^{-2}$ was taken, which gives $E_{\mathrm{FE}} = 15\,\mathrm{meV}$ according to

$$E_{\mathrm{F}} = \frac{\pi \hbar^2 n_{\mathrm{e}}}{m^*}, \tag{5.9}$$

where E_{F} is the Fermi energy level for a given areal electron density n_e.

Quantum Well Electron Density Determination

An approximate calculation of n_{W} can be made by examining the electric fields generated by the charge densities in the emitter and QW. This is illustrated graphically in Figure 5.8, where (middle) the carrier concentration $-\rho_e$ and (bottom) electric field $-\frac{\rho_e z e}{\varepsilon_0 \varepsilon_{\mathrm{r}}}$, both against distance, have been sketched for an idealised RTD biased at the resonance peak. (top) The conduction band diagram is only shown to indicate the device dimensions, which can be found in Table 5.1.

[1] Determined from Figure 3.8, p. 52 of Leadbeater [99]

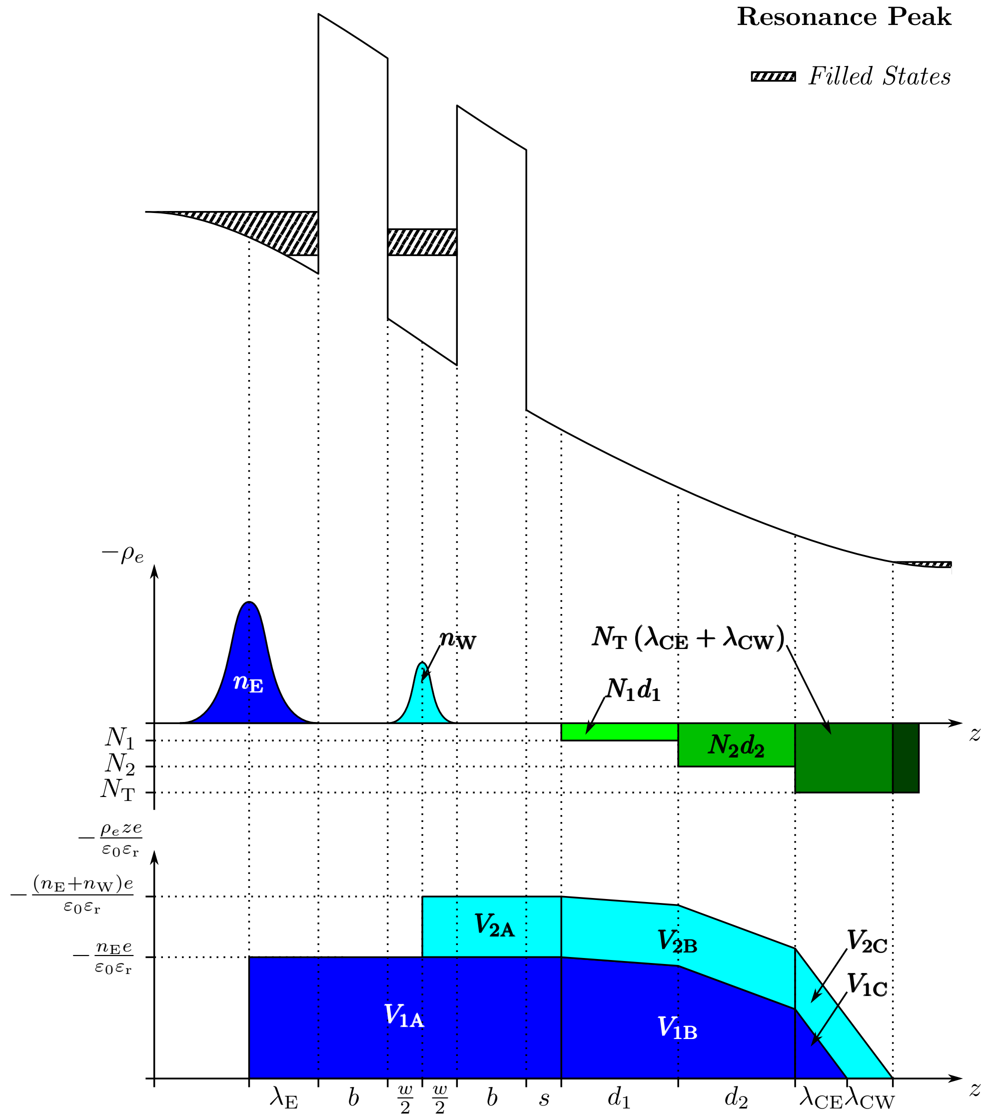

Figure 5.8: Calculation of stationary resonant tunnelling diode (RTD) characteristics by examining charge densities at the resonance threshold and peak. λ_E, b, w, s, d_1, d_2, λ_{CE}, and λ_{CW} are the average electron distance from the emitter barrier, barrier width, quantum well (QW) width, spacer layer width, two lightly doped collector region widths, and the depletion lengths of the electric field due to field from the emitter and the QW, respectively, in the heavily doped top contact. Note that the illustration is not to scale, as λ_E, d_1, and d_2 have been shortened for simplicity. (top) RTD conduction band diagram identical to Figure 5.2 with labels removed for clarity; this diagram is only used to establish the dimensions of the structure, shown with dotted lines, in relation to the other sketches. (middle) Carrier concentration $-\rho_e$ against distance z showing electron distribution in the emitter, QW, two lightly doped collector regions N_1 and N_2, and the top contact N_T. (bottom) Corresponding electric field $-\frac{\rho_e z e}{\varepsilon_0 \varepsilon_r}$ against z in the regions due to electron density in the emitter n_E and QW n_W, and the resultant reduction due the positively charged doping collector and top contact regions.

At the resonance threshold, it was assumed that $n_{\mathrm{W}} \approx 0$, thus the voltage across the idealised RTD $V_1 = V_{1\mathrm{A}} + V_{1\mathrm{B}} + V_{1\mathrm{C}}$ (shaded dark blue) is subject only to the electric field generated by the negative charge density in the emitter n_{E}, and the opposing field generated by the positive charge densities in the collector ($N_1 d_1$ and $N_2 d_2$) and top contact region $N_{\mathrm{T}}\lambda_{\mathrm{CE}}$; here, N_1, N_2, d_1, and d_2 are the doping concentrations and widths of the collector, respectively, and N_{T} and λ_{CE} are the doping concentration and depletion length of n_{E} in the top contact. The components of V_1 can be deduced from the figure as

$$V_{1\mathrm{A}} = \frac{e}{\varepsilon_0\varepsilon_{\mathrm{r}}} n_{\mathrm{E}} \left(\lambda_{\mathrm{E}} + 2b + w + s\right), \tag{5.10}$$

$$V_{1\mathrm{B}} = \frac{e}{\varepsilon_0\varepsilon_{\mathrm{r}}} \left[n_{\mathrm{E}} \left(d_1 + d_2\right) - N_1 d_1 d_2 - \frac{N_1 d_1^2}{2} - \frac{N_2 d_2^2}{2} \right], \tag{5.11}$$

$$V_{1\mathrm{C}} = \frac{e}{\varepsilon_0\varepsilon_{\mathrm{r}}} \frac{\lambda_{\mathrm{CE}}}{2} \left(n_{\mathrm{E}} - N_1 d_1 - N_2 d_2\right), \tag{5.12}$$

where b, w, and s are the barrier, QW, and spacer widths, and $\lambda_{\mathrm{E}} = 11\,\mathrm{nm}$ from Equation 5.8. The depletion length λ_{CE} is given by

$$\begin{aligned} \lambda_{\mathrm{CE}} &= \frac{n_{\mathrm{E}} - N_1 d_1 - N_2 d_2}{N_{\mathrm{T}}}, \\ &= 1.7\,\mathrm{nm}. \end{aligned} \tag{5.13}$$

This gives the voltage drop across the idealised RTD at the resonance threshold as

$$\begin{aligned} V_1 = \frac{e}{\varepsilon_0\varepsilon_{\mathrm{r}}} \Bigg[& n_{\mathrm{E}} d_{\mathrm{E}\to\mathrm{C}} - N_1 d_1 d_2 - \frac{N_1 d_1^2}{2} - \frac{N_2 d_2^2}{2} \\ & - \frac{\lambda_{\mathrm{CE}}}{2} \left(N_1 d_1 + N_2 d_2\right) \Bigg], \end{aligned} \tag{5.14}$$

where $d_{\mathrm{E}\to\mathrm{C}} = \lambda_{\mathrm{E}} + 2b + w + s + d_1 + d_2 + \frac{1}{2}\lambda_{\mathrm{CE}} = 81\,\mathrm{nm}$ for the parameters given in Table 5.1.

Similarly, at the resonance peak it can be generalised that the voltage drop across the idealised RTD is given by $V_1 + V_2$, where $V_2 = V_{2\mathrm{A}} + V_{2\mathrm{B}} + V_{2\mathrm{C}}$ (shaded light blue) is the voltage difference between the resonance peak and threshold. Assuming that n_{E} is constant at these voltages, as discussed above, V_2 is therefore solely due to the electric fields generated by the negative charge density in the QW n_{W}, which is at a maximum at the resonance

peak, and by $N_1 d_1$, $N_2 d_2$ and $N_\mathrm{T}\left(\lambda_\mathrm{CE}+\lambda_\mathrm{CW}\right)$, where λ_CW is the additional depletion length in the top contact due to n_W. Thus it can be inferred in an equivalent manner to Equations 5.10–5.12 that

$$V_{2\mathrm{A}} = \frac{e}{\varepsilon_0\varepsilon_\mathrm{r}} n_\mathrm{W}\left(\frac{w}{2}+b+s\right), \tag{5.15}$$

$$\begin{aligned} V_{2\mathrm{B}} &= \frac{e}{\varepsilon_0\varepsilon_\mathrm{r}}\left[n_\mathrm{E}\left(d_1+d_2\right)+n_\mathrm{W}\left(d_1+d_2\right)-N_1 d_1 d_2-\frac{N_1 d_1^2}{2}\right. \\ &\qquad \left.-\frac{N_2 d_2^2}{2}\right]-V_{1\mathrm{B}}, \\ &= \frac{e}{\varepsilon_0\varepsilon_\mathrm{r}} n_\mathrm{W}\left(d_1+d_2\right), \end{aligned} \tag{5.16}$$

$$\begin{aligned} V_{2\mathrm{C}} &= \frac{e}{\varepsilon_0\varepsilon_\mathrm{r}}\left[\frac{\lambda_\mathrm{CE}}{2}\left(n_\mathrm{E}+n_\mathrm{W}-N_1 d_1-N_2 d_2\right)\right. \\ &\qquad \left.+\frac{\lambda_\mathrm{CW}}{2}\left(n_\mathrm{E}+n_\mathrm{W}-N_1 d_1-N_2 d_2\right)\right]-V_{1\mathrm{C}}, \\ &= \frac{e}{\varepsilon_0\varepsilon_\mathrm{r}}\left[\frac{n_\mathrm{W}\lambda_\mathrm{CE}}{2}+\frac{\lambda_\mathrm{CW}}{2}\left(n_\mathrm{E}+n_\mathrm{W}-N_1 d_1-N_2 d_2\right)\right]. \end{aligned} \tag{5.17}$$

The increased depletion length due to n_W is given by

$$\lambda_\mathrm{CW} = \frac{n_\mathrm{W}}{N_\mathrm{T}}, \tag{5.18}$$

and so the increased voltage drop at the resonance peak due solely to n_W for this idealised RTD is

$$V_2 = \frac{e}{\varepsilon_0\varepsilon_\mathrm{r}}\frac{1}{2N_\mathrm{T}}\left[n_\mathrm{W}^2+n_\mathrm{W}\left(2N_\mathrm{T}d_{\mathrm{W}\to\mathrm{C}}+n_\mathrm{E}+N_1 d_1-N_2 d_2\right)\right], \tag{5.19}$$

where $d_{\mathrm{W}\to\mathrm{C}} = \frac{1}{2}w+b+s+d_1+d_2+\frac{1}{2}\lambda_\mathrm{CE} = 61\,\mathrm{nm}$ for the values in Table 5.1. Given the definitions of both V_1 and V_2, it can be considered that the ratio of these two voltages is equivalent to

$$\frac{V_2}{V_1} = \frac{V_\mathrm{pk}-V_\mathrm{th}}{V_\mathrm{th}}, \tag{5.20}$$

Thus by substituting Equations 5.14 and 5.19 into Equation 5.20, it can be

shown that

$$\begin{aligned} n_{\mathrm{W}}^2 &+ n_{\mathrm{W}}\left(2N_{\mathrm{T}}d_{\mathrm{W}\to\mathrm{C}} + n_{\mathrm{E}} - N_1 d_1 - N_2 d_2\right) \\ &= 2N_{\mathrm{T}}\frac{V_{\mathrm{pk}} - V_{\mathrm{th}}}{V_{\mathrm{th}}}\left[n_{\mathrm{E}}d_{\mathrm{E}\to\mathrm{C}} - N_1 d_1 d_2 - \frac{N_1 d_1^2}{2}\right. \\ &\qquad \left. - \frac{N_2 d_2^2}{2} - \frac{\lambda_{\mathrm{CE}}}{2}\left(N_1 d_1 + N_2 d_2\right)\right], \end{aligned} \tag{5.21}$$

and solving the quadratic equation for positive n_{W} provides

$$n_{\mathrm{W}} = 1.5 \times 10^{11}\,\mathrm{cm}^{-2},$$

for $V_{\mathrm{th}} = 0.47\,\mathrm{V}$ and $V_{\mathrm{pk}} = 0.61\,\mathrm{V}$ from Figure 5.7, and assuming a doping of $N_1 = 5 \times 10^{14}\,\mathrm{cm}^{-3}$ and $N_2 = 2 \times 10^{16}\,\mathrm{cm}^{-3}$ across each half of the collector region $d_1 + d_2 = 2d_1 = 2d_2 = 50\,\mathrm{nm}$. The corresponding QW Fermi energy according to Equation 5.9 is $E_{\mathrm{FW}} = 5.7\,\mathrm{meV}$, which implies that $E_{\mathrm{FW}} \approx 0.4E_{\mathrm{FE}}$ at the resonance peak.

Assumptions of Quantum Well Electron Density Analysis and Resonant Tunnelling Mechanism Considerations

It is worth noting that various approximations have been made in the calculation of n_{W}. Firstly, the electric field in $V_{1\mathrm{A}}$ and $V_{2\mathrm{A}}$ were assumed to begin abruptly, although in reality they would be dependent on the distribution of the 2DEG in the emitter and QW. Secondly, the concentration of the doped collector layer is not constant throughout each half of the layer, as assumed in the calculation but instead linearly increases with greater distance from the QW. As such, the electric field in this region would fall more rapidly as the collector doping concentration increased than depicted in Figure 5.8. Finally, the presence and effect of electrons in the bulk of the system have also been neglected in these calculations.

The electron QW dwell time prior to tunnelling through the collector barrier τ_{C} [111, 120], and the corresponding tunnelling rate w_{C} are determined

by

$$\tau_{\mathrm{C}} = \frac{n_{\mathrm{W}} e}{J_{\mathrm{pk}}} \tag{5.22}$$
$$= 89\,\mathrm{ps},$$
$$w_{\mathrm{C}} = w_{\mathrm{R}} = \tau_{\mathrm{C}}^{-1} \tag{5.23}$$
$$= 11 \times 10^{9}\,\mathrm{s}^{-1},$$

where $J_{\mathrm{pk}} = 270\,\mathrm{A\,cm^{-2}}$ is the current density of the 100 µm diameter RTD mesa, and w_{R} is the tunnelling rate through the emitter barrier at the resonance peak.

Given that the QW relaxation time of an electron via acoustic phonon emission was estimated to be $\tau_{\mathrm{ph}} \approx 1\,\mathrm{ns}$ [111, 112], and hence $\tau_{\mathrm{C}} < \tau_{\mathrm{ph}}$, it cannot be said that this device operates completely via sequential tunnelling. However, as stated previously in Section 5.2, the dominant resonant tunnelling mechanism does not need to be exactly determined to understand the effects of acoustic modulation, given that the energy width in the emitter ($\sim E_{\mathrm{FE}}$) is much greater than that in the QW ($\sim \hbar/\tau_{\mathrm{C}} = 7.4\,\mathrm{\mu eV}$) [99, 106].

5.6 Fast Electrical Measurements

Fast electrical measurements were conducted in accordance with the electrical-optical setup described in Section 3.2.3. The voltage drop recorded across the 50 Ω load resistor shown in Figure 5.6(b) was amplified by two 10 dB amplifiers for various applied voltage biases V_{b}, and these measurements were recorded with a 4 ps resolution averaged 500 times.

The left panel of Figure 5.9 provides the results of these measurements over $V_{\mathrm{b}} = 0.20\,\mathrm{V}$ to $2.50\,\mathrm{V}$ for a pump fluence $W = 12.7\,\mathrm{mJ\,cm^{-2}}$; note that the data is focused on the arrival time of the strain pulse at the RTD $t_0 = z_0/v_{\mathrm{LA}} \approx 58\,\mathrm{ns}$, and a scale corresponding to 0.1 mA is given in the figure. The right panel displays the corresponding I_0-V_{b} characteristic of the device with dotted lines to identify V_{b} for each given measurement; this is dissimilar to the I_0-V characteristic given in Figure 5.7 due to the inclusion of both R and R_{SP}. Thus the voltage bias is applied across the entire circuit in Figure 5.6(b), not just the device, and was taken using the setup depicted in Figure 3.4(a).

As shown in Figure 5.9, below the resonance threshold voltage ($V_{\mathrm{b}} =$

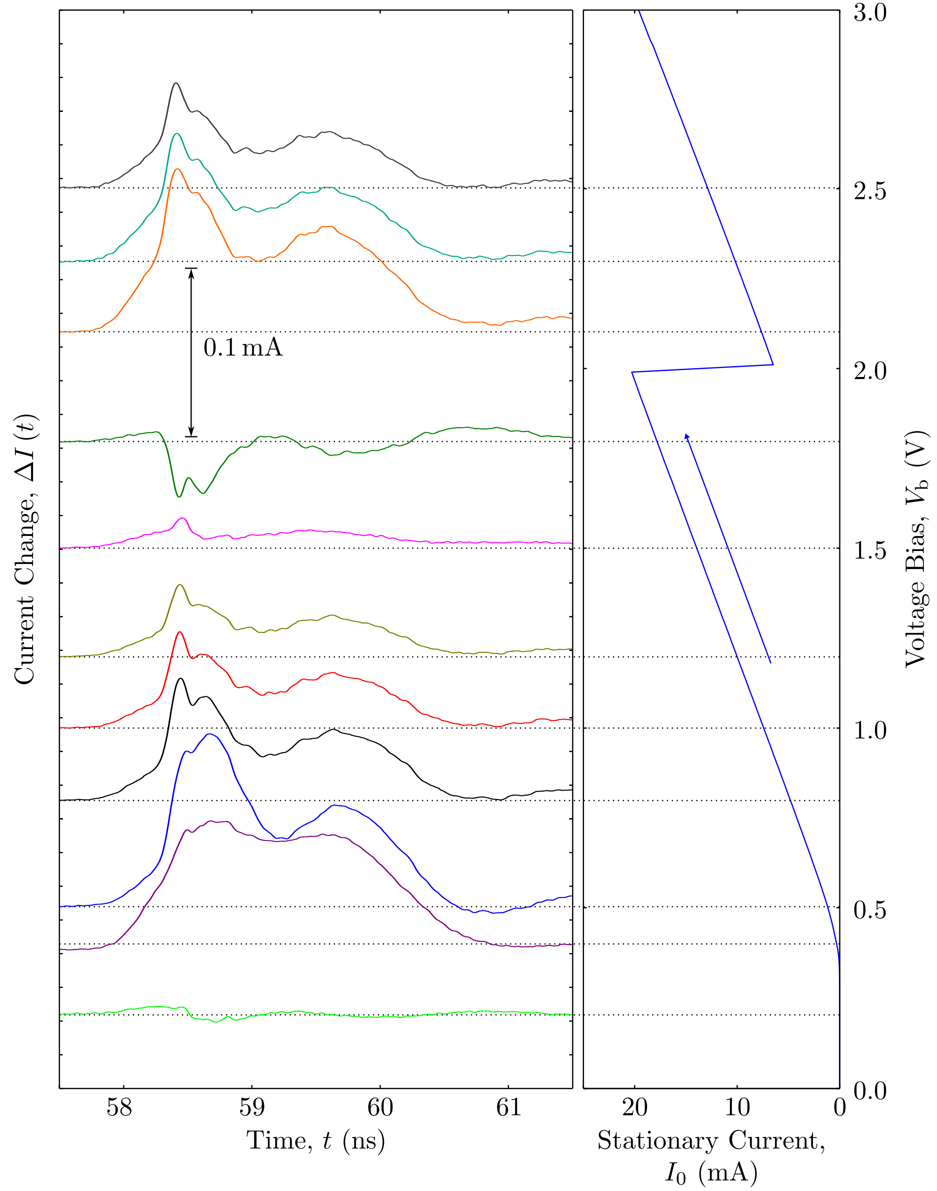

Figure 5.9: Fast electrical measurements conducted on a NU165 100 µm diameter resonant tunnelling diode (RTD) for various applied biases, recorded with 4 ps resolution and 500 averages at a pump beam fluence $W = 12.7\,\mathrm{mJ\,cm^{-2}}$. (left) These measurements indicate that there was a minimal change in current $\Delta I\,(t)$ far from the resonance threshold due the arrival of a strain pulse at $t_0 \approx 58\,\mathrm{ns}$. At the resonance threshold, there was a large increase in $\Delta I\,(t)$ that fell as the system was biased towards the resonance peak, before changing polarity. This was due to the system satisfying the conditions for acoustic modulation at the extremes of threshold and peak biases, given in Section 5.3. Beyond the resonance peak, the signal returned and remained positive. (right) The equivalent stationary current-voltage bias (I_0-V_b) characteristics of the device, which include both the $R = 50\,\Omega$ resistor, and the spreading resistance $R_{SP} = 6\,\Omega$. The dotted lines drawn across both panels indicate the applied bias for the given fast electrical measurement.

0.20 V) there was no change in current $\Delta I(t)$ due to the incoming strain pulse. However, when the system was biased just below the resonance threshold ($V_b = 0.40$ V), the acoustic wavepacket modulated the current, such that a maximum change $\Delta I(t) = 77$ µA was measured. This was even greater just after the threshold ($V_b = 0.50$ V), where $\Delta I(t) = 0.10$ mA was recorded. The modulated current fell between the resonance threshold and peak biases, with $\Delta I(t) = 57$ µA at the mid-resonance point ($V_b = 1.00$ V), to a minimum $\Delta I(t)$ for $V_b = 1.50$ V. Beyond this bias, the signal became negative, with a maximum negative value of $\Delta I(t) = -33$ µA just below the resonance peak ($V_b = 1.80$ V). After the resonance peak, the signal returned to a positive polarity, and remained so for increasing V_b.

The decrease in $\Delta I(t)$ within the resonance biases of the device, and subsequent change in signal polarity, can be explained by the fact that the system is reaching a balance at $V_b = 1.50$ V ($V \approx 0.58$ V) between the two acoustic modulation conditions that are most prominent at the threshold and peak. Specifically, any negative shift near the threshold, i.e. $\Delta(t) - \Delta_0 < 0$, brings the system into resonance and so increases the current, whereas any shift near the peak, i.e. $|\Delta(t) - \Delta_0| < 0$ causes a reduction in current. The signal after the resonance peak was most likely due to strain-induced scattering transitions; this does not form the main conclusion of this work, and thus is not considered further here.

The signal behaviour depicted in Figure 5.9 has already been qualitatively summarised in Section 5.3, and was due to the acoustic modulation of $\Delta(t)$ by the incoming strain pulse. A rigorous mathematical approach to the RTD acoustic modulation will be presented in Sections 5.6.1–5.6.2, including an examination of strain-induced effects, and acoustic modulation of the QW Fermi energy level E_{FW}.

5.6.1 Strain-Induced Effects in a Resonant Tunnelling Diode

The strain-induced effects caused by the wavepacket on the RTD can be calculated by examining the pulse within both the emitter and QW regions. As the strain pulse was also reflected off the free (top surface) after passing through the RTD, the strain pulses in the emitter region η_E and in the QW η_W must include reflected components; the strain pulse in these regions can

be calculated by

$$\eta_{\mathrm{E}}(t) = \eta(t) - \eta(t - t_{\mathrm{R}}), \tag{5.24}$$

$$\eta_{\mathrm{W}}(t) = \eta(t + t_{\mathrm{E}\to\mathrm{W}}) - \eta(t - t_{\mathrm{E}\to\mathrm{W}} - t_{\mathrm{R}}), \tag{5.25}$$

where t_{R} is the propagation time to travel from the active region to the free surface and back [42, 47], and $t_{\mathrm{E}\to\mathrm{W}}$ is the propagation time between the emitter and QW regions. Accordingly, the temporal shift of the detuning parameter $\Delta(t) - \Delta_0$ can be calculated by [20]

$$\Delta(t) - \Delta_0 = \Xi(\eta_{\mathrm{E}} - \eta_{\mathrm{W}}). \tag{5.26}$$

Here, the strain pulses were modelled with the inclusion of an experimental scaling factor Λ in Equation 2.9 to account for experimental setup differences between the present study and the work by Akimov et al. [47], such that

$$\eta(t) = \Lambda \frac{2A_{\mathrm{F}}\zeta_{\mathrm{F}}}{v_{\mathrm{F}}\tau^2}(1 - R_{\mathrm{I}})(t - t_{\mathrm{F}}) \exp\left[-\frac{(t - t_{\mathrm{F}})^2}{\tau^2}\right], \tag{5.27}$$

$$= \eta_0 \frac{\eta(t)}{\|\eta(t)\|}, \tag{5.28}$$

where $\Lambda = 3.0$ for $\tau = 10\,\mathrm{ps}$, η_0 is the initial strain amplitude, and all other parameters are defined as in Equation 2.9; Λ was determined by experimental comparison with simulations. For an initial amplitude of the strain pulse $\eta_0 = 10^{-4}$, the equivalent pump beam fluence was $W = 2.6\,\mathrm{mJ\,cm^{-2}}$. These values were used in conjunction with Equation 5.26 to calculate the strain-induced effects on a RTD, as graphically represented in Figure 5.10 for a deformation potential constant $\Xi = -7\,\mathrm{eV}$ [95].

The polarity of $\Delta(t) - \Delta_0$ in Figure 5.10 agrees with the qualitative explanation given above in Section 5.3, and, if the signal is integrated with respect to time, the strain-induced effect is mainly positive due to signal asymmetry. This figure also shows that this effect occurs on a picosecond timescale, and thus it can be deduced that the net current is also modulated on this timescale, given that

$$\Delta I \propto \Delta(t) - \Delta_0, \tag{5.29}$$

where ΔI is the change in current [20]. In addition, it can be seen that there

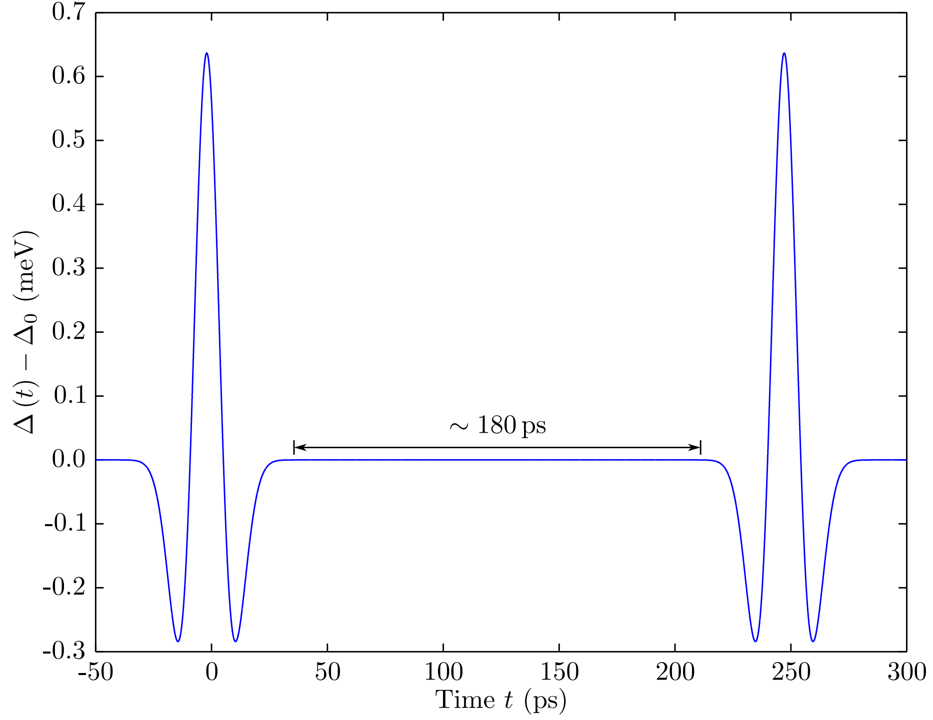

Figure 5.10: Strain-induced shift of energy levels within the emitter and quantum well (QW) regions of a resonant tunnelling diode (RTD). This figure was calculated using Equations 5.24–5.28, and was made for a RTD biased at the resonance threshold using a bipolar strain pulse η with initial amplitude $\eta_0 = 10^{-4}$, and a deformation potential constant $\Xi = -7\,\text{eV}$. The difference between the time-dependent and stationary detuning parameters $\Delta(t) - \Delta_0$ modulates on a picosecond timescale and, although the signal polarity changes, time-integration of the signal provides an overall positive contribution.

is an approximately 180 ps delay between the polarity changes in Figure 5.10, which matches the fast double peak structure in the experimental results presented in Figure 5.9.

5.6.2 Calculation of the Quantum Well Fermi Energy Level

A simple model was employed to simulate the results given in Figure 5.9, and was based on sequential tunnelling analysis of the tunnelling rates through the RTD in the four main conditions considered qualitatively in Section 5.1.

In the zero applied voltage case given in Figure 5.1, E_{FW} is far from the resonance threshold, and therefore $\Delta(t) > E_{\text{FE}}$. Due to this large energy difference, electrons cannot tunnel into the QW, but any QW filled states can be emptied via tunnelling through either the emitter or collector barriers.

Consequently, it can be shown that

$$\Delta n_{\mathrm{W}} = -w_{\mathrm{C}} n_{\mathrm{W}} \Delta t - w_{\mathrm{E}} n_{\mathrm{W}} \Delta t, \tag{5.30}$$

where Δn_{W} is the change in QW electron density n_{W} for a given time interval Δt. The tunnelling rate through the emitter barrier w_{E} was calculated using a Lorentzian resonance profile, according to the Breit-Wigner formula [95, 99, 121, 122], such that

$$w_{\mathrm{E}} = w_{\mathrm{R}} \frac{\Gamma^2}{\Gamma^2 + \Delta^2 (t)}, \tag{5.31}$$

where $\Gamma = 12\,\mathrm{meV}$ is the resonance damping constant, and $w_{\mathrm{R}} = w_{\mathrm{C}} = \tau_{\mathrm{C}}^{-1} = 11 \times 10^9\,\mathrm{s}^{-1}$ from Equation 5.23; the value of Γ was determined by fitting simulations to the experimental data. In the limit of $\Delta t \to \mathrm{d}t$, Equation 5.30 can be reduced using Equation 5.9 to the form

$$\frac{\mathrm{d}E_{\mathrm{FW}}}{\mathrm{d}t} = -\left(w_{\mathrm{C}} + w_{\mathrm{E}}\right) E_{\mathrm{FW}}, \tag{5.32}$$

using Equation 5.9. At the resonance threshold case (Figure 5.2(a)), $\Delta (t) \approx E_{\mathrm{FE}}$, and electrons may tunnel out of the QW, as in Equation 5.32, but can now also tunnel into the well. Thus the tunnelling rate through the emitter barrier is dependent on the energy difference between $\Delta (t)$ and E_{FE}, such that

$$\begin{aligned} \frac{\mathrm{d}E_{\mathrm{FW}}}{\mathrm{d}t} &= -w_{\mathrm{E}} \left(E_{\mathrm{FW}} + \Delta (t) - E_{\mathrm{FE}}\right) - w_{\mathrm{C}} E_{\mathrm{FW}}, \\ &= -\left(w_{\mathrm{C}} + w_{\mathrm{E}}\right) E_{\mathrm{FW}} + w_{\mathrm{E}} \left(E_{\mathrm{FE}} - \Delta (t)\right). \end{aligned} \tag{5.33}$$

Similarly, at the resonance peak (Figure 5.2(b)) $\Delta (t) \approx 0 < E_{\mathrm{FE}}$, but the change in E_{FW} is identical to the resonance threshold, given that

$$\begin{aligned} \frac{\mathrm{d}E_{\mathrm{FW}}}{\mathrm{d}t} &= w_{\mathrm{E}} \left(E_{\mathrm{FE}} - E_{\mathrm{FW}} - \Delta (t)\right) - w_{\mathrm{C}} E_{\mathrm{FW}}, \\ &= -\left(w_{\mathrm{C}} + w_{\mathrm{E}}\right) E_{\mathrm{FW}} + w_{\mathrm{E}} \left(E_{\mathrm{FE}} - \Delta (t)\right). \end{aligned}$$

For the above three cases, $\Delta (t) > 0$ as E_n is always above E_{E0}. However, when the system is biased off resonance (Figure 5.3), $\Delta (t) \leq 0$ as $E_n \leq E_{\mathrm{E0}}$,

although $|\Delta(t)| < E_{\mathrm{FE}}$. Consequently,

$$\begin{aligned}\frac{\mathrm{d}E_{\mathrm{FW}}}{\mathrm{d}t} &= w_{\mathrm{E}}\left(E_{\mathrm{FE}} - E_{\mathrm{FW}} + \Delta(t)\right) - w_{\mathrm{C}}E_{\mathrm{FW}}, \\ &= -\left(w_{\mathrm{C}} + w_{\mathrm{E}}\right)E_{\mathrm{FW}} + w_{\mathrm{E}}\left(E_{\mathrm{FE}} + \Delta(t)\right). \end{aligned} \tag{5.34}$$

The Heaviside step function can be introduced to account for the above four cases given in Equations 5.32–5.34, so that the following general equation was formulated to describe the change in E_{FW}

$$\frac{\mathrm{d}E_{\mathrm{FW}}}{\mathrm{d}t} = -\left(w_{\mathrm{C}} + w_{\mathrm{E}}\right)E_{\mathrm{FW}} + \left(E_{\mathrm{FE}} - \Delta(t)\right)w_{\mathrm{E}}\left\{H\left[E_{\mathrm{FE}} - \Delta(t)\right]\right\} \tag{5.35}$$

where

$$H\left[E_{\mathrm{FE}} - \Delta(t)\right] = \begin{cases} 0, & \text{if } \Delta(t) > E_{\mathrm{FE}}, \\ 1, & \text{if } \Delta(t) \leq E_{\mathrm{FE}}. \end{cases}$$

The solution to Equation 5.35 was calculated using an ordinary differential equation solver script written in MATLAB®. The change in current $\Delta I(t)$ due to n_{W} and E_{FW} can be determined from considering tunnelling of charge through the collector barrier, such that

$$\Delta I(t) = \omega_{\mathrm{C}} n_{\mathrm{W}} e A_{\mathrm{W}} = \omega_{\mathrm{C}} \frac{m^* E_{\mathrm{FW}}}{\pi\hbar^2} e A_{\mathrm{W}}, \tag{5.36}$$

where A_{W} is the device area. The resultant simulations determined from Equations 5.35 and 5.36 are considered alongside relevant experimental data in Section 5.6.3.

5.6.3 Acoustic Modulation of Current

Fast electrical measurements were conducted over a range of pump beam fluences $W = 1.3\,\mathrm{mJ\,cm^{-2}}$ to $17.8\,\mathrm{mJ\,cm^{-2}}$ in addition to those depicted in Figure 5.9. The experimental results for the highest fluence are shown alongside corresponding simulations in Figure 5.11 when the device is biased at the resonance threshold, mid-resonance, and resonance peak.

The data depicted in Figure 5.11(a) has a similar shape to those seen previously for $W = 12.7\,\mathrm{mJ\,cm^{-2}}$, with a characteristic double peak structure just after the arrival time of the strain pulse (58.25 ns to 58.75 ns) regardless of applied bias. For each of these biases, there was a significant change in

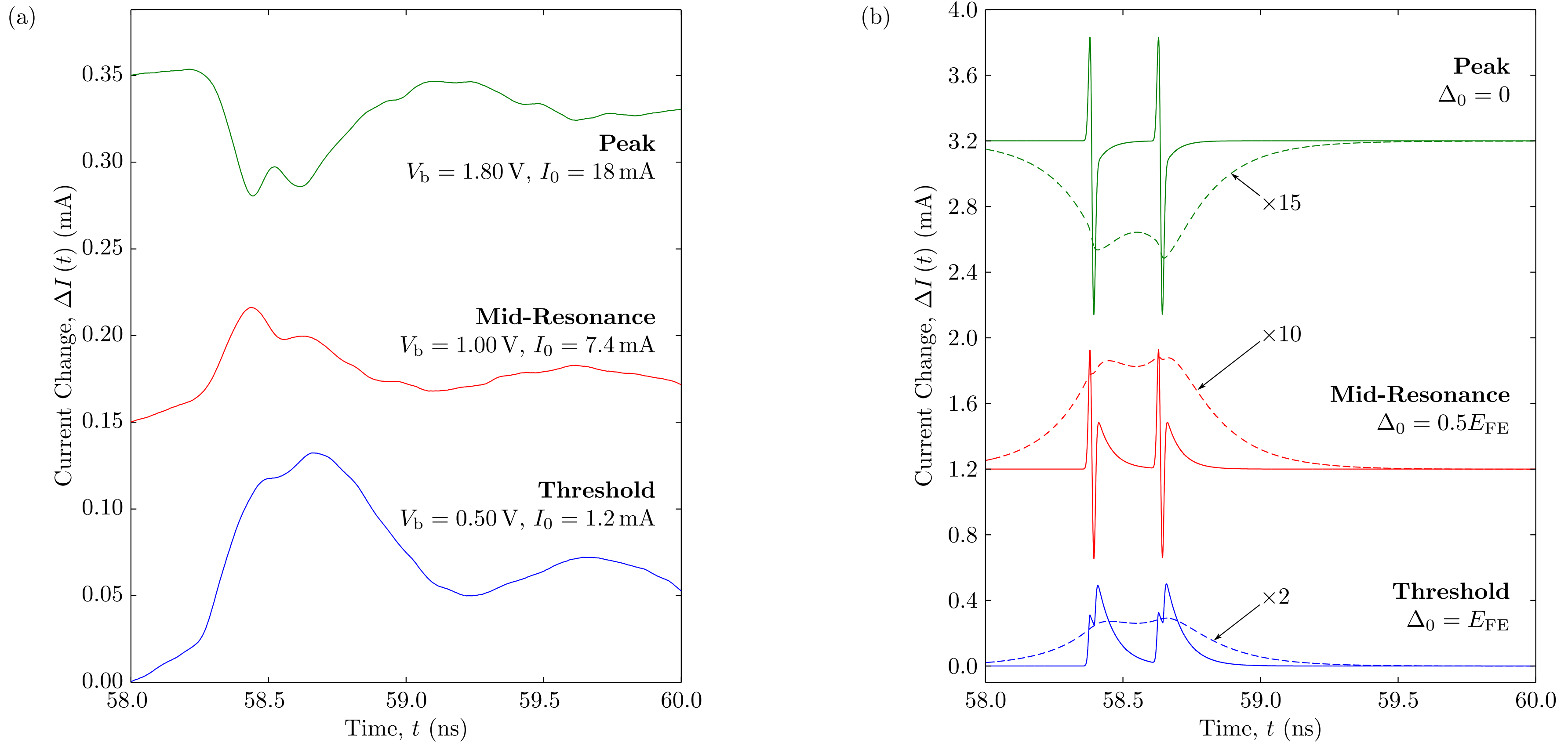

Figure 5.11: (a) Experimental and (b) simulated results for current change due to acoustic modulation in a resonant tunnelling diode (RTD) $\Delta I\,(t)$ against time at the resonance threshold, mid-resonance, and resonance peak. (a) The relative current change ranges from 12 % at the threshold to 0.36 % at the peak, with finer structure resolvable in the latter. (b) The simulations were generated by solving Equation 5.35 numerically, and reflect the experimental data albeit with greater resolution and structure. The current values differed due to the limited temporal response of the experiment, which was mimicked by low-pass Butterworth filtering the signal with a 1 GHz frequency cutoff, as shown by the dashed lines with corresponding magnifications labelled.

current due to acoustic modulation that amounted to 12 % at the resonance threshold, 1.0 % at mid-resonance, and 0.36 % at the resonance peak for the maximum fluence.

The temporal delay between the double peak structure is approximately 170 ps to 175 ps at the resonance threshold and peak biases, respectively, and was attributed to propagation time of the strain pulse from the device to the free surface and back. This was estimated to be approximately 180 ps, as labelled in Figure 5.10, when accounting for the width of the strain pulse, and therefore the strain-induced effect. The most pronounced double peak structure was found when the system was biased at the resonance peak, which provides evidence of sub-nanosecond current modulation by acoustic pulses. The other slowly varying oscillations that occur in the signal profile with approximately 1 ns separation were due to ringing effects in the external circuit, and are considered in more depth later in this section.

The solutions to Equation 5.35 for the equivalent situations of resonance threshold ($\Delta_0 = E_{\mathrm{FE}}$), mid-resonance ($\Delta_0 = 0.5E_{\mathrm{FE}}$), and resonance peak ($\Delta_0 = 0$) are displayed in Figure 5.11(b). Here, there was a fast temporal response to the incident strain pulse given in Figure 5.10 in the order of 1 ps to 10 ps that led to changes in signal polarity at mid-resonance and the resonance peak. Also, there were two strain-induced interactions due to the incident and reflected strain pulses with a delay equivalent to that seen experimentally. This supports the previous supposition that the double peaked structure was due to an additional interaction with the returning strain pulse from the free surface. In addition, the simulations reflect the differences between the experimental data sets with regards to both polarity and resolution. Specifically, the model indicated that the resonance threshold signal would be definitively positive in polarity, the mid-resonance signal would also be positive overall, and the total contribution at the resonance peak would be negative.

Furthermore, at the resonance threshold and mid-resonance, the simulations calculated that there would not be the finer structure evident in the resonance peak, due to the integration of the signal by the temporal response of the circuit. This temporal response also limited the amount of current measured in the system, hence the differences in the experimentally obtained and numerically calculated data; this slow temporal response was mimicked by applying a low-pass Butterworth filter with a 1 GHz frequency cutoff, and is shown by the magnified, dashed lines in Figure 5.11(b). Consequently, to

remove this hindrance, it was more useful to consider the charge transferred in the RTD due to acoustic modulation rather than the current changes, as detailed in Section 5.6.4.

Ringing in the Experimental Setup

In Figure 5.11(a), a slowly oscillating signal was present after the arrival of the strain pulse with a time period of approximately 1 ns. This 1 GHz signal was not found in the simulated results based on the model given in Section 5.6.2, and can be more clearly seen when examining a larger segment of the data, such as that shown in Figure 5.12(a) for the same threshold signal as in Figure 5.11(a).

Here, it is clear that a 1 GHz signal is superimposed upon the decaying tail of the signal (dashed, red line), and it was determined that this ringing signal was generated from parasitic components of the device. The AC equivalent circuit of the RTD biased near the resonance threshold is given in Figure 5.12(b) based on Miles et al. [123]. In this figure, the D and P subscripts denote device and parasitic components, respectively, where the former is bias dependent, whilst the latter is not and originates from the device packaging and mounting. The values for these components were estimated from the device structure and packaging to be $R_{\mathrm{P}} = 0.2\,\Omega$, $L_{\mathrm{P}} = 17\,\mathrm{nH}$, $C_{\mathrm{P}} = 1\,\mathrm{pF}$, $C_{\mathrm{D}} = 16\,\mathrm{pF}$, and $R_{\mathrm{D}} = 10\,\Omega$. By examining the parallel impedance of this equivalent circuit, a resonance frequency of $\sim 1\,\mathrm{GHz}$ was determined, hence verifying that which is seen experimentally[2].

[2]See *Supplementary Material* in Young et al. [95].

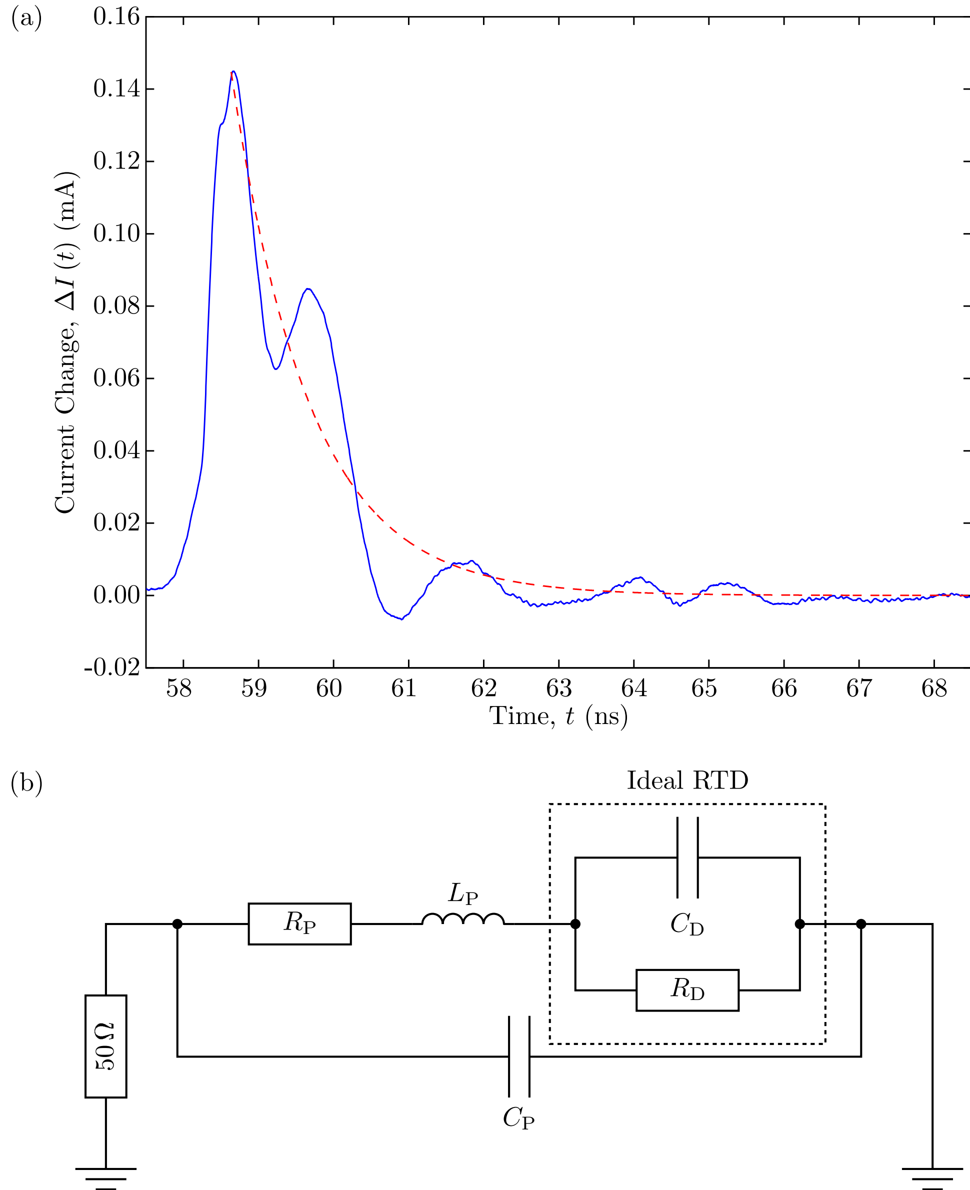

Figure 5.12: (a) Current change $\Delta I\,(t)$ against time t in a 10 ns window after the arrival time of the strain pulse and (b) the AC equivalent circuit of the resonant tunnelling diode (RTD). (a). An approximately 1 GHz oscillation is superimposed on the RTD signal (dashed, red line) due to ringing effects caused by the circuit shown in (b), where the D and R subscripts denote device and parasitic components, and $R_\mathrm{P} = 0.2\,\Omega$, $L_\mathrm{P} = 17\,\mathrm{nH}$, $C_\mathrm{P} = 1\,\mathrm{pF}$, $C_\mathrm{D} = 16\,\mathrm{pF}$, and $R_\mathrm{D} = 10\,\Omega$ just below the resonance threshold.

5.6.4 Picosecond Charge Transfer and the Acousto-electronic Pumping Effect

As above mentioned in Section 5.6.3, by examining the charge transferred due to strain-induced effects, the temporal response no longer becomes a limiting factor in the analysis. The total charge transferred across the RTD ΔQ is given by

$$\Delta Q = \int_{t_i}^{t_f} \Delta I\left(t\right) \mathrm{d}t, \tag{5.37}$$

where $t_i = 58\,\mathrm{ns}$ and $t_f = 59\,\mathrm{ns}$ are the initial and final time values for the integration window. The charge transferred for both the experimental and modelled data for the entire range of pump beam fluences $W = 1.3\,\mathrm{mJ\,cm^{-2}}$ to $17.8\,\mathrm{mJ\,cm^{-2}}$ is graphically represented in Figure 5.13.

An examination of both the experimental and theoretical charge dependencies in Figures 5.13(a) and 5.13(b), respectively, shows that the model matches well to the experimental results, where $W = 17.8\,\mathrm{mJ\,cm^{-2}}$ is equivalent to $\eta_0 = 6.8 \times 10^{-4}$, and transferred approximately 97 fC at the resonance threshold. This confirmed the validity of the simple model given in Section 5.6.2, and allows estimates of charge transfer in a real device to be made from it.

Figure 5.13 also demonstrates that these dependencies are generally non-linear in the RTD. This is due to the bipolar nature of the strain pulse, which when integrated with respect to time is zero, and the fact that current modulation is dependent on the strain-induced effects. The exception is at the resonance threshold, where the simulation provides a linear dependence on ΔQ with η_0, which is reflected experimentally for $W > 2.6\,\mathrm{mJ\,cm^{-2}}$; below this fluence, the weak super linear behaviour is considered to be due to thermal smearing of the electrons at low temperatures [95]. The exception arises due to the fact that only $\Delta\left(t\right) - \Delta_0 < 0$ has a modulating effect on the current, and therefore the charge, at the threshold. As such, there is a "rectifying" effect in the system that is linear to the strain pulse amplitude.

In spite of these linearity and non-linearity differences in charge transfer, the polarity of the signals remains clearly positive or negative at the extremes of resonance threshold and peak. Thus it could be considered that, at these extremes, a RTD can be used to transfer charge on a picosecond timescale in a "rectifying" manner, analogous to a mechanical pumping. In this analogy,

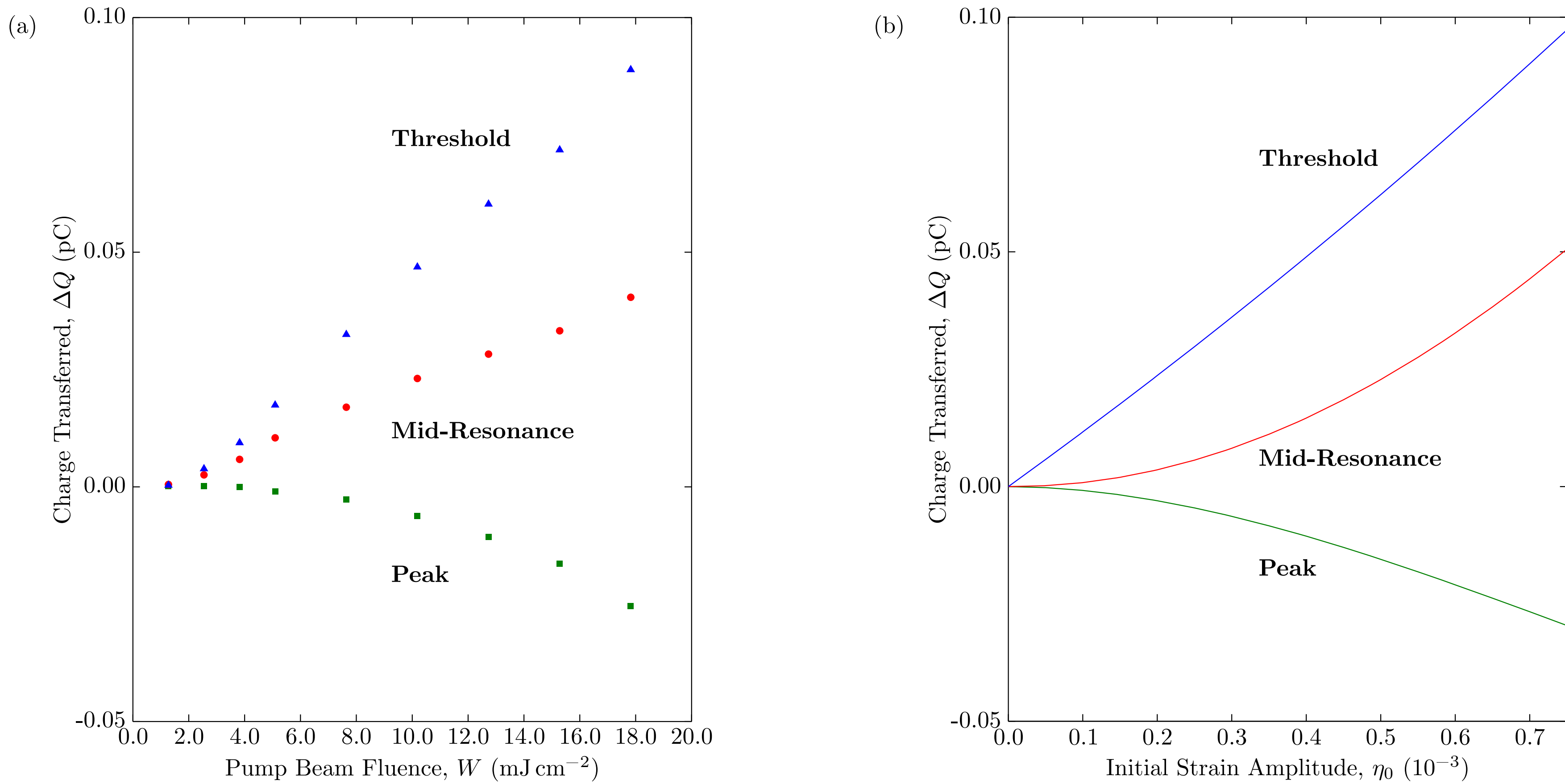

Figure 5.13: (a) Experimental and (b) simulated charge transfer across a resonant tunnelling diode (RTD) due to strain-induced effects. At $W = 17.8\,\mathrm{mJ\,cm^{-2}}$, equivalent to $\eta_0 = 6.8 \times 10^{-4}$, $\Delta Q = 97\,\mathrm{fC}$ was transferred. The overall shape and linearity/non-linearity of the two figures matches well, thus validating the simple model expressed in Section 5.6.2. The figures also indicate that picosecond charge transfer is possible, with a set polarity of the signal at the extremes of threshold and peak leading to "rectification" of the signal, and the *acoustoelectronic pumping effect*.

a mechanical pump admits and expels fluid when it is moving forwards and backwards respectively, whilst in the RTD charge is admitted and expelled when E_n is shifted closer to or further from E_{E0}, hence we have called this effect the *acoustoelectronic pumping effect*.

5.7 Conclusions

The discussions presented in this chapter have shown that sub-THz acoustic pumping of charge across a RTD is possible. Estimates of the amount of pumped charge can be made from the simple model presented in Section 5.6.2, and it was demonstrated that this amount could be controlled by varying either the applied voltage across the device, and/or the strain amplitude.

At high strain amplitudes, the experimental results indicated that acoustic modulation of the device resulted in greater than 10 % increase of carriers tunnelling through the barriers at the resonance threshold, and these results were supported by the model. As the sign of the charge transfer remains constant regardless of strain amplitude, it can be considered that acoustic modulation of the RTD is “rectifying”. This is due to exploitation of the non-linear I_0-V characteristics of the device and, in conjunction with its sub-nanosecond temporal resolution, it is possible to use this device either as a hypersonic detector or as a method of charge control, as the *acousto-electronic pumping effect* could be utilised in integrated acoustoelectronic devices.

Given the significant effects in this experiment, it is clear that the next logical development of this work would be to examine increasingly confined nanostructures, such as a double barrier quantum dot (QD) resonant tunnelling diode. Preliminary studies have been conducted on such a nanostructure, and the initial limitations and difficulties found in these studies are considered further in Section 6.1.3.

Chapter 6

Conclusions and Potential Future Research

In the initial chapters of this thesis, previous research conducted into ultrafast acoustic strain effects in nanostructures were discussed alongside general theoretical background knowledge. This background covered the various mechanisms required to comprehend the underlying phonon processes that allow for the observed strain effects, of which the deformation potential electron-phonon coupling mechanism is the most relevant for the current body of work.

Chapter 3 broadly reported microfabrication techniques that were essential for the processing of viable samples for the thesis. In addition, this methodology chapter also divulged the circuitry and electrical-optical experimental configurations utilised to conduct transport, photocurrent pump-probe, and fast electrical measurements. The latter two measurements were conducted using a Ti:Sapphire amplified laser system with the sample maintained at 4.7 K with liquid He in an optical flow cryostat.

Strain generation methods in a bulk GaAs transducer were investigated in Chapter 4 using the aforementioned photocurrent pump-probe technique. This transducer was pumped with ultrafast 400 nm wavelength optical pulses, and the coherent phonons were remotely and electrically probed using a hypersonic detector. This detector comprised a double quantum well (QW)-embedded *p-i-n* diode photoexcited with ultrafast 800 nm wavelength optical pulses, where the rate of photoexcitation, and therefore photocurrent, could be acoustically modulated by exploiting the piezospectroscopic effect. Consequently, the change in photocurrent provided a direct electrical method

of detecting the propagated strain pulse, as determined in Moss et al. [19] and Moss et al. [20].

From these investigations, it was determined that a combination of the deformation potential and thermoelasticity was responsible for strain generation in bulk GaAs. Specifically, a strongly asymmetrical pulse with a damped leading edge was remotely resolved in measurements at low fluences, whereas an asymmetric signal with multiple solitons in its leading edge was observed after propagation at high fluences; the presence of solitons and other non-linear effects in the latter case denoted the generation of an initially ultrafast acoustic wavepacket in the GaAs transducer. Both these linear and non-linear cases were correlated directly to a strongly asymmetrical initial strain pulse that was generated predominantly by the deformation potential and thermoelastic effects, respectively, in a supersonically expanding electron-hole (e-h) plasma. The ratio of compressive to tensile amplitude of this initial asymmetric pulse was calculated to be $M_0^{\mathrm{GaAs}} = 6.3$ for a e-h plasma ambipolar diffusivity $D = 4\,\mathrm{cm}^2\,\mathrm{s}^{-1}$, with a leading edge duration of between 8.2 ps to 15.5 ps; this is much larger than the expected ~ 3 ps leading edge duration of initially bipolar strain pulses formed in a static region, such as those found for thin metal films.

The e-h plasma was photogenerated in GaAs as part of the opto-acoustic conversion of the incoming laser pump pulse. Various properties of this plasma result in the generation of the acoustic pulse, including modifications of the interatomic interactions, instantaneous carrier relaxation, and non-radiative recombination of e-h pairs. Initially, the plasma velocity exceeded the GaAs longitudinal acoustic (LA) velocity, and so the generated acoustic waves could not escape the plasma waves until the latter had decelerated to subsonic velocities. It is for this reason that the experimentally detected signals were numerically determined to possess strongly asymmetric initial strain pulses. The profile of these initial strain pulses was based on a deformation potential model theorised by Gusev [91], with propagation simulated numerically using the Korteweg-de Vries-Burgers (KdV-Burgers) equation solved with a composite Runge-Kutta algorithm. These simulated propagations fitted the experimental data excellently, but an examination of the recombination times and duration of the leading edge revealed stark differences between the linear and non-linear regimes.

In the linear regime, the recombination rate increased linearly with fluence, whilst the leading edge duration remained relatively constant. Con-

versely, these rates increase with square-law behaviour and near-linearly, respectively, in the non-linear regime. By showing that both instantaneous relaxation and non-radiative recombination of the *e*-*h* pairs were negligible in the linear regime, it was deduced that the deformation potential was the main strain generation mechanism in bulk GaAs transducers at these low fluences. As non-radiative recombination is dependent on plasma density, it cannot be ignored at high fluences, where the exhibited square-law behaviour indicated that this was predominantly due to Auger processes. Accordingly, it was reasoned that thermoelasticity was the dominant mechanism for strain pulse generation in the non-linear regime.

In Chapter 5, a novel hypersonic detector was discovered using a well-known device, the resonant tunnelling diode (RTD), which comprised a double barrier structure encompassing an effective QW. The chapter established the basic operational principles of the device in the absence of strain to provide a full description of its characteristics; this included a general overview of the resonant tunnelling mechanism, described by a sequential tunnelling model, and other phenomena, such as space-charge buildup and bistability. This progressed to a qualitative discussion of acoustic modulation of the RTD by exploiting the piezospectroscopic effect, which could in turn directly affect the amount of resonant tunnelling. The effect was most pronounced when the device was biased at the resonance threshold and peak, where small strain-induced shifts in the active region energy levels resulted in large changes in resonant tunnelling rates, and therefore measured current/charge transfer.

Various parameters were analytically calculated from transport measurements of the device, such as the maximum QW electron density, and the tunnelling time through the collector barrier (QW dwell time). Fast electrical measurements were conducted on a RTD, where strain pulses were generated by optically transducing an Al film at a remote distance from the device itself. The results indicated no change in the current below the resonance threshold, but a significant current modulation within the resonance region; at the maximum pump fluence, changes of 12 % and 0.36 % were recorded at the resonance threshold and peak, respectively.

A theoretical model using the abovementioned stationary parameters was formulated by considering tunnelling in the system, and the simulated signals from this model displayed features that matched the experimental data, such as a doublet corresponding to interaction of the device with

the incident and reflected strain pulses. Finer features in the simulated signals were not observed in experiment, as the limited temporal response of the device and ringing in the electrical circuit reduced the resolution of the measurement. To remedy the former problem, the current signals were integrated with respect to time to obtain the total charge transferred across the RTD; the experimental and simulated outcomes matched excellently with one another, thus providing a simple model to estimate the charge transferred across a RTD due to strain-induced effects. It was noted that the polarity of the signal at the extremes of resonance threshold and peak remained static, leading to a "rectifying" effect in the system at these biases. From these observations, an analogy between charge transfer in a RTD and mechanical pumping of fluid was made, and this effect was named the *acoustoelectronic pumping effect*. Thus by demonstrating that a RTD was susceptible to strain-induced effects on a picosecond timescale, it was shown that such a device could be used suitably as either a hypersonic detector or as a method of charge control by exploiting the *acoustoelectronic pumping effect* described herein.

The ultrafast acoustic strain generation and effects in the semiconductor nanostructures disclosed in this thesis clearly show that the deformation potential and thermoelasticity are competing mechanisms for strain generation within a supersonically expanding *e-h* plasma in a GaAs transducer, and that a RTD can be applied to strain detection and picosecond charge transfer control.

6.1 Potential Future Research

The present work gives rise to many potential future research projects related to strain generation and detection methods that are disclosed in this section. These include RTD charge transfer by strain generated in bulk GaAs, and charge transfer in further reduced dimensions of RTDs, such as in quantum wire (QWR) and quantum dot (QD) RTD structures. Both these potential projects are discussed briefly in Sections 6.1.1 and 6.1.2, respectively. Preliminary electrical-optical measurements on a QD RTD have already been conducted, and suggestions for improvements and advancements in this research are provided in Section 6.1.3.

6.1.1 Asymmetric Strain Pulse Effects on a Resonant Tunnelling Diode

Strain-induced effects in a RTD for a given initial strain pulse can be estimated by applying Equation 5.26, as graphically represented in Figure 5.10 for a 100 nm thick Al film transducer. The acoustic modulation shown in this figure was formed from a bipolar strain pulse, and it would be interesting to observe the effects that an asymmetric strain pulse has on the RTD itself, as disclosed for bulk GaAs transduction in Chapter 4.

By applying identical methods as in Section 5.6.1 to an initially asymmetric strain pulse, the resultant strain-induced shift is given by Figure 6.1. Here, the modelled pump beam fluence[1] is $W = 0.2\,\mathrm{mJ\,cm^{-2}}$ for an emitter to QW propagation time $t_{\mathrm{E}\to\mathrm{W}} = 4\,\mathrm{ps}$, and deformation potential constant $\Xi = -7\,\mathrm{eV}$; note that only the strain-induced effect from the incident pulse is depicted. It is clear from this figure that the majority of the strain-induced shift is positive, with an almost rectangular profile for $t \approx t_{\mathrm{E}\to\mathrm{W}}$. It also possesses sharp spikes at the beginning and end of this profile, where the first of these spikes is positive, and the second is distinctly negative.

As observed previously in Chapter 5, a strain pulse induces effects in a typical RTD when the device is biased within its resonance region, with the most pronounced effects occurring at the extremes of resonance peak and resonance threshold. At these extremes, and as a consequence of the conditions discussed in Section 5.6, it could be predicted that a current change profile similar to that shown in Figure 6.1 will be recorded at the resonance peak, i.e. a sudden but constant current change over a duration of $\sim t_{\mathrm{E}\to\mathrm{W}}$, since any acoustic modulation reduces the amount of resonant tunnelling. Furthermore, at the resonance threshold, only the sharp negative spike and its subsequently damped tail will have an effect, given that only strain-induced shifts towards resonance cause current changes; this would result in a sharp increase of current over a short duration. It would follow that the consequential charge transferred across the diode would have a relatively large decrease or small increase depending on which of the biases is applied to the device.

[1]Based on the initial strain pulse given in the insert of Figure 4.7(a).

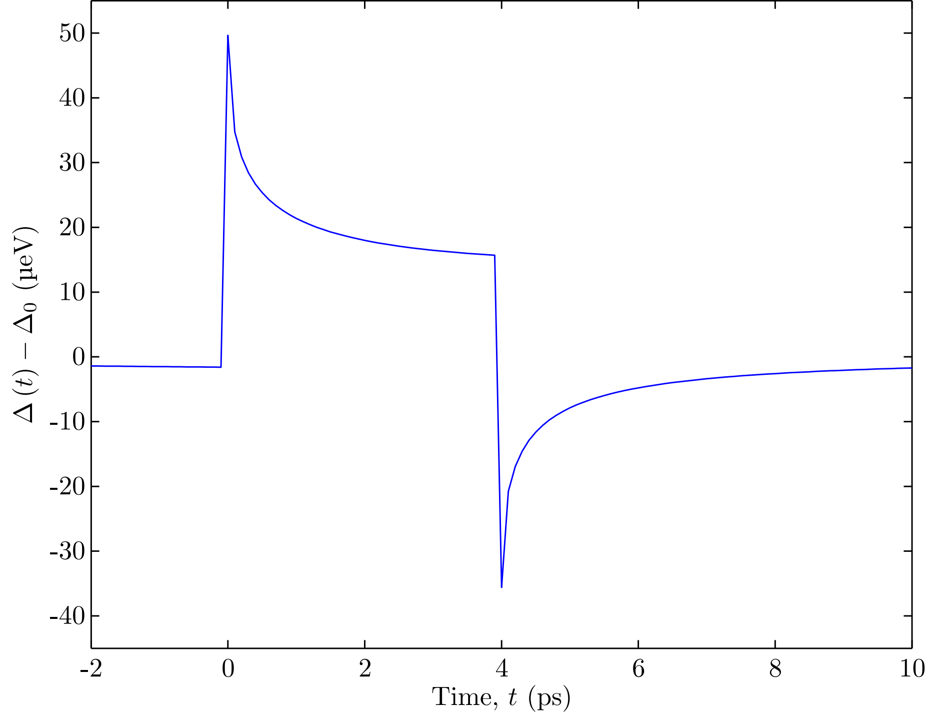

Figure 6.1: Strain-induced shift ($\Delta(t) - \Delta_0$) modelling of a highly asymmetric strain pulse transduced from bulk GaAs ($M_0^{\mathrm{GaAs}} = 6.3$) in a resonant tunnelling diode (RTD). The propagation time from the emitter to the quantum well (QW) is $t_{\mathrm{E}\to\mathrm{W}} = 4\,\mathrm{ps}$, for a deformation potential constant $\Xi = -7\,\mathrm{eV}$, and electron-hole (e-h) plasma ambipolar diffusivity $D = 4\,\mathrm{cm}^2\,\mathrm{s}^{-1}$. The signal shows a mainly positive rectangular profile, with sharp spikes at the beginning and end of this profile. The entire signal should be replicated in experimental current changes when the device is biased at the resonance peak, whereas only the negative spike should appear when biased at the resonance threshold, in accordance with the conditions discussed in Section 5.6.

6.1.2 Acoustoelectronic Pumping in Other Resonant Tunnelling Structures

A natural extension of the work in Chapter 5 is to examine strain-induced effects in more confined nanostructures, such as in QWRs and QDs, and to ascertain the *acoustoelectronic pumping effect* in these structures. Resonant tunnelling in these confined nanostructures has been confirmed in other works, where the devices all exhibit non-linear stationary current-voltage (I_0-V) characteristics that could be exploited by strain-induced effects.

In a double barrier QWR resonant tunnelling diode [110, 124–126], carriers are confined to only one dimension that is perpendicular to the growth plane of the wafer, and so can only fill the QWR subband. Therefore it would be expected that resonant tunnelling would firstly generate smaller current changes for a given strain amplitude, and secondly be more sensitive to strain-induced shifts due to the comparably narrower energy width of the

	NU2217 Wafer Profile		
	Material	**Thickness (nm)**	**Doping (cm^{-3})**
TC	n-GaAs	500	2×10^{18}
C	n-GaAs	50	2×10^{17}
S	GaAs	20	–
W	p-InAs	0.389	4.5×10^{18}
S	GaAs	4	–
B	$Al_{0.4}Ga_{0.6}As$	4	–
QD	InAs	0.574	–
B	$Al_{0.4}Ga_{0.6}As$	3	–
S	GaAs	40	–
BE	n-GaAs	1000	2×10^{18}
	375 µm n-GaAs Substrate		

Table 6.1: Wafer profile for NU2217 double barrier quantum dot (QD) resonant tunnelling diode (RTD) samples. This wafer was grown by Mohamed Henini at the University of Nottingham by molecular beam epitaxy (MBE). It comprised a bottom contact/emitter layer (**BE**), several spacer layers (**S**), two $Al_{0.4}Ga_{0.6}As$ barriers (**B**) encompassing a layer (**QD**) of InAs quantum dots (QDs), p-doped wetting layer (**W**), collector region (**C**), and top contact layer (**TC**).

QWR subband than in an equivalent QW structure.

A QD resonant tunnelling diode [127–132] completely confines each carrier into a single given energy state. By examining this zero-dimensional structure, it may be possible to control single charge transfer by an ultrafast acoustic wavepacket. Preliminary attempts were made at conducting such experiments, as discussed in Section 6.1.3, although the results were inconclusive due to equipment limitations; the QD samples used in these experiments were kindly provided by Oleg Makarovsky, who located individual QDs active in tunnelling at low device voltage.

6.1.3 Quantum Dot Resonant Tunnelling Diode

Preliminary measurements were conducted on a double barrier QD RTD sample from wafer NU2217 grown via molecular beam epitaxy (MBE) by Mohamed Henini at the University of Nottingham; the growth profile of this wafer is shown in Table 6.1.

NU2217 was grown on a 375 µm thick n-doped GaAs substrate with a 1 µm thick n-GaAs bottom contact/emitter layer (**GE**), Si-doped to a concentration of $2 \times 10^{18}\,cm^{-3}$. An undoped 40 nm thick GaAs spacer layer (**S**) separated this contact layer from the active region, which began with two undoped $Al_{0.4}Ga_{0.6}As$ barriers (**B**) of thickness 3 nm and 4 nm each,

encompassing a 5.74 Å layer of InAs QDs (**QD**). The QDs have a random spatial distribution and, across the wafer, have an average QD areal density $n_{\mathrm{QD}} = 2 \times 10^{11}\,\mathrm{cm}^{-2}$.

An additional spacer layer (**S**) of 4 nm thick undoped GaAs separated the barriers from the wetting layer (**W**) consisting of *p*-InAs, Be-doped to a concentration of $4.5 \times 10^{18}\,\mathrm{cm}^{-3}$ to conclude the active region; this wetting layer allowed for the formation of the self-assembled QDs [133] and for easier tunnelling of electrons out of the QDs [132]. An additional 20 nm undoped GaAs spacer layer (**S**) separated the wetting layer from the 50 nm thick *n*-doped GaAs collector region (**C**), which had a doping concentration of $2 \times 10^{17}\,\mathrm{cm}^{-3}$. The growth was completed with a final 500 nm thick *n*-GaAs top contact layer (**TC**) with a Si concentration of $2 \times 10^{18}\,\mathrm{cm}^{-3}$.

Samples from this wafer were processed at the EPSRC National Centre for III-V Technologies at the University of Sheffield, and consisted of 25 µm diameter cylindrical optical mesas. Due to the relatively small size in comparison to the Al bond wire, an insulating layer coated the majority of the exposed bottom contact, and $200 \times 200\,\mu\mathrm{m}$ offset bond pads were evaporated onto this insulator so that electrical connection to the top and bottom contacts could be made without damaging or short circuiting the device, as shown by the photograph and sketch in Figure 6.2.

As aforementioned, transport measurements had been conducted on these samples prior to testing of strain-induced effects by Oleg Makarovsky, which determined viable single QD devices. An individual QD is required in this experiment, since acoustic modulation of multiple QDs would have a net effect of transferring an equivalent amount of carriers across the RTD; experimental methods and theory behind the location of these individual QDs at low bias voltages has been disclosed elsewhere [127, 130, 133, 134]. This search was ameliorated by processing small devices to reduce the number of QDs at each given voltage bias and in each given device, and therefore increased the likelihood of finding individual QD devices. To adapt the sample for ultrafast acoustic experiments, the rear (substrate-exposed) side of the sample was first polished using the processes described in Section 3.1.1, before a 30 nm thick Al film was deposited by thermal evaporation to act as an acoustic transducer.

The samples had been already scribed so that they were $1.5 \times 2.0\,\mathrm{mm}$ in size prior to acquisition. Accordingly, a variant of the sample holder in Figure 5.6(a) was designed, and this is sketched alongside the experimental

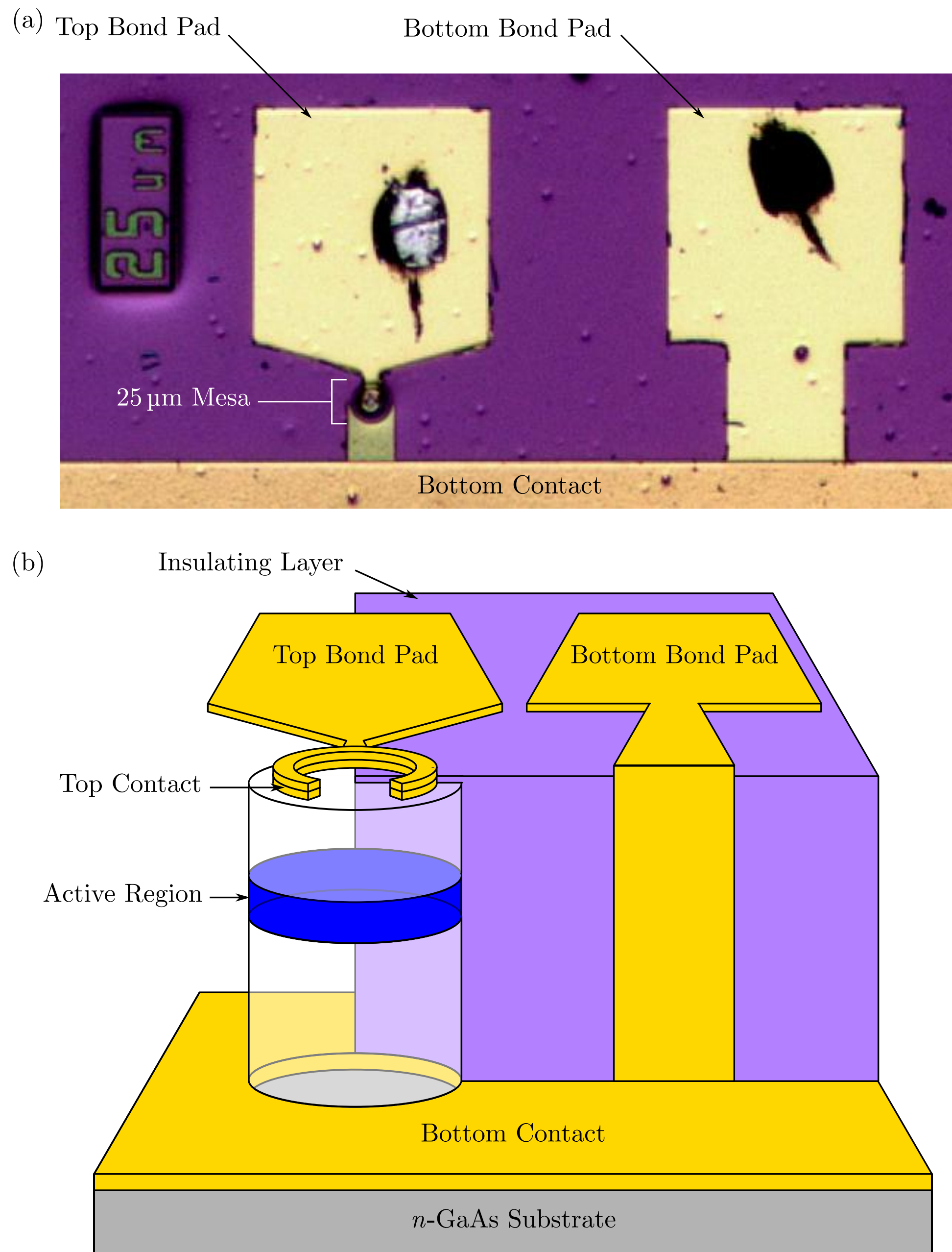

Figure 6.2: (a) Top-down photograph and (b) side-on, cutaway sketch (not to scale) of samples processed from wafer NU2217. The diameter of the protruding cylindrical mesa was 25 µm, and so complicated wire bonding of the top contact. To alleviate this problem, an insulating layer was deposited onto the majority of the bottom contact, leaving only the top contact and a small area for bottom contact bonding exposed. A secondary deposition of bond pads that were offset from the device provided sufficient surface area for wire bonding of the contact layers without damaging or short circuiting the devices.

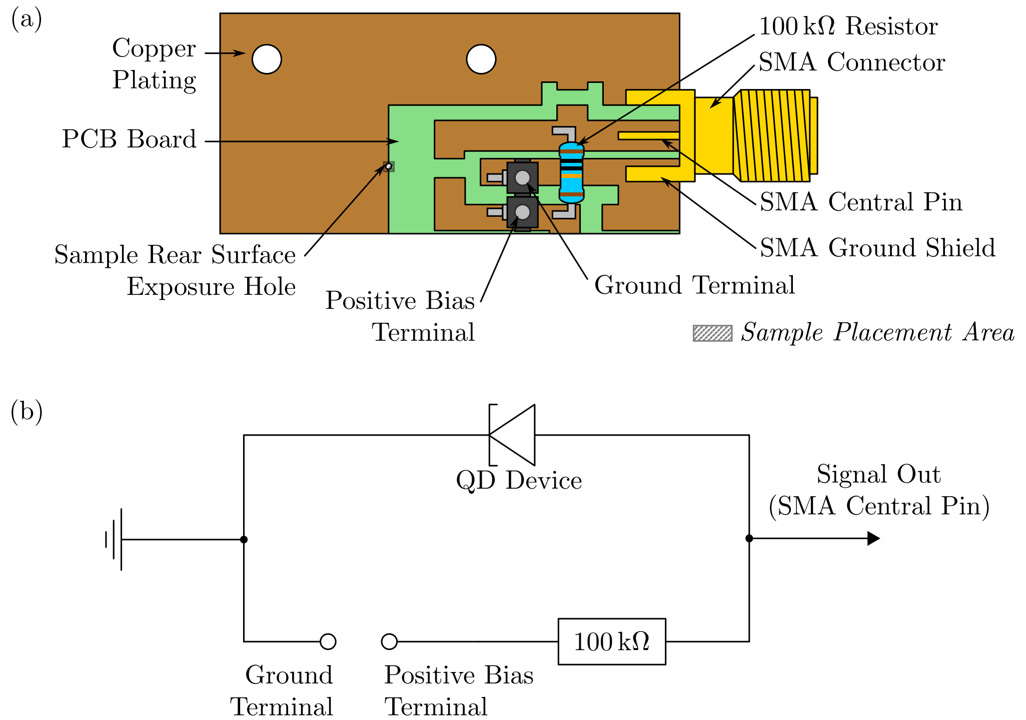

Figure 6.3: (a) Sample holder and (b) circuitry used to conduct transport and preliminary electrical-optical measurements on a sample processed from wafer NU2217. A 100 kΩ resistor was mounted onto the board, and the top and bottom contacts of the device were bonded to the copper plate connected to the SMA central pin and ground shield, respectively.

circuit diagram given in Figure 6.3. The relatively small size of the sample provided some difficulty in preventing stray reflections from interacting with the QD, as discussed later in this section.

Transport Measurements

Transport measurements conducted on this sample in dark conditions revealed the presence of an individual QD located at a device voltage $V_b \approx 91.0\,\text{mV}$, as represented by the solid, blue line in Figure 6.4. These stationary current-voltage bias (I_0-V_b) characteristics were taken using the system depicted in Figure 3.4(a) over a resistor $R = 100\,\text{k}\Omega$.

However, under $62.1\,\mu\text{J}\,\text{cm}^{-2}$ continuous-wave (CW) illumination by the oscillator system previously described in Section 4.2, the voltage of the QD shifted by approximately $\Delta V_b = 3.91\,\text{mV}$. This voltage shift indicated that the transport properties of the device change under illumination, and therefore that the device itself has a strong optical response.

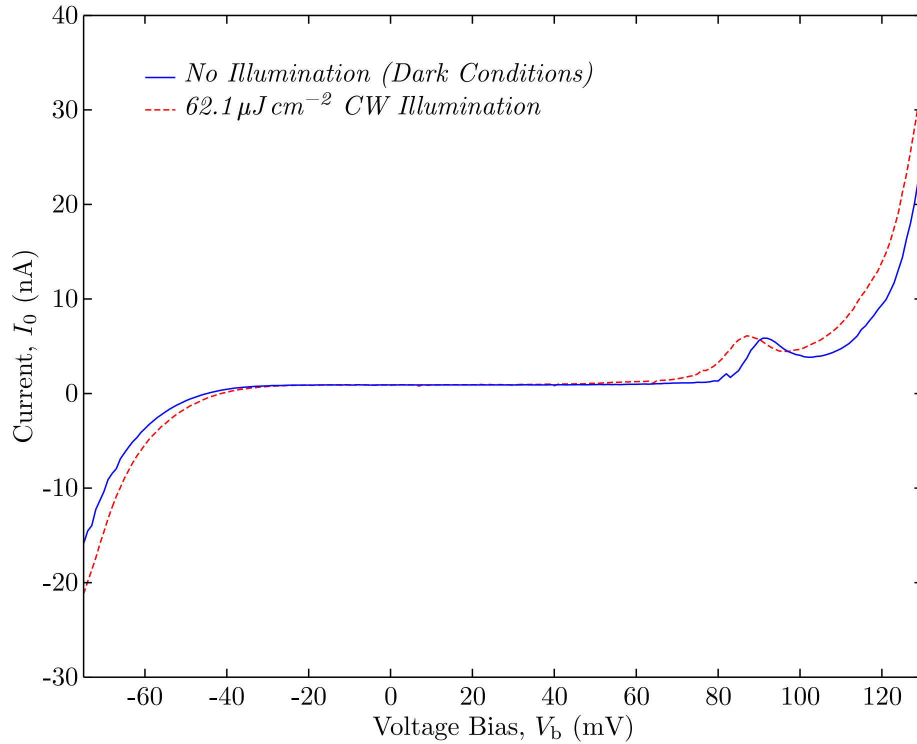

Figure 6.4: Stationary current-voltage bias (I_0-V_b) characteristics taken using an Agilent 34401A Digital Multimeter over a resistor $R = 100\,\mathrm{k\Omega}$, with voltage bias applied from Keithley 230 Programmable Voltage Source. These characteristics were measured under dark conditions (solid, blue line) and when illuminated by a Ti:Sapphire oscillator system emitting a continuous-wave (CW) beam (dashed, red line) of fluence $62.1\,\mathrm{\mu J\,cm^{-2}}$, as previously utilised in Section 4.2.

Preliminary Electrical-Optical Measurements

An electrical-optical measurement similar to that considered in Section 3.2.3 was used to measure an electrical signal from the QD device. This setup utilised the same oscillator system and bath cryostat on which the transport characteristics of the *p*-*i*-*n* hypersonic detector were determined (see Section 4.2).

The Al film transducer was pumped by the oscillator optical pulses at 960 nm wavelength, and the signal from the device was fed through a 50× gain high impedance amplifier with $> 20\,\mathrm{MHz}$ bandwidth into a Stanford Research Systems SR830 DSP Lock-In Amplifier. This lock-in amplifier was referenced to a chopper in the optical beam path set at a frequency of 1.14 kHz, and the signal was recorded with a time constant of 300 ms. A bias range of 0 mV to 130 mV was applied across the device packaging in steps of 0.25 mV, with a 1 s delay between bias application and data sampling; a typical recording is shown in Figure 6.5 under $0.3\,\mathrm{\mu J\,cm^{-2}}$ pulsed excitation.

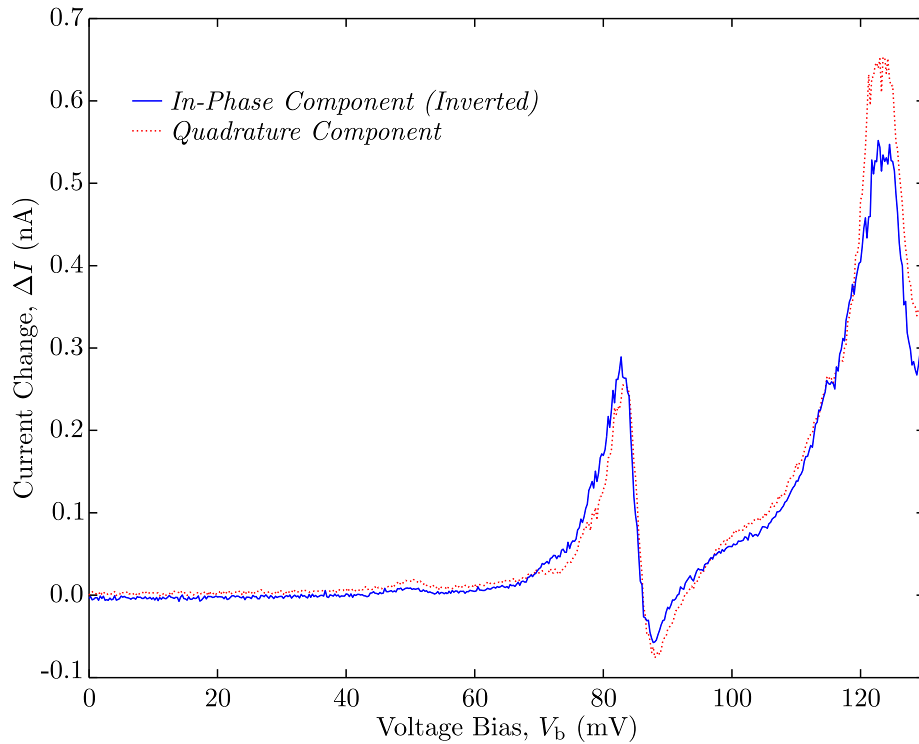

Figure 6.5: Preliminary electrical-optical measurements of current change ΔI against voltage bias V_{b} taken from a sample processed from wafer NU2217. Both the inverted in-phase (solid, blue line) and quadrature (dotted, red line) taken from the lock-in amplifier are shown and, as evident from these near-identical signals, it is difficult to resolve a fast acoustic signal, if any, from the slow optical response of the quantum dot (QD) device itself.

Both the in-phase (solid, blue line) and quadrature (dotted, red line) components of the lock-in amplifier are displayed in Figure 6.5. The former measures the signal when the optical pulses are not blocked by the chopper, and are therefore incident on the Al transducer film, whilst the latter records the *dark* response of the system when the pulses are blocked by the chopper. In an ideal case, only the in-phase component should measure any response from the device using this system. However, the signals are near identical for the two components over the applied bias range, especially in the expected bias range of the QD ($V_{\mathrm{b}} = 87.0\,\mathrm{mV}$ to $91.0\,\mathrm{mV}$).

From the transport measurements disclosed previously in this section, it was determined that the QD has a strong optical response and, due to device packaging and experimental setup limitations, it was not possible to completely eliminate stray reflections incident on the device itself. As such, the signals displayed in both the in-phase and quadrature component shown in Figure 6.5 were attributed to the slow but strong optical response of the QD that has a duration in excess of the rotation time of the chopper, i.e.

greater than 1.75 ms. This slow optical response masked the fast acoustic signal from the device, if discernible at all.

As aforementioned in Chapter 5, a less confined QW RTD structure can exhibit picosecond charge transfer via strain-induced effects, caused by the *acoustoelectronic pumping effect*. If this effect could similarly be exploited in an individual QD nanostructure, one would expect a single electron to be transferred in the system for each given strain pulse, and therefore for each individual optical pulse incident on the Al transducer. On this basis, it can be estimated that the current changes recorded by the lock-in amplifier should be of the order of $\sim$ 0.01 nA; this is equivalent to a 50 µV signal given the present circuitry, and should be detectable on the sensitivity range of the lock-in amplifier [135]. If all extraneous noise in the system can be suppressed, only Johnson noise from the 100 kΩ load resistor affects the signal-to-noise ratio of the measurement. This noise is approximately 10 nV for a 1 Hz bandwidth at liquid He temperatures, and therefore 0.5 µV after amplification, which provides a high signal-to-noise ratio. Nonetheless, the optical response of the device is at least an order of magnitude larger than this acoustic signal, and so it would be extremely difficult to resolve the acoustic signal given the present sample and setup.

These difficulties are compounded by a lack of remaining sample material to process additional devices, the complexity of locating individual QD devices, and the size of the present sample. Problems arise from the final issue, as the diameter of the sample rear surface exposure hole in Figure 6.3(a) was limited to $\sim$ 1 mm by the manufacturing equipment available, which was comparable to the size of the sample. Accordingly, the sample only partially obscured the exposure hole, and therefore the device was susceptible to optical excitation by stray light.

In conclusion, if the optical response of the device can be tailored such that it is minimised for the optical pump excitation wavelengths, and other microfabrication issues are resolved, it may be possible to observe strain-induced effects in a double barrier QD RTD experimentally, as evident from the above estimations.

Appendix A

Useful Formulae, and Derivations

The following appendix contains a list of useful equations and derivations implemented in the main body of this thesis, with references where relevant.

Acoustic Impedance *Z*

The acoustic impedance of a material Z is given by

$$Z = \rho v_{\mathrm{LA}}, \tag{A.1}$$

where ρ is the material density, and v_{LA} is the longitudinal acoustic velocity of the material.

Reflection Coefficient *R*

The reflection coefficient R at the interface of two materials 1 and 2 is given by

$$R = \left| \frac{Z_2 - Z_1}{Z_2 + Z_1} \right|, \tag{A.2}$$

where Z_1 and Z_2 are the acoustic impedances of the first and second materials, respectively. Note that the absolute value is taken, where a negative sign of the function within the vertical bars implies a π-phase change on reflection at the interface.

Phonon Dispersion Relationship

For small wavenumber k, the following approximation can be made for the dispersion relationship of a medium [12, 52]

$$\omega_k = vk - \chi k^3 + \ldots, \tag{A.3}$$

where ω_k is the angular frequency, v is the acoustic velocity in the medium, and χ is the dispersion parameter.

Given the group velocity $v_{\mathrm{g}} = \partial\omega_k/\partial k = v - 3\chi k^2$, and the propagation distance $z_0 = v_{\mathrm{g}}t = vt_0$,

$$\begin{aligned}
\therefore \quad k^2 &= \frac{1}{3\chi}\left(v - \frac{z_0}{t}\right) \\
\therefore \quad k^2 &= \frac{v\left(t - t_0\right)}{3\chi t} \\
\therefore \quad k &= \sqrt{\frac{v\left(t - t_0\right)}{3\chi t}} \qquad \text{(A.4)} \\
\therefore \quad \omega_{k,\mathrm{disp}} &= v\sqrt{\frac{v\left(t - t_0\right)}{3\chi t}} \\
\therefore \quad \omega_{k,\mathrm{disp}} &= v^2\sqrt{\frac{\tau_0}{3\chi z_0}}, \qquad \text{(A.5)}
\end{aligned}$$

where t_0 is the arrival time of low frequency components, $\tau_0 = (t - t_0)$, $k = \omega_{k,\mathrm{disp}}/v$, and $\omega_{k,\mathrm{disp}}$ is the dispersed angular phonon frequency. Note that Equation A.5 is only valid when the condition $t_0 \gg \tau_0 \gg \omega_{k,\mathrm{disp}}^{-1}$ is satisfied [12].

Second-Order Elastic Constant C_{11}

The second-order elastic constant C_{11} of a given material in the [100]-direction is defined by [14]

$$C_{11} = v^2\rho, \tag{A.6}$$

where v is the acoustic velocity and ρ is the density of the given material.

Ripple Effect $\Xi_\mathbf{r}$

The ground state energy shift in a quantum well due to the ripple effect $\Xi_\mathrm{r} = dE_1$ can be derived from the energy at the ground state for an unstrained quantum well E_1 [122] as follows

$$\begin{aligned}
E_1 &= \frac{\pi^2\hbar^2}{2m^*w^2} \\
\therefore \quad \frac{dE_1}{dw} &= -\frac{\pi^2\hbar^2}{m^*w^3} \\
\therefore \quad dE_1 &= -\frac{\pi^2\hbar^2}{m^*w^3}dw \\
\therefore \quad dE_1 &= -\frac{\pi^2\hbar^2}{m^*w^3}w\eta \\
\therefore \quad \Xi_\mathrm{r} &= -\frac{\pi^2\hbar^2}{m^*w^2}\eta, \qquad \text{(A.7)}
\end{aligned}$$

where m^* is the effective mass, w is the quantum well width, and $dw = w\eta$ is the change in quantum well width due to a strain η.

Appendix B

Material, and Figure Calculation Parameters

The following tables contain a list of parameters for Al, GaAs, and for generating figures used in this thesis, with references where relevant. Calculated parameters were determined using the equations listed either in the main body of this thesis, or in Appendix A.

Material Parameters

Aluminium (Al) Parameters			
Parameter	**Units**	**Value**	
Absorption length ζ_{Al} at $\lambda = 795\,\mathrm{nm}$	(nm)	7.54	
Absorption length ζ_{Al} at $\lambda = 800\,\mathrm{nm}$	(nm)	7.62	
Acoustic impedance Z_{Al}	$(\mathrm{N\,s\,m^{-3}})$	1.73×10^{7}	
Bulk modulus B_{Al}	(GPa)	70.3	[136]
Complex refractive index κ_{Al} at $\lambda = 795\,\mathrm{nm}$		8.39	[137]
Complex refractive index κ_{Al} at $\lambda = 800\,\mathrm{nm}$		8.35	[137]
Density ρ_{Al}	$(\mathrm{kg\,m^{-3}})$	2700	[138]
Linear expansion coefficient β_{Al}	$(\mathrm{K^{-1}})$	2.31×10^{-6}	[138]
Longitudinal acoustic velocity v_{Al}	$(\mathrm{m\,s^{-1}})$	6420	[138]
Reflection coefficient R_{Al} at $\lambda = 795\,\mathrm{nm}$		0.87	[137]
Specific heat capacity c_{Al}	$(\mathrm{J\,kg^{-1}\,K^{-1}})$	897	[138]

Table B.1: Referenced and calculated material parameters for aluminium (Al). Calculations were made using the equations presented in Appendix A.

Gallium Arsenide (GaAs) Parameters			
Parameter	**Units**	**Value**	
Absorption coefficient α_{GaAs} at $\lambda =$ 400 nm	(m^{-1})	6.54×10^{7}	
Acoustic impedance Z_{GaAs}	($\mathrm{N\,s\,m}^{-3}$)	2.54×10^{7}	
Acoustic nonlinearity C_3^{GaAs}	($\mathrm{kg\,m}^{-1}\,\mathrm{s}^{-2}$)	-5.32×10^{11}	[80]
Ambipolar plasma diffusivity parameter D_{GaAs}	($\mathrm{cm}^{2}\,\mathrm{s}^{-1}$)	4	[80]
Bulk modulus B_{GaAs}	(GPa)	75.3	[29]
Density ρ_{GaAs}	($\mathrm{kg\,m}^{-3}$)	5317	[29]
Dispersion parameter χ_{GaAs} in [100] orientation	($\mathrm{m}^{3}\,\mathrm{s}^{-1}$)	7.40×10^{-18}	[12]
Effective mass m^{*}	(kg)	5.74×10^{-32}	[29]
Lattice constant a	(Å)	5.65	[29]
Linear expansion coefficient β_{GaAs}	(K^{-1})	5.73×10^{-6}	[29]
Longitudinal acoustic velocity v_{GaAs}	($\mathrm{m\,s}^{-1}$)	4730	[29]
Reflection coefficient R_{GaAs} at $\lambda =$ 400 nm		0.4	
Relative permittivity ε_{r}		12.9	[29]
Second-order elastic constant C_{11} in [100] orientation	(GPa)	119	[29]
Specific heat capacity c_{GaAs}	($\mathrm{J\,kg}^{-1}\,\mathrm{K}^{-1}$)	330	[29]
Thermal diffusivity D_T^{GaAs}	($\mathrm{cm}^{2}\,\mathrm{s}^{-1}$)	0.31	[29]
Transverse acoustic velocity v_{TA}	($\mathrm{m\,s}^{-1}$)	3350	[29]
Viscosity/acoustic attenuation ϵ_{GaAs}	($\mathrm{m}^{2}\,\mathrm{s}^{-1}$)	5.50×10^{-11}	[80]

Table B.2: Referenced and calculated material parameters for gallium arsenide (GaAs). Calculations were made using the equations presented in Appendix A

Figure Calculation Parameters

Figure 2.1 Parameters	Units	Value
Al film thickness	(nm)	100
Al/GaAs interface reflection coefficient $R_{\mathrm{Al/GaAs}}$		0.19
Diffusion and film quality dependent parameter τ	(ps)	4
Pump fluence W	($\mathrm{mJ\,cm}^{-2}$)	0.05

Figure 2.2 Parameters	Units	Value
Initial strain amplitude η_0		10^{-6}

Figure 2.4 Parameters	Units	Value
Initial strain amplitude η_0		10^{-3}

Table B.3: Simulation parameters for figures in Chapter 2. Other material-specific parameters and equations are given in the respective chapters, and in Appendix A.

Figure 4.7 Parameters	Units	Value
Al film thickness	(nm)	30
First temporal parameter T_1	(ps)	0.3
Initial strain amplitude η_0^{Al}		10^{-6}
Initial strain amplitude η_0^{GaAs}		10^{-6}
Recombination time τ_{R}	(ps)	100
Resolution	(ps)	0.1
Second temporal parameter T_2	(ps)	7

Figure 4.8 Parameters	Units	Value
Initial strain amplitude $\eta_0^{1.0\,\mathrm{mJ\,cm^{-2}}}$		1.9×10^{-4}
Initial strain amplitude $\eta_0^{2.0\,\mathrm{mJ\,cm^{-2}}}$		7×10^{-4}
Initial strain amplitude $\eta_0^{3.0\,\mathrm{mJ\,cm^{-2}}}$		1.3×10^{-3}
Recombination time $\tau_{\mathrm{R}}^{1.0\,\mathrm{mJ\,cm^{-2}}}$	(ps)	57
Recombination time $\tau_{\mathrm{R}}^{2.0\,\mathrm{mJ\,cm^{-2}}}$	(ps)	14
Recombination time $\tau_{\mathrm{R}}^{3.0\,\mathrm{mJ\,cm^{-2}}}$	(ps)	7
Resolution	(ps)	0.1

Figure 4.9 Parameters	Units	Value	
Auger non-radiative recombination rate A	($\mathrm{cm^6\,s^{-1}}$)	7×10^{-30}	[80]
Deformation potential Ξ	(eV)	-1	[80]
Maximum plasma density n_{eh}	($\mathrm{cm^{-3}}$)	2×10^{20}	[80]
Recombination time $\tau_{\mathrm{R}}^{0.1\,\mathrm{mJ\,cm^{-2}}}$	(ps)	120	
Recombination time $\tau_{\mathrm{R}}^{0.2\,\mathrm{mJ\,cm^{-2}}}$	(ps)	100	
Recombination time $\tau_{\mathrm{R}}^{0.5\,\mathrm{mJ\,cm^{-2}}}$	(ps)	80	
Recombination time $\tau_{\mathrm{R}}^{1.0\,\mathrm{mJ\,cm^{-2}}}$	(ps)	57	
Recombination time $\tau_{\mathrm{R}}^{2.0\,\mathrm{mJ\,cm^{-2}}}$	(ps)	14	
Recombination time $\tau_{\mathrm{R}}^{3.0\,\mathrm{mJ\,cm^{-2}}}$	(ps)	7	

Table B.4: Simulation parameters for figures in Chapter 4. Other material-specific parameters and equations are given in the respective chapters, and in Appendix A.

Figure 5.10 Parameters	Units	Value	
Collector barrier tunnelling rate w_C	(s^{-1})	11×10^9	
Deformation potential constant Ξ	(eV)	-7	[95]
Diffusion and film quality dependent parameter τ	(ps)	10	
Initial strain amplitude η_0		10^{-4}	
Propagation time between emitter and QW regions $t_{\mathrm{E}\to\mathrm{W}}$	(ps)	4.1	
Propagation time to free surface and back t_R	(ps)	250	
Resonance damping constant Γ	(meV)	12	
Stationary detuning parameter Δ_0	(meV)	15	

Figure 5.11(b) Parameters	Units	Value	
Collector barrier tunnelling rate w_C	(s^{-1})	11×10^9	
Deformation potential constant Ξ	(eV)	-7	[95]
Diffusion and film quality dependent parameter τ	(ps)	10	
Emitter barrier tunnelling rate at resonance peak w_R	(s^{-1})	11×10^9	
Emitter Fermi energy level E_FE	(meV)	15	
Low-pass, first-order Butterworth filter cutoff frequency	(GHz)	1	
Ordinary differential equation solver resolution	(ps)	0.25	
Propagation time to free surface and back t_R	(ps)	250	
Propagation time between emitter and QW regions $t_{\mathrm{E}\to\mathrm{W}}$	(ps)	4.1	
Resonance damping constant Γ	(meV)	12	

Figure 5.13 Parameters	Units	Value	
Collector barrier tunnelling rate w_C	(s^{-1})	11×10^9	
Deformation potential constant Ξ	(eV)	-7	[95]
Diffusion and film quality dependent parameter τ	(ps)	10	
Emitter barrier tunnelling rate at resonance peak w_R	(s^{-1})	11×10^9	
Emitter Fermi energy level E_FE	(meV)	15	
Final integration time t_f	(ns)	59	
Initial integration time t_i	(ns)	58	
Ordinary differential equation solver resolution	(ps)	0.25	
Propagation time to free surface and back t_R	(ps)	250	
Propagation time between emitter and QW regions $t_{\mathrm{E}\to\mathrm{W}}$	(ps)	4.1	
Resonance damping constant Γ	(meV)	12	

Table B.5: Simulation parameters for figures in Chapter 5. Other material-specific parameters and equations are given in the respective chapters, and in Appendix A.

Figure 6.1 Parameters	**Units**	**Value**	
Deformation potential constant Ξ	(eV)	-7	[95]
Initial strain amplitude η_0		10^{-6}	
Propagation time between emitter and QW regions $t_{\mathrm{E}\rightarrow\mathrm{W}}$	(ps)	4	
Resolution	(ps)	0.10	
Stationary detuning parameter Δ_0	(meV)	15	

Table B.6: Simulation parameters for figures in Chapter 6. Other material-specific parameters and equations are given in the respective chapters, and in Appendix A.

Bibliography

[1] C. Thomsen, J. Strait, Z. Vardeny, H. J. Maris, J. Tauc, and J. J. Hauser. Coherent Phonon Generation and Detection by Picosecond Light Pulses. *Physical Review Letters*, 53:989–992, September 1984. doi: 10.1103/PhysRevLett.53.989. URL http://link.aps.org/doi/10.1103/PhysRevLett.53.989.

[2] C. Thomsen, H. T. Grahn, H. J. Maris, and J. Tauc. Surface generation and detection of phonons by picosecond light pulses. *Physical Review B*, 34:4129–4138, September 1986. doi: 10.1103/PhysRevB.34.4129. URL http://link.aps.org/doi/10.1103/PhysRevB.34.4129.

[3] G. L. Eesley, B. M. Clemens, and C. A. Paddock. Generation and detection of picosecond acoustic pulses in thin metal films. *Applied Physics Letters*, 50(12):717–719, March 1987. doi: 10.1063/1.98077. URL http://scitation.aip.org/content/aip/journal/apl/50/12/10.1063/1.98077.

[4] G. Tas and H. J. Maris. Electron diffusion in metals studied by picosecond ultrasonics. *Physical Review B*, 49:15046–15054, June 1994. doi: 10.1103/PhysRevB.49.15046. URL http://link.aps.org/doi/10.1103/PhysRevB.49.15046.

[5] O. B. Wright. Ultrafast nonequilibrium stress generation in gold and silver. *Physical Review B*, 49:9985–9988, April 1994. doi: 10.1103/PhysRevB.49.9985. URL http://link.aps.org/doi/10.1103/PhysRevB.49.9985.

[6] H. T. Grahn, H. J. Maris, and J. Tauc. Picosecond ultrasonics. *Quantum Electronics, IEEE Journal of*, 25(12):2562–2569, December 1989. ISSN 0018–9197. doi: 10.1109/3.40643. URL http://ieeexplore.ieee.org/xpl/articleDetails.jsp?arnumber=40643.

[7] H.-N. Lin, R. J. Stoner, H. J. Maris, and J. Tauc. Phonon attenuation and velocity measurements in transparent materials by picosecond acoustic interferometry. *Journal of Applied Physics*, 69(7):3816–3822, April 1991. doi: 10.1063/1.348958. URL http://scitation.aip.org/content/aip/journal/jap/69/7/10.1063/1.348958.

[8] O. B. Wright. Thickness and sound velocity measurement in thin transparent films with laser picosecond acoustics. *Journal of Applied Physics*, 71(4):1617–1629, February 1992. doi: 10.1063/1.351218. URL http://link.aip.org/link/?JAP/71/1617/1.

[9] A. Bartels, T. Dekorsy, H. Kurz, and K. Köhler. Coherent Zone-Folded Longitudinal Acoustic Phonons in Semiconductor Superlattices: Excitation and Detection. *Physical Review Letters*, 82:1044–1047, February 1999. doi: 10.1103/PhysRevLett.82.1044. URL http://link.aps.org/doi/10.1103/PhysRevLett.82.1044.

[10] C.-K. Sun, J.-C. Liang, and X.-Y. Yu. Coherent Acoustic Phonon Oscillations in Semiconductor Multiple Quantum Wells with Piezoelectric Fields. *Physical Review Letters*, 84:179–182, January 2000. doi: 10.1103/PhysRevLett.84.179. URL http://link.aps.org/doi/10.1103/PhysRevLett.84.179.

[11] A. Huynh, B. Perrin, N. D. Lanzillotti Kimura, B. Jusserand, A. Fainstein, and A. Lemaître. Subterahertz monochromatic acoustic wave propagation using semiconductor superlattices as transducers. *Physical Review B*, 78:233302, December 2008. doi: 10.1103/PhysRevB.78.233302. URL http://link.aps.org/doi/10.1103/PhysRevB.78.233302.

[12] H.-Y. Hao and H. J. Maris. Dispersion of the long-wavelength phonons in Ge, Si, GaAs, quartz, and sapphire. *Physical Review B*, 63:224301, May 2001. doi: 10.1103/PhysRevB.63.224301. URL http://link.aps.org/doi/10.1103/PhysRevB.63.224301.

[13] O. B. Wright, B. Perrin, O. Matsuda, and V. E. Gusev. Ultrafast carrier diffusion in gallium arsenide probed with picosecond acoustic pulses. *Physical Review B*, 64:081202, August 2001. doi: 10.1103/PhysRevB.64.081202. URL http://link.aps.org/doi/10.1103/PhysRevB.64.081202.

[14] H.-Y. Hao and H. J. Maris. Experiments with acoustic solitons in crystalline solids. *Physical Review B*, 64:064302, July 2001. doi:

10.1103/PhysRevB.64.064302. URL http://link.aps.org/doi/10.1103/PhysRevB.64.064302.

[15] E. Péronne and B. Perrin. Generation and detection of acoustic solitons in crystalline slabs by laser ultrasonics. *Ultrasonics*, 44, Supplement: e1203–e1207, December 2006. ISSN 0041–624X. doi: 10.1016/j.ultras.2006.05.072. URL http://www.sciencedirect.com/science/article/pii/S0041624X06001053.

[16] A. J. Kent, G. A. Hardy, P. Hawker, V. W. Rampton, M. I. Newton, P. A. Russell, and L. J. Challis. Detection of Heat Pulses by the Two-Dimensional Electron Gas in a Silicon Device. *Physical Review Letters*, 61:180–182, July 1988. doi: 10.1103/PhysRevLett.61.180. URL http://link.aps.org/doi/10.1103/PhysRevLett.61.180.

[17] F. F. Ouali, N. N. Zinov'ev, L. J. Challis, F. W. Sheard, M. Henini, D. P. Steenson, and K. R. Strickland. Nonequilibrium Acoustic Phonon-Assisted Tunneling in GaAs/(AlGa)As Double Barrier Devices. *Physical Review Letters*, 75:308–311, July 1995. doi: 10.1103/PhysRevLett.75.308. URL http://link.aps.org/doi/10.1103/PhysRevLett.75.308.

[18] D. R. Fowler, A. V. Akimov, A. G. Balanov, M. T. Greenaway, M. Henini, T. M. Fromhold, and A. J. Kent. Semiconductor charge transport driven by a picosecond strain pulse. *Applied Physics Letters*, 92(23):232104, June 2008. doi: 10.1063/1.2942389. URL http://link.aip.org/link/?APL/92/232104/1.

[19] D. Moss, A. V. Akimov, O. Makarovsky, R. P. Campion, C. T. Foxon, L. Eaves, A. J. Kent, and B. A. Glavin. Ultrafast acoustical gating of the photocurrent in a *p-i-n* tunneling diode incorporating a quantum well. *Physical Review B*, 80:113306, September 2009. doi: 10.1103/PhysRevB.80.113306. URL http://link.aps.org/doi/10.1103/PhysRevB.80.113306.

[20] D. Moss, A. V. Akimov, R. P. Campion, M. Henini, C. T. Foxon, L. Eaves, A. J. Kent, and B. A. Glavin. Picosecond strain pulses probed by the photocurrent in semiconductor devices with quantum wells. *Physical Review B*, 83:245303, June 2011. doi: 10.1103/PhysRevB.83.245303. URL http://link.aps.org/doi/10.1103/PhysRevB.83.245303.

[21] D. M. Moss, A. V. Akimov, B. A. Glavin, M. Henini, and A. J. Kent. Ultrafast Strain-Induced Current in a GaAs Schottky Diode. *Physical Review Letters*, 106:066602, February 2011. doi: 10.1103/PhysRevLett.106.066602. URL http://link.aps.org/doi/10.1103/PhysRevLett.106.066602.

[22] J. S. Blakemore. Semiconducting and other major properties of gallium arsenide. *Journal of Applied Physics*, 53(10):R123–R181, October 1982. doi: 10.1063/1.331665. URL http://scitation.aip.org/content/aip/journal/jap/53/10/10.1063/1.331665.

[23] S. Adachi. GaAs, AlAs, and $Al_xGa_{1-x}As$: Material parameters for use in research and device applications. *Journal of Applied Physics*, 58(3): R1–R29, August 1985. doi: 10.1063/1.336070. URL http://scitation.aip.org/content/aip/journal/jap/58/3/10.1063/1.336070.

[24] S. Adachi. *Physical Properties of III–V Semiconductor Compounds: InP, InAs, GaAs, GaP, InGaAs, and InGaAsP*. Wiley-Interscience Publication. John Wiley & Sons, Inc., November 1992. ISBN 9780471573296.

[25] M. R. Brozel and G. E. Stillman, editors. *Properties of Gallium Arsenide*. Number 16 in EMIS Datareviews Series. INSPEC, The Institution of Electrical Engineers, 3rd edition, 1996. ISBN 9780852968857.

[26] K. K. Ng. *Complete Guide to Semiconductor Devices*. Wiley-Interscience Publication. John Wiley & Sons, Inc., 2nd edition, 2002. ISBN 9780471202400.

[27] S. M. Sze and K. K. Ng. *Physics of Semiconductor Devices*. Wiley-Interscience Publication. John Wiley & Sons, Inc., 3rd edition, 2006. ISBN 9780470068304.

[28] J. C. Brice, D. J Dunstan, and S. Adachi. Basic Physical Properties of Gallium Arsenide. In M. R. Brozel and G. E. Stillman, editors, *Properties of Gallium Arsenide*, number 16 in EMIS Datareviews Series, chapter 1, pages 1–38. INSPEC, The Institution of Electrical Engineers, 3rd edition, 1996. ISBN 9780852968857.

[29] M.E. Levinshtein and S.L Rumyantsev. Gallium Arsenide (GaAs). In M.E. Levinshtein, S.L. Rumyantsev, and M. Shur, editors, *Handbook*

Series on Semiconductor Parameters, number 1, chapter 4, pages 77–103. World Scientific Publishing Company, Incorporated, 1996. ISBN 9789810229344.

[30] Y. S. Yung. A tutorial on GaAs vs silicon. In *ASIC Conference and Exhibit, 1992., Proceedings of Fifth Annual IEEE International*, pages 281–287, September 1992. doi: 10.1109/ASIC.1992.270234. URL http://ieeexplore.ieee.org/xpl/articleDetails.jsp?arnumber=270234.

[31] B.G. Streetman. *Solid state electronic devices*. Prentice Hall Series in Solid State Physical Electronics. Prentice Hall, 4th edition, 1995. ISBN 9780131587670.

[32] J. F. Creemer, F. Fruett, G. C. M. Meijer, and P. J. French. The piezojunction effect in silicon sensors and circuits and its relation to piezoresistance. *Sensors Journal, IEEE*, 1(2):98–108, August 2001. ISSN 1530–437X. doi: 10.1109/JSEN.2001.936927. URL http://ieeexplore.ieee.org/xpl/articleDetails.jsp?arnumber=936927.

[33] H. H. Hall, J. Bardeen, and G. L. Pearson. The Effects of Pressure and Temperature on the Resistance of p-n Junctions in Germanium. *Physical Review*, 84:129–132, October 1951. doi: 10.1103/PhysRev.84.129. URL http://link.aps.org/doi/10.1103/PhysRev.84.129.

[34] W. Shockley. The Theory of p-n Junctions in Semiconductors and p-n Junction Transistors. *Bell System Technical Journal*, 28(3):435–489, July 1949. URL http://alcatel-lucent.com/bstj/vol28-1949/articles/bstj28-3-435.pdf.

[35] W. Rindner and E. Pittelli. Effects of Stress-Induced Band-Gap Widening and Defects in GaAs Junctions. *Journal of Applied Physics*, 37 (12):4437–4439, November 1966. doi: 10.1063/1.1708056. URL http://scitation.aip.org/content/aip/journal/jap/37/12/10.1063/1.1708056.

[36] F. H. Pollak, M. Cardona, and K. L. Shaklee. Piezoelectroreflectance in GaAs. *Physical Review Letters*, 16:942–944, May 1966. doi: 10.1103/PhysRevLett.16.942. URL http://link.aps.org/doi/10.1103/PhysRevLett.16.942.

[37] F. H. Pollak and M. Cardona. Piezo-Electroreflectance in Ge, GaAs, and Si. *Physical Review*, 172:816–837, August 1968. doi: 10.1103/

PhysRev.172.816. URL http://link.aps.org/doi/10.1103/PhysRev.172.816.

[38] M. Chandrasekhar and F. H. Pollak. Effects of uniaxial stress on the electroreflectance spectrum of Ge and GaAs. *Physical Review B*, 15: 2127–2144, February 1977. doi: 10.1103/PhysRevB.15.2127. URL http://link.aps.org/doi/10.1103/PhysRevB.15.2127.

[39] D. M. Moss, A. V. Akimov, R. P. Campion, and A. J. Kent. Ultrafast Strain-Induced Electronic Transport in a GaAs *p-n* Junction Diode. *Chinese Journal of Physics*, 49(1):499–505, February 2011. URL http://psroc.phys.ntu.edu.tw/cjp/download.php?type=full&vol=49&num=1&page=499.

[40] D. A. B. Miller, D. S. Chemla, T. C. Damen, A. C. Gossard, W. Wiegmann, T. H. Wood, and C. A. Burrus. Electric field dependence of optical absorption near the band gap of quantum-well structures. *Physical Review B*, 32:1043–1060, July 1985. doi: 10.1103/PhysRevB.32.1043. URL http://link.aps.org/doi/10.1103/PhysRevB.32.1043.

[41] A. A. Kaplyanskii and A. K. Przhevuskii. The Piezospectroscopic Effect in Ruby Crystals. *Soviet Physics - Doklady*, 7(1):37–40, July 1962. [Translated from *Doklady Akademii Nauk SSSR*, 142(2):313–316, January 1962].

[42] A. V. Scherbakov, P. J. S. van Capel, A. V. Akimov, J. I. Dijkhuis, D. R. Yakovlev, T. Berstermann, and M. Bayer. Chirping of an Optical Transition by an Ultrafast Acoustic Soliton Train in a Semiconductor Quantum Well. *Physical Review Letters*, 99:057402, August 2007. doi: 10.1103/PhysRevLett.99.057402. URL http://link.aps.org/doi/10.1103/PhysRevLett.99.057402.

[43] A. V. Scherbakov, T. Berstermann, A. V. Akimov, D. R. Yakovlev, G. Beaudoin, D. Bajoni, I. Sagnes, J. Bloch, and M. Bayer. Ultrafast control of light emission from a quantum-well semiconductor microcavity using picosecond strain pulses. *Physical Review B*, 78: 241302, December 2008. doi: 10.1103/PhysRevB.78.241302. URL http://link.aps.org/doi/10.1103/PhysRevB.78.241302.

[44] D. M. Moss. *Ultrafast Acoustic Modulation of Transport in Semiconductor Devices*. PhD thesis, University of Nottingham, July 2013.

[45] W. Maryam, A. V. Akimov, R. P. Campion, and A. J. Kent. Dynamics of a vertical cavity quantum cascade phonon laser structure. *Nature Communications*, 4:2184, July 2013. doi: 10.1038/ncomms3184. URL http://www.nature.com/ncomms/2013/130725/ncomms3184/full/ncomms3184.html.

[46] R. M. White. Generation of Elastic Waves by Transient Surface Heating. *Journal of Applied Physics*, 34(12):3559–3567, December 1963. doi: 10.1063/1.1729258. URL http://link.aip.org/link/?JAP/34/3559/1.

[47] A. V. Akimov, A. V. Scherbakov, D. R. Yakovlev, C. T. Foxon, and M. Bayer. Ultrafast Band-Gap Shift Induced by a Strain Pulse in Semiconductor Heterostructures. *Physical Review Letters*, 97:037401, July 2006. doi: 10.1103/PhysRevLett.97.037401. URL http://link.aps.org/doi/10.1103/PhysRevLett.97.037401.

[48] T. Saito, O. Matsuda, and O. B. Wright. Picosecond acoustic phonon pulse generation in nickel and chromium. *Physical Review B*, 67:205421, May 2003. doi: 10.1103/PhysRevB.67.205421. URL http://link.aps.org/doi/10.1103/PhysRevB.67.205421.

[49] H. J. Maris. Interaction of Sound Waves with Thermal Phonons in Dielectric Crystals. In W.P. Mason and R.N. Thurston, editors, *Physical Acoustics: Principles and Methods*, number VIII, chapter 6. Academic Press, 1971. ISBN 9780123956682.

[50] W. Chen, H. J. Maris, Z. R. Wasilewski, and S. Tamura. Attenuation and velocity of 56 GHz longitudinal phonons in gallium arsenide from 50 to 300 K. *Philosophical Magazine Part B*, 70(3):687–698, 1994. doi: 10.1080/01418639408240242. URL http://www.tandfonline.com/doi/abs/10.1080/01418639408240242.

[51] J. L. T. Waugh and G. Dolling. Crystal Dynamics of Gallium Arsenide. *Physical Review*, 132:2410–2412, December 1963. doi: 10.1103/PhysRev.132.2410. URL http://link.aps.org/doi/10.1103/PhysRev.132.2410.

[52] H.-Y. Hao and H. J. Maris. Study of Phonon Dispersion in Silicon and Germanium at Long Wavelengths Using Picosecond Ultrasonics. *Physical Review Letters*, 84:5556–5559, June 2000. doi:

10.1103/PhysRevLett.84.5556. URL http://link.aps.org/doi/10.1103/PhysRevLett.84.5556.

[53] N. J. Zabusky and M. D. Kruskal. Interaction of "Solitons" in a Collisionless Plasma and the Recurrence of Initial States. *Physical Review Letters*, 15:240–243, August 1965. doi: 10.1103/PhysRevLett.15.240. URL http://link.aps.org/doi/10.1103/PhysRevLett.15.240.

[54] P. J. S. van Capel and J. I. Dijkhuis. Time-resolved interferometric detection of ultrashort strain solitons in sapphire. *Physical Review B*, 81:144106, April 2010. doi: 10.1103/PhysRevB.81.144106. URL http://link.aps.org/doi/10.1103/PhysRevB.81.144106.

[55] T. A. Driscoll. A Composite Runge-Kutta Method for the Spectral Solution of Semilinear PDEs. *Journal of Computational Physics*, 182 (2):357–367, November 2002. ISSN 0021–9991. doi: 10.1006/jcph.2002.7127. URL http://www.sciencedirect.com/science/article/pii/S0021999102971275.

[56] O. L. Muskens. *High-amplitude, Ultrashort Strain Solitons in Solids*. PhD thesis, Universiteit Utrecht, 2004. URL http://igitur-archive.library.uu.nl/dissertations/2004-0405-090235/UUindex.html.

[57] B. Perrin, C. Rossignol, B. Bonello, and J.-C. Jeannet. Interferometric detection in picosecond ultrasonics. *Physica B: Condensed Matter*, 263-264:571–573, March 1999. doi: 10.1016/S0921--4526(98)01479--3. URL http://www.sciencedirect.com/science/article/pii/S0921452698014793.

[58] J. Bardeen and W. Shockley. Deformation Potentials and Mobilities in Non-Polar Crystals. *Physical Review*, 80:72–80, October 1950. doi: 10.1103/PhysRev.80.72. URL http://link.aps.org/doi/10.1103/PhysRev.80.72.

[59] M. Cardona. Stress Modulation. In F. Seitz, D. Turnbull, and H. Ehrenreich, editors, *Modulation Spectroscopy*, number 11 in Solid State Physics: Advances in Research and Applications Supplement, chapter VI, pages 137–164. Academic Press, 1969. ISBN 9780126077711.

[60] D. D. Nolte, W. Walukiewicz, and E. E. Haller. Band-edge hydrostatic deformation potentials in III–V semiconductors. *Physical Review*

Letters, 59:501–504, July 1987. doi: 10.1103/PhysRevLett.59.501. URL http://link.aps.org/doi/10.1103/PhysRevLett.59.501.

[61] A. Blacha, H. Presting, and M. Cardona. Deformation Potentials of $k = 0$ States of Tetrahedral Semiconductors. *Physica Status Solidi B*, 126(1):11–36, November 1984. ISSN 1521–3951. doi: 10.1002/pssb.2221260102. URL http://onlinelibrary.wiley.com/doi/10.1002/pssb.2221260102/abstract.

[62] C. G. Van de Walle. Band lineups and deformation potentials in the model-solid theory. *Physical Review B*, 39:1871–1883, January 1989. doi: 10.1103/PhysRevB.39.1871. URL http://link.aps.org/doi/10.1103/PhysRevB.39.1871.

[63] S. Zollner and M. Cardona. Intra- and intervalley deformation potentials for electrons in GaAs. In M. R. Brozel and G. E. Stillman, editors, *Properties of Gallium Arsenide*, number 16 in EMIS Datareviews Series, chapter 4.5, pages 162–176. INSPEC, The Institution of Electrical Engineers, 3rd edition, 1996.

[64] A. J. Kent and J. K. Wigmore. Energy relaxation by hot two-dimensional carriers in zero magnetic field. In L. J. Challis, editor, *Electron-phonon Interactions in Low-dimensional Structures*, number 10 in Series on Semiconductor Science and Technology, chapter 2, pages 5–58. Oxford University Press, 2003. ISBN 9780198507321.

[65] D. J. Robbins. Piezoelectric properties of GaAs. In M. R. Brozel and G. E. Stillman, editors, *Properties of Gallium Arsenide*, number 16 in EMIS Datareviews Series, chapter 6.3, pages 223–224. INSPEC, The Institution of Electrical Engineers, 3rd edition, 1996. ISBN 9780852968857.

[66] S. I. Pekar. Electron-Phonon Interaction Proportional to the External Applied Field and Sound Amplification in Semiconductors. *Soviet Physics JETP*, 22(2):431–436, February 1966. URL http://www.jetp.ac.ru/cgi-bin/e/index/e/22/2/p431?a=list. [Translated from *Zhurnal Eksperimental'noi i Teoreticheskoi Fiziki*, 49(2):621–629, August 1965].

[67] Y. V. Gulyaev. Electron-Phonon Interaction Proportional to the Externally Applied Field. *Soviet Physics - Solid State*, 9(6):1425–1426,

December 1967. [Translated from *Fizika Tverdogo Tela*, 9(6):1816–1818, June 1967].

[68] B. A. Glavin, V. A. Kochelap, T. L. Linnik, and K. W. Kim. Electron-phonon interaction via the Pekar mechanism in nanostructures. *Physical Review B*, 71:081305, February 2005. doi: 10.1103/PhysRevB.71.081305. URL http://link.aps.org/doi/10.1103/PhysRevB.71.081305.

[69] P. A. Knipp and T. L. Reinecke. Coupling between electrons and acoustic phonons in semiconductor nanostructures. *Physical Review B*, 52:5923–5928, August 1995. doi: 10.1103/PhysRevB.52.5923. URL http://link.aps.org/doi/10.1103/PhysRevB.52.5923.

[70] UK Kemet International Ltd. Kemet Type KD Diamond Compound, October 2006. URL http://www.kemet.co.uk/_uploads/downloads/Diamond_compound_Type_KD.pdf. [Online; Accessed 8 February 2014].

[71] UK Kemet International Ltd. Kemet Diamond Products, January 2004. URL http://www.kemet.co.uk/_uploads/downloads/diamond_products.pdf. [Online; Accessed 8 February 2014].

[72] Japan Fujimi, Inc. INSEC Compound Semiconductor Polish Product Information, October 2011. URL http://www.fujimiinc.co.jp/service/catalog/file/insec.pdf. [Online; Accessed 8 February 2014].

[73] A. G. Baca and C. I. H. Ashby. *Fabrication of GaAs Devices*. The Institution of Engineering and Technology, September 2005. ISBN 9780863413537. URL http://app.knovel.com/hotlink/toc/id:kpFGAD000H/fabrication-gaas-devices. [Online; Accessed 8 February 2014].

[74] S. H. Jones and D. K. Walker. Highly anisotropic wet chemical etching of GaAs using NH_4OH:H_2O_2:H_2O. *Journal of The Electrochemical Society*, 137(5):1653–1654, May 1990. doi: 10.1149/1.2086747. URL http://jes.ecsdl.org/content/137/5/1653.abstract.

[75] A. R. Clawson. Guide to references on III-V semiconductor chemical etching. *Materials Science and Engineering: R: Reports*, 31(1–6):1–438, January 2001. ISSN 0927–796X. doi: 10.1016/S0927--

796X(00)00027-9. URL http://www.sciencedirect.com/science/article/pii/S0927796X00000279.

[76] S. Franssila. *Introduction to Microfabrication*. John Wiley & Sons, Inc., Chichester, UK, 2nd edition, September 2010. ISBN 9780470749838.

[77] S. M. Sze. *Physics of Semiconductor Devices*. Wiley-Interscience Publication. John Wiley & Sons, Inc., 2nd edition, 1981. ISBN 9780471056614.

[78] G. Hill. Semiconductor Processing. In *Experimental Techniques of Semiconductor Research: Course Notes*, pages 28–47. The Semiconductor Physics Group, Institute of Physics, March 2000.

[79] UK Cambridge Magnetic Refrigeration. CMRdirect Product Specification: GE/IMI 7031 [02-33-001], October 2007. URL http://www.cmr-direct.com/en/product/download/get?download_id=4. [Online; Accessed 8 February 2014].

[80] E. S. K. Young, A. V. Akimov, R. P. Campion, A. J. Kent, and V. Gusev. Picosecond strain pulses generated by a supersonically expanding electron-hole plasma in GaAs. *Physical Review B*, 86: 155207, October 2012. doi: 10.1103/PhysRevB.86.155207. URL http://link.aps.org/doi/10.1103/PhysRevB.86.155207.

[81] H. J. Maris and W. Singhsomroje. Picosecond ultrasonic experiments to study phonon solitons. *Physica Status Solidi B*, 241(15):3463–3468, December 2004. ISSN 1521–3951. doi: 10.1002/pssb.200405334. URL http://onlinelibrary.wiley.com/doi/10.1002/pssb.200405334/abstract.

[82] H. J. Maris and S. Tamura. Propagation of acoustic phonon solitons in nonmetallic crystals. *Physical Review B*, 84:024301, July 2011. doi: 10.1103/PhysRevB.84.024301. URL http://link.aps.org/doi/10.1103/PhysRevB.84.024301.

[83] O. L. Muskens and J. I. Dijkhuis. Inelastic light scattering by trains of ultrashort acoustic solitons in sapphire. *Physical Review B*, 70: 104301, September 2004. doi: 10.1103/PhysRevB.70.104301. URL http://link.aps.org/doi/10.1103/PhysRevB.70.104301.

[84] B. C. Daly, T. B. Norris, J. Chen, and J. B. Khurgin. Picosecond acoustic phonon pulse propagation in silicon. *Physical Review B*, 70: 214307, December 2004. doi: 10.1103/PhysRevB.70.214307. URL http://link.aps.org/doi/10.1103/PhysRevB.70.214307.

[85] V. E. Gusev. Generation of Picosecond Acoustic Pulses by Laser Radiation in Piezosemiconductors. *Physica Status Solidi B*, 158 (1):367–381, March 1990. ISSN 1521–3951. doi: 10.1002/pssb.2221580137. URL http://onlinelibrary.wiley.com/doi/10.1002/pssb.2221580137/abstract.

[86] S. A. Akhmanov and V. É. Gusev. Laser excitation of ultrashort acoustic pulses: New possibilities in solid-state spectroscopy, diagnostics of fast processes, and nonlinear acoustics. *Soviet Physics Uspekhi*, 35 (3):153–191, March 1992. doi: 10.1070/PU1992v035n03ABEH002221. URL http://stacks.iop.org/0038-5670/35/i=3/a=R01. [Translated from *Uspekhi Fizicheskikh Nauk*, 162:3–87, March 1992].

[87] N. V. Chigarev, D. Yu. Paraschuk, X. Y. Pan, and V. E. Gusev. Coherent phonon emission in the supersonic expansion of photoexcited electron-hole plasma in Ge. *Physical Review B*, 61:15837–15840, June 2000. doi: 10.1103/PhysRevB.61.15837. URL http://link.aps.org/doi/10.1103/PhysRevB.61.15837.

[88] P. Babilotte, P. Ruello, T. Pezeril, G. Vaudel, D. Mounier, J.-M. Breteau, and V. Gusev. Transition from piezoelectric to deformation potential mechanism of hypersound photogeneration in n-doped GaAs semiconductors. *Journal of Applied Physics*, 109(6):064909, March 2011. doi: 10.1063/1.3552912. URL http://scitation.aip.org/content/aip/journal/jap/109/6/10.1063/1.3552912.

[89] O. B. Wright and V. E. Gusev. Ultrafast generation of acoustic waves in copper. *Ultrasonics, Ferroelectrics and Frequency Control, IEEE Transactions on*, 42(3):331–338, May 1995. ISSN 0885-3010. doi: 10.1109/58.384440. URL http://ieeexplore.ieee.org/xpl/articleDetails.jsp?arnumber=384440.

[90] V. E. Gusev and O. B. Wright. Ultrafast nonequilibrium dynamics of electrons in metals. *Physical Review B*, 57:2878–2888, February

1998. doi: 10.1103/PhysRevB.57.2878. URL http://link.aps.org/doi/10.1103/PhysRevB.57.2878.

[91] V. E. Gusev. Mathematical derivations of the deformation potential and thermoelastic contributions to the strain pulse profile in a supersonically-expanding electron-hole (e-h) plasma in bulk GaAs. Private Communication, January 2012.

[92] K. F. Riley, M. P. Hobson, and S. J. Bence. *Mathematical Models for Physics and Engineering*. Cambridge University Press, 3rd edition, 2006. ISBN 9780521861533.

[93] B. P. Zakharchenya, D. N. Mirlin, V. I. Perel', and I. I. Reshina. Spectrum and polarization of hot-electron photoluminescence in semiconductors. *Soviet Physics Uspekhi*, 25(3):143–166, March 1982. doi: 10.1070/PU1982v025n03ABEH004519. URL http://stacks.iop.org/0038-5670/25/i=3/a=R03. [Translated from *Uspekhi Fizicheskikh Nauk*, 132:459–499, March 1982].

[94] U. Strauss, W. W. Rühle, and K. Köhler. Auger recombination in intrinsic GaAs. *Applied Physics Letters*, 62(1):55–57, January 1993. doi: 10.1063/1.108817. URL http://scitation.aip.org/content/aip/journal/apl/62/1/10.1063/1.108817.

[95] E. S. K. Young, A. V. Akimov, M. Henini, L. Eaves, and A. J. Kent. Subterahertz Acoustical Pumping of Electronic Charge in a Resonant Tunneling Device. *Physical Review Letters*, 108:226601, May 2012. doi: 10.1103/PhysRevLett.108.226601. URL http://link.aps.org/doi/10.1103/PhysRevLett.108.226601.

[96] L. L. Chang, L. Esaki, and R. Tsu. Resonant tunneling in semiconductor double barriers. *Applied Physics Letters*, 24(12):593–595, June 1974. doi: 10.1063/1.1655067. URL http://link.aip.org/link/?APL/24/593/1.

[97] M. Tsuchiya, H. Sakaki, and J. Yoshino. Room Temperature Observation of Differential Negative Resistance in an AlAs/GaAs/AlAs Resonant Tunneling Diode. *Japanese Journal of Applied Physics*, 24(6):L466–L468, June 1985. doi: 10.7567/JJAP.24.L466. URL http://jjap.jsap.jp/link?JJAP/24/L466/.

[98] M. Tsuchiya and H. Sakaki. Precise Control of Resonant Tunneling Current in AlAs/GaAs/AlAs Double Barrier Diodes with Atomically-Controlled Barrier Widths. *Japanese Journal of Applied Physics*, 25(3):L185–L187, March 1986. doi: 10.7567/JJAP.25.L185. URL http://jjap.jsap.jp/link?JJAP/25/L185/.

[99] M. L. Leadbeater. *Resonant Tunnelling in Semiconductor Heterostructures*. PhD thesis, University of Nottingham, January 1990.

[100] R. Tsu and L. Esaki. Tunneling in a finite superlattice. *Applied Physics Letters*, 22(11):562–564, June 1973. doi: 10.1063/1.1654509. URL http://link.aip.org/link/?APL/22/562/1.

[101] B. Ricco and M. Ya. Azbel. Physics of resonant tunneling. The one-dimensional double-barrier case. *Physical Review B*, 29:1970–1981, February 1984. doi: 10.1103/PhysRevB.29.1970. URL http://link.aps.org/doi/10.1103/PhysRevB.29.1970.

[102] M. C. Payne. Transfer Hamiltonian description of resonant tunnelling. *Journal of Physics C: Solid State Physics*, 19(8):1145–1155, March 1986. doi: 10.1088/0022--3719/19/8/013. URL http://stacks.iop.org/0022-3719/19/i=8/a=013.

[103] S. Luryi. Frequency limit of double-barrier resonant-tunneling oscillators. *Applied Physics Letters*, 47(5):490–492, September 1985. doi: 10.1063/1.96102. URL http://scitation.aip.org/content/aip/journal/apl/47/5/10.1063/1.96102.

[104] T. C. L. G. Sollner, W. D. Goodhue, P. E. Tannenwald, C. D. Parker, and D. D. Peck. Resonant tunneling through quantum wells at frequencies up to 2.5 THz. *Applied Physics Letters*, 43 (6):588–590, September 1983. doi: 10.1063/1.94434. URL http://scitation.aip.org/content/aip/journal/apl/43/6/10.1063/1.94434.

[105] T. Weil and B. Vinter. Equivalence between resonant tunneling and sequential tunneling in double-barrier diodes. *Applied Physics Letters*, 50(18):1281–1283, May 1987. doi: 10.1063/1.97884. URL http://scitation.aip.org/content/aip/journal/apl/50/18/10.1063/1.97884.

[106] M. Jonson and A. Grincwajg. Effect of inelastic scattering on resonant and sequential tunneling in double barrier heterostructures. *Applied*

Physics Letters, 51(21):1729–1731, November 1987. doi: 10.1063/1.98995. URL http://scitation.aip.org/content/aip/journal/apl/51/21/10.1063/1.98995.

[107] F. F. Ouali and L. J. Challis. Phonon-assisted tunneling. In L. J. Challis, editor, *Electron-phonon Interactions in Low-dimensional Structures*, number 10 in Series on Semiconductor Science and Technology, chapter 6, pages 185–238. Oxford University Press, 2003. ISBN 9780198507321.

[108] S. Luryi and A. Zaslavsky. Quantum-Effect and Hot-Electron Devices. In S. M. Sze, editor, *Modern semiconductor device physics*, Wiley-Interscience Publication, chapter 5, pages 253–343. John Wiley & Sons, Inc., 1998. ISBN 9780471152378.

[109] A. Y. Shik. *Quantum Wells: Physics and Electronics of Two-dimensional Systems*. World Scientific, 1997. ISBN 9789810232795.

[110] F. Capasso, K. Mohammed, and A. Y. Cho. Resonant tunneling through double barriers, perpendicular quantum transport phenomena in superlattices, and their device applications. *Quantum Electronics, IEEE Journal of*, 22(9):1853–1869, September 1986. ISSN 0018–9197. doi: 10.1109/JQE.1986.1073171. URL http://ieeexplore.ieee.org/xpl/articleDetails.jsp?arnumber=1073171.

[111] M. L. Leadbeater, E. S. Alves, F. W. Sheard, L. Eaves, M. Henini, O. H. Hughes, and G. A. Toombs. Observation of space-charge bulk-up and thermalisation in an asymmetric double-barrier resonant tunnelling structure. *Journal of Physics: Condensed Matter*, 1 (51):10605, December 1989. doi: 10.1088/0953-8984/1/51/029. URL http://stacks.iop.org/0953-8984/1/i=51/a=029.

[112] M. L. Leadbeater and L. Eaves. Sequential tunnelling and magnetically enhanced bistability in double barrier resonant-tunnelling structures. *Physica Scripta*, 1991(T35):215–220, 1991. doi: 10.1088/0031-8949/1991/T35/045. URL http://stacks.iop.org/1402-4896/1991/i=T35/a=045.

[113] L. Eaves, G. A. Toombs, F. W. Sheard, C. A. Payling, M. L. Leadbeater, E. S. Alves, T. J. Foster, P. E. Simmonds, M. Henini, O. H.

Hughes, J. C. Portal, G. Hill, and M. A. Pate. Sequential tunneling due to intersubband scattering in double-barrier resonant tunneling devices. *Applied Physics Letters*, 52(3):212–214, January 1988. doi: 10.1063/1.99522. URL http://scitation.aip.org/content/aip/journal/apl/52/3/10.1063/1.99522.

[114] R. Lassnig and W. Boxleitner. Tunneling from quasi two-dimensional space charge layers. *Solid State Communications*, 64(6):979–982, November 1987. ISSN 0038–1098. doi: 10.1016/0038--1098(87)90576--X. URL http://www.sciencedirect.com/science/article/pii/003810988790576X.

[115] F. F. Fang and W. E. Howard. Negative Field-Effect Mobility on (100) Si Surfaces. *Physical Review Letters*, 16:797–799, May 1966. doi: 10.1103/PhysRevLett.16.797. URL http://link.aps.org/doi/10.1103/PhysRevLett.16.797.

[116] F. Stern and W. E. Howard. Properties of Semiconductor Surface Inversion Layers in the Electric Quantum Limit. *Physical Review*, 163:816–835, November 1967. doi: 10.1103/PhysRev.163.816. URL http://link.aps.org/doi/10.1103/PhysRev.163.816.

[117] V. J. Goldman, D. C. Tsui, and J. E. Cunningham. Observation of intrinsic bistability in resonant tunneling structures. *Physical Review Letters*, 58:1256–1259, March 1987. doi: 10.1103/PhysRevLett.58.1256. URL http://link.aps.org/doi/10.1103/PhysRevLett.58.1256.

[118] T. C. L. G. Sollner. Comment on "Observation of intrinsic bistability in resonant-tunneling structures". *Physical Review Letters*, 59:1622–1622, October 1987. doi: 10.1103/PhysRevLett.59.1622. URL http://link.aps.org/doi/10.1103/PhysRevLett.59.1622.

[119] V. J. Goldman, D. C. Tsui, and J. E. Cunningham. Goldman, Tsui, and Cunningham reply. *Physical Review Letters*, 59:1623–1623, October 1987. doi: 10.1103/PhysRevLett.59.1623. URL http://link.aps.org/doi/10.1103/PhysRevLett.59.1623.

[120] F. W. Sheard and G. A. Toombs. Space-charge buildup and bistability in resonant-tunneling double-barrier structures. *Applied Physics Letters*, 52(15):1228–1230, April 1988. doi: 10.1063/1.99165. URL http://scitation.aip.org/content/aip/journal/apl/52/15/10.1063/1.99165.

[121] M. Büttiker. Coherent and sequential tunneling in series barriers. *IBM Journal of Research and Development*, 32(1):63–75, January 1988. ISSN 0018–8646. doi: 10.1147/rd.321.0063. URL http://ieeexplore.ieee.org/xpl/articleDetails.jsp?arnumber=5390027.

[122] J. H. Davies. *The Physics of Low-dimensional Semiconductors: An Introduction*. Cambridge University Press, 1997. ISBN 9780521484916.

[123] R. E. Miles, G. Millington, R. D. Pollard, D. P. Steenson, J. M. Chamberlain, and M. Henini. Accurate equivalent circuit model of resonant tunnelling diodes. *Electronics Letters*, 27(5):427–428, February 1991. ISSN 0013–5194. doi: 10.1049/el:19910270. URL http://ieeexplore.ieee.org/xpls/abs_all.jsp?arnumber=64305.

[124] A. Zaslavsky, D. C. Tsui, M. Santos, and M. Shayegan. Resonant tunneling of two-dimensional electrons into one-dimensional subbands of a quantum wire. *Applied Physics Letters*, 58(13):1440–1442, April 1991. doi: 10.1063/1.105192. URL http://scitation.aip.org/content/aip/journal/apl/58/13/10.1063/1.105192.

[125] N. Mori, P. H. Beton, J. Wang, and L. Eaves. Theory of resonant tunneling through a quantum wire. *Physical Review B*, 51:1735–1742, January 1995. doi: 10.1103/PhysRevB.51.1735. URL http://link.aps.org/doi/10.1103/PhysRevB.51.1735.

[126] S. Luryi and F. Capasso. Resonant tunneling of two-dimensional electrons through a quantum wire: A negative transconductance device. *Applied Physics Letters*, 47(12):1347–1349, December 1985. doi: 10.1063/1.96276. URL http://scitation.aip.org/content/aip/journal/apl/47/12/10.1063/1.96276.

[127] I. E. Itskevich, T. Ihn, A. Thornton, M. Henini, T. J. Foster, P. Moriarty, A. Nogaret, P. H. Beton, L. Eaves, and P. C. Main. Resonant magnetotunneling through individual self-assembled InAs quantum dots. *Physical Review B*, 54:16401–16404, December 1996. doi: 10.1103/PhysRevB.54.16401. URL http://link.aps.org/doi/10.1103/PhysRevB.54.16401.

[128] M. Fukuda, K. Nakagawa, S. Miyazaki, and M. Hirose. Resonant tunneling through a self-assembled Si quantum dot. *Applied Physics Let-*

ters, 70(17):2291–2293, April 1997. doi: 10.1063/1.118816. URL http://scitation.aip.org/content/aip/journal/apl/70/17/10.1063/1.118816.

[129] T.-K. Suzuki, K. Nomoto, K. Taira, and I. Hase. Tunneling Spectroscopy of InAs Wetting Layers and Self-Assembled Quantum Dots: Resonant Tunneling through Two- and Zero-Dimensional Electronic States. *Japanese Journal of Applied Physics*, 36(3B):1917–1921, March 1997. URL http://stacks.iop.org/1347-4065/36/i=3S/a=1917.

[130] E. E. Vdovin, A. Levin, A. Patanè, L. Eaves, P. C. Main, Y. N. Khanin, Yu. V. Dubrovskii, M. Henini, and G. Hill. Imaging the Electron Wave Function in Self-Assembled Quantum Dots. *Science*, 290(5489):122–124, October 2000. doi: 10.1126/science.290.5489.122. URL http://www.sciencemag.org/content/290/5489/122.abstract.

[131] E. E. Vdovin, Y. N. Khanin, O. Makarovsky, Y. V. Dubrovskii, A. Patanè, L. Eaves, M. Henini, C. J. Mellor, K. A. Benedict, and R. Airey. Magnetoanisotropy of electron-correlation-enhanced tunneling through a quantum dot. *Physical Review B*, 75:115315, March 2007. doi: 10.1103/PhysRevB.75.115315. URL http://link.aps.org/doi/10.1103/PhysRevB.75.115315.

[132] O. Makarovsky, E. E. Vdovin, A. Patanè, L. Eaves, M. N. Makhonin, A. I. Tartakovskii, and M. Hopkinson. Laser Location and Manipulation of a Single Quantum Tunneling Channel in an InAs Quantum Dot. *Physical Review Letters*, 108:117402, March 2012. doi: 10.1103/PhysRevLett.108.117402. URL http://link.aps.org/doi/10.1103/PhysRevLett.108.117402.

[133] A. Patanè, R. J. A. Hill, L. Eaves, P. C. Main, M. Henini, M. L. Zambrano, A. Levin, N. Mori, C. Hamaguchi, Y. V. Dubrovskii, E. E. Vdovin, D. G. Austing, S. Tarucha, and G. Hill. Probing the quantum states of self-assembled InAs dots by magnetotunneling spectroscopy. *Physical Review B*, 65:165308, April 2002. doi: 10.1103/PhysRevB.65.165308. URL http://link.aps.org/doi/10.1103/PhysRevB.65.165308.

[134] E. E. Vdovin, O. Makarovsky, A. Patanè, L. Eaves, and Y. N. Khanin. Sensitive detection of photoexcited carriers by resonant tunneling through a single quantum dot. *Physical Review B*, 79:193311, May

2009. doi: 10.1103/PhysRevB.79.193311. URL http://link.aps.org/doi/10.1103/PhysRevB.79.193311.

[135] USA Stanford Research Systems, Inc. Digital Lock-In Amplifiers: SR810 and SR830 - DSP lock-in amplifiers February 2013. URL http://www.thinksrs.com/downloads/PDFs/Catalog/SR810830c.pdf. [Online; Accessed 17 April 2014].

[136] G. W. C. Kaye and T. H. Laby. *Tables of physical and chemical constants*. Longman, 1995. ISBN 9780582226296. URL http://www.kayelaby.npl.co.uk/. [Online; Accessed 8 February 2014].

[137] A. D. Rakić. Algorithm for the determination of intrinsic optical constants of metal films: application to aluminum. *Applied Optics*, 34(22):4755–4767, August 1995. doi: 10.1364/AO.34.004755. URL http://ao.osa.org/abstract.cfm?URI=ao-34-22-4755.

[138] W. M. Haynes. *CRC Handbook of Chemistry and Physics*. CRC Handbook of Chemistry and Physics. Taylor & Francis Limited, 94 edition, 2013. ISBN 9781466571143. URL http://www.hbcpnetbase.com/. [Online; Accessed 8 February 2014].